COMPRESSION BEHAVIOR, STRENGTH, AND DUCTILITY OF CONFINED CONCRETE AFTER INELASTIC TENSILE CYCLIC LOADING

CHARLES PANKOW FOUNDATION
Building Innovation through Research

Report to
Charles Pankow Foundation
RGA#3-10

by

Mujahid Noor

Stephen Pessiki

Richard Sause

ATLSS Report No. 13-04

September 2013

ATLSS is a National Center for Engineering Research on Advanced Technology for Large Structural Systems

117 ATLSS Drive
Bethlehem, PA 18015-4729

Phone: (610)758-3525
Fax: (610)758-5902

www.atlss.lehigh.edu
Email:inatl@lehigh.edu

COMPRESSION BEHAVIOR, STRENGTH, AND DUCTILITY OF CONFINED CONCRETE AFTER INELASTIC TENSILE CYCLIC LOADING

CHARLES PANKOW FOUNDATION
Building Innovation through Research

Report to
Charles Pankow Foundation
RGA#3-10

by

Mujahid Noor
Graduate Research Assistant

Stephen Pessiki
Professor of Structural Engineering
pessiki@lehigh.edu

Richard Sause
Professor of Structural Engineering
rs0c@lehigh.edu

ATLSS Report No. 13-04

September 2013

ATLSS is a National Center for Engineering Research on Advanced Technology for Large Structural Systems

117 ATLSS Drive
Bethlehem, PA 18015-4729

Phone: (610)758-3525
Fax: (610)758-5902

www.atlss.lehigh.edu
Email:inatl@lehigh.edu

ACKNOWLEDGEMENTS

The first author would like to appreciate the U.S. Department of State for providing his study program funding through a scholarship from the Fulbright Program.

The assistance of the Technical Staff of the Department of Civil and Environmental Engineering, ATLSS Engineering Research Center at Lehigh University, and Fritz Engineering Laboratory, where the tests were performed, is acknowledged.

The opinions, findings, and conclusions expressed in this report are those of the authors.

TABLE OF CONTENTS

LIST OF TABLES

LIST OF FIGURES

ABSTRACT

In this investigation, confined concrete specimens were tested to study the effects of inelastic tensile cyclic loading of the longitudinal mild steel reinforcement embedded in a confined concrete core on the behavior, strength, and ductility of the confined concrete. Repeated inelastic tensile deformations of the longitudinal mild steel reinforcement bars inside the confined concrete core cause large cracks in the confined concrete. Whether these inelastic steel deformations and cracks in the concrete affect the compression behavior, strength, and ductility of the confined concrete is studied.

The test specimens represent the critical confined concrete crushing height of the boundary zone confined concrete in a well-detailed reinforced concrete lateral-load-resisting wall. In this investigation, two identical 10 in. x 15 in. cross-section confined concrete test specimens were tested under two different ranges of quasi-static inelastic tensile cyclic loading.

The first specimen was tested under increasing tensile cyclic loading up to 4 times the tensile yielding strain limit of the longitudinal mild steel reinforcement bars of the confined concrete core. Then, the specimen was failed under compression loading. The second specimen was tested under increasing tensile cyclic loading up to 16 times the tensile yielding strain limit of the longitudinal mild steel reinforcement bars of the confined concrete core. Then, the specimen was failed under compression loading.

The test results for the two test specimens were compared to observe the effects of different levels of inelastic tensile cyclic loading of the longitudinal mild steel reinforcement bars inside the confined concrete. The test results were also compared with the theoretical results from previously developed confined concrete models under monotonic compression loading. These comparisons focused on the effects of tensile loading on the compression behavior, strength, and ductility of confined concrete under compression loading.

The confined concrete compression behavior, strength, and ductility were similar for the two test specimens with the two different inelastic tensile cyclic loading ranges. The difference in peak compression strength was 4.5%. The axial force versus axial deformation curves for the two test specimens were similar.

It was noted that after inelastic tensile deformation of the longitudinal mild steel reinforcement inside the confined concrete core, a compression load greater than the prior tensile load was required to close the cracks. In the inelastic tensile deformation load steps, the reversing compression strain in the reinforcement was small compared to the tensile strain. The compression stiffness and ductility of the confined concrete were not affected by inelastic tensile cyclic loading of the longitudinal mild steel reinforcement of the confined concrete core. There was a noticeable reduction in the compression strength of confined concrete. The peak compression strength of the confined concrete was smaller than the results of any of the theoretical confined concrete models that were considered.

CHAPTER 1

INTRODUCTION

1.1 OVERVIEW

In this investigation, confined concrete specimens were tested to study the effects of inelastic tensile cyclic loading of the longitudinal mild steel reinforcement embedded in a confined concrete core on the behavior, strength, and ductility of the confined concrete under compression loading. Repeated inelastic tensile deformations of the longitudinal mild steel reinforcement bars inside the confined concrete core cause large cracks in the confined concrete. Whether these inelastic steel deformations and cracks in the concrete affect the compression behavior, strength, and ductility of the confined concrete is studied.

This investigation focuses on the critical confined concrete crushing height of the boundary zone confined concrete in a well-detailed reinforced concrete lateral-load-resisting wall where the longitudinal mild steel reinforcement inside the confined core yields and develops a plastic hinge at the base of the wall. Figure 1-1 shows an unbonded post-tensioned cast-in-place concrete special structural wall. The figure shows a wall specimen tested by Rivera (2013). The test specimens in this report represent the confined concrete crushing height of boundary zone confined concrete of this lateral-load-resisting wall. Therefore, the material properties, concrete confinement geometry, and loading procedure for the test specimens are representative of the boundary zone confined concrete of the unbonded post-tensioned cast-in-place concrete special structural wall system. In this investigation, two identical 10 in. x 15 in. cross-section confined concrete specimens were studied to observe the effects of two different ranges of quasi-static inelastic tensile cyclic loading of the longitudinal mild steel reinforcement bars on the behavior, strength, and ductility of the confined concrete under compression loading.

Figure 1-2 shows an unbonded post-tensioned cast-in-place concrete special structural wall subjected to lateral loading with the critical confined concrete crushing height of the boundary zone confinement. Figure 1-3 shows base stress response in an unbonded PT CIP concrete special structural wall subjected to lateral loads. Confined concrete is often used in boundaries of a lateral-load-resisting wall. The confinement is referred to as boundary zone concrete confinement. Longitudinal mild steel reinforcement bars are embedded in the confined concrete to provide flexural strength to the wall, and for energy dissipation, these bars yield to dissipate seismic energy. Once the bars yield, a plastic hinge develops at the base of the wall. Unbonded post-tensioning, which gives inherent advantages to the seismic performance of the walls, is utilized in some lateral-load-resisting walls. The post-tensioning tendons contribute to lateral resistance and also provide an elastic restoring force to eliminate post-earthquake permanent deformations. In such walls, the tension and compression cycling loading ranges will exceed the elastic limit of the longitudinal mild steel reinforcement inside the confined concrete core under the design earthquake load.

It is unclear whether current concrete confinement models reported in the literature accurately predict the behavior and strength of confined concrete under compression after inelastic tensile cyclic loading is imposed on the longitudinal mild steel reinforcement bars of the confined concrete core. These models were developed for different loading conditions (i.e., only compression or cyclic compression loadings) and smaller tensile loading ranges (i.e., in the tensile elastic range). As reported by most researchers, the monotonic compression loading stress-strain curve forms an envelope to the cyclic-compression loading stress-strain response. The models do not include inelastic tensile deformations of the longitudinal mild steel reinforcement of the confined concrete core, along with the associated concrete cracking and gradual crack closure affects under reversal compression loading. Therefore, this research examines if the current confined concrete models accurately predict the behavior, strength, and ductility of boundary zone concrete confinement in reinforced concrete lateral-load-resisting walls where inelastic tensile cyclic loading is applied to the confined concrete.

1.2 RESEARCH OBJECTIVES

The core objective of this study is to investigate the effects of inelastic tensile cyclic loading of the longitudinal mild steel reinforcement bars inside the confined concrete core on the compression behavior, strength, and ductility of boundary zone confined concrete in unbonded post-tensioned lateral-load-resisting walls.

1.3 SUMMMARY OF APPROACH

In order to achieve the defined objective, the following approach is followed:

1. Conduct literature review of unbonded post-tensioned lateral-load-resisting walls; study boundary zone concrete confinements in unbonded post-tensioned lateral-load-resisting walls; and understand the code (i.e., ACI 318-11code) requirements for boundary zone concrete confinements in lateral-load-resisting reinforced concrete walls.

2. Conduct literature review of past research concerning unconfined concrete models for monotonic compression loading, confined concrete, and confined concrete models for monotonic compression and cyclic compression loading.

3. Develop an experimental program to evaluate the effect of tension and compression cyclic loading on the boundary zone confined concrete. This includes the design, reinforcement, instrumentation, concrete casting, curing, load setup, instrumentation calibration, and loading history of the test specimens.

4. Test the confined concrete specimens; plot and analyze test data; compare the tests results of the test specimens for the effect of different ranges of inelastic tensile cyclic loading of the longitudinal reinforcement inside the confined concrete on the behavior, strength, and ductility of confined concrete; and compare the test results with theoretical confined concrete models of monotonic compression loading for behavior, strength, and ductility.

1.4 SUMMARY OF FINDINGS

Below is a summary of the findings from this research:

1. The confined concrete behavior, compression strength, and ductility were similar for the two test specimens with two different inelastic tensile cyclic loading ranges. The difference in peak compression strength was 4.5%, and the compression stiffness and ductility were similar.

2. Based on comparison of the tests results with the theoretical models for monotonic compression loading, the compression stiffness and ductility of the confined concrete were not affected by inelastic tensile cyclic loading of the longitudinal mild steel reinforcement inside the confined concrete core.

3. It was noted that after inelastic tensile deformation of the longitudinal mild steel reinforcement inside the confined concrete core, the compression load required to close the cracks was greater than the prior tensile load. In the inelastic tensile deformation load steps, the reversing confined concrete compression strain was small compared to the tensile strain, and the reversing compression strain in longitudinal reinforcement bars was small compared to tensile strain.

4. In this research, it was assumed that the field-cured concrete cylinders correctly represented the in situ compression strength of the concrete in the test specimens. Based on this assumption and a comparison of experimental results with the theoretical models, there was a considerable reduction in the compression strength of the confined concrete of the test specimens. On average for the two test specimens, the strength reduction was 18% compared to the Mander (1988) model, 18% compared to the Chang and Mander (1994) model, and 14% compared to the Oh (2002) model for confined concrete.

1.5 ORGANIZATION OF REPORT

In total, this report has six chapters. The remainder of this report is organized into 5 chapters in accordance with the research approach summarized above.

Chapter 2 presents the literature review, including: (1) a review of the unbonded post-tensioned lateral-load-resisting walls; (2) a detailed study of boundary zone concrete confinements in unbonded post-tensioned walls including the ACI 318-11 Code requirements; (3) unconfined concrete models; (4) background information about confined concrete; and, (5) confined concrete models for monotonic compression, and the effects of compression cyclic loading on confined concrete.

Chapter 3 presents the details of the experimental program. This includes details of the test matrix, geometry of the test specimens, the loading configuration and procedure, instrumentation and instrumentation calibration, specified and actual properties of materials, design and actual capacities of test specimens, and fabrication details.

Chapter 4 presents the experimental data. This includes the instrumentation data, concrete cracking, and photographs and observations from different load steps.

Chapter 5 presents different analysis and findings of the investigation. The chapter includes: (1) obtaining the testing region deformation data from the specimen deformation plots; (2) load versus deformation models for the testing region of the test specimens based on theoretical concrete and confined concrete models for monotonic compression loading; (3) comparison of test specimens results for different ranges of inelastic tensile cyclic loading; (4) comparison of test results with the theoretical models for monotonic compression loading; and, (5) a detailed summary of finding of the investigation.

Chapter 6 summarizes important findings and conclusions obtained from the experimental program. Recommendations for future research work are ending the chapter and the report.

1.6 NOTATION

The following notation is used in this report. To the extent possible, the notation from Perez (2004) is followed.

A = cross-section area, in^2
A_g = gross area of concrete section at the testing region, in^2
A_b = area of a single longitudinal reinforcement bar, in^2
A_{st} = total area of all longitudinal reinforcement bars, in^2
A_c = area of confined concrete core, $b_c d_c$, in^2
A_{cc} = area of confined concrete core within centerlines of perimeter hoops excluding area of longitudinal reinforcement steel bars, in^2
A_e = area of effectively confined concrete core, in^2
A_{sh} = cross-sectional area of hoop, in^2
A_{sx} = total area of transverse reinforcement parallel to x-axis, in^2
A_{sy} = total area of transverse reinforcement parallel to y-axis, in^2
a = longer side of the rectangular concrete area enclosed by the hoop, in^2
a'' = equivalent confined concrete stress-block length measured from centerline of confining reinforcement, in.
b = testing region concrete dimension in x-direction (east-west direction), in.
b_c = confined concrete core dimension to center lines of perimeter hoop in x-direction (east-west direction), in.
CCC = limit state corresponding to crushing of confined concrete
CIP = cast-in-place
DEC = limit state corresponding to decompression at the wall base
c = distance from extreme compression fiber to neutral axis, in.
c_c = column concrete cover, in.
c_b = beam concrete cover, in.
c''_{llp} = post-spalling contact length at wall base measured from centerline of confining reinforcement at LLP, in.
d = testing region concrete dimension in y-direction (north-south direction), in.

d_b = nominal diameter of bar, in.
d_{fb} = nominal diameter of flexural bar, in.
d_c = concrete core dimension to center lines of perimeter hoop in y-direction (north-south direction), in.
d_s = diameter of circular hoops, in.
E_{ac} = secant slope of nonlinear ascending region of confined concrete, ksi
E_{au} = secant slope of nonlinear ascending region of unconfined concrete, ksi
E_c = elastic modulus of concrete, ksi
ELL = effective linear limit state
E_p = modulus of elasticity of PT steel, ksi
E_s = modulus of elasticity of steel, ksi
E_{su} = secant slope of unconfined concrete, ksi
E_{sc} = secant slope of confined concrete, ksi
E_{sec} = secant modulus of confined and unconfined concrete at peak stress, ksi
f_c = longitudinal concrete stress, ksi
f'_c = peak compressive strength of unconfined concrete, ksi
f_{cc} = confined concrete stress, ksi
f'_{cc} = peak compressive strength of confined concrete, ksi
f_{ci} = stress at the linear elastic limit, ksi
f_l = maximum lateral confining stress on concrete from transvers reinforcement, ksi
f'_l = effective lateral confining stress due to transverse reinforcement, ksi
f_{lx} = maximum lateral confining stress on concrete in x-direction, ksi
f'_{lx} = effective lateral confining stress on concrete in x-direction, ksi
f_{ly} = maximum lateral confining stress on concrete in y-direction, ksi
f'_{ly} = effective lateral confining stress on concrete in y-direction, ksi
f'_t = direct tensile strength of concrete, ksi
f_{l1} = smaller lateral confining stress, ksi
f_{l2} = larger lateral confining stress, ksi
f_{pu} = tensile strength of PT steel, ksi
f_s = longitudinal steel stress, ksi
f_{sh} = hoop reinforcement stress, ksi
f_{sl} = stress in longitudinal steel reinforcement, ksi
f_{ys} = yield stress of longitudinal reinforcement bars, ksi
f_{yh} = yield strength of confining steel or confining hoop, ksi
$g(\phi_c)$ = function reflecting the effect of confining pressure
H_{cr} = critical confined concrete crushing height, in.
HL = concrete crack size as small as hair line
HT = head-travel instrument, head-travel
H_w = total wall height, in.
h_b = height of beams, in.
h_c = total height of confined concrete column, in.
h_{cr} = height over which confining reinforcement is provided from the wall base, in.
h_s = clear spacing between top and bottom beams of the specimen, in.

h_x	=	maximum center-to-center horizontal spacing of crossties or hoop legs on all faces of the column, in.
k	=	stiffness, kip/in.
k_e	=	confinement effectiveness coefficient
k_1	=	triaxial factor for confined concrete
k_2	=	factor in confined concrete (as function of k_1)
LLP	=	limit state corresponding to yielding of PT steel
LC	=	load cell
LVDT	=	linear variable differential transformer
L_w	=	wall length, in.
l_b	=	width of test specimen (or length of beams), in.
l_{cr}	=	length over which confining reinforcement is provided from each end of the wall, in.
l_{dh}	=	development length in tension of deformed bar or deformed wire with a standard hook, measured from critical section to outside end of hook, in.
M_n	=	nominal moment, kip-in.
M_{nb}	=	nominal flexural capacity of beams, kip-in.
M_u	=	factored moment at a section, in.-lb
NLC	=	north-side load cell
NLVDT	=	displacement transducer on the north side
n	=	parameter in stress-strain function of confined concrete
PT	=	post-tensioned, post-tensioning
P	=	net load in the testing region of confined concrete column, kip
$P_{com\varepsilon 0}$	=	compression load in longitudinal mild steel reinforcement bar at zero strain at the last compression load step, kip
P_e	=	elastic compression load limit for the testing region, kip
P_{maxc}	=	maximum recorded axial compression load in the testing region at ε_{maxc}, kip
P_{maxt}	=	maximum recorded axial tensile load in the testing region at ε_{maxt}, kip
P_u	=	compression load from Universal Testing Machine, kip
P_y	=	tensile yielding load limit for the testing region, kip
RC	=	reinforced concrete
r	=	parameter in stress-strain function of confined concrete
r_a	=	ascending branch parameter for axial stress of confined concrete
r_{au}	=	ascending branch parameter for axial stress of unconfined concrete
r_d	=	descending branch parameter for axial stress of confined concrete
r_{du}	=	descending branch parameter for axial stress of unconfined concrete
SLC	=	south-side load cell
SLVDT	=	displacement transducer on the south side
s	=	center-to-center spacing between confinement hoop-pairs, in.
s'	=	clear vertical spacing between confinement hoop-pairs, in.
s''	=	least lateral dimension of the confined concrete section, in.
s_h	=	longitudinal spacing of the circular hoop reinforcement, in.
s_{vs}	=	vertical spacing of the shear stirrups in beams, in.
s_{hs}	=	horizontal spacing of the shear stirrups in beams, in.
TS01	=	test specimen 1

TS02	=	test specimen 2
t_w	=	wall thickness, in.
$t_w^{"}$	=	wall thickness measured between centerlines of confining reinforcement, in.
UTM	=	Universal Testing Machine
U_{cc}	=	strain energy stored by confined concrete per unit volume
U_{co}	=	strain energy stored by unconfined concrete per unit volume
U_{sc}	=	strain energy stored by longitudinal reinforcing steel in compression per unit volume of concrete core
U_{sh}	=	strain energy capacity of transverse confining steel per unit volume of concrete core
V	=	base shear, kip
V_{act}	=	total force applied by north and south side actuators, $V_{actn} + V_{acts}$, kip
V_{actn}	=	force applied by north-side actuator, kip
V_{acts}	=	force applied by south-side actuator, kip
V_t	=	total shear strength of a section, $V_c + V_s$, kip
V_c	=	shear strength capacity of the concrete section, kip
V_s	=	shear strength capacity of section due to shear stirrups, kip
V_{us}	=	upper bound for steel shear capacity in a concrete section, kip
V_u	=	factored shear force at a concrete section, kip
w	=	spacing of longitudinal bars in rectangular section, in.
w'	=	clear transverse spacing between adjacent longitudinal bars, in.
w_c	=	unit weight of concrete, pcf
β	=	stress-block depth factor
Δ	=	deformation, in.
Δ_t	=	deformation in the testing region, in.
Δ_h	=	deformation of the other parts of the test specimen (excluding testing region), in.
δ_u	=	design deformation, in.
ε	=	strain, in./in.
ε_c	=	strain in concrete, in./in.
ε'_c	=	strain at the peak strength of unconfined concrete, in./in.
ε'_{cc}	=	strain at the peak strength of confined concrete, in./in.
ε_{ci}	=	strain at the linear elastic limit of concrete, in./in.
ε_{cu}	=	ultimate concrete compressive strain, defined as strain at first hoop fracture, in./in.
ε_{maxc}	=	maximum compression strain in longitudinal mild steel reinforcement bar recorded by a strain gage, in./in.
ε_{maxe}	=	strain at the end of the test at zero axial load, in./in.
ε_{maxt}	=	maximum tensile strain in longitudinal mild steel reinforcement bar recorded by a strain gage, in./in.
ε_s	=	strain in reinforcement bar, in./in.
ε_{uh}	=	confinement steel strain at ultimate tensile stress, in./in.
ε_u	=	ultimate strain of reinforcement bars, in./in.
ε_y	=	yield strain of reinforcement bars, in./in.
ε_{us}	=	ultimate strain of longitudinal reinforcement bars, in./in.

ε_{ys}	=	yield strain of longitudinal reinforcement bars, in./in.
ε_{fs}	=	fracture strain of longitudinal reinforcement bars, in./in.
ε_{uh}	=	ultimate strain of confining reinforcement bars, in./in.
ε_{yh}	=	yield strain of confining reinforcement bars, in./in.
ε_{fh}	=	fracture strain of confining reinforcement bars, in./in.
Θ	=	lateral drift, in.
ρ_{cc}	=	ratio of area of longitudinal steel to area of core concrete of the section
ρ_h	=	ratio of area of hoop reinforcement
ρ_s	=	ratio of volume of transverse confining steel to volume of confined concrete core
ρ_{hor}	=	area ratio of horizontal reinforcement
ρ_{vert}	=	area ratio of vertical reinforcement
σ	=	stress, ksi
σ_{lat}	=	lateral stress due to confinement, ksi
ω_a	=	a strain ratio for the ascending branch of the Oh (2002) confined concrete stress-strain model
ω_u	=	a strain ratio for the ascending branch of the Oh (2002) concrete stress-strain model
ϕ	=	strength reduction factor for moment
ϕ_c	=	confining pressure ratio (f_l'/f_c')
ψ_e	=	factor used to modify development length based on reinforcement coating

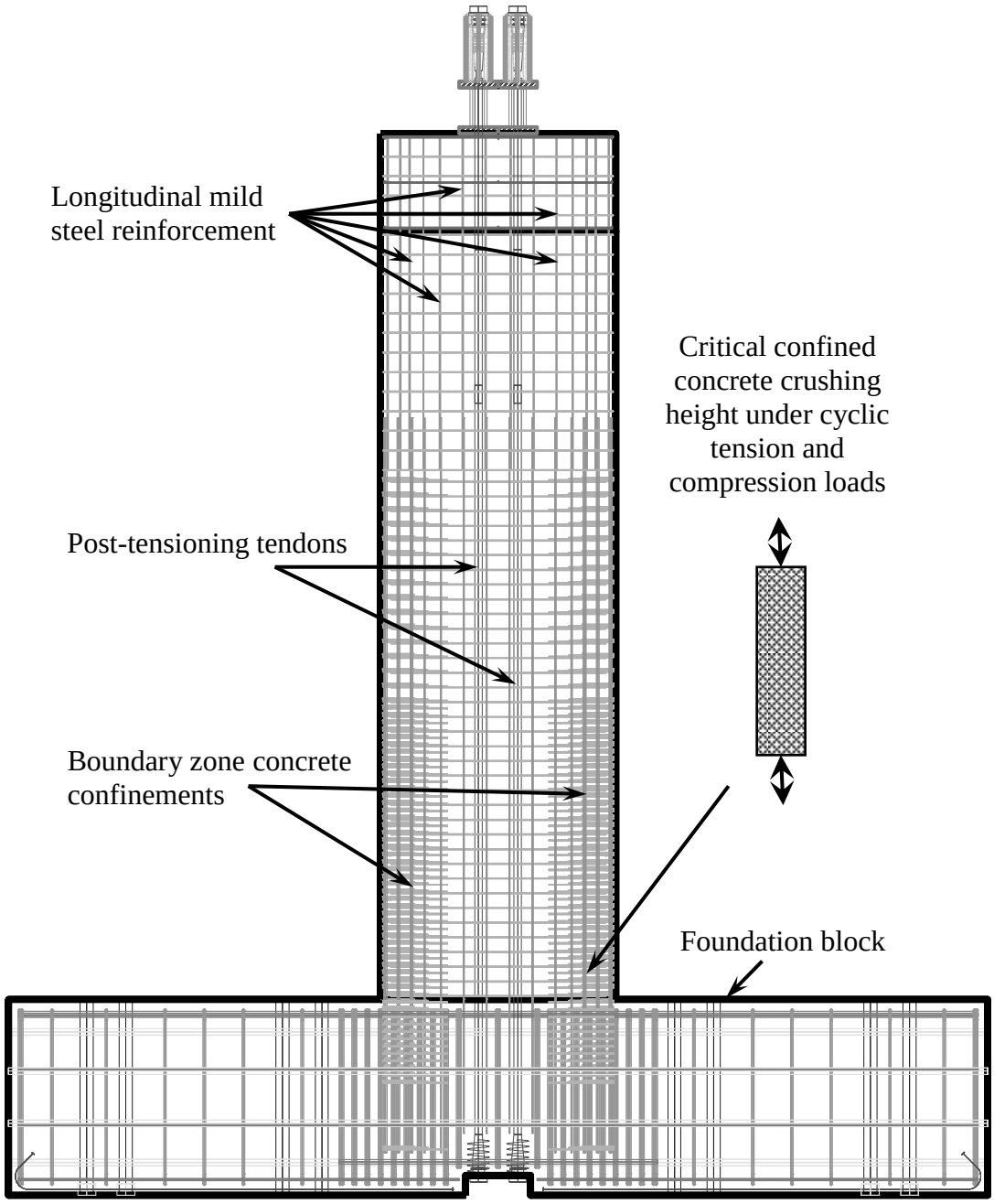

Figure 1-1: Unbonded PT CIP concrete special structural wall test specimen (Rivera, 2013)

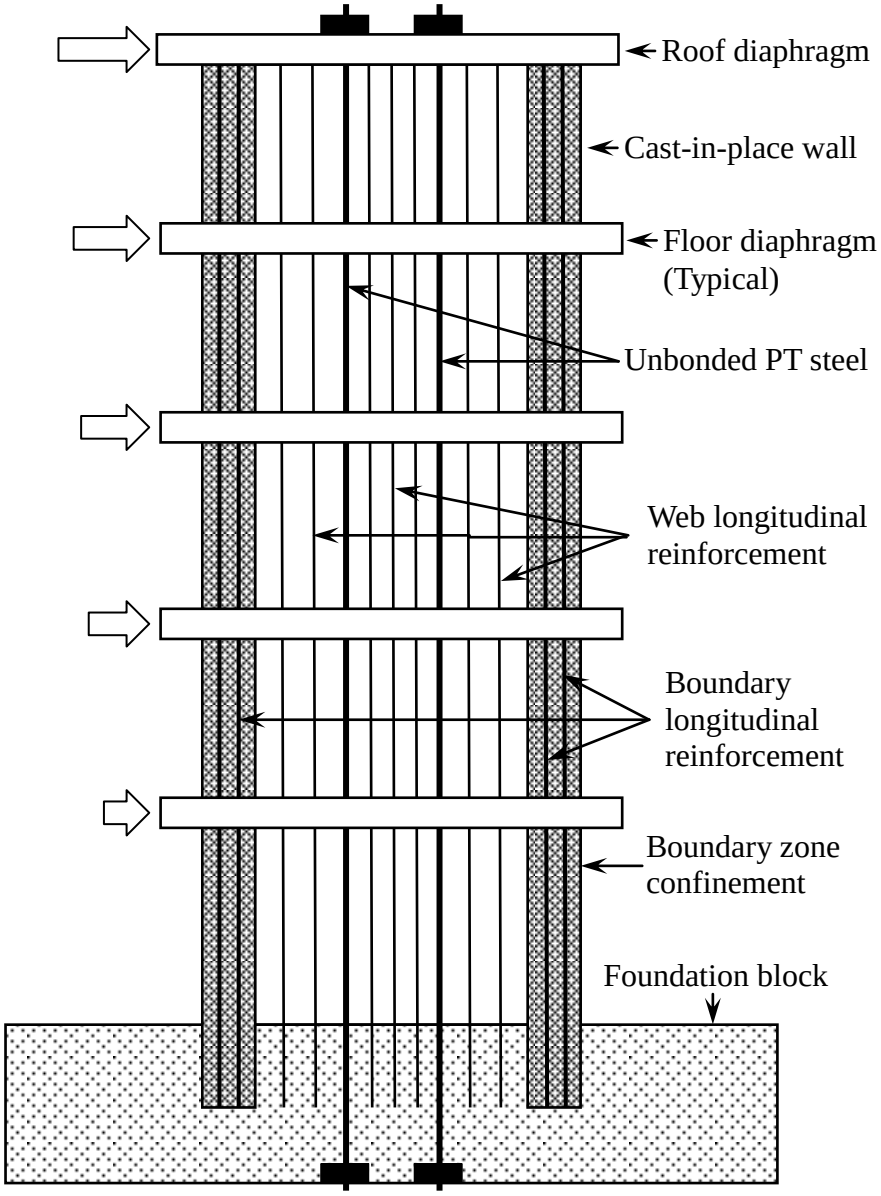

Figure 1-2: Unbonded PT CIP concrete special wall subjected to lateral loading

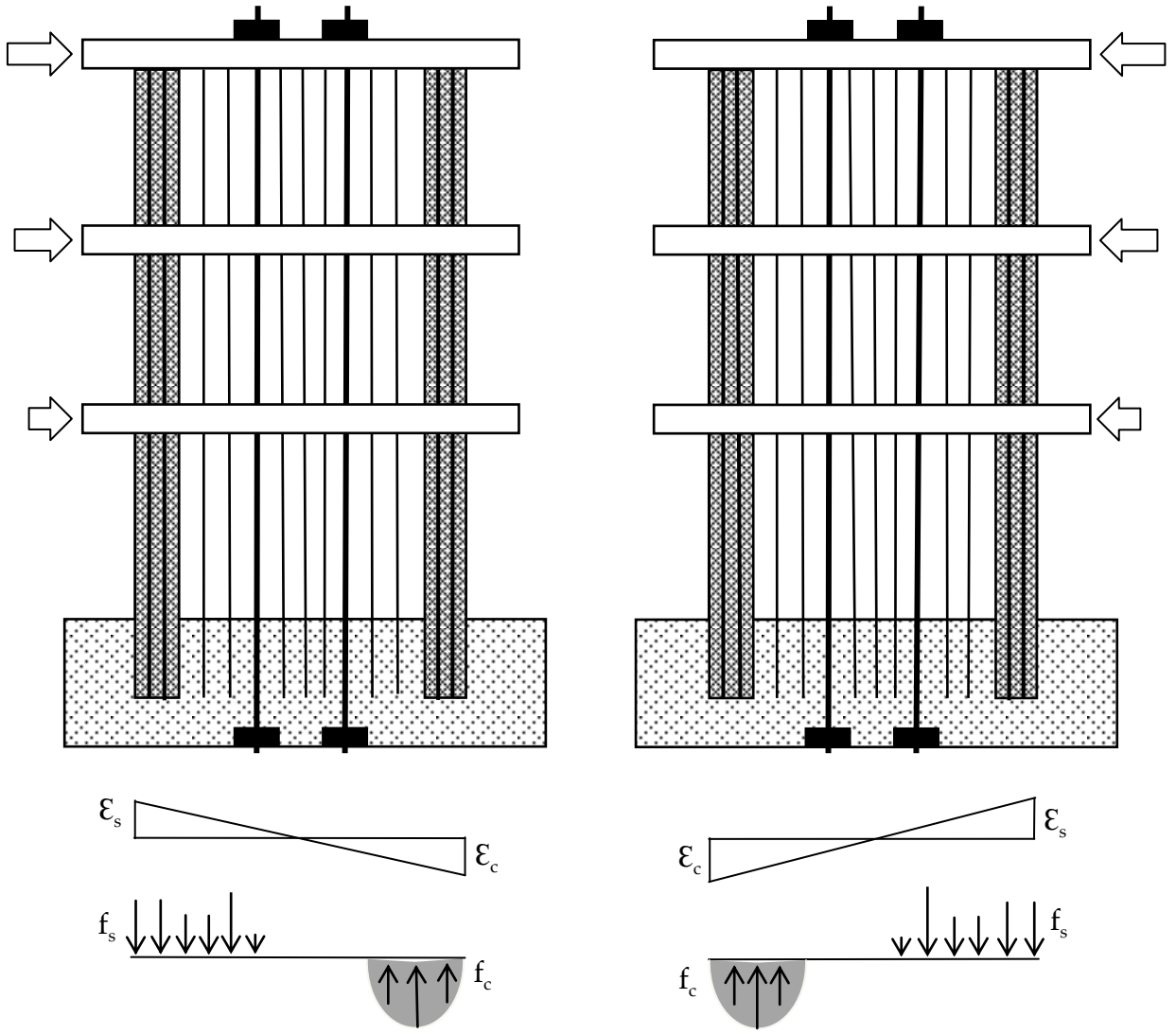

Figure 1-3: Base cyclic stresses in Unbonded PT CIP concrete special structural wall due to lateral loads

CHAPTER 2

BACKGROUND

2.1 INTRODUCTION

This chapter presents the background information relevant to the research. In this chapter lateral-load-resisting walls; concrete confinement in lateral-load-resisting walls; confined concrete crushing limit state; critical confined concrete crushing height; code requirements for confining reinforcement; concrete parameters; confined concrete, models for concrete and confined concrete under monotonic compression load, and ultimate concrete compressive strain are discussed.

All compression stresses, loads, strains, and deformations are treated as positive quantities. Conversely, all tensile stresses, loads, strains, and deformations are treated as negative quantities. This sign convention is followed throughout the report.

The transverse reinforcement (i.e., confinement hoop) can have different shape (i.e., circular, rectangular, or spiral). The test specimens in this report, which represent the boundary zone concrete confinement in a well-detailed reinforced concrete lateral-load-resisting wall, use rectangular confinement hoops. Therefore, all the formulation and details in this chapter cover concrete confinement details based on rectangular confinement hoops.

2.2 LATERAL-LOAD-RESISTING WALLS

Past experience indicates damage requiring significant repair occurs in structures constructed of conventional cast-in-place concrete due to strong earthquake ground motion. Therefore, investigations have been conducted to improve the performance of concrete structural walls.

Two intrinsic limitations in reinforced concrete structural walls are: (1) the required nonlinearity or softening of the wall caused by damage (i.e., yielding of reinforcing steel and softening of concrete in compression), and (2) post-earthquake residual lateral drift.
In some of the recent lateral-load-resisting wall systems the following methods are used to resolve the two problems: (1) the yielding of reinforcing steel and concrete softening is controlled by good detailing and proportioning practices, and utilizing well-confined concrete; and, (2) the post-earthquake residual lateral deformation of the wall is controlled by using post-tensioning tendons, which provides restoring force against the lateral load that enables the wall to return towards its original upright position.

In recent decades, several analytical and experimental studies have been conducted to develop more effective structural walls addressing the issue of self-centering, energy dissipation, increased performance, and less damage. The new lateral-load-resisting walls have performed better with less damage.

In all lateral-load-resisting walls, boundary zone concrete confinement is utilized. In some of the recent research on lateral-load-resisting walls, unbonded post-tensioning is

utilized. The defining features of post-tensioned lateral-load-resisting system are: (1) low damage; (2) good ductility; and, (3) self-centering tendency following an earthquake, which can minimize or virtually eliminate residual deformations following a major earthquake. The high-strength unbonded post-tensioning tendons allow gap opening at the base of the wall, providing ductility, and also providing an elastic restoring force which provides self-centering. The mild-steel reinforcement yields to dissipate seismic energy. The post-tensioning tendons are placed in ducts that remain ungrouted. This eliminates strain compatibility between post-tensioning tendons and the concrete. The deformation in post-tensioning steel is distributed uniformly over the entire unbonded length. Therefore, the unbonded post-tensioning tendons can achieve larger overall deformation before the post-tensioning tendons reach the yielding strain limit (Kurama, 1997).

Recently, many researches were conducted on different types of unbonded post-tensioned lateral-load-resisting wall systems. Some of the noticeable of such wall types are: (1) unbonded post-tensioned precast concrete wall; (2) unbonded post-tensioned hybrid precast concrete wall; and, (3) unbonded post-tensioned special reinforcement concrete wall (current research at Lehigh University). Table 2-1 adopted from Srivastava (2013) provides summary of the details of these concrete structural walls. For more details, the reader is referred to the referenced publications of the respective authors provided in the table.

The confined concrete test specimens in this report is representing the boundary zone concrete confinement of a reduced-scale prototype of unbonded post-tensioned cast-in-place concrete special structural wall being tested in Lehigh University. Figure 2-1 shows the reduced-scale prototype of unbonded post-tensioned cast-in-place concrete special structural wall. The prototype wall is 20 ft. long, 150 ft. high, and 2 ft. thick. Due to space limitation of the lab, the test wall dimensions were scaled down to 40% of the prototype wall. The confined concrete test specimens in this report are full-scale specimens of the 40% reduced scale boundary zone concrete confinement of the prototype wall.

Unbonded post-tensioned special RC wall is an alternative to the conventional special reinforced concrete wall. This alternative wall has the potential to significantly reduce reinforcement congestion and improve seismic performance compared to conventionally reinforced concrete wall deigned in compliance with ACI 318-11 Code. Post-tensioning is utilized as a means of self-centering of the wall. The unbonded PT special RC wall has distinct advantages over conventional cast-in-place special RC wall.

2.2.1 Concrete Confinement in Lateral-Load-Resisting Walls

The aspects of seismic performance of each concrete structural wall are fundamentally different to each other depending on materials proportioning, material types, performance mechanism and other factors. For the most part, in contemporary concrete structural walls, the components of construction are: (1) concrete; (3) mild steel reinforcement; (4) confinement reinforcement and longitudinal reinforcement inside the confined core; and, (2) post-tensioning tendons.

A PT wall develops relatively higher compressive stresses at the boundary zones. Therefore, for efficient proportioning of construction components, typically concrete compressive strength of 6-10 ksi is used. Post-tensioning tendons are left unbonded. The tendons are fixed at both ends (i.e., fixed end and stressing end) using a multi-strand anchorage. This way the change in stress in tendons can only occur by vertical deformation between anchors. Mild steel reinforcement is used in wall boundaries for increasing ductility. ASTM A706 reinforcement is recommended by ACI 318-11 Code. The boundary zone mild steel reinforcement is essential for both tension and compression. To preclude undesirable shear failure modes, heavy horizontal reinforcing is also used.

The confinement reinforcement is part of the mild steel reinforcement responsible for ensuring a ductile flexural response. Concrete confinements at the boundary zones prevent premature crushing of the concrete and buckling of the longitudinal reinforcement bars. Sometime concrete confinements are utilized between boundaries, in the body of the wall to stabilize the diagonal compression struts that form the shear mechanisms. ASTM A706 headed reinforcement is typically preferred to be used; to facilitate constructability by minimizing congestion and provide superior confinement.

2.2.2 Confined Concrete Crushing Limit State

A structural limit state for a wall is defined as the state of the wall beyond which the wall does not fulfill all the relevant criteria and assumptions associated with that state of the wall. These wall structural limit states may be based on strains, deformations, stresses, forces, or extent of damage to the wall (Srivastava, 2013).

Figure 2-2 and Figure 2-3 show the base shear-roof drift (V-Θ) relationship with idealized structural limit states from Kurama (1997) and Perez (2004), respectively, for a hybrid wall with longitudinal mild steel reinforcement under monotonic lateral load. Based on this idealization, crushing of the boundary zone concrete confinement (CCC) is the last limit state. That is, in a well-designed wall, failure of the wall occurs when the boundary zone confined concrete at the base of the wall fails in compression. Crushing of the confined concrete happens at an ultimate concrete compressive strain, ε_{cu}, which is reached when the first transverse confinement hoop fracture.

From the studies conducted by Kurama (1997), Perez (2004), and Srivastava (2013), it is concluded that in a well-designed lateral-load-resisting wall, crushing of the confined concrete is not the early controlling limit state. However, the boundary zone concrete confinement is the critical structural part of the wall, and need to be properly detailed. Once the boundary zone concrete confinement fails, the wall is considered to have failed. Therefore, an investigation is conducted to understand the behavior, strength, and ductility of boundary zone concrete confinement in lateral-load-resisting walls.

2.2.3 Critical Confined Concrete Crushing Height

In lateral-load resisting walls, the critical confined concrete crushing height is the height of the boundary zone concrete confinement from the wall base over which the confined concrete crushing is expected to occur. This height is denoted by H_{cr}.

In lateral-load-resisting walls, the crushing of the confined concrete occurs at the ultimate confined concrete strain, ε_{cu}, at the extreme compression edge of wall. This is reached when the first confining hoop fractures. ε_{cu} is obtained from experiments or from analytical confined concrete stress-strain relationships (e.g., Mander et al. 1988).
According to El-sheikh et al. (1997), H_{cr} can be determined as follows:

$$H_{cr} = 2t_w'' \quad \text{if} \quad t_w'' \leq 2a'' \qquad (2\text{-}1)$$

$$H_{cr} = 2a'' \quad \text{if} \quad t_w'' > 2a'' \qquad (2\text{-}2)$$

where,
t_w'' is the wall thickness measured between centerlines of confining reinforcement, and a'' is the equivalent confined concrete stress block length measured from centerline of confining reinforcement.

$$a'' = \beta c_{llp}'' \qquad (2\text{-}3)$$

β is the equivalent stress block parameter for confined concrete and is equal to 1; and c_{llp}'' is the post-spalling contact length at wall base measured from centerline of confining reinforcement at LLP. For more details, the reader is referred to Perez et al. (2004).

2.3 ACI 318 CODE REQUIREMENTS FOR CONFINING REINFORCEMENT

As detailed by ACI 318-11 Code, the critical confined concrete crushing regions in reinforced concrete structures for lateral loads need to be carefully detailed for ductility to ensure that large earthquakes do not cause collapse. An important design consideration for ductility of plastic hinge region of reinforced concrete element is the provision of sufficient transverse reinforcement (i.e., rectangular hoops) to: (1) improve compression ductility of concrete; (2) prevent buckling of longitudinal reinforcement; and, (3) to prevent shear failure. Based on this criterion, heavy concrete confinement reinforcement is utilized at the wall boundaries.

Figure 2-4 and Figure 2-5 show the details and locations of the vertical mild steel reinforcement bars for the two unbonded post-tensioned cast-in-place concrete special structural wall specimens to be tested in ATLSS Center at Lehigh University. The longitudinal (i.e., vertical) mild steel reinforcement used in lateral-load-resisting walls for flexural strength and ductility is separated into two zones, field and boundary reinforcement. The flexural strength of the wall varies depending on the amount and location of the longitudinal (i.e., vertical) mild steel reinforcement bars.

According to ACI 318-11 Section 21.9.6.2, the compression zones need to be reinforced with confining reinforcement (referred to as special boundary element reinforcement in the code) up to a distance equal to the largest neutral axis depth from the wall ends where the largest neutral axis depth should be taken greater or equal to $L_w/(600(\delta_u/H_w))$ (See ACI 318-11 Code Section 21.9.6.4). According to the ACI 318-11 Code Section 21.9.6.2, the confining reinforcement is to extend vertically from the wall base no less than the larger of L_w (here 72 in.) or $M_u/4V_u$. The height of the plastic hinge confining reinforcement is denoted by H_{cr}, which is measured 16.5 in. in current unbonded post-

tensioned cast-in-place concrete special structural wall investigation, measured from the wall base. According to ACI 318-11 Code Section 21.9.6.3, the confining reinforcement is permitted to be discontinued where the calculated compressive stress is less than $0.15f'_c$.

The minimum amount of confining reinforcement specified by the ACI 318-11 Code depends on the confining reinforcement details used (e.g., hoop or spiral reinforcement). For hoop reinforcement, the amount of confining reinforcement is defined in terms of an area ratio, ρ_h (i.e., the ratio of hoop reinforcement cross-sectional area to the transverse core area confined by the hoop reinforcement). According to the ACI 318-11 Code Section 21.6.4.4, ρ_h should not be less than $0.09(f'_c/f_{sy})$ (Eq. 21-5 of ACI 318-11).

According to the ACI 318-11 Code Chapter 21 Section 21.9.6.4, the minimum length of the confining reinforcement should be the larger of $(c - 0.1L_w)$ and $(c/2)$, where c is the largest neutral axis depth. Therefore, as shown in Figure 2-4, confining reinforcement length, l_{cr}, measured from each end of the wall, is determined to be 13.5 in. on both ends of the wall. The primary longitudinal steel of the boundary element (eight bars as shown in Figure 2-4) are located within the first 9.5 in. from the wall ends. The transverse reinforcement is extended another 4.0 in. to include two longitudinal web reinforcement bars within the confined concrete. The confining reinforcement (i.e., boundary element longitudinal reinforcement) is defined as the eight bars as shown in Figure 2-4).

According to the ACI 318-11 Code Section 21.6.4.3, spacing of the confining reinforcement, s, should not exceed the smallest of $t_w/4$ (in.), six times the diameter of the longitudinal reinforcement bar (in.), nor $4+((14-h_x)/3)$(in.) (this term not to exceed 6 in. nor be less than 4 in.), where h_x is the maximum center-to-center horizontal spacing of crossties or hoop legs on all faces of the wall (in.).

In the light of the above detailing and requirements, the confined concrete test specimens reported in this report were developed and designed. The confined concrete test specimens represent the critical confined concrete crushing height, H_{cr}, of the boundary zone concrete confinements of unbonded post-tensioned cast-in-place concrete special structural wall.

2.4 CONCRETE PARAMETERS

This section presents formulas that are used to estimate the modulus of elasticity, strain at the maximum stress, and tensile strength of concrete.

The equation proposed by Pauw (1960) for modulus of elasticity of concrete that was adopted into the ACI 318 Code (1963) is still used in ACI 318-11 for both normal and lightweight concrete.

$$E_c = 33w_c^{1.5}\sqrt{f'_c} \qquad (2\text{-}4)$$

in which f'_c is in psi and w_c is in pcf.

For normal weight concrete, the ACI code assumes a weight of 145 pcf; therefore Eq. 2-4 can be simplified as follow:

$$E_c = 57000\sqrt{f'_c} \quad \text{psi} \qquad (2\text{-}5)$$

Unless specifically state, this equation is used to estimate modulus of elasticity of concrete throughout the report.

The strain ε'_c corresponding to the maximum stress f'_c for concrete has been found to be a function of the maximum stress, however, some authors have taken it a constant value, normally 0.002 (Park and Paulay, 1975). Different researchers proposed different functions for estimating the strain at the maximum stress, ε'_c.

Sulayfani and Lamirault (1987) suggested the following expression:

$$\varepsilon'_c = 2.5 \text{ x } 10^{-4} f_c'^{0.246} \qquad (2\text{-}6)$$

In this equation f'_c is in psi (Chang and Mander, 1994).

Unless specifically stated, the following simplified form of the above equation is used to estimate concrete strain at the maximum stress, ε'_c, throughout the report.

$$\varepsilon'_c = 2.5 \text{ x } 10^{-4} f_c'^{0.25} \qquad (2\text{-}7)$$

Different researcher proposed different formula for direct tensile strength of concrete. Paulay and Priestley in their book "Seismic Design of Reinforced Concrete and Masonry Buildings" (1992) proposed the following formula:

$$f'_t = 6.0\sqrt{f'_c(\text{psi})} \qquad (2.8)$$

Unless specifically stated, the this equation is used to estimate the direct tensile strength of concrete, f'_t, throughout the report.

2.5 CONFINED CONCRETE

Figure 2-6 and Figure 2-7 shows a 3D and 2D schematic of the effective confined concrete core based on different setups of longitudinal mild steel reinforcement inside the confined concrete. Figure 2-8 shows schematic of the effect of addition of longitudinal reinforcement bars and cross-ties on confined concrete core from the top. The figures are adopted from Paultre and Légeron (2008).

Richart et al. (1928) were the first to observe that confined concrete showed greatly increased maximum compressive strength, increased stiffness, and extended strain at which the peak stress was reached. The confined concrete can sustain large deformation without substantial reduction of the load-bearing capacity and fails gradually in a ductile way.

Ductility of concrete is achieved by providing adequate transverse reinforcement to confine the concrete within the core region and to prevent buckling of the longitudinal compression reinforcement. Particularly sensitive are the critical confined concrete crushing regions in members supporting large axial loads, such as the base of boundary zones of reinforced concrete lateral-load-resisting walls, where inelastic deformation occurs to develop a full plastic hinge mechanism.

When unconfined concrete is stressed to large deformation values, high lateral tensile strains develop because of the formation and propagation of longitudinal microcracks. This results in instability and failure of the compression zone concrete. Closely-spaced transverse reinforcement in conjunction with longitudinal reinforcement is used to restrain the lateral expansion of the concrete, giving concrete higher capacity and sustaining higher compressive strain before failing.

The transverse reinforcement (confinement hoops) can be spiral, circular, rectangular, or square shape. Unlike the spiral and circular hoops, the rectangular or square hoops can only apply full confining reactions near the corners of the hoops as the pressure of the concrete against the sides of the hoops tends to bend the sides outward. This problem can be controlled by using overlapping hoops or cross-ties.

The presence of longitudinal reinforcement bars that are well distributed around the perimeter of the section, and tied across the section, improve the concrete confinement. The concrete bears against the longitudinal reinforcement bars and the transverse reinforcement provide the confining reactions to the longitudinal bars.

Confinement of concrete is improved if transverse reinforcement spacing is reduced. There is a critical spacing of transverse reinforcement spacing above which the section midway between the transverse hoops will be ineffectively confined. However, investigations show that a more strict limitation on longitudinal spacing of confinement hoops is imposed by the need to avoid buckling of longitudinal reinforcement under compression load. Investigations indicates that this spacing, in plastic hinging regions, should not exceed more than six times the diameter of the longitudinal reinforcement bars to be restrained.

Concrete is considered confined when subjected to triaxial compression; the triaxial compression increases concrete capacity to sustain larger compressive strengths and deformations. (Montoya et al., 2001). As an example, KotsovosI (1987) shows the variation of the peak axial compressive stress sustained by a concrete cylinder with increasing confining pressure. It was noted that a small confining pressure of about 10 percent of the uniaxial cylinder compressive strength was sufficient to increase the load-bearing capacity of the specimen by as much as 50 percent.

To consider the increased strength of concrete due to confinement, Richart et al. (1928) proposed the well-known empirical formulas:

$$f'_{cc} = f'_c + k_1 \sigma_{lat} \qquad (2\text{-}9)$$

$$\varepsilon'_{cc} = \varepsilon'_c(1 + k_2 \frac{f_l}{f'_c}) \quad (2\text{-}10)$$

Where k_1 is the so-called triaxial factor and is found to be 4.1 and $k_2 = 5k_1$. Although newer test results have suggested a modification of this relation, the basic approach for determining the confined strength is the same.

The maximum effective lateral pressure f_l that can be applied to concrete by the hoops happens when the hoops are stressed to their yield strength, f_{yh}. Referring to the free body diagram in Figure 2-9, the maximum effective lateral stress in a circular confinement hoops can be found:

$$f_l = \frac{2 f_{yh} A_{sh}}{d_s s_h} \quad (2\text{-}11)$$

where, A_{sh} is the cross-section area of hoop; d_s is the diameter of the circular hoops; and s_h is the longitudinal spacing of the circular hoop reinforcement.

Blume, Newmark and Corning (1961) proposed an expression to calculate the strength increase in concrete confinements by rectangular hoops. They used the following expression to calculate the lateral confinement stress;

$$f_l = 0.5(\frac{2 f_{sh} A_{sh}}{a s_h}) \quad (2\text{-}12)$$

where the term a is the longer side of the rectangular concrete area enclosed by the hoop; f_{sh} is the stress in hoop; and A_{sh} is the hoop cross-sectional area.

Many other researchers proposed new expressions and stress-strain relation for confined concrete.

2.6 CONCRETE STRESS-STRAIN MODELS

This section presents some of the axial stress-strain models for concrete and unconfined concrete under monotonic compression loading used in this report.

2.6.1 Unconfined Concrete Models

Different equations were developed for axial stress-strain relations of concrete, but the stress-strain relation equation known as Popovics (1973) (Mander et al. 1988a; Tsai 1988) has proven to be very useful in describing the monotonic compressive stress-strain curve for concrete (Chang and Mander, 1994).

$$y = \frac{rx}{r-1+x^r} \quad (2\text{-}13)$$

where, r = n/(n-1).

Figure 2-10 shows this equation for different values of n. The equation proposed by Popovics, has been used extensively in representing the complete stress-strain relationship for unconfined and confined concrete. The descending branch of this

equation is very sensitive to the value of n (initial stiffness ratio); therefore, if precise estimation of the descending branch is needed, it is necessary to choose this value carefully (Chang and Mander, 1994).

Tsai (1988) recommend a generalized form of the Popovics equation as follows:

$$y = \frac{nx}{1+\left(n-\frac{r}{r-1}\right)x+\frac{x^r}{r-1}} \qquad (2\text{-}14)$$

Where, r = factor to control the descending branch of the stress-strain relation.

Figure 2-11 shows this equation for n=1.5 and different values of r. By taking n = r/(r-1), Eq. 2-14 reduces to Eq. 2-13 (Popovics equation). The ascending branch and descending branch of Popovics' equation have control on the initial slope. Tsai's equation has control on both the ascending branch (initial slope) and the descending branch.

From among the different equations proposed by investigators, the equations proposed by Tsai and Popovics are found to be the most flexible and general, and by comparing their behavior it was concluded that Tsai's equation is the most suitable to represent the behavior of both confined and unconfined concrete.

Mander et al. (1988a) concrete model uses Popovics' equation which is really a special case of Tsai's equation. The Mander et al. (1988a) model in its present form has difficulty managing the slope of the falling (descending) branch when high strength concrete or high strength transverse confining reinforcement is used (Chang and Mander, 1994).

However, different axial stress-strain models for unconfined concrete under monotonic compression loading exist in literatures. Here three of such models: (1) Mander et al. (1988); (2) Chang and Mander (1994); and, (3) Oh (2002) are discussed. For simplicity, hereafter, Mander et al. (1988) model for unconfined concrete is referred as Mander (1988) model.

Mander (1988) Concrete Model

Figure 2-12 shows the stress-strain models plotted for 6 ksi, 8 ksi, 10 ksi, and 12 ksi concrete compressive strength based on Mander (1988) concrete model.

The stress-strain model developed by Mander (1988) can be applied to both confined and unconfined concrete. The stress-strain formulation for axial compression loading of concrete developed by Mander (1988) is based on Popovics' model. Same as Popovics, Mander model uses one parameter controlling the ascending and descending regions of the curve. That is, the descending region is not independent of the ascending region of the curve.

Chang and Mander (1994) Concrete Model

Figure 2-13 shows the stress-strain models plotted for 6 ksi, 8 ksi, 10 ksi, and 12 ksi concrete compressive strength based on Chang and Mander (1994) concrete model.

The equation to describe the monotonic compressive stress-strain curve for unconfined concrete is based on Tsai's equation. Chang and Mander (1994) proposed their own equation to estimate the modulus of elasticity of concrete. The strain at the peak stress of concrete is estimated using the equation from Sulayfani and Lamirault (1987).

The stress-strain equation obtained by Chang and Mander (1994) compared well with those suggested by Collins and Mitchell (1991). In the original equation used by Collins and Mitchell (1991), a non-continuous factor is used while the single equation developed by Chang and Mander (1994) has the advantage of being adaptable for both confined and unconfined concrete. This allows the descending branch to shift either upward or downward, using parameters n and r.

Oh (2002) Concrete Model

Figure 2-14 shows the stress-strain models plotted for 6 ksi, 8 ksi, 10 ksi, and 12 ksi concrete compressive strength based on Oh (2002) concrete model.

Oh (2002) model for unconfined concrete under monotonic compression loading is composed of three distinct regions: (1) elastic branch; (2) ascending; and, (3) descending branch. Unlike Popovics and Mander models, Oh model uses two separate parameters to control the ascending and descending regions of the curve. The descending region is independent of the ascending region of the curve. In Oh (2002) model, the linear elastic region is between 0-30 percent of the peak stress of unconfined concrete. The descending region is defined using a function different than the ascending region, which gives the descending region independent behavior. The function is confirming to the one used in Popovics model.

2.6.2 Confined Concrete Models

This section presents the monotonic compression models for confined concrete. The monotonic compression stress-strain models for confined concrete are based on the theory of the stress-strain function developed for unconfined concrete. The parts that remain different are: (1) the correlation between the effective lateral stress and axial loading; (2) peak stress and corresponding strain; and, (3) post-peak behavior.

Many models exist for the stress-strain functions of confined concrete under monotonic compression loading. Among the recent proposed models are the models by Kent and Park (1971); Park et al. (1982); Sheikh and Uzumeri (1982); Fafitis and Shah (1985); Mander et al. (1988); Yeh and Sheikh (1988); and Sheikh and Yeh (1990).

The pre-peak (ascending) branch of stress-strain functions in all models was presented using a curve function. But researchers are different on the post-peak (descending) branch of the stress-strain function. Some researchers such as Mander et al. (1988)

proposed a continuous curve from the pre-peak (ascending) branch while others researchers such as Sheikh and Uzumeri (1982) and Kent and Park (1971) proposed linear descending functions.

However, different axial stress-strain models for confined concrete under monotonic compression loading exist in literatures. Here three of such models: (1) Mander et al. (1988); (2) Chang and Mander (1994); and, (3) Oh (2002) are discussed. For simplicity, hereafter, Mander et al. (1988) model for confined concrete is referred as Mander (1988) model.

Mander (1988) model claims to be a generalized model that is applicable to different section shapes. Chang and Mander (1994) is a modification of some parameters of the Mander (1988) model. Oh (2002) plasticity model, unlike Mander (1988) model, uses two distinct parameters controlling the slope of the ascending and descending branches of the stress-strain functions for confined concrete.

The point to be noticed from Kent and Park (1971) model, Park et al. (1982) model, and Sheikh and Uzumeri (1982) model is the minimum stress limit at the post-peak (descending) branch of the stress-strain model for monotonic compression loading. In Sheikh and Uzumeri (1982) model, the descending branch of the stress-strain curve up to 30 percent of the maximum stress is a straight line, the slope of which is given in Sheikh and Uzumeri (1982), and after the 30 percent of the maximum stress, the stress is presented by a horizontal line, $f_{cc}(\varepsilon) = 0.3f'_{cc}$. Kent and Park (1971) proposed a minimum stress limit of $0.2f'_{cc}$ at the post-peak branch of the model.

Mander (1994) Confined Concrete Model

Mander (1988) developed a stress-strain model for concrete subjected to monotonic compression loading and confined by any common types of transverse confining steel (i.e., rectangular hoops) with or without additional cross ties. A single equation was derived for stress-strain relation where the maximum unconfined concrete stress and effective lateral confining stress are the determining factors as was in previous researches. The effective lateral confining stress is dependent on the configuration of the transverse and longitudinal reinforcement which, in turn, determine the type of confinement.

The Mander et al. (1988) model for stress-strain curve of confined concrete under monotonic compression loading is based on the empirical formula proposed by Popovics (1973). As Popovics (1973) stress-strain function is a single-piece function; therefor, in Mander (1988) model there is only one parameter that controls the slope of both ascending and descending branch of the function.

Chang and Mander (1994) Confined Concrete Model

Chang and Mander (1994) proposed simplified equations for estimating the peak strength and the corresponding strain of confined concrete used in Mander (1988). The confined concrete stress-strain function for Chang and Mander (1994) is the same as in Mander

(1988). As the post-peak (i.e., descending) region slope of the confined concrete model of Mander (1988) is sensitive to the peak strength and the corresponding strain value of the confined concrete; therefore, the confined concrete stress-strain function for Chang and Mander (1994) differs with Mander (1988).

Oh (2002) Confined Concrete Model

The empirical monotonic compression loading stress-strain model developed in Oh (2002) for confined concrete is a plasticity model. The descending branch is defined using a function and *r*-parameter different than the ascending branch, which gives the descending branch independent behavior.

Based on Oh's observations the *r*-parameter from Mander (1988) model provides reasonable values for $\phi_c > 0.5$, but for $\phi_c \leq 0.5$, the *r*-parameter from Mander model overestimate post-peak strength. That is, the descending region slope is too flat. Therefore, Oh (2002) developed a criterion to rectify this difference.

Based on Oh's model, when:

$$\phi_c = 0,\ r_d = \left(1 - \frac{E_{su}}{E_c}\right) r_{du} \quad (2\text{-}15)$$

when $0 < \phi_c \leq 0.5$, then;

$$g(\phi_c) = \left(1 - \frac{E_{su}}{E_c}\right) r_{du}(1 - 2\phi_c) + 2\phi_c, \quad (2\text{-}16)$$

and when $\phi_c > 0.5$, then r_d equals to the r-parameter from Mander (1988). That is, the value of $g(\phi_c) = 1$. Figure 2-15 shows the relation between ϕ_c versus $g(\phi_c)$ for different values of ϕ_c. Figure 2-16 shows the function $g(\phi_c)$ for different concrete strength.

2.7 ULTIMATE CONCRETE COMPRESSION STRAIN

The end of the useful strain limit of compression stress-strain model of confined concrete is called the ultimate concrete compression strain, ε_{cu}. The ultimate concrete compressive strain is defined as the longitudinal strain at which the first hoop (transverse reinforcement) fracture occurs, and that strain is considered the end of the useful limit of the stress-strain curve for confined core of the concrete (Scott et al. (1982), Mander et al. (1988)). As shown in current investigation, when the first hoop fractures, a sudden drop occurs in the compression strength of the confined concrete core due to reduction in confinement strength, and the compressed longitudinal bars start to buckle in large.

Number of investigators developed empirical equations for calculating the ultimate concrete compressive strain. Some of those equations are reported in Park and Paulay (1975). Mander et al. (1988) proposed a rational method for predicting the longitudinal concrete compressive strain at first hoop fracture based on energy balance approach.

$$U_{sh} = U_{cc} + U_{sc} - U_{co} \quad (2\text{-}17)$$

$$110\rho_s = \int_0^{\varepsilon_{cu}} f_{cu}\, d\varepsilon_c + \rho_{cc} \int_0^{\varepsilon_{cu}} f_{sl}\, d\varepsilon_c - 0.017\sqrt{f'_{co}}\ \frac{MJ}{m^3} \quad (2\text{-}18)$$

A simplified form of this equation is given in Paulay and Priestley (1992).

$$\varepsilon_{cu} = 0.004 + 1.4\rho_s f_{yh}\varepsilon_{uh}\frac{1}{f'_{cc}} \qquad (2\text{-}19)$$

where,
ε_{uh} is the ultimate strain of confinement hoop steel, and ρ_s is the volumetric ratio of confining steel.

Typical values for ε_{cu} range from 0.012 to 0.05, a 4 to 16 times more than typical assumed value for unconfined concrete.

Oh (2002) used the following equation to find ε_{cu}:

$$\varepsilon_{cu} = 0.008 + 0.1\phi_c \qquad (2\text{-}20)$$

Table 2-1: Summary of various types of concrete structural walls (Srivastava, 2013)

Structural Wall Type	Reference	Concrete		Post-tensioning Reinforcement Steel	Longitudinal Web Reinforcement		Longitudinal Boundary Reinforcement	
		Cast-in-place	Precast	Unbonded	Bonded	Debonded	Bonded	Debonded
Reinforced Concrete Structural Wall	ACI 318-11 Code	●			●		●	
Unbonded Post-tensioned Precast Concrete Wall	Kurama et al. (1996), Kurama (1997), Perez (2004), Perez et al. (2007)		●	●				
Unbonded Post-tensioned Hybrid Precast Concrete Wall	Holden et al. (2003), Restrepo and Rahman (2007), Smith and Kurama (2009), Smith et al. (2011)		●	●	●			
Unbonded Post-tensioned Special Reinforced Concrete Wall	Lehigh University (In Progress)	●		●	●		●	
Unbonded Post-tensioned Special Reinforced Concrete Wall	Lehigh University (In Progress)	●		●		●		●

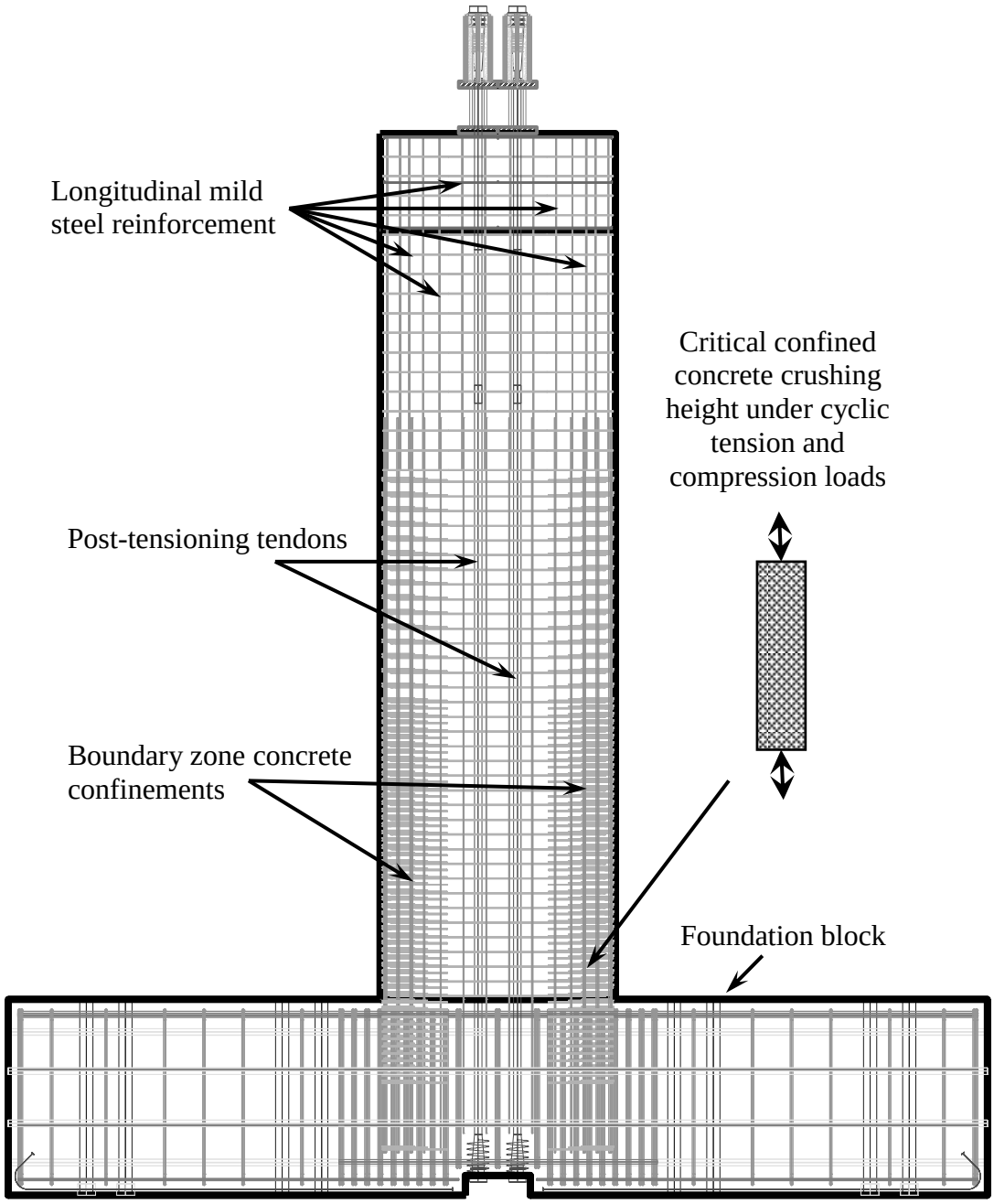

Figure 2-1: Unbonded PT CIP concrete special structural wall test specimen (Rivera, 2013)

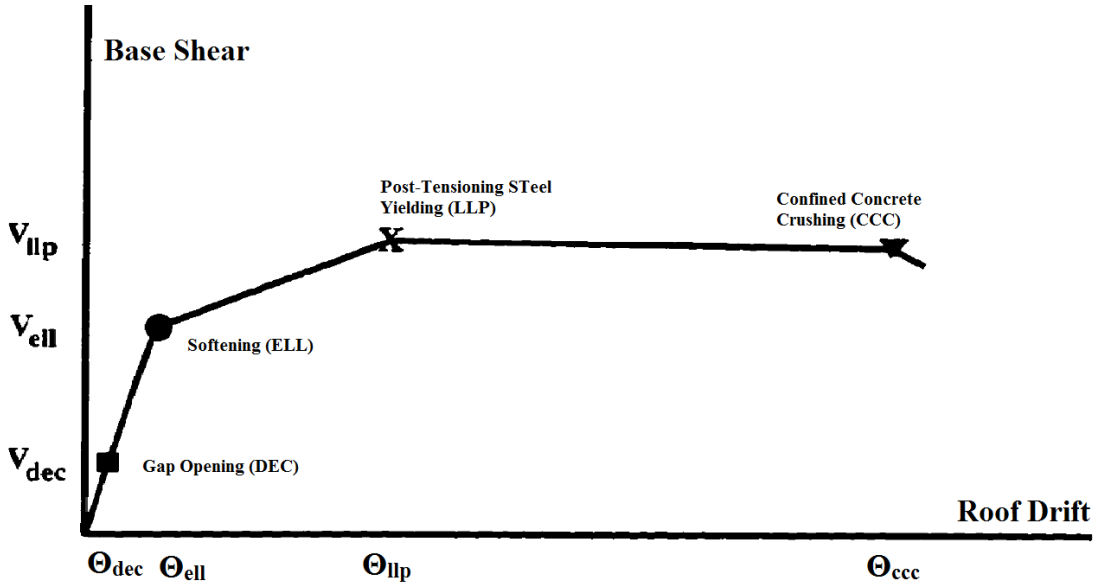

Figure 2-2: Wall limit states for base shear versus roof drift (Kurama, 1997)

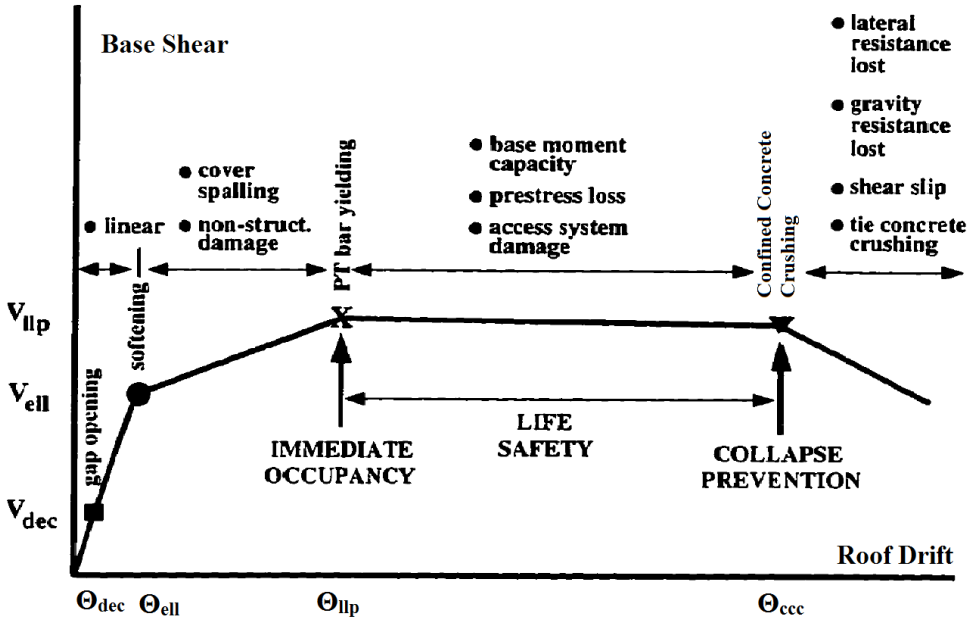

Figure 2-3: Wall limit states and expected performance levels (Perez, 2004)

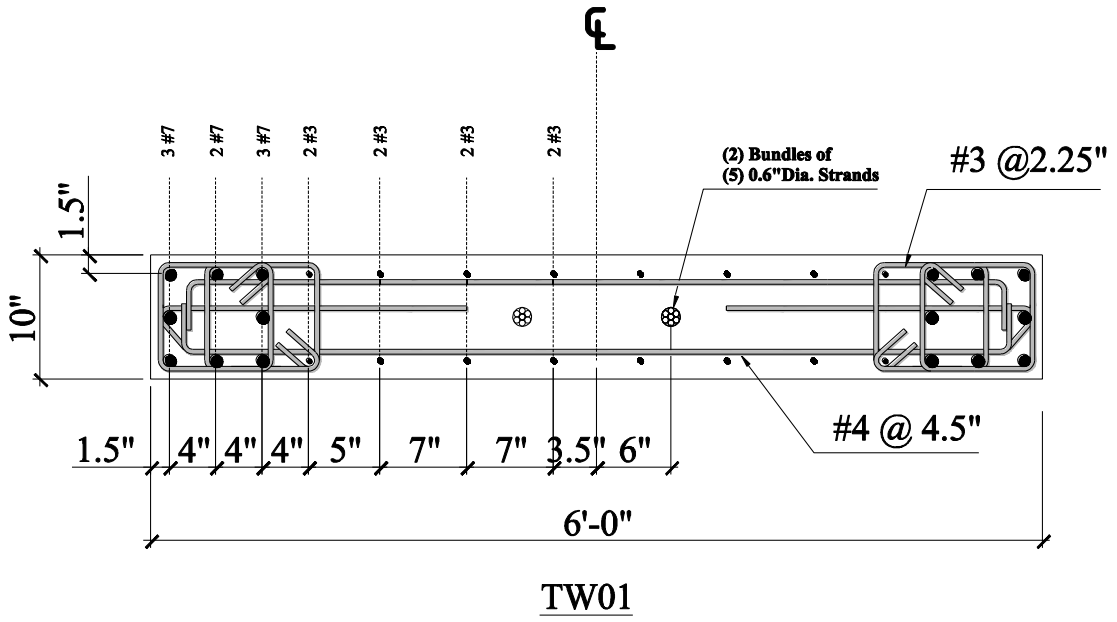

Figure 2-4: Cross-section view of unbonded PT CIP concrete special structural wall (TW01) (Rivera, 2013)

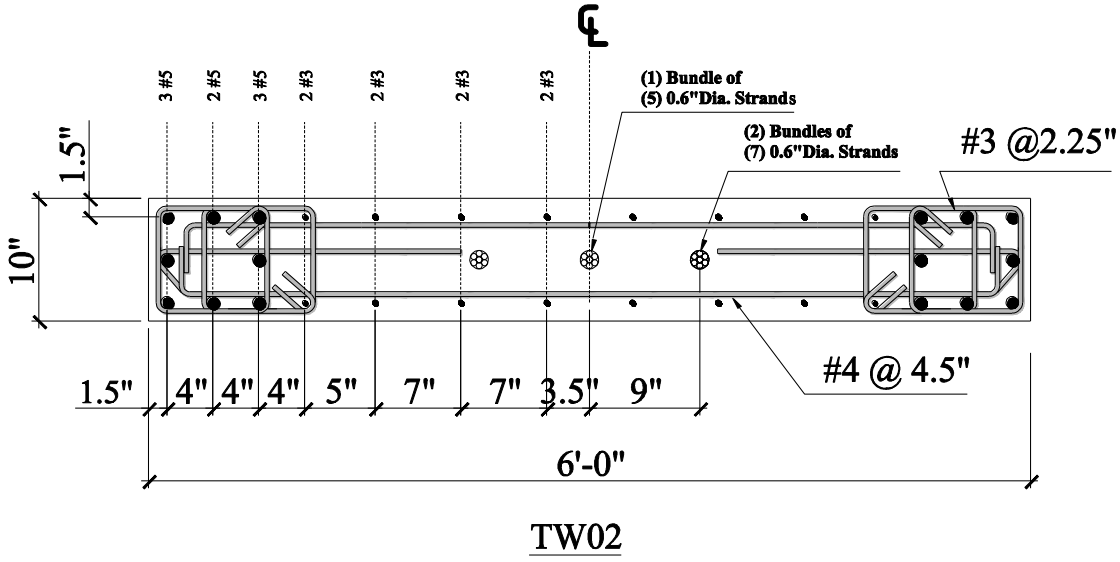

Figure 2-5: Cross-section view of unbonded PT CIP concrete special structural wall (TW02) (Rivera, 2013)

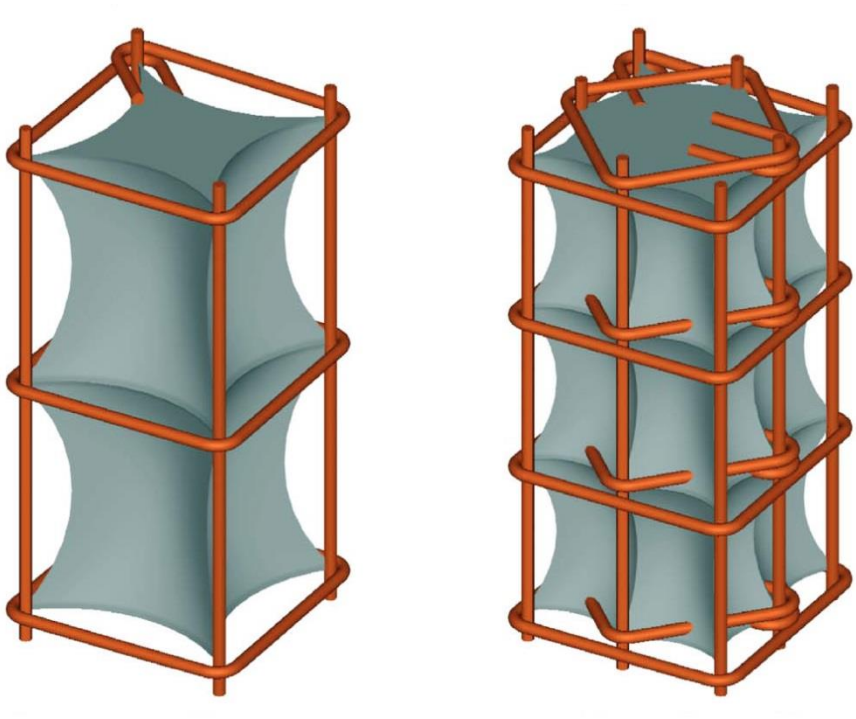

Figure 2-6: 3D schematic of concrete confinement (Paultre and Légeron, 2008)

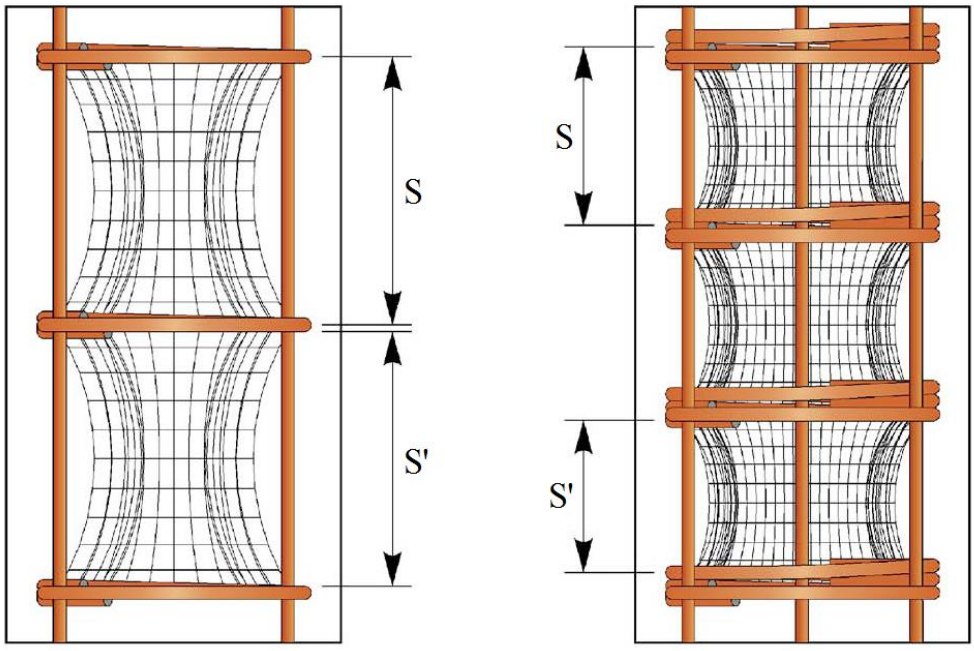

Figure 2-7: 2D schematic of concrete confinement (Paultre and Légeron, 2008)

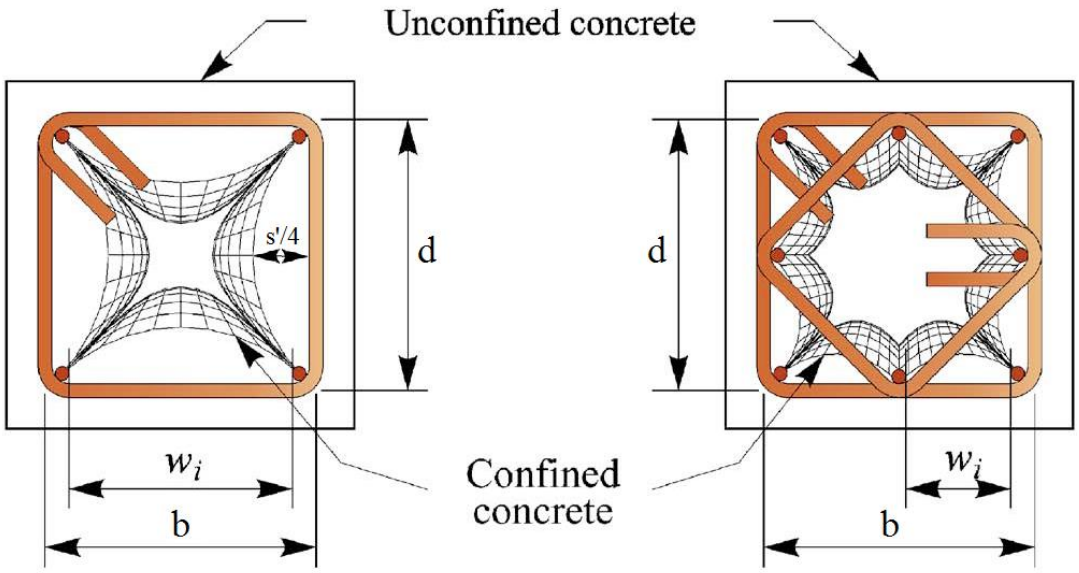

Figure 2-8: Schematic of confined concrete core (Paultre and Légeron, 2008)

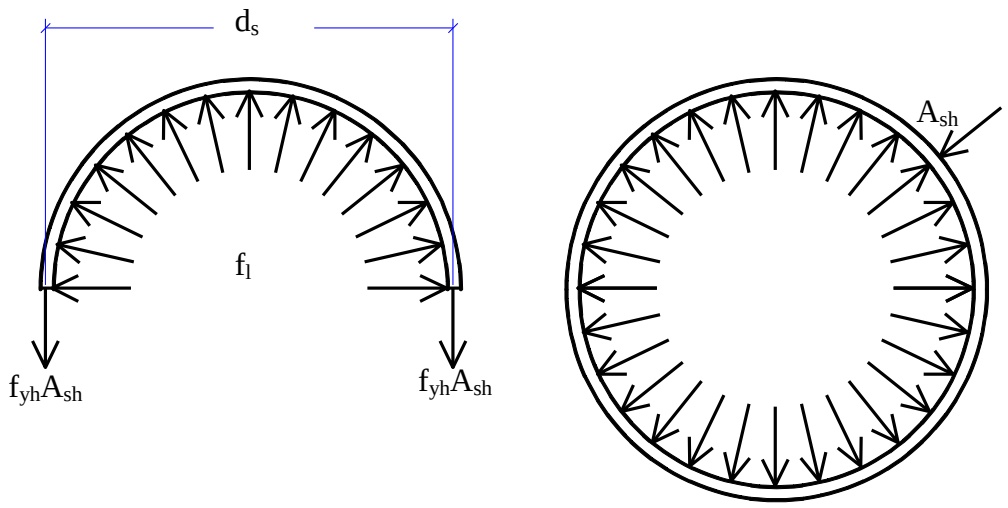

Figure 2-9: Circular hoops for concrete confinement

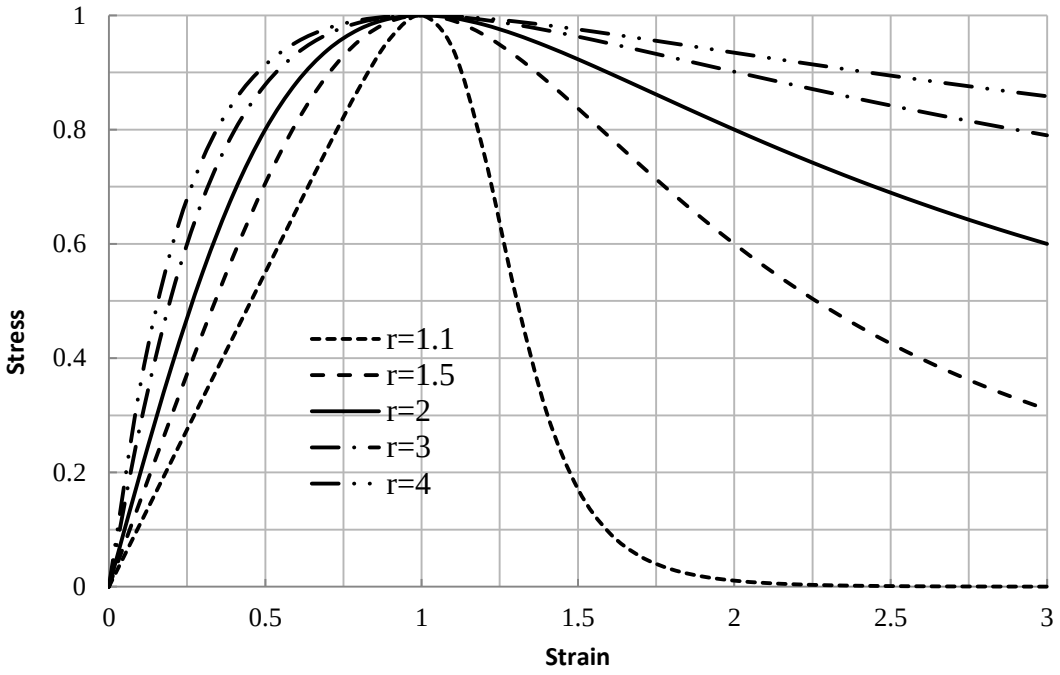

Figure 2-10: Popovics (1973) proposed equation

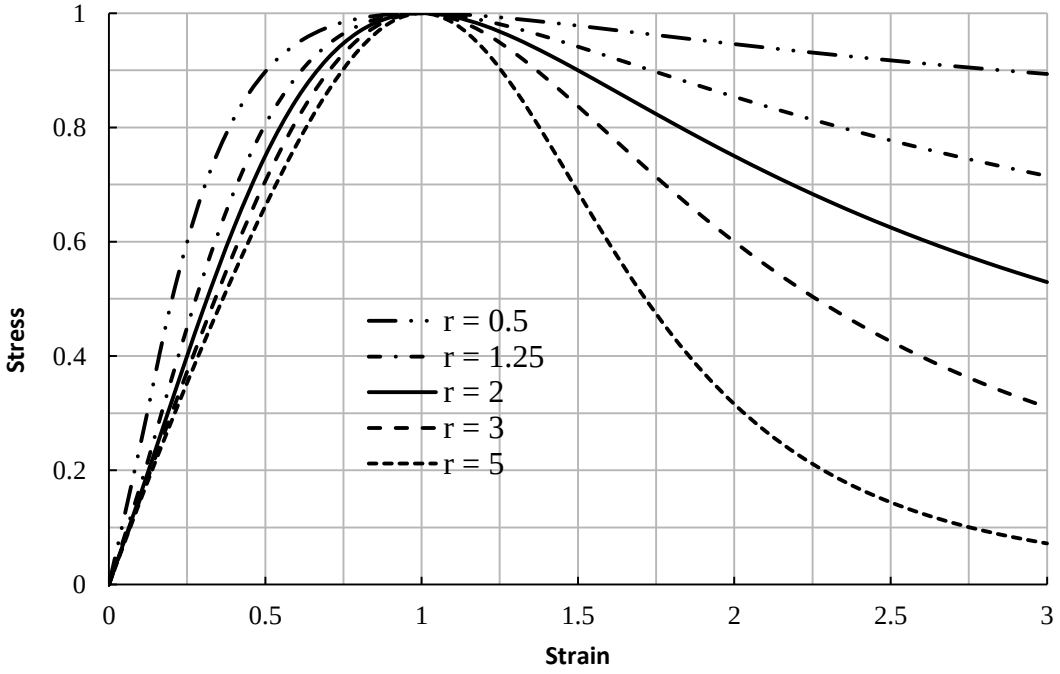

Figure 2-11: Tsai (1988) proposed equation for n = 1.5

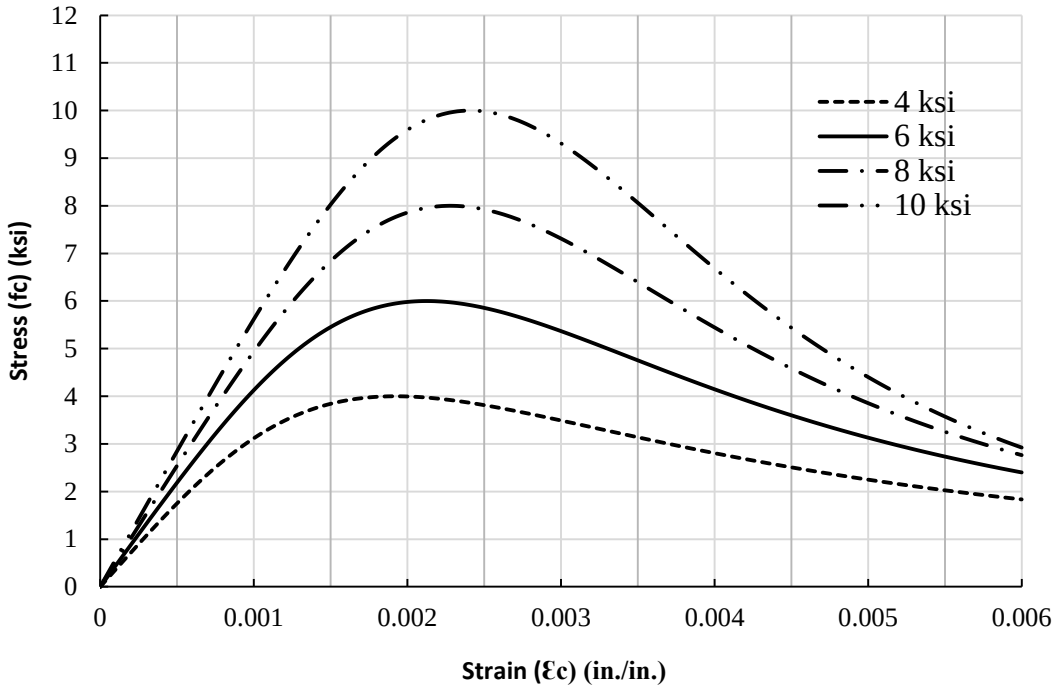

Figure 2-12: Mander (1988) unconfined concrete curves

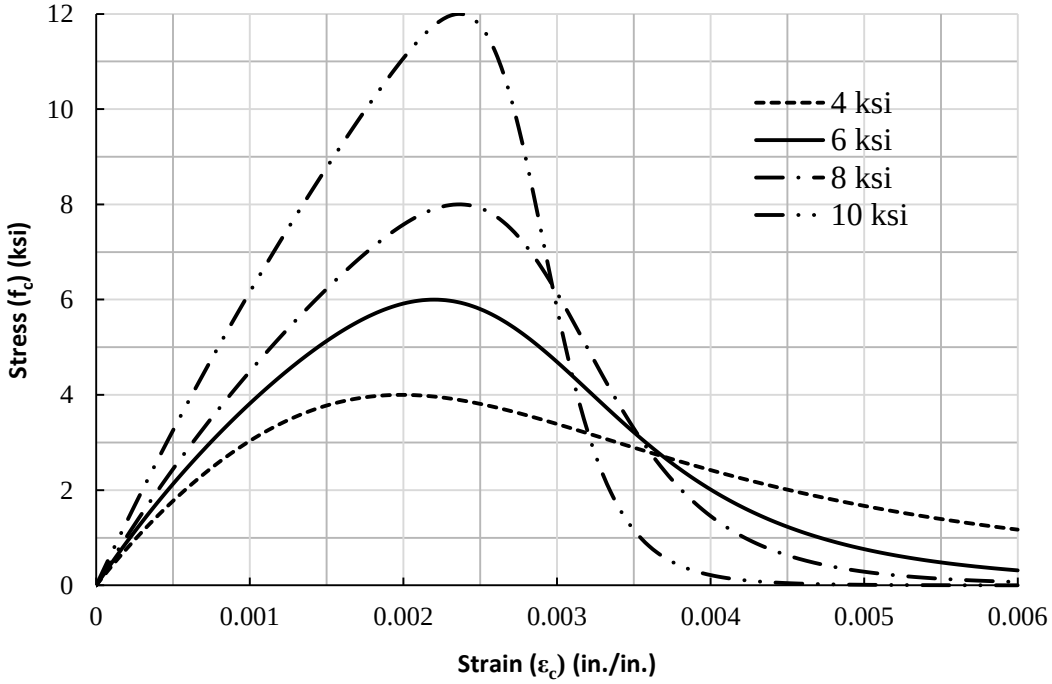

Figure 2-13: Chang and Mander (1994) unconfined concrete curves

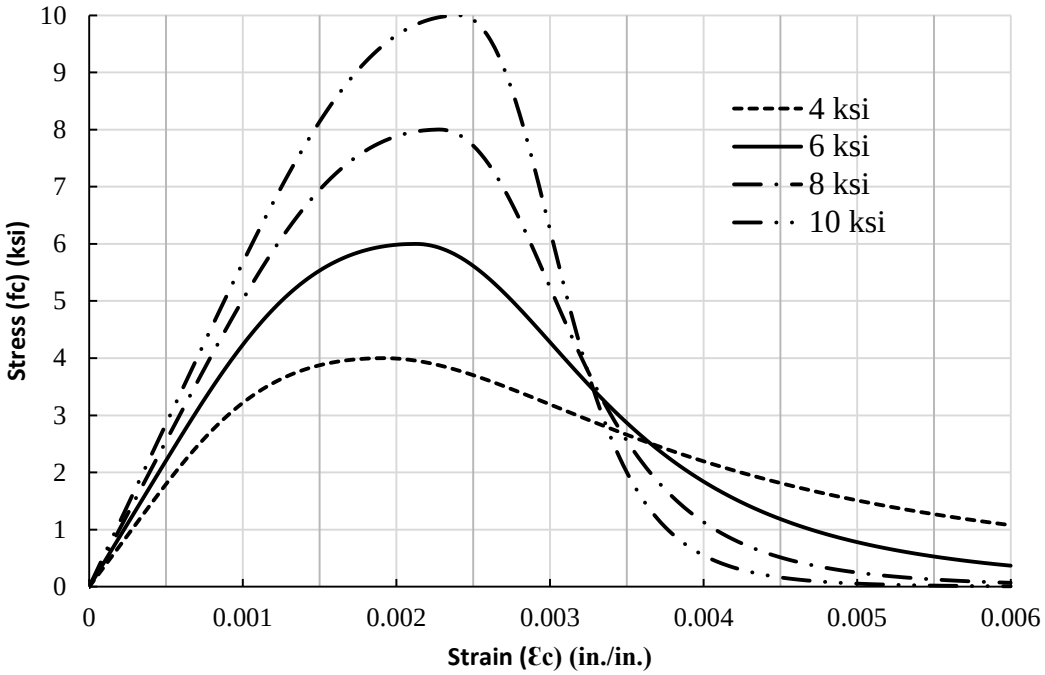

Figure 2-14: Oh (2002) unconfined concrete curves

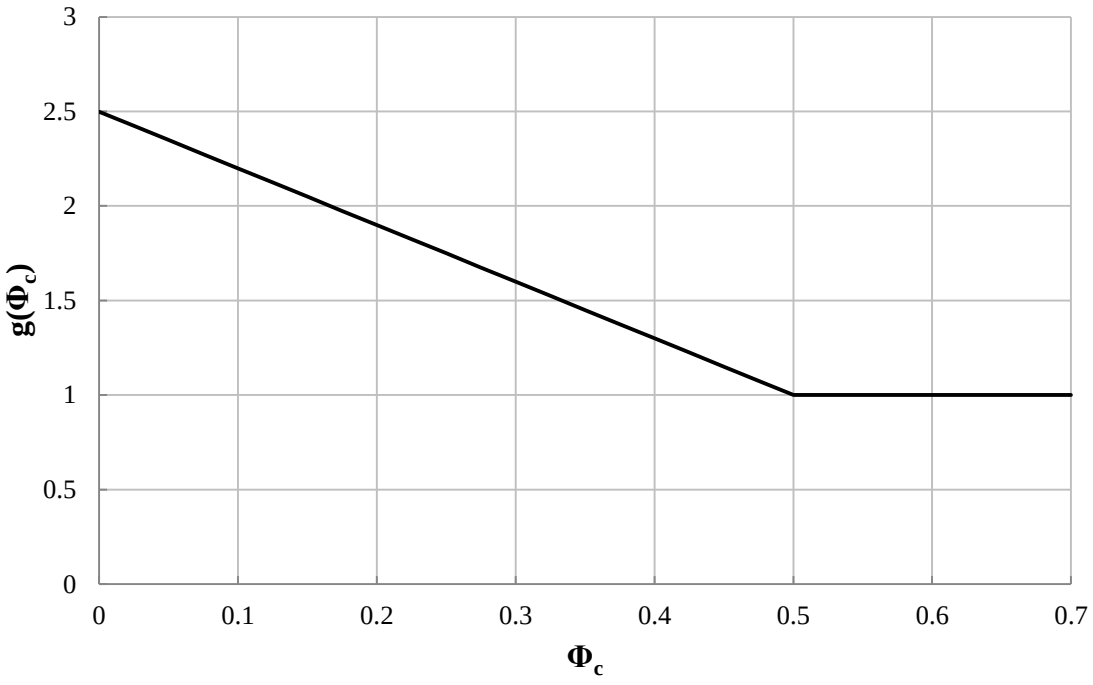

Figure 2-15: Function g(Φc) schematic

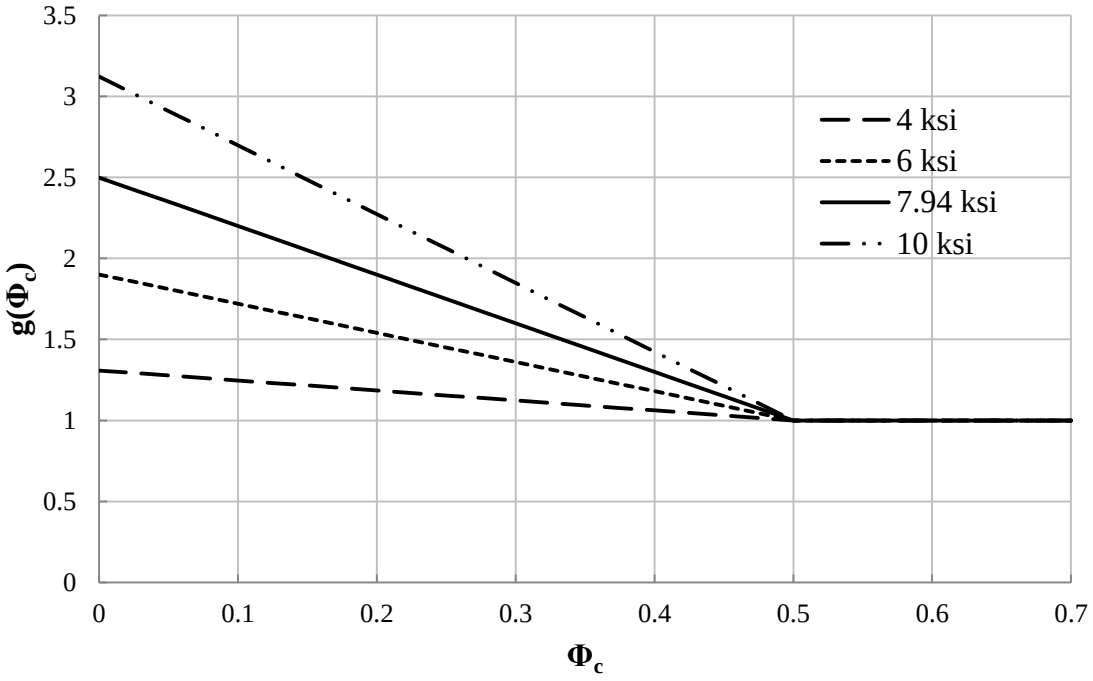

Figure 2-16: Modification function g(Φc)

Figure 2-17: Universal Testing Machine at Fritz Laboratory

CHAPTER 3

EXPERIMENTAL PROGRAM

3.1 INTRODUCTION

This chapter describes the experimental program conducted in Fritz Engineering Laboratory at Lehigh University. The chapter gives detailed description about test matrix; geometry of test specimens; loading configuration and setup; testing procedure; instrumentation; instrumentation calibration; specified and actual properties of materials; design and actual capacities of test specimens; testing assumptions; and fabrication details.

3.2 TEST MATRIX FOR SPECIMENS

Two identical confined concrete test specimens named TS01 and TS02 (corresponding to test specimen 1 and test specimen 2, respectively) were tested. The test specimens represent the critical confined concrete crushing height, H_{cr}, of boundary zone concrete confinement in unbonded post-tensioned cast-in-place concrete special structural wall test specimens to be tested in Lehigh University ATLSS Center. For more details about the wall, reader is referred to Rivera (2013) and Pakiding (2014). In this report, the term testing region refers to the critical confined concrete crushing height, H_{cr}, of boundary zone concrete confinement in unbonded post-tensioned cast-in-place concrete special structural wall.

The test specimens were identical in design and geometry. The instrumentation setup and details were the same. The specimens were tested under two different ranges of inelastic tensile cyclic loadings. Loading details for each test specimen are presented in Section 3.4.

3.3 SPECIMEN GEOMETRY DETAILS

Figure 3-1 is a drawing of test specimen in isometric view which describes various components of the test specimens. Figure 3-2 shows dimensions and parts of test specimens. Each of the test specimens is comprised of two parts, a column and two beams (a top beam and a bottom beam). Table 3-1 summarizes dimensions and other geometric parameters of test specimens.

The total height, h_c, of each specimen was 104 in. The width, l_b, of each specimen was 72 in. Each specimen had a uniform thickness, b, of 15 in. The height of the testing region, H_{cr}, in the wall tests was 16.5 in. (Rivera, 2013 and Pakiding, 2014). In the test specimens, this height was intended to be 20 in. and centered at the mid-height of the confined concrete column of each test specimen. The vertical clear spacing between the top and bottom beams was 40 in. The clear spacing between the beams was chosen to accommodate the hydraulic load actuators, load cells, and other loading fixtures.

3.3.1 Concrete Details

The beams were designed to transfer the hydraulic actuator loads to the column. A concrete cover of 2 in. was used for the sides and outside faces of the beams; a concrete cover of 2.5 in. was used for the inside faces of the beams; and a concrete cover of 3.5 in. was used at the end faces of the beams. The confined concrete column design cover was 0.75 in. in all sides.

3.3.2 Reinforcement Details

Figure 3-3 shows reinforcement details for the entire test specimen. Figure 3-4 shows reinforcement details in a cross-section of the confined concrete column. Figure 3-5 shows dimensions of the confinement hoop-pair. Figure 3-6 shows reinforcement details in a cross-section of top and bottom beams. Figure 3-7 show reinforcement details in the confined concrete column. Figure 3-8 shows reinforcement details in confined concrete column and beams of each test specimen. The reinforcement details are presented separately for the confined concrete column and the two beams of the test specimens.

Column Reinforcement

The column dimensions were 10 in. in the north-south direction (denoted as y-direction on the confined concrete column cross-section) and 15 in. in the east-west direction (denoted as x-direction on the confined concrete column cross-section). A concrete cover of 0.75 in. was used on all sides of the confined concrete column. Eight ASTM A706 Grade 60 #7 deformed steel bars were used for the longitudinal mild steel reinforcement bars inside the confined concrete of the column. The selection of ASTM A706 reinforcement bars were based on the recommendations of ACI 318-11 Code Section 21.1.5.2. The longitudinal mild steel reinforcement bars were extended in the entire column height (i.e., 104 in.). The longitudinal mild steel reinforcement bars were headed bars spaced at 6.70 in. center-to-center in the north-south direction and 3.90 in. center-to-center in the east-west direction as shown in Figure 3-4. The total amount of longitudinal mild steel reinforcement that was provided inside the confinement concrete was 4.8 in.^{2}, corresponding to a vertical reinforcement area ratio, ρ_{vert}, of $0.031A_g$, which satisfies the $0.01A_g$ minimum and $0.06A_g$ maximum requirements specified in the ACI 318-11 Code Section 21.6.3.

Figure 3-5 shows the confinement hoop-pair that was comprised of two same size confinement hoops one on the top of another. Each confinement hoop measure 9.75 in. x 8.50 in. center-to-center. As shown in Figure 3-7 and Figure 3-8, the confinement hoops were tied to the eight longitudinal mild steel reinforcement bars in the column. The confinement hoops for the entire confined concrete column were fabricated using ASTM A615 Grade 60 #3 deformed steel bars.

The confinement hoop sets at the column were spaced at 2 in. center-to-center along the entire 104-in. height of the confined concrete column except for the 20 in.-long testing region where the confinement hoop sets were spaced at 2.25 in. center-to-center. The first confinement hoop set for the testing region, H_{cr}, was spaced at 1.125 in. from the center (i.e., mid-height) of the confined concrete column corresponding to a center-to-center spacing, s, of 2.25 in. between the confinement hoop sets in the testing region. A total of

10 confinement hoop sets were used in the testing region. The hoop spacing, s, of 2.00 in. was lower than the maximum allowable limit of 2.5 in. as per ACI 318-11 Code Section 21.6.4.3, but this spacing was sufficient to easily cast concrete into the confinement. The ratio of volume of transverse reinforcement to volume of concrete core, ρ_s, was 0.027.

Beam Reinforcement

Figure 3-3 and Figure 3-6 show flexural reinforcement position and details. For flexural reinforcement in the beams, 3 ASTM A615 Grade 60 #10 bars were used to accommodate the actuator loads applied to the beams at a distance of 15 inch from column face (20 in. from column center).

Figure 3-3, Figure 3-6, and Figure 3-8 show details of horizontal and vertical shear reinforcement in beams. The total amount of #4 horizontal shear reinforcement steel area was 7.5 in.^{2}, corresponding to a horizontal reinforcement ratio, ρ_{horiz}, of 2.5%, which satisfies the 0.25% minimum requirement of the ACI 318-11 Code Section 11.7.4.2. The total amount of vertical shear reinforcement provided by a set of two double leg stirrups in each beam was 0.8 in.^{2} at each 4 in. spacing, corresponding to a vertical reinforcement area ratio, ρ_{vert}, of 3.34%, which satisfies the 0.25% minimum requirement of the ACI 318-11 Code Section 11.7.4.1. Furthermore, the 4 in. spacing of the horizontal and vertical shear reinforcement satisfies the maximum allowable spacing of 0.2 times the distance from extreme compression fiber to centroid of longitudinal tension reinforcement as per the ACI 318-11 Code Sections 11.7.4.1 and 11.7.4.2.

3.4 LOADING CONFIGURATION AND DETAILS

Figure 3-9 shows isometric of loads on test specimens. Figure 3-10 shows loading diagram of test specimens. Figure 3-11 shows external and internal loadings in a section of the test specimen. The vertical loads were applied to each test specimen using two 300 kip-capacity hydraulic actuators on the north and south sides of the test specimen, and the Universal Testing Machine (UTM). The two hydraulic actuators were pushing against the two beams; therefore, loading the testing region in tension. The Universal Testing Machine only applied axial compression loading to the confined concrete column of the test specimen; therefore, it was compressing the testing region. After initial adjustment, each hydraulic actuator was applying a constant 270 kip load on the beams of the test specimen for the entire test duration of each specimen.

To adjust the net load in the testing region, the compression loading from the Universal Testing Machine was varied. The net column load of the testing region ($P_u - V_{act}$) was the summation of the tensile loadings from the two hydraulic actuators (i.e., 270 kip each, 540 kip from both actuators) and the compression loading from the Universal Testing Machine. That is:

$$P = P_u - V_{act} \quad (3\text{-}1)$$

where,

$$V_{act} = V_{actn} + V_{acts} \quad (3\text{-}2)$$

3.4.1 Loading Setup and Details

Both of the specimens were tested under cyclic axial tension and compression loadings on the confined concrete testing region. The net load in the testing region of the confined concrete column of each test specimen was controlled by changing the compression loading from UTM. The UTM load ranged from 180 kip to 1020 kip before the compression failure step (i.e., step 24) for TS01; and from 65 kip to 1530 kip before the compression failure step (i.e., step 29) for TS02.

Figure 3-11 shows free body diagrams of the external and internal loadings developed at different parts of the test specimens in a section of the test specimen. The UTM load (compression load) is considered positive quantity and each actuator loading (tension load) is considered negative quantity.

Prior to testing, each specimen was centered and aligned accurately below the UTM by the laboratory technicians. The confined concrete column of each test specimen was centered-placed on a 2 in.-thick 15 in. x 24 in. steel plate at the base of the column. A 2 in.-thick 17 in. x 23 in. steel plate was centered-placed on the top of the confined concrete column of each test specimen. The small difference in plate sizes is unimportant and resulted from using readily available material in the laboratory.

Figure 3-12 and Figure 3-13 show the hydraulic actuators and loading fixtures on the north and south side of the test specimens. The two beams were designed to transfer the actuator loads to the confined concrete column. The two hydraulic actuators were applying loads to the beams by stressing the 2 in.-thick steel plates resting against the beams. The hydraulic actuators were exerting a compressive force at the centerline (mid-thickness) of the beams at 15 in. from the north and south side faces of the confined concrete column.

Figure 3-14 shows the details of the hydraulic actuators and their loading fixtures. Figure 3-15 shows hydraulic actuators at loading. The hydraulic actuators were placed on a 4.3 in.-long W8x67 wide flange steel column welded to a 2 in.-thick steel plates on both ends set-rested on the base beam. A 2 in.-thick steel plate was placed between each hydraulic actuator stroke and the load cell (i.e., load cells were placed on the top of the 2 in.-thick steel plate that were capped to the actuator stroke). A 2 in.-thick steel plate was placed between top beam and each load cell. The top steel plate was pressing against the bottom of the top beam.

Figure 3-16 shows the 2 in.-thick steel plate on the top of each load cell that was attached to the top beam by using the steel rod-ring attachments to prevent the steel plate from falling.

3.4.2 Loading History

Figure 3-17 and Figure 3-18 show loading history for TS01 and TS02, respectively. Figure 3-19 to Figure 3-26 shows net load at the testing region at different load steps. Table 3-2 and Table 3-3 provide loading details at each load step for TS01 and TS02, respectively. The two hydraulic actuators and the UTM were used to create a net axial load (vertical tension or compression load) in the testing region, H_{cr}, of confined concrete column at each load step.

The duration of each test was, on average, from 3.5-4.5 hours. The testing of TS02 took longer than TS01 because of the increased number of load steps (see load details, Table 3-2 and Table 3-3). During each test, photographs were taken to document appearance of test specimens at the various load steps.

The loading protocols were divided into nine loading phases consisting of: (1) Initial condition phase: this phase was intended to adjust the loads in actuators (i.e., to 270 kip in each actuator) that were then kept constant throughout the test; (2) PT phase: this phase was intended to simulate the load from post-tensioning tendons on confined concrete in the reduced scale specimens of the prototype walls; (3) Concrete cracking phase: this phase was intended to crack the concrete in the testing region so that in the next load steps only the longitudinal mild steel reinforcement bars carry the tension load, (4) Return to PT phase: this phase was intended to simulate the load from post-tensioning tendons on confined concrete in typical reduced scale specimens of the prototype wall where the concrete is fully cracked; (5) Cracking cycles phase: this phase was intended to simulate the cyclic loading on a fully cracked confined concrete section; (6) 2/3 of yield cycles phase: this phase was intended to simulated the cyclic loading up to 2/3 of the tensile yielding capacity of longitudinal bars of the confined concrete; (7) Yield cycles phase: this phase was planned to yield the longitudinal mild steel reinforcement bars inside the confined concrete of the testing region in tension; (8) Multiples of strain phase: this phase was intended to elongate the longitudinal mild steel reinforcement bars inside the confined concrete to different multiples of their tensile yield strain limit; and, (9) Compression failure phase: this phase was intended to apply increasing compression loading to the specimen until failure. In TS01, the multiples of strain load phase (Load Phase 08) did not exist; therefore, the compression failure phase (Load Phase 09) is numbered as Load Phase 08. TS02 was tested for all the loading steps. Each load phase is comprised of a number of cyclic loading steps.

The peak compressive strength and the ultimate concrete compression strain, ε_{cu}, was recorded at Load Phase 09 for each test specimen. This load phase has only two load steps for each test specimen. In the first load step, the 270 kip load of the two actuators, which were constant during the entire test, were reduced slowly to 20 kip to prevent the extreme compression of the hydraulic actuators due to increasing compression loading from the UTM in the next step. In the second load step, the specimen was set under increasing compression loading from the UTM until complete failure. In TS01, the testing region was compressed to 980 kip in compression in Load Step 23 and to compression failure in Load Step 24. For TS02, the longitudinal mild steel reinforcement bars of the confined core were elongated to twelve and sixteen times of their tensile

yielding strain limit in Load Step 23 and Load Step 25, respectively. Load Step 27 was ignored due to uncertainties about the ultimate strain limit of the longitudinal mild steel reinforcement from testing samples of the bars (i.e., to prevent tensile fractures of the mild steel longitudinal reinforcement bars of the confined concrete). In TS02, the testing region was compressed to 1060 kip in compression in Load Step 28 and to compression failure in Load Step 29.

A 60 kip compression load exists during all the loading cycles to represent the prestress force of post-tensioning tendons of the typical reduced scale test specimens. That is, the tension and compression cyclic loading simulation was done about the +60 kip axis not about the 0 kip loading axis of the loading history.

3.5 INSTRUMENTATION

Figure 3-27, Figure 3-28, and Figure 3-29 show the location, designation and setup of the instrumentation. Table 3-4 summarizes the instrumentations that were used in each test specimen. The instrumentation setup was the same for both test specimens. Instrumentation in each test specimen included: twelve strain gages on longitudinal bars; eighteen strain gages on confinement hoops; and, two displacement transducers, one on the north face and one on the south face of the testing region. Head-travel of the UTM (deformation of the test specimen) was also recorded. Two load cells were used to record the load in north and south side actuators. A single load cell was used for each actuator. The UTM load was recorded by instrument installed in the UTM system.

During each test, the data from all instrumentation was recorded using a computer-based data acquisition system. The data was recorded at a speed of one record per second for TS01 and five records per seconds for TS02. All channels were read and recorded. Pertinent data for monitoring the test specimen was displayed on the computer monitor during each test.

3.5.1 Load Cells

Figure 3-13 shows the positioning of load cells in test specimen. There were two load cells installed at each specimen denoted as NLC and SLC. The NLC denotes the load cell installed between the north side hydraulic actuator and the top beam, and SLC denotes the load cell installed between the south side hydraulic actuator and top beam. NLC recorded the load applied by north side hydraulic actuator to the specimen, V_{actn}, and SLC recorded the load applied by south side hydraulic actuator to the specimen, V_{acts}. The load cell data quantities are considered negative. V_{act} denotes the summation of load recorded by NLC and SLC.

3.5.2 LVDTs

Figure 3-27 show details of the threaded rods to which the LVDTs were attached. Figure 3-29 shows details of the LVDTs. LVDTs were used to measure the vertical deformation of the testing region of the confined concrete in each test specimen. LVDTs were installed at each specimen after the specimen was placed and aligned for testing under the UTM. Two LVDTs were used in each test specimen, one on the north face and the other on the south face of the testing region. The north face LVDT is denoted by NLVDT, and

the south face LVDT is denoted by SLVDT. Each LVDT was attached to the top and bottom threaded rods in the testing region at a distance of 2 in. from the concrete cover of the testing region. The vertical deformation of the testing region was recorded between the two threaded rods.

The ¼ in.-diameter threaded rods to which the LVDTs were attached were positioned in the specimens before concrete casting. The two 18 in.-long threaded rods were installed on the top and bottom part of the testing region of each test specimen. These rods were placed in the mid-thickness of each specimen in the north-south direction passing the 10 in. confined concrete column and extended by 4 in. from the north and south faces of the confined concrete column. The center-to-center spacing between the threaded rods were intended to be placed 20 in. (i.e., equivalent to the testing region height) but because of confinement hoops and longitudinal mild steel reinforcement congestions this distance varies within 2 in. more or less from the specified 20 in. spacing. The exact center-to-center spacing of threaded rods on the north and south faces of each specimen were recorded prior to testing and after the testing.

Table 3-5 summarizes the center-to-center distance values between the two threaded rods. The center-to-center distance between the two threaded rods were measured 22.2 in. on the north side, and 21.9 in. on the south side before the test; and 21.2 in. on the north side, and 20.8 in. on the south side after the compression failure of the column (i.e. end of the test) for TS01. The center-to-center distance between the two threaded rods were measured 21.3 in. on the north side, and 21.5 in. on the south side before the test; and 20.1 in. on the north side, and 20.2 in. on the south side after the compression failure of the column (i.e. end of the test) for TS02.

Figure 3-41 shows the 1 in.-thick by 2 in.- diameter rigid insulations that were placed to avoid contact between column cover and threaded rods. The insulations were placed before concrete casting. This was to make sure that the cover spalling does not alter the performance of the threaded rods or LVDTs attached to the threaded rods.

3.5.3 Head-travel

A single head-travel instrument was used for each test specimen. Head-travel instrument records the deformation of the test specimen placed between the top and bottom heads of the UTM. The head-travel instrument was attached to the top and bottom heads of the UTM. The head-travel instrument was installed after the specimen was placed and aligned for testing under the UTM.

3.5.4 Strain Gages

To study the behavior and performance of longitudinal mild steel reinforcement bars and confinement hoops, 30 strain gages were installed at each test specimen. 18 strain gages were installed at three confinement hoop pairs, and 12 strain gages were installed at longitudinal mild steel reinforcement bars. The 30 strain gages were located at 3 confinement hoop pairs named as hoop-pair 1, hoop-pair 2, and hoop-pair 3. At each hoop-pair there were 10 strain gages, 6 strain gages attached to the confinement hoop set and 4 strain gages attached to the longitudinal mild steel reinforcement bars.

Figure 3-30 provides details of strain gage notation and location. The strain gages that were damaged during concrete casting are marked with X notation in Figure 3-31 and Figure 3-32 for TS01 and TS02, respectively. The damaged strain gages are marked in Table 3-4 with X notation. The strain gages were installed after the steel reinforcement cages were completed and before the cages were positioned in the wooden forms. Strain gages were used both on selected locations of the longitudinal mild steel reinforcement bars inside the confined core and confinement hoops to record the strains at the steel reinforcement of each test specimen.

The strain gages were manufactured by Vishay Micro-Measurements, and designated as EP-08-125BT-120 for the confinement hoops and EP-08-250BG-120 for the longitudinal mild steel reinforcement bars. The strain gages were 0.125 in. (for EP-08-125BT-120) and 0.150 in. (for EP-08-250BG-120) long and had a strain range of ±20%. Both strain gages types were general purpose high elongation linear pattern strain gages. The strain gages record the strain data in micro-strain.

After concrete curing and prior to testing, all the strain gages in each specimen were checked for functionality and continuity. The check showed that several of the strain gages were damaged during concrete casting, so no data was recorded for damaged strain gages.

Strain Gages in Longitudinal Reinforcement Bars

Figure 3-30, Figure 3-31, and Figure 3-32 show notations and locations of confined concrete strain gages, which were attached to #7 longitudinal mild steel reinforcement bars inside the confined core of each test specimen. The strain measurements thus obtained are assumed to represent the strains in #7 longitudinal mild steel reinforcement bars inside the confined concrete at load steps. These strain gages are labeled as LX-R7-X. LX represents the vertically designated regions near the three confinement hoop pairs where the strain gage is located on the longitudinal bars ranging from 1 to 3 (i.e., the vertical location of the strain gages that range from 1 to 3), R7 stands for No. 7 longitudinal mild steel reinforcement bars, and the next X defines the horizontal in-plane location of each strain gage on the longitudinal reinforcement bar (i.e., it shows the horizontal location of the strain gage).

Strain Gages in Confinement Hoops

Figure 3-30, Figure 3-31, and Figure 3-32 show details, notations, numbers, and locations of confinement hoop strain gages at three vertically designated and six horizontally designated locations at each of the three confinement hoop pairs of the testing region for both specimens. That is, the confinement hoop strain gages were attached to three sets of confinement hoops. Six hoop strain gages were used in each of the three vertically designated confinement hoop sets. Four of the strain gages were attached to the legs parallel to north-south direction (or y-axis) and two of the strain gages were attached on the legs parallel to east-west direction (x-axis). These strain gages are labeled as HX-R3-X. HX represents the vertical location of the strain gages on the three vertically designed

confinement hoop sets, R3 stands for #3 steel deformed bars used for the confinement hoops, and the next X defines the horizontal in-plane location of the strain gages in a confinement hoop set that ranges from 1-6.

3.5.5 Instrumentation Calibration

The actuators were initially calibrated using both an analogue pressure gage and an electronic pressure transducer. The actuators were calibrated at 2 in., 4 in., 6 in., and 8 in. stroke extension and for 50 kip loading increments between 50 kip to 300 kip. The pressure in the actuators was read from both the analogue pressure gage and electronic pressure transducer. The load cells were calibrated for 300 kip load. The LVDTs were calibrated prior to testing.

3.6 DESIGN AND ACTUAL MATERIAL PROPERTIES

This section presents details on the design and actual properties of the concrete and reinforcement steel used in test specimens. Table 3-6 and Table 3-7 summarizes the design and actual concrete properties used for the test specimens. Table 3-8 summarizes the design and actual properties of steel reinforcement used for the test specimens.

The design compressive strength of unconfined concrete of the test specimens was 6 ksi. Twelve, 6 in. x 12 in., concrete cylinders were cast during the casting operation. The concrete cylinders were cured under the same conditions as the test specimens. The concrete cylinders were tested in compression at ages of 14, 21, 28, and 55 days. Table 3-7 presents the test results. For test data analysis throughout the report, the peak compression strength of concrete at 55^{th} day ($f'_c = 7.94$ ksi) is used for the test specimens. This is the actual strength of concrete from the cylinder test performed closest to the age when the confined concrete column specimens were tested. The design strain at compressive strength, ε'_c, was 0.0023 in./in. Unless specified, a design value of 5080 ksi is used for modulus of elasticity of concrete, E_c, based on equation from ACI 318-11 Code.

The estimated actual values for the compressive strength of confined concrete, f'_{cc}, based on the theoretical models, was 11.58 ksi based on Mander (1988) model, 11.86 ksi based on Chang and Mander (1994) model, and 10.48 ksi based on Oh (2002) model. The estimated actual values for the compressive strength of confined concrete, f'_{cc}, for all the theoretical models are based on the actual strength value of unconfined concrete (7.94 ksi). The ultimate concrete compression strain of the confined concrete based on actual strength value of unconfined concrete (7.94 ksi), ε_{cu}, was estimated 0.028 in./in. based on simplified equation of the Mander (1988) model presented in Paulay and Priestley (1992) and 0.016 in./in. based on formula presented in Oh (2002).

For all the reinforcement bars which includes the confining hoops, longitudinal mild steel reinforcement bars inside the confined concrete, and for all the reinforcement bars used in beams, the design yielding strength, f_y, was 60 ksi and the corresponding design yielding strain, ε_y, was 0.002 in./in. The design ultimate strength of all reinforcement bars, f_u, was 75 ksi. The design modulus of elasticity of steel, E_s, was taken as 29000 ksi.

Figure 3-33 shows stress-strain relationship for the tested sample of the reinforcement used for the confinement hoops. ASTM A615 Grade 60 #3 deformed steel reinforcement bars were used for the confinement hoops of the confined concrete column of each test specimen. For the confinement hoops reinforcement, the actual yielding strain with the corresponding load based on 0.2% offset from the linear-elastic region along the strain axis (i.e., offset on the yielding strain plateau), ε_{yh}, was 0.002 in./in., and the ultimate strain, ε_{uh}, was 0.1 in./in. For the confinement hoops reinforcement, the actual yielding stress, f_{yh}, was 69 ksi and the actual ultimate stress, f_{uh}, was 110 ksi.

Figure 3-34 shows the simplified stress-strain relationship for ASTM A706 Grade 60 #7 mild steel reinforcement bars used inside the confined concrete. ASTM A706 Grade 60 #7 reinforcement bars were used as longitudinal mild steel reinforcement inside the confined concrete. Based on testing two bar samples, the actual yielding strain, ε_{ys}, was 0.0026 in/in. and the actual ultimate strain, ε_{us}, was 0.0416 ksi. The actual yielding stress, f_{ys}, was 75 ksi and the actual ultimate stress, f_{us}, was 108 ksi. A simplified bi-linear model based on actual yielding and ultimate values was used to estimate design capacities of the confined concrete column at the testing region in all theoretical models.

Two types of concrete stress-strain relationships were defined for the test specimens as follows: (1) cover concrete (unconfined concrete); and (2) confined concrete (concrete within the confining reinforcement). The design strength of confined concrete core of the test specimens was estimated using the three confined concrete models: (1) Mander (1988) model; Chang and Mander (1994) model; and, Oh (2002) model.

3.7 DESIGN AND ACTUAL SPECIMEN CAPACITIES

Table 3-9 summarizes design and actual properties of confined concrete column (including testing region). Table 3-10 summarizes design and actual properties of beams. The design and actual properties of each structural element of the test specimens are presented in a separate section. The design properties of the test specimens are based on design material properties, and actual properties of the test specimens are based on actual material properties.

There were only tension and compression loading in the testing region of the confined concrete column; therefore, the design and actual tension and compression details for the testing region of the confined concrete column is presented.
There were flexural and shear loads in the two beams. The beams were designed for the following demands: (1) shear demand for transferring the actuators loads, V_{actn} and V_{acts}, to the confined concrete column; (2) flexural demand to resist the moment caused by actuators loads, V_{actn} and V_{acts}; (3) development length, l_{dh}, demand of the main flexural bars (i.e., tension ties) in the beams not to fail because of bond deficiency; and, (4) diagonal strut strength to transfer load from horizontal tension tie (i.e., main flexural bars in the beams) to horizontal compression strut in each beam.

3.7.1 Column

Figure 3-3, Figure 3-4, Figure 3-7, and Figure 3-8 show reinforcement details of confined concrete column of the test specimens. The design details of the confined concrete column are explained for tension capacity, compression capacity, and development length of the longitudinal mild steel reinforcement bars inside the confined concrete.

Tension Capacity of Column

To ensure that the concrete cracking will initiate at the center of the confined concrete column (or testing region), additional #4 mild steel reinforcement bars were added in other parts of the column (except in the testing region part) to increase the strength and stiffness of other parts of the column.

The design direct tensile cracking capacity of the confined concrete column cross-section was estimated 83 kip based on $6\sqrt{f'_c(psi)}$ (0.535 ksi) tensile stress capacity. The design tensile yielding and ultimate strength capacities of the longitudinal mild steel reinforcement bars inside the confined concrete were 288 kip and 360 kip, respectively. The actual tensile yielding and ultimate strength capacities of the longitudinal mild steel reinforcement bars inside the confined concrete were 360 kip and 518 kip, respectively.

Compression Capacity of Column

The design compression capacity of the confined concrete column cross-section at the testing region for monotonic compression loading was estimated based on theoretical confined and unconfined concrete models of: (1) Mander (1988); (2) Chang and Mander (1994); and, (3) Oh (2002). The design compression capacity of the confined concrete column cross-section at the testing region is the summation of the individual theoretical models for confined and unconfined concrete, and the simplified bilinear model of the longitudinal mild steel reinforcement inside the confined concrete presented in Section 3.6.

The design compressive strength of the confined concrete column cross-section at the testing region was 1711 kip based on Mander (1988) model, 1720 kip based on Chang and Mander (1994) model, and 1658 kip based on Oh (2002) model.

Development Length of Column Bars

To reduce beam height and increase bond between beam and column, headed bars were utilized as longitudinal mild steel reinforcement bars inside the confined concrete. The design development length for mild steel headed bars in tension was estimated 11.0 in. based on equations from ACI 318-11 Code Section 12.6.1 and 12.6.2 and design material properties. The development length of the headed bars in tension based on actual material properties was 12.0 in.

3.7.2 Beams

The beams were designed based on ACI 318-11 Code Sections 10.7, 11.7, 12.5 and ACI 318-11 Code Appendix A, "strut-and-tie models". The design details of beams are presented for: (1) shear capacity; (2) flexural capacity; and, (3) bond and development length. The shear demand and development length demand of the flexural bars were critical parameters in the design of the beams.

Shear Capacity of Beams

The total shear strength of each beam, V_t, is the sum of the shear strength provided by concrete, V_c, and the shear strength provided by shear reinforcement, V_s. To increase the shear strength of the beams, a set of two double legs shear stirrups were used as per ACI 318-11 Code provision of Chapter 11 and Appendix A. For the shear strength of concrete, the minimum strength was assumed as per ACI 318-11 Code Section 11.1, 11.5, and 11.7. Total design shear capacity of each beam based on design material properties was estimated as 255 kip. The shear capacity of each beam based on actual concrete strength (7.94 ksi) and design strength of shear reinforcement was estimated as 294 kip.

Flexural Capacity of Beams

The moment demand was estimated to be 5,400 kip-in. based on the 20 in. distance from the center of the confined concrete column cross-section to load application point of hydraulic actuators and 270 kip load from each hydraulic actuator.

The design flexural strength of the beams based on design material properties, using a reduction factor of 0.9, was estimated as 5,730 kip-in. The flexural strength of the beams based on actual concrete strength (7.94 ksi) and design strength of flexural reinforcement (60 ksi), using a reduction factor of 0.9, was estimated as 5,800 kip-in. The actual material properties for the flexural reinforcement bars did not exist.

Bond and Development Length in Beams

In the beams, the joints between diagonal compression strut, flexural reinforcement bars (tension tie), and the actuator load were considered as hydraulic joints. To reduce the length of the beams and develop bond for flexural reinforcement, the bars were hooked at 90 degree at the end as per ACI 318-11 Code Chapter 12 requirements. To prevent cover spalling at the ends of the beams, horizontal stirrups were used for the end-hooks of the flexural reinforcement.

The design development length of the flexural reinforcement bars using design material properties were estimated 19.7 in. based on the design material properties and 17.1 in. based on actual concrete strength (7.94 ksi) and design strength of flexural reinforcement (60 ksi).

3.8 FABRICATION OF TEST SPECIMENS

Figure 3-35 to Figure 3-50 show details of reinforcement, instrumentation, concrete casting, transferring, and placement of the test specimens. The test specimens were fabricated in the laboratory. The fabrication included the reinforcement, instrumentation, forming, concrete casting, and curing. Instrumentation details of the test specimens are

given in Section 3.5. The concrete casting was performed in a single placement operation on January 2 2013 using ready mixed concrete delivered by a local supplier.
The concrete was wet-cured for two weeks using wet burlap and plastic sheeting. The concrete cylinders tests at two weeks showed an average compressive strength higher than the design compressive strength (i.e., the cylinders tests showed an average compressive strength of 7.5 ksi compared to the design compressive strength of 6.0 ksi); therefore, wet-curing was terminated at that point.

Wooden forms were made from ¾-in. thick 48 in. x 96 in. plywood sheets and 2x4-in lumber (as studs, kickers, and supports). The inside surfaces of forms were lubricated with formwork oil so that the forms can be easily stripped off. The forms were entirely stripped off on the 7^{th} day of concrete casting.

Figure 3-42 shows the placement and installation details of the lifting inserts. Figure 3-43 shows the locations of the six lifting inserts that were installed in each test specimen for transferring the specimens from the concrete casting location to the testing site. Four lifting inserts were installed on the front (west face) of each test specimen, for vertical lifting and loading of the specimens to the carrying trolleys. Two lifting inserts were installed on the top of each specimen for upright-standing, locating, aligning, and vertical-centering of the specimen under the UTM. To ensure soundness of the specimens during the transfer, the specimens were analyzed for tensile cracking in the column section, flexural cracking in the column section, and shear and bond failures of the lifting inserts installed on the top of each specimen. Furthermore, to ensure safe transfer, the lifting inserts were chosen based on their tensile capacity and development length criteria. No cracking or other damage was observed in either test specimen prior to testing.

Table 3-1: Test specimen design dimensions and parameters

Description	Notation	Value	Unit
Confined concrete column			
Height	h_c	104	in.
Design height of testing region	H_{cr}	20	in.
Clear spacing between top and bottom beams	h_s	40	in.
Design width (north-south direction)	d	10	in.
Design depth (east-west direction)	b	15	in.
Design area of confinement core within the centerline of hoops	A_c	106.6	in^2
Design area of confined core within the centerline of hoops excluding longitudinal reinforcement bars area	A_{cc}	101.8	in^2
Area of effectively confined concrete core	A_e	69.9	in^2
Area of longitudinal mild steel reinforcement bars	A_s	4.8	in^2
Design concrete cover	c_c	0.75	in.
Center-to-center spacing of confinement hoop sets in testing region	s	2.25	in.
Center-to-center spacing of confinement hoop sets in other than the testing region height	s	2	in.
Design length for #7 longitudinal headed bars in tension	l_{dt}	11	in.
Beams			
length	l_b	72	in.
height	h_b	32	in.
thickness	d	15	in.
Diameter of main flexural bars	d_{fb}	1.27	in.
Beam cover	c_b	2.5	in.
Beam cover at the ends	c_b	3.0	in.
Vertical stirrup spacing	s_{sv}	4.0	in.
Horizontal stirrup spacing	s_{sh}	4.0	in.
Stress block depth factor, ACI 318-11 Code Section 10.2.7.3 (based on concrete strength of 7.94 ksi)	β_1	0.653	
Development length for #10 bars with 90 degrees hooked	l_{dh}	19.7	in.

The values for the dimensions and parameters of the test specimens are based on design material properties.

Table 3-2: Loading protocol for TS01

Load Phase	Load Step	Test Machine (kip)	Actuator 1 (kip)	Actuator 2 (kip)	RC Column (kip)	Details
Create Initial Condition (Phase 1)	Step 00	0	0	0	0	
	Step 01	270	0	0	270	
	Step 02	270	-135	-135	0	
	Step 03	540	-135	-135	270	
	Step 04	540	-270	-270	0	
Simulate PT (Phase 2)	Step 05	600	-270	-270	60	
Concrete Cracking (Phase 3)	Step 06	480	-270	-270	-60	
	Step 07	460	-270	-270	-80	
	Step 08	440	-270	-270	-100	
	Step 09	420	-270	-270	-120	
Simulate PT (Phase 4)	Step 10	600	-270	-270	60	
Cracking Cycles (Phase 5)	Step 11	420	-270	-270	-120	
	Step 12	780	-270	-270	240	
	Step 13	420	-270	-270	-120	
	Step 14	780	-270	-270	240	
Cycles to 2/3 Yield (Phase 6)	Step 15	300	-270	-270	-240	
	Step 16	900	-270	-270	360	
	Step 17	300	-270	-270	-240	
	Step 18	900	-270	-270	360	
Yield Cycles (Phase 7)	Step 19	180	-270	-270	-360	
	Step 20	1020	-270	-270	480	
	Step 21	180	-270	-270	-360	
	Step 22	1020	-270	-270	480	
To Failure (Phase 8)	Step 23	1020	-20	-20	980	
	Step 24	To Failure	-20	-20		Variable compression

Table 3-3: Loading protocol for TS02

Load Phase	Load Step	Test Machine (kip)	Actuator 1 (kip)	Actuator 2 (kip)	RC Column (kip)	Details
Create Initial Condition (Phase 1)	Step 00	0	0	0	0	
	Step 01	270	0	0	270	
	Step 02	270	-135	-135	0	
	Step 03	540	-135	-135	270	
	Step 04	540	-270	-270	0	
Simulate PT (Phase 2)	Step 05	600	-270	-270	60	
Concrete Cracking (Phase 3)	Step 06	480	-270	-270	-60	Labeled as Step 05 on specimen
	Step 07	460	-270	-270	-80	
	Step 08	440	-270	-270	-100	
	Step 09	420	-270	-270	-120	
Simulate PT (Phase 4)	Step 10	600	-270	-270	60	
Cracking Cycles (Phase 5)	Step 11	420	-270	-270	-120	
	Step 12	780	-270	-270	240	
	Step 13	420	-270	-270	-120	
	Step 14	780	-270	-270	240	
Cycles to 2/3 Yield (Phase 6)	Step 15	300	-270	-270	-240	
	Step 16	900	-270	-270	360	
	Step 17	300	-270	-270	-240	
	Step 18	900	-270	-270	360	
Yield Cycles (Phase 7)	Step 19	180	-270	-270	-360	
	Step 20	1020	-270	-270	480	
	Step 21	180	-270	-270	-360	
	Step 22	1020	-270	-270	480	
	Step 22(b)	1530	-270	-270	990	Mistakenly happened
Multiples of Strain (Phase 8)	Step 23	100	-270	-270	-440	$12\varepsilon_y$ (3.1% of ε_y)
	Step 24	1200	-270	-270	660	
	Step 25	65	-270	-270	-475	$16\varepsilon_y$ (4.1% of ε_y)
	Step 26	1200	-270	-270	1060	
	Step 27					$16\varepsilon_y$ (4.1% of ε_y) (Not tested)
To Failure (Phase 9)	Step 28	1200	-20	-20	1060	
	Step 29	To Failure	-20	-20		Variable compression load

Table 3-4: Instrumentation notation

Hoop Pair/Location	Notation	Description	Instruments w/ no record in TS01	Instruments w/ no record in TS02
Longitudinal Bars Strain Gages				
Hoop-pair 1 (Top)	L1-R7-1	No. 7 longitudinal rebar		
	L1-R7-2	No. 7 longitudinal rebar		
	L1-R7-3	No. 7 longitudinal rebar	X	
	L1-R7-4	No. 7 longitudinal rebar		
Hoop-pair 2 (Middle)	L2-R7-1	No. 7 longitudinal rebar	X	
	L2-R7-2	No. 7 longitudinal rebar		
	L2-R7-3	No. 7 longitudinal rebar		
	L2-R7-4	No. 7 longitudinal rebar		
Hoop-pair 3 (Bottom)	L3-R7-1	No. 7 longitudinal rebar		
	L3-R7-2	No. 7 longitudinal rebar		
	L3-R7-3	No. 7 longitudinal rebar		
	L3-R7-4	No. 7 longitudinal rebar		
Hoop Pair Strain Gages				
Hoop-pair 1 (Top)	H1-R3-1	No. 3 bar transverse		
	H1-R3-2	No. 3 bar transverse	X	
	H1-R3-3	No. 3 bar transverse		
	H1-R3-4	No. 3 bar transverse		
	H1-R3-5	No. 3 bar transverse		
	H1-R3-6	No. 3 bar transverse		
Hoop-pair 2 (Middle)	H2-R3-1	No. 3 bar transverse		
	H2-R3-2	No. 3 bar transverse		
	H2-R3-3	No. 3 bar transverse	X	X
	H2-R3-4	No. 3 bar transverse		
	H2-R3-5	No. 3 bar transverse	X	
	H2-R3-6	No. 3 bar transverse		
Hoop-pair 3 (Bottom)	H3-R3-1	No. 3 bar transverse		
	H3-R3-2	No. 3 bar transverse		
	H3-R3-3	No. 3 bar transverse		X
	H3-R3-4	No. 3 bar transverse		
	H3-R3-5	No. 3 bar transverse		
	H3-R3-6	No. 3 bar transverse		
LVDTs				
North Side	NLVDT	LVDT on North side		
South Side	SLVDT	LVDT on South side		
Load Cells				
North Side	NLC	Load cell on north side		
South Side	SLC	Load cell on south side		
Head-travel				
Head-travel	HT	Specimen		

Table 3-5: Spacing of threaded rods for LVDTs attachment

	LVDT Location	Measurement Side	Notation	Measurement (inch)
Before Test	North LVDT	Outside	d_{ftn}	22.56
		Inside	d_{ftn}	21.75
		Center-to-center	d_{ftnc}	22.17
	South LVDT	Outside	d_{fts}	22.31
		Inside	d_{fts}	21.56
		Center-to-center	d_{ftsc}	21.94
After Test	North LVDT	Outside	d_{ftn}	21.56
		Inside	d_{ftn}	20.75
		Center-to-center	d_{ftnc}	21.16
	South LVDT	Outside	d_{fts}	21.12
		Inside	d_{fts}	20.38
		Center-to-center	d_{ftsc}	20.75
Before Test	North LVDT	Outside	d_{ftn}	-
		Inside	d_{ftn}	-
		Center-to-center	d_{ftnc}	21.31
	South LVDT	Outside	d_{fts}	-
		Inside	d_{fts}	-
		Center-to-center	d_{ftsc}	21.50
After Test	North LVDT	Outside	d_{ftn}	20.50
		Inside	d_{ftn}	19.75
		Center-to-center	d_{ftnc}	20.12
	South LVDT	Outside	d_{fts}	20.50
		Inside	d_{fts}	19.85
		Center-to-center	d_{ftsc}	20.18

Table 3-6: Materials properties for concrete

Description	Notation	Actual	Design	Unit
Concrete properties				
Modulus of elasticity of concrete	E_c	-	5080	ksi
Modification factor for normal-weight concrete, ACI 318 Sec. 11.6.4.3	λ	-	1.0	
Unconfined concrete strength				
Compressive strength	f'_c	7.94	6.0	ksi
Strain at (peak) compressive strength	ε'_c	-	0.0023	in./in.
Confined concrete strength				
Maximum concrete stress based on Mander (1988)	f'_{cc}	-	11.6	ksi
Maximum concrete stress based on Chang and Mander (1994)	f'_{cc}	-	11.9	ksi
Maximum concrete stress based on Oh (2002)	f'_{cc}	-	10.5	ksi
Strain at maximum stress based on Mander (1988)	ε'_{cc}	-	0.008	in./in.
Strain at maximum stress based on Chang and Mander (1994)	ε'_{cc}	-	0.006	in./in.
Strain at maximum stress based on Oh (2002)	ε'_{cc}	-	0.006	in./in.

Table 3-7: Concrete cylinder compressive strengths

Age (Days)	Testing Date	Cylinder No.	Load (kip)	Strength (ksi)	Average strength (ksi)
14	02/01/2013	Cylinder 1	201.5	7.13	6.96
		Cylinder 2	191.5	6.78	
21	01/16/2013	Cylinder 1	215.5	7.60	7.55
		Cylinder 2	212.0	7.50	
28	01/22/2013	Cylinder 1	215.0	7.60	7.68
		Cylinder 2	219.0	7.75	
55	02/27/2013	Cylinder 1	232.5	8.22	7.94
		Cylinder 2	216.5	7.66	

Table 3-8: Materials properties for reinforcement steel

Description	Notation	Actual	Design	Unit
Steel properties				
Modulus of elasticity of steel	E_s	-	29000	ksi
ASTM A706 Grade 60 #7 longitudinal reinforcement				
Yielding strength	f_y	75	60	ksi
Ultimate strength	f_u	108	75	ksi
Yielding strain	ε_y	0.0026	0.002	in./in.
Ultimate strain	ε_u	0.0416	-	in./in.
Fracture strain	ε_f	0.0540	-	in./in.
ASTM A615 Grade 60 #3 hoop reinforcement				
Yielding strength	f_{yh}	69	60	ksi
Ultimate strength	f_{uh}	110	75	ksi
Yield strain	ε_{yh}	0.002	0.002	in./in.
Ultimate strain	ε_{uh}	0.10	-	in./in.
Fracture strain	ε_{fh}	0.135	-	in./in.
ASTM A615 Grade 60 #4 shear reinforcement in beams				
Yielding strength	f_{ys}	-	60	ksi
Ultimate strength	f_{us}	-	75	ksi
Yielding strain	ε_{ys}	-	0.002	in./in.
Ultimate strain	ε_{us}	-	-	in./in.
ASTM A615 Grade 60 #10 flexural reinforcement in beams				
Yielding strength	f_{yf}	-	60	ksi
Ultimate strength	f_{uf}	-	75	ksi
Yielding strain	ε_{sf}	-	0.002	in./in.
Ultimate strain	ε_{sf}	-	-	in./in.

Table 3-9: Testing region section properties

Description	Notation	Actual	Design	Unit
Compression properties				
compression yielding capacity of longitudinal steel bars	P_y	360	288	kip
Compressive strength capacity based on Mander (1988)	P_c	-	1711	kip
Compressive strength capacity based on Chang and Mander (1994)	P_c	-	1720	kip
Compressive strength capacity based on Oh (2002)	P_c	-	1658	kip
Ultimate concrete compressive strain based on simplified Mander (1988)	ε_{cu}	-	0.028	in./in.
Ultimate concrete compressive strain based on formula from Oh (2002)	ε_{cu}	-	0.016	in./in.
Ultimate concrete compressive strain based on test results	ε_{cu}	0.0385	-	in./in.
Tension properties				
Direct tensile strength of concrete	f_t'	65	83	kip
Tensile yielding strength of longitudinal reinforcement bars	P_{yt}	360	288	kip
Ultimate tensile strength of longitudinal reinforcement	P_{ut}	518	360	kip

The design properties are based on design material properties, and actual properties are based on actual material properties.

Table 3-10: Beam properties

Description	Notation	Actual	Design	Unit
Flexural strength				
Flexural capacity of beams	M_{nb}	-	6366	kip-in.
Reduced flexural capacity of beams	ϕM_{nb}	-	5730	kip-in.
Shear strength				
Shear capacity of concrete	V_c	78	68	kip
Shear capacity of double steel stirrups	V_s	-	352	kip
Maximum steel shear capacity of a section (ACI 318-11 Section 11.4.7.9)	V_{us}	-	272	kip
Shear capacity of beam section	V_t	-	386	kip
Reduction factor for shear	ϕ_{sh}	-	0.75	
Reduced shear strength (total section shear strength of section as per ACI 318 Section 11.7.3)	$\phi_{sh} V$	294	255	kip
Development length				
Development of #10 flexural reinforcement bars	L_{dh}	-	10	in.

The design properties are based on design material properties, and actual properties are based on actual material properties.

Table 3-11: Beams spacing

	LVDT Location	Measurement Side	Notation	Measurement (inch)
Before Test	North Side	Inside	h_{sn}	40.00
	South Side	Inside	h_{ss}	40.00
After Test	North Side	Inside	h_{sn}	39.00
	South Side	Inside	h_{ss}	38.94
Before Test	North Side	Inside	h_{sn}	40.00
	South Side	Inside	h_{ss}	40.00
After Test	North Side	Inside	h_{sn}	-
	South Side	Inside	h_{ss}	-

Table 3-12: Testing region actual cross-section area

Location	East Dimension, b (in.)	West Dimension, (in.)	Average Dimension, (b) (in.)	Average Area, A_c (in.^{2})
Top	10.45	10.50	10.48	157.1
Middle	10.33	10.48	10.40	156.0
Bottom	10.20	10.40	10.30	154.5
			Average	155.9
Actual Section Area for Specimen TS02				
Location	East Dimension, b (in.)	West Dimension, (in.)	Average Dimension, (b) (in.)	Average Area, A_c (in.^{2})
Top	10.75	10.75	10.75	161.3
Middle	-	-	-	157.0
Bottom	10.25	10.12	10.19	152.8
			Average	157.0

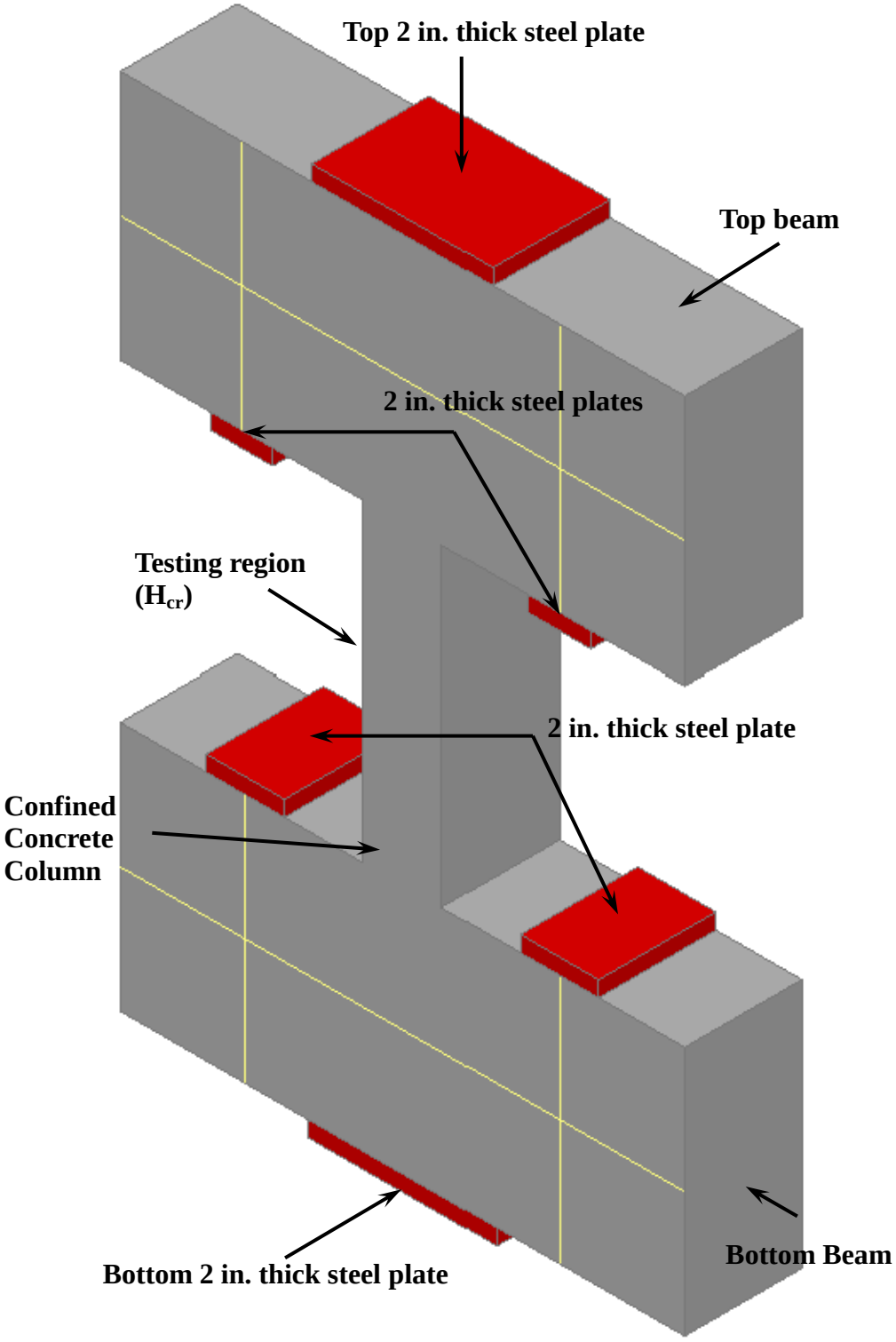

Figure 3-1: Isometric of test specimen parts

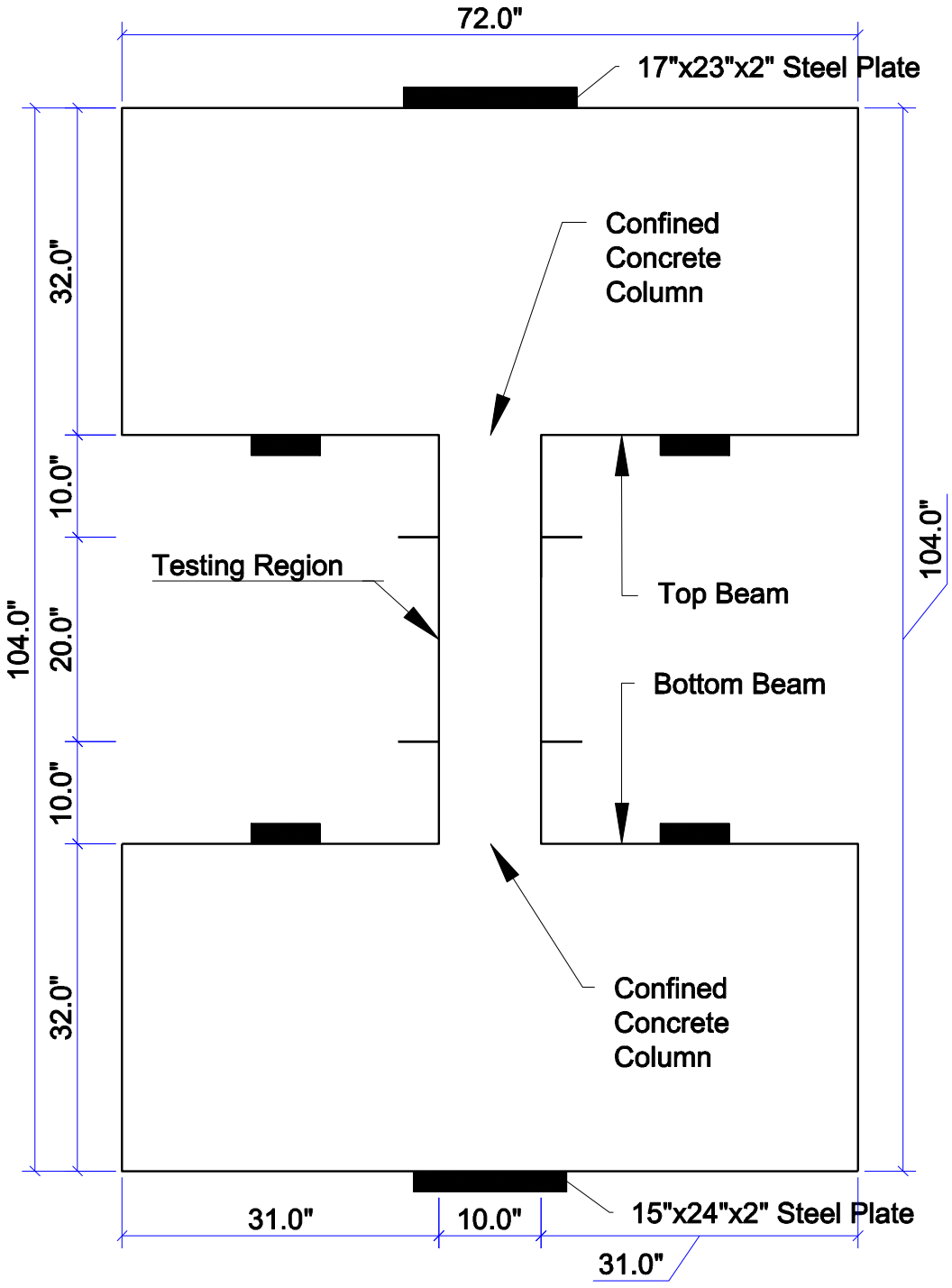

Figure 3-2: Test specimen dimensions

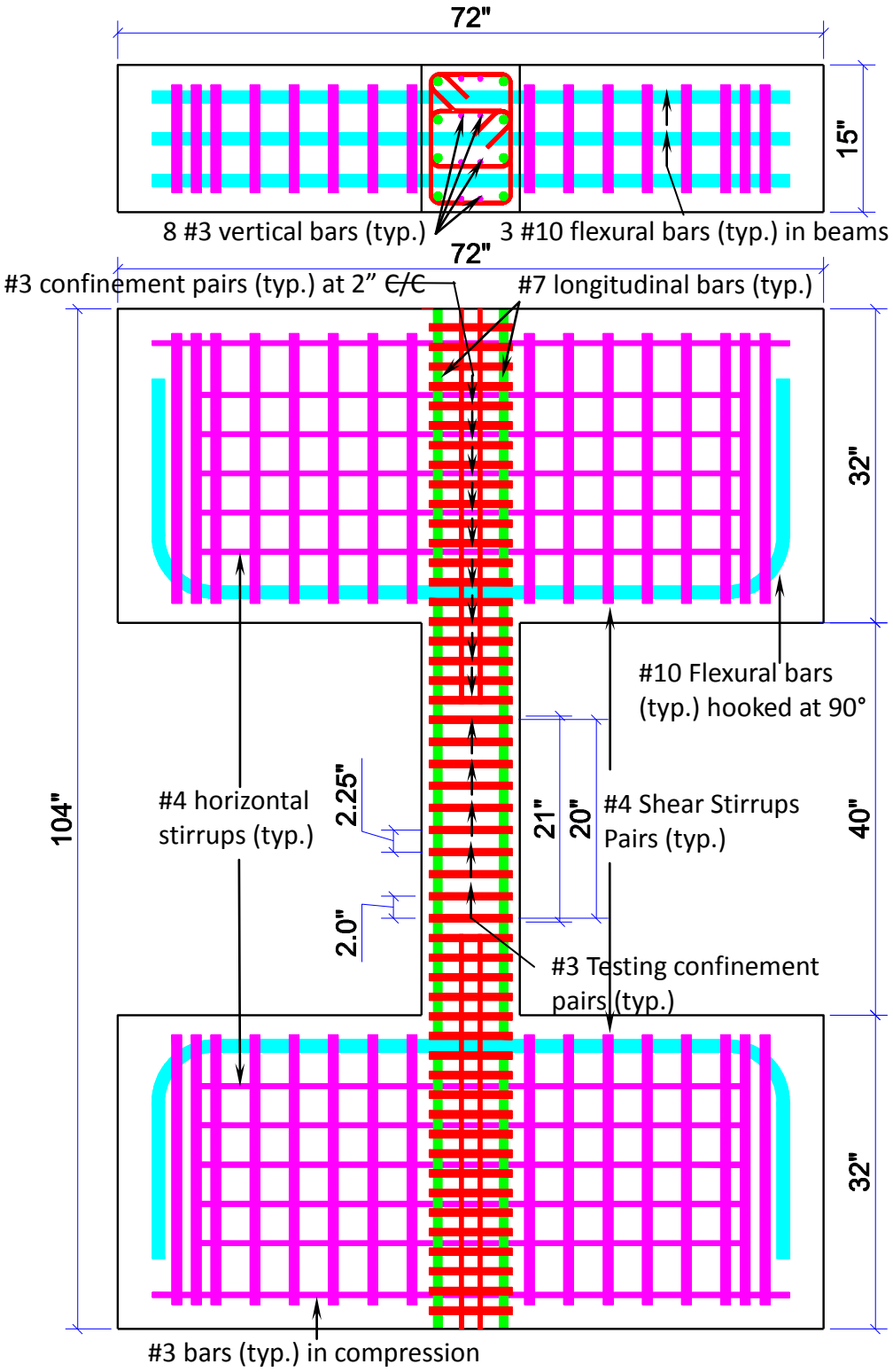

Figure 3-3: Test specimen reinforcement details

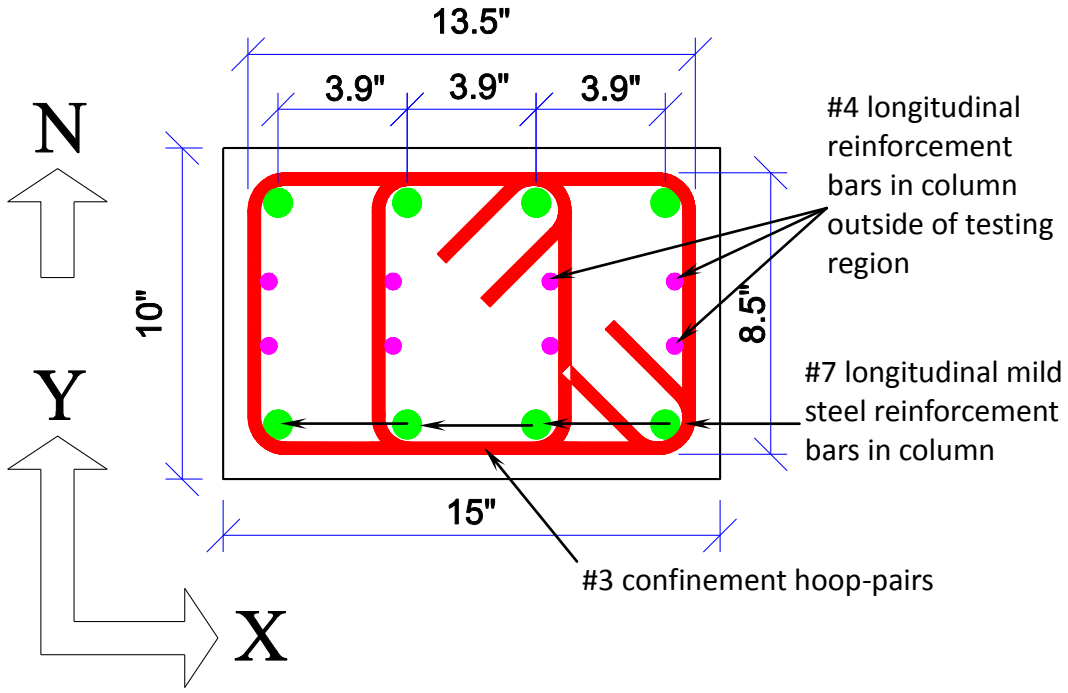

Figure 3-4: Column section and confinement hoop-pair details

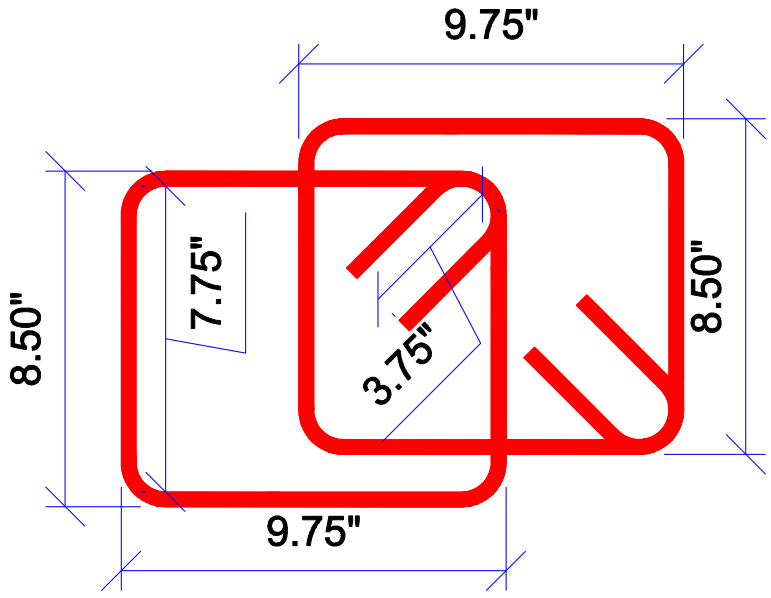

Figure 3-5: Confinement hoop-pair size

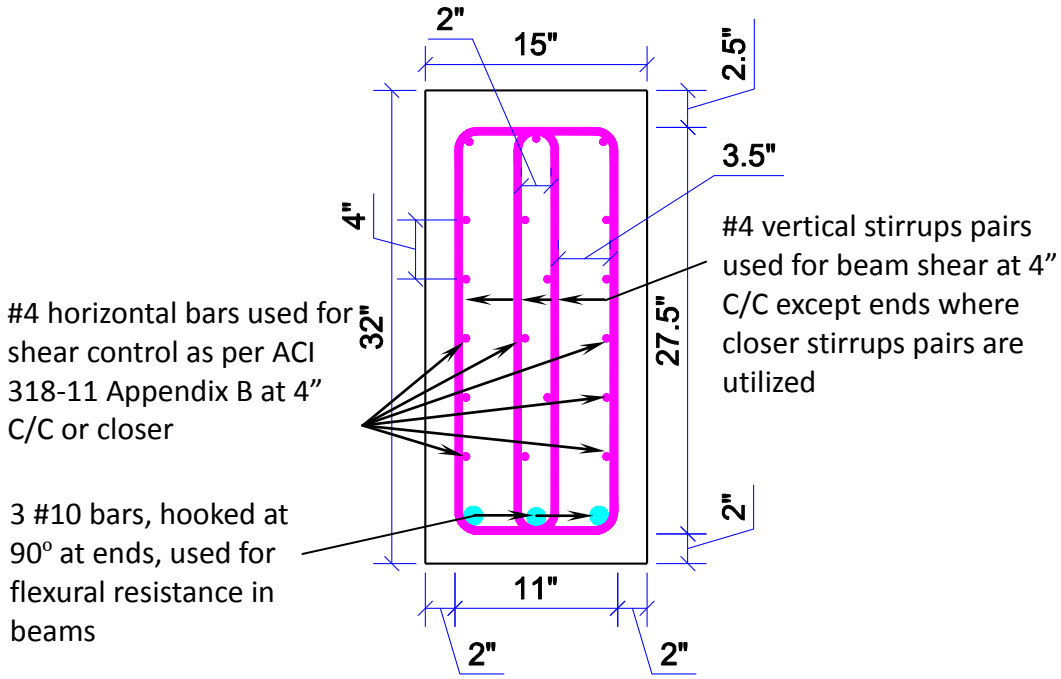

Figure 3-6: Beam section reinforcement details

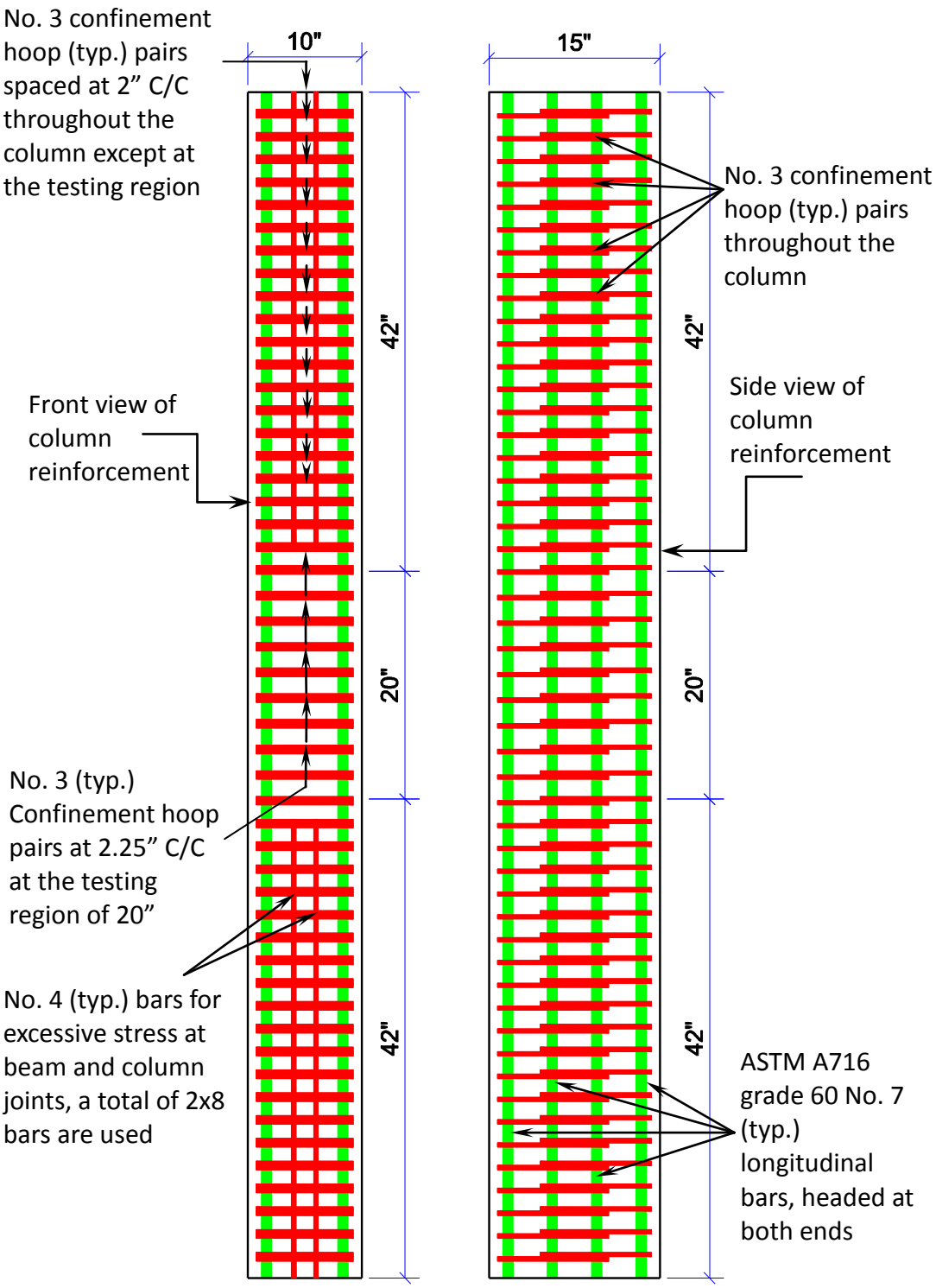

Figure 3-7: Confined concrete column reinforcement details

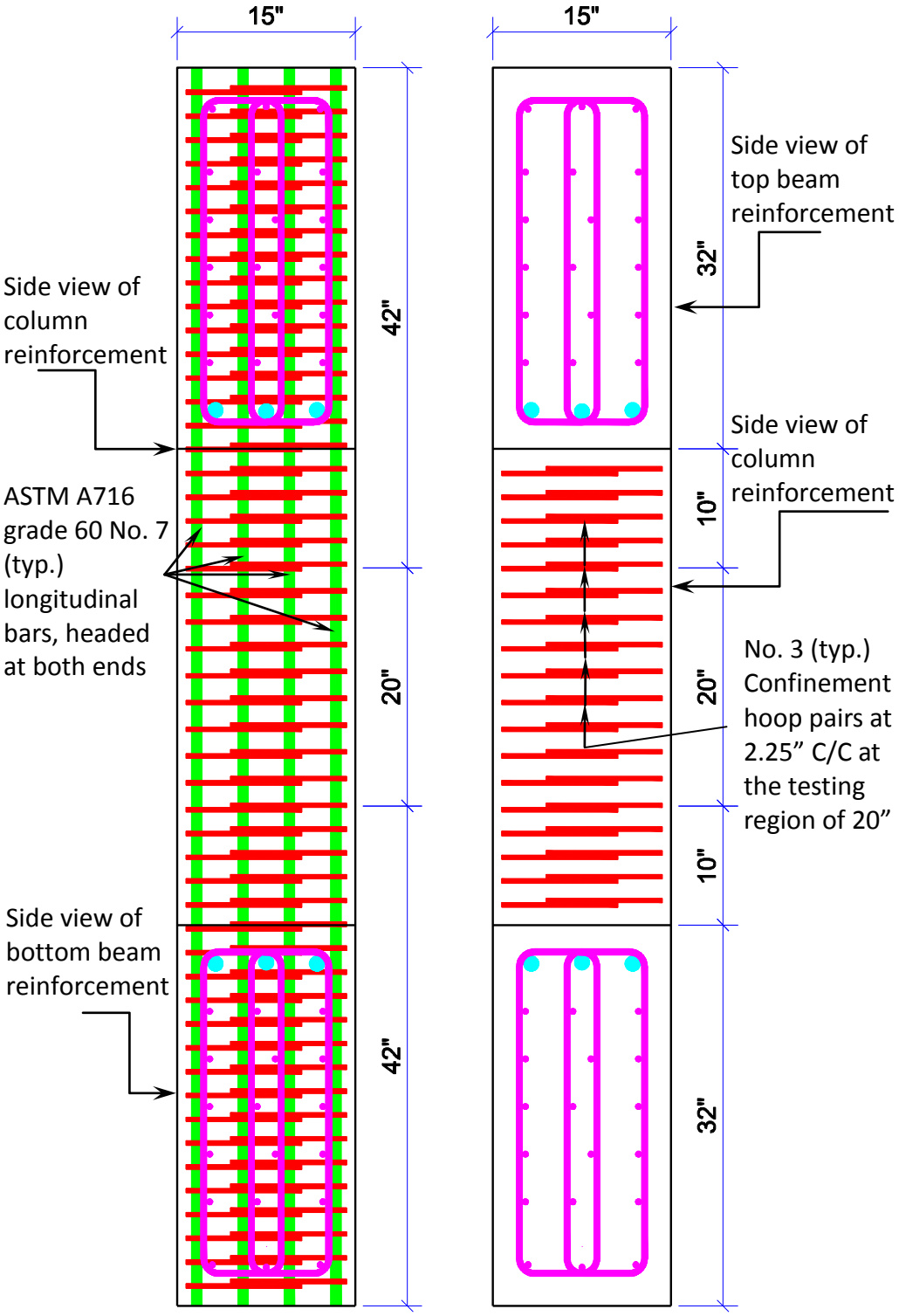

Figure 3-8: Confined concrete column and beams reinforcement details

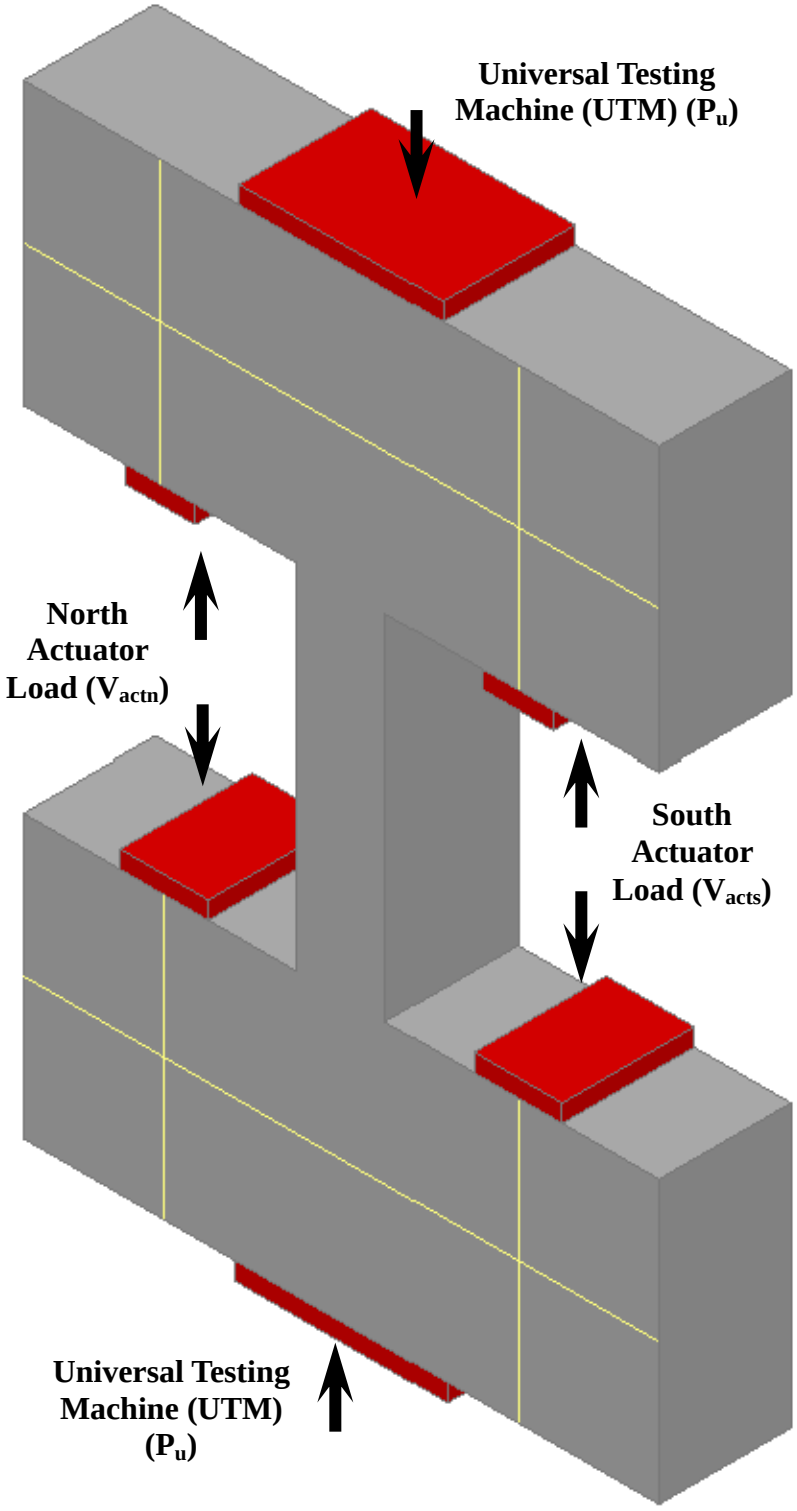

Figure 3-9: Isometric of loads on test specimens

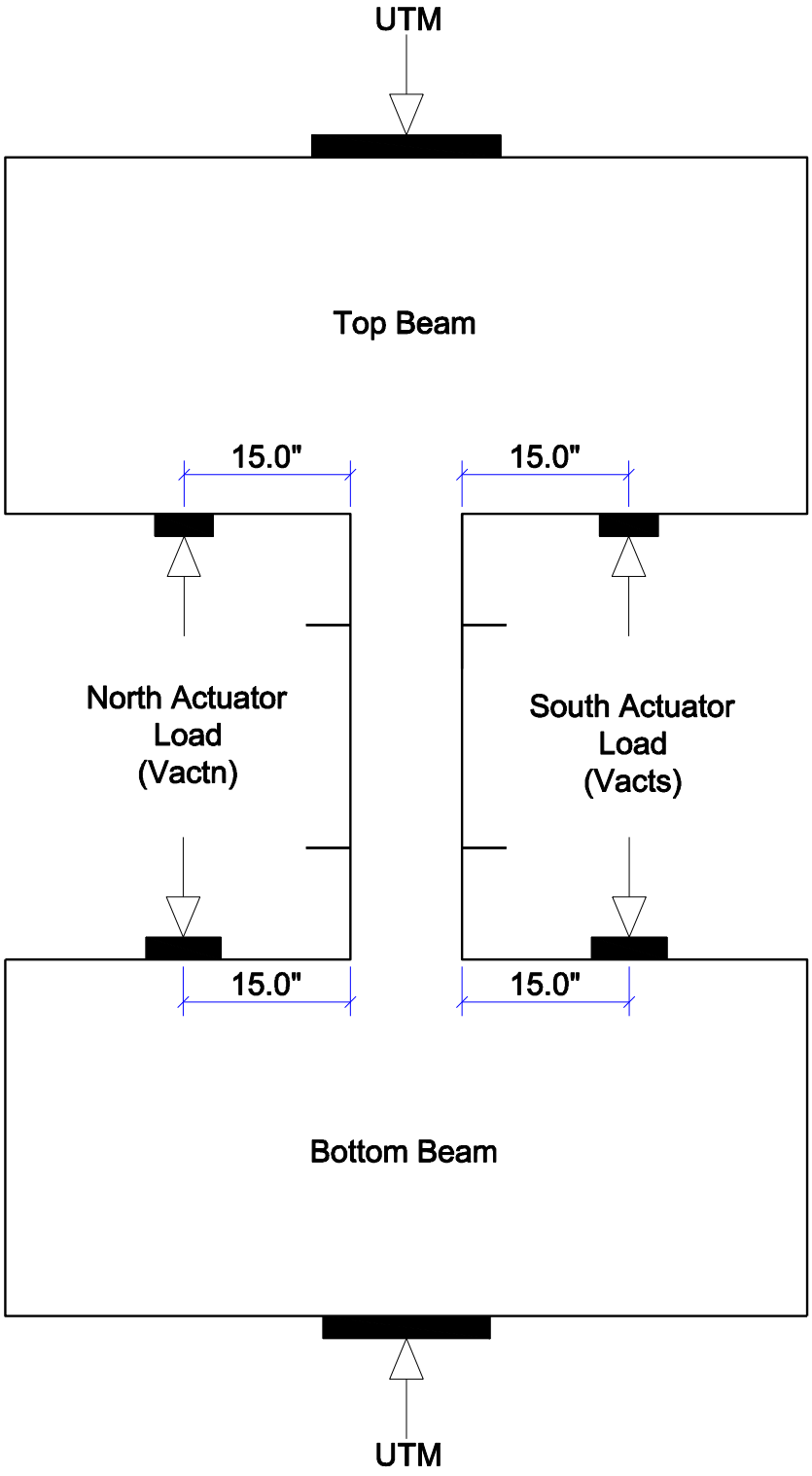

Figure 3-10: Loading diagram of test specimens

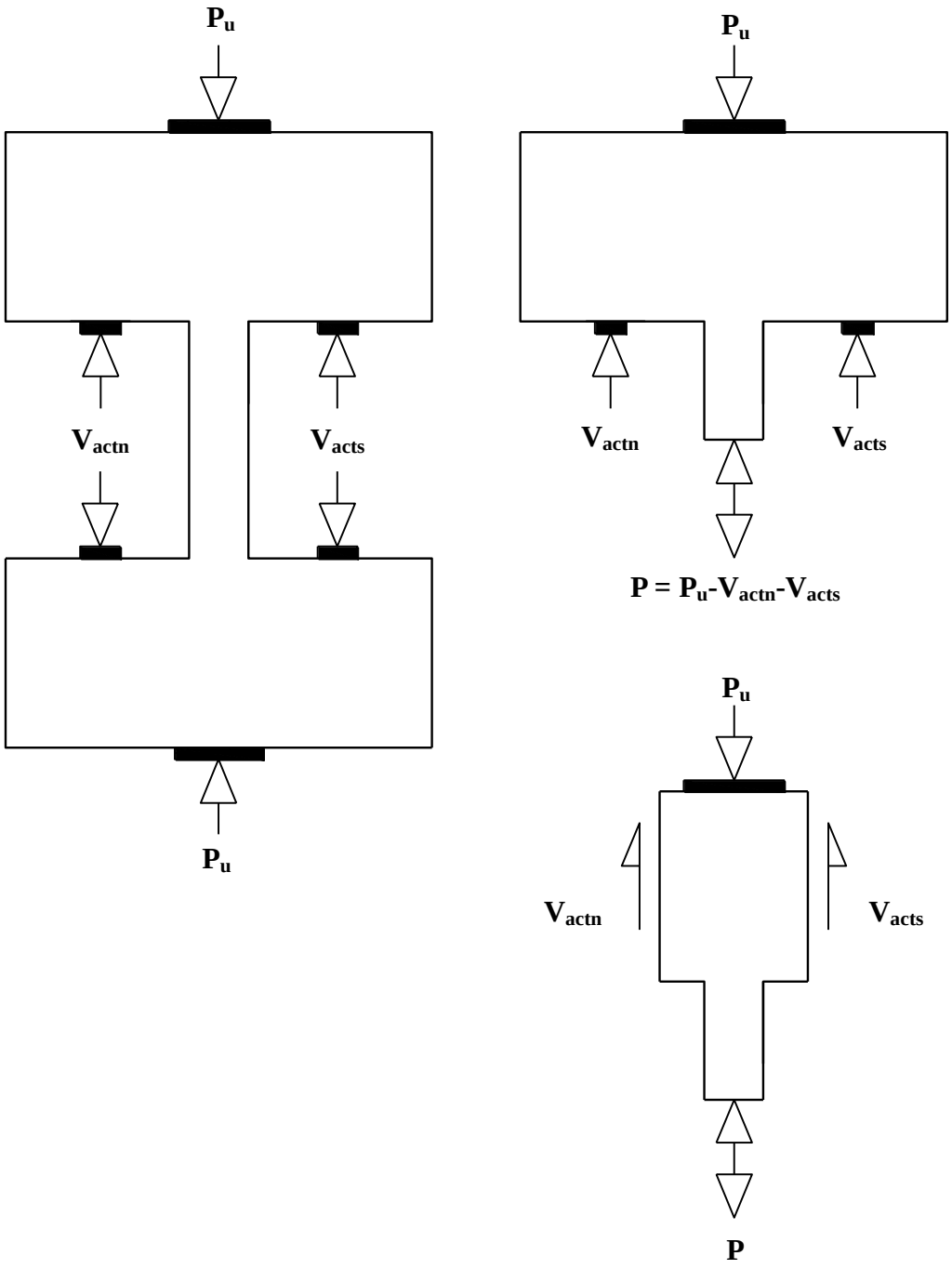

Figure 3-11: External and internal loading diagram of specimen

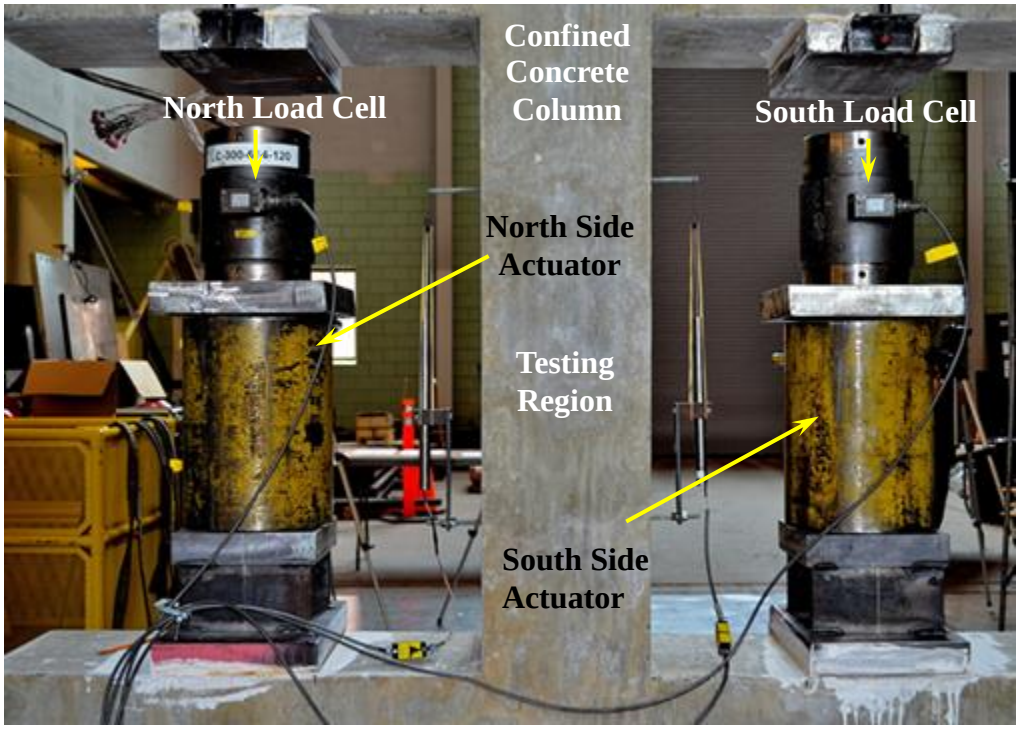

Figure 3-12: Actuator setup before loading

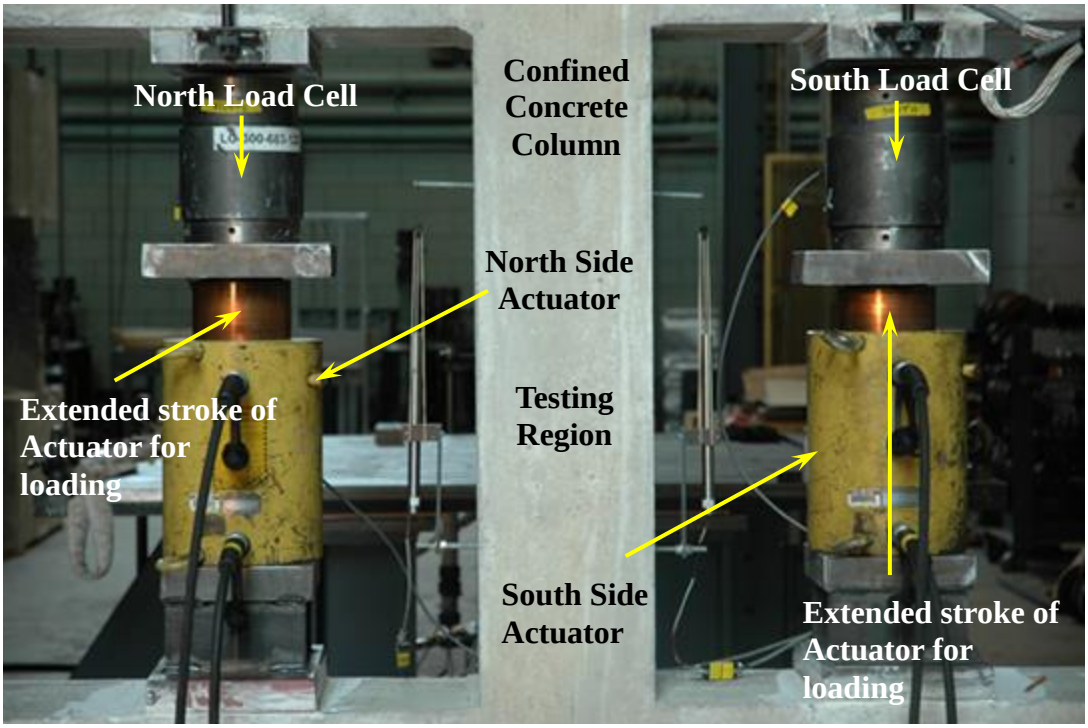

Figure 3-13: Actuator setup after loading

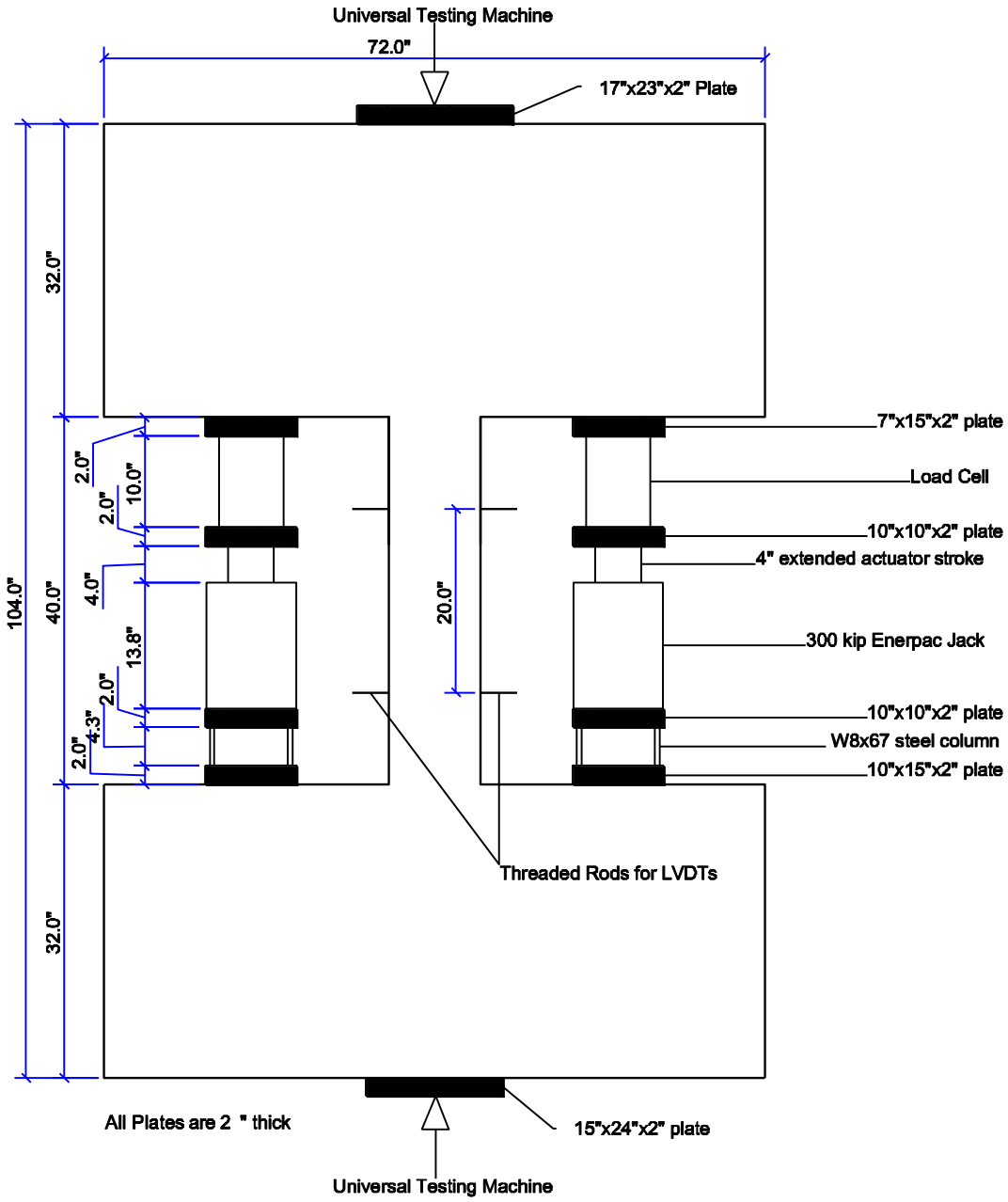

Figure 3-14: Loading setup, plates, and fixtures details

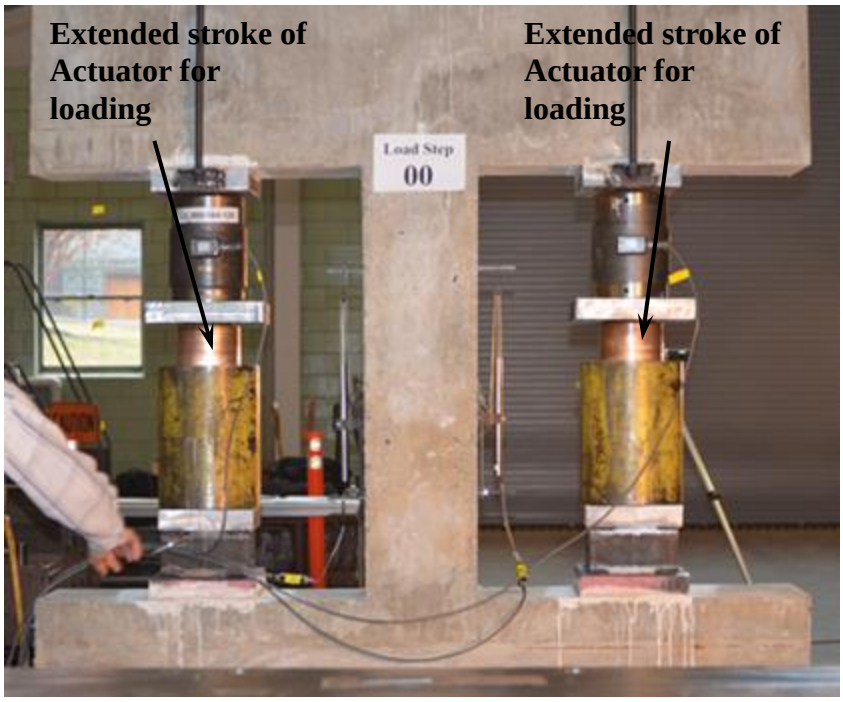

Figure 3-15: Loading setup

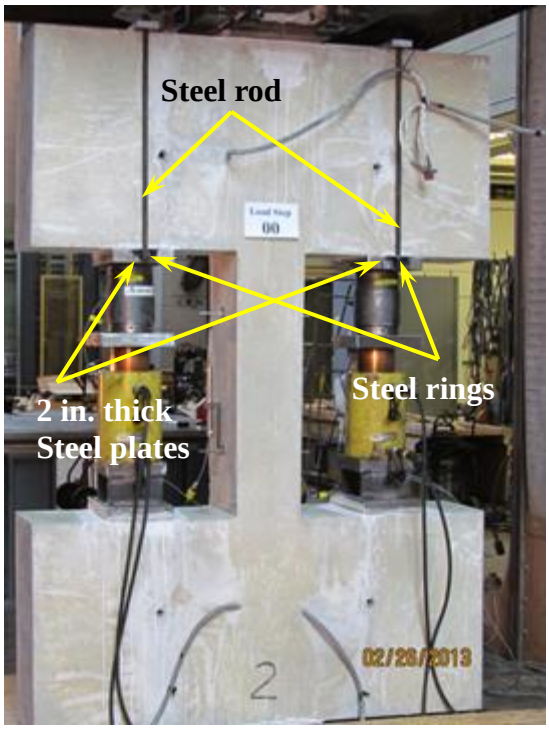

Figure 3-16: Steel rings-rod fixtures

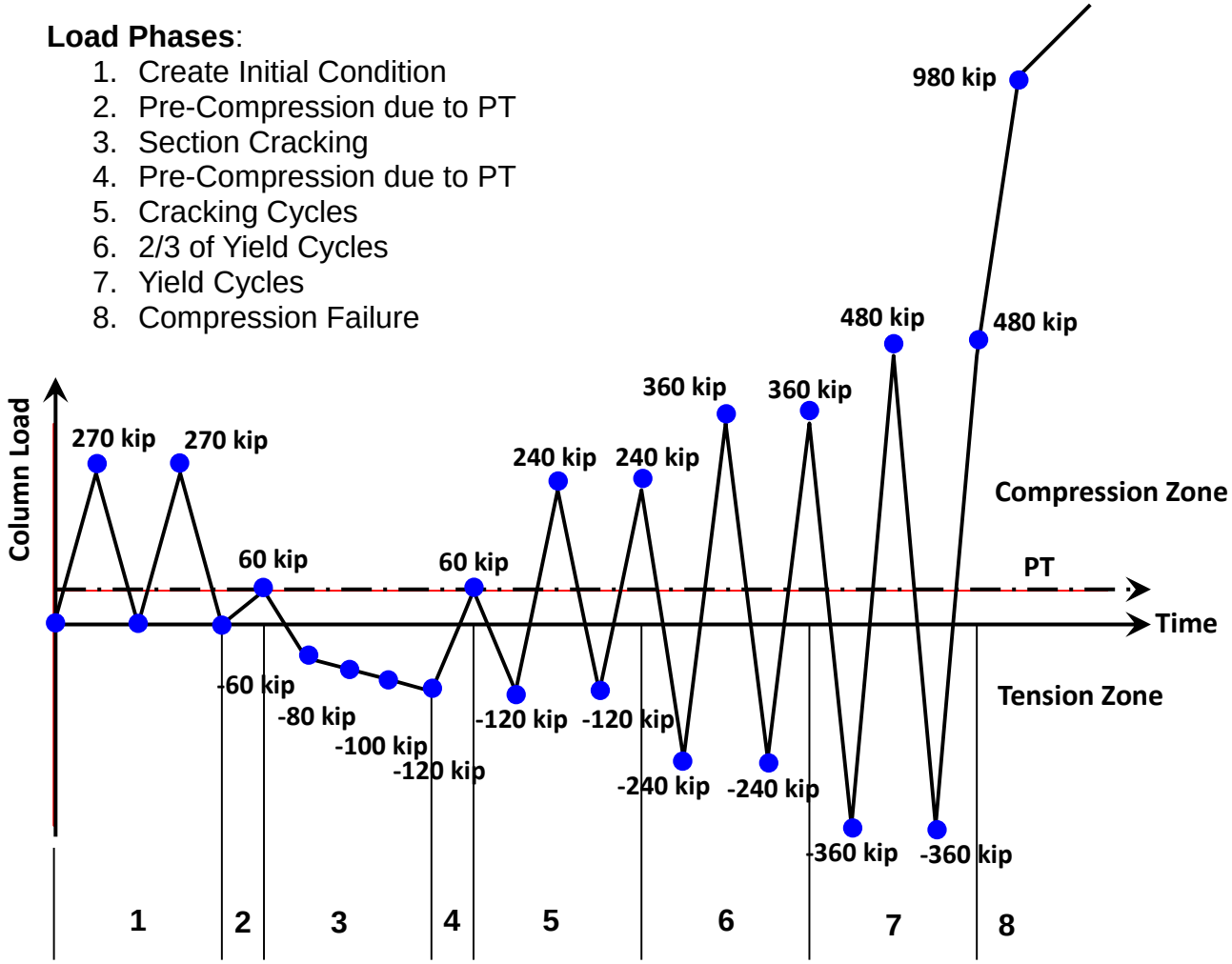

Figure 3-17: Loading protocol for TS01 including load phases notation

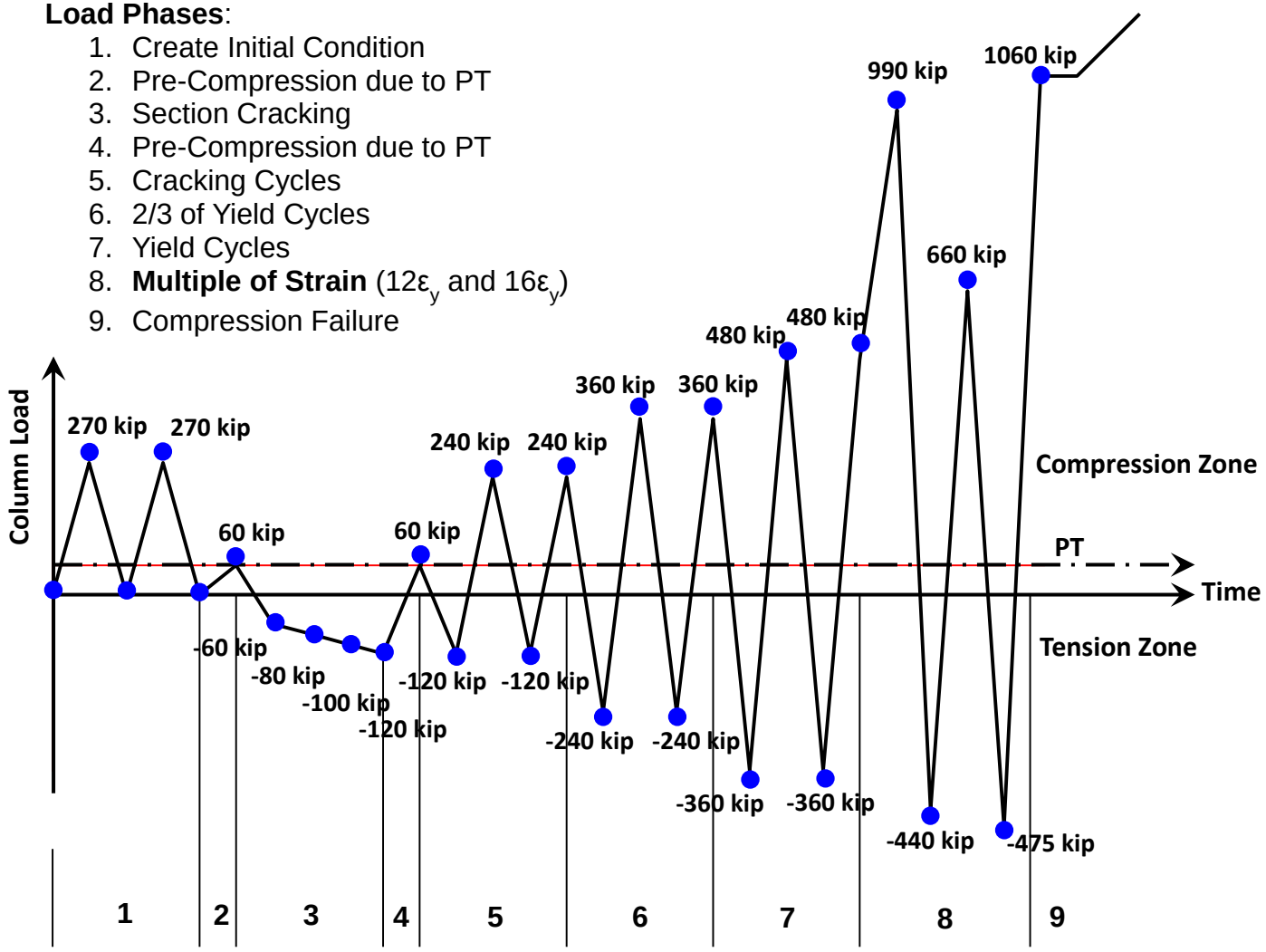

Figure 3-18: Loading protocol for TS02 including load phases notation

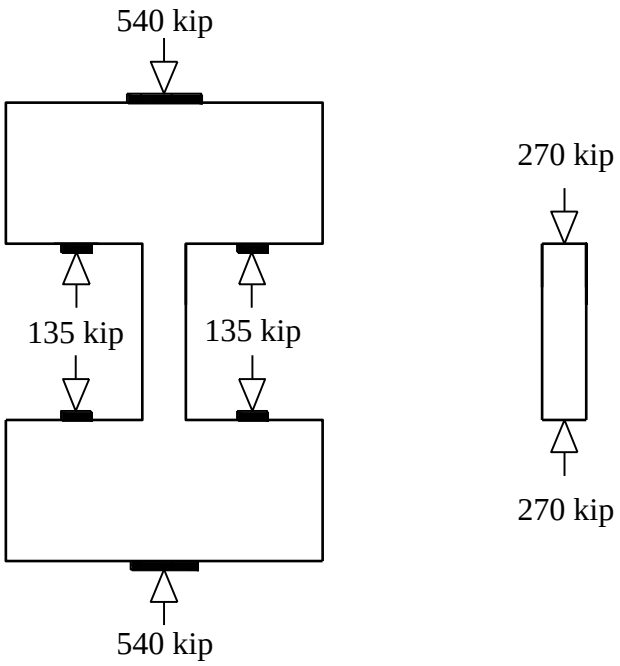

Figure 3-19: Load diagram at Load Step 03

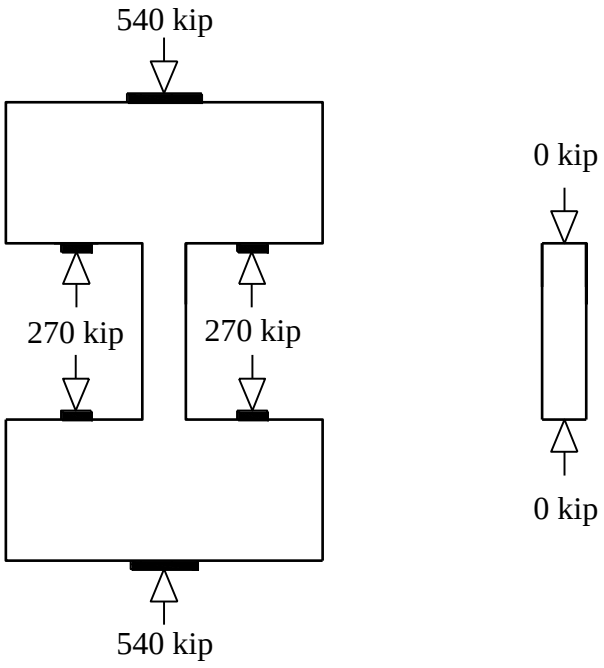

Figure 3-20: Load diagram at Load Step 04

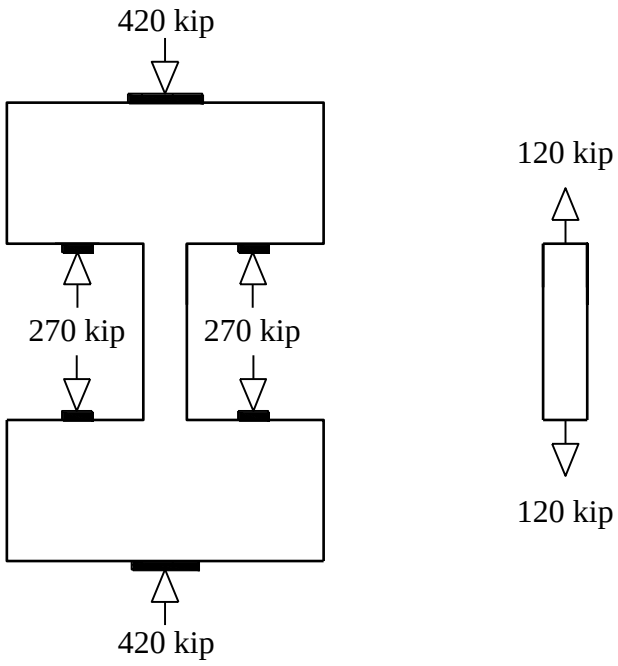

Figure 3-21: Load diagram at Load Steps 09, 11, and 13

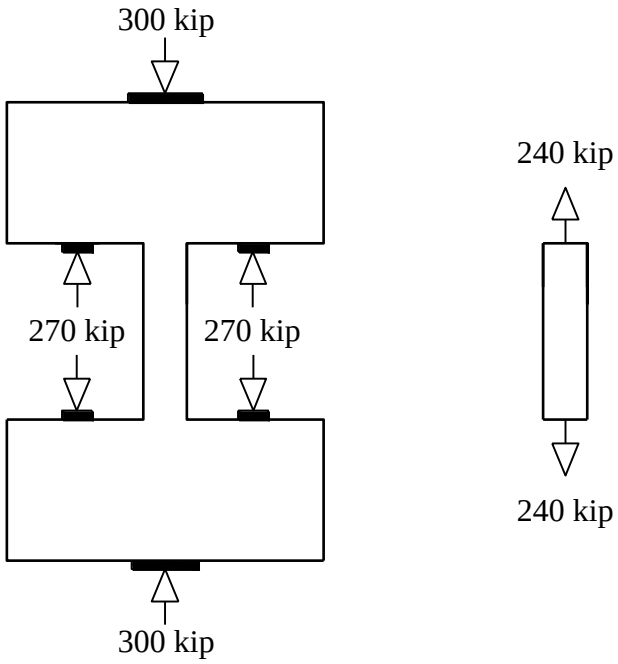

Figure 3-22: Load diagram at Load Steps 15 and 17

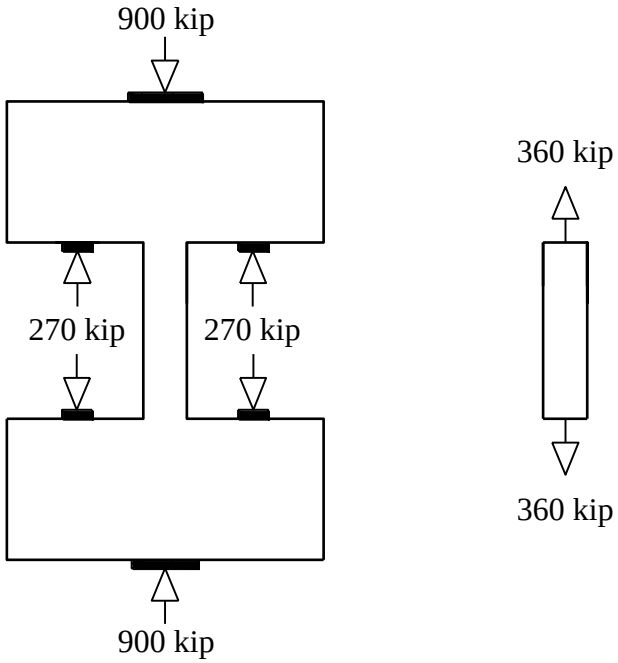

Figure 3-23: Load diagram at Load Steps 16 and 18

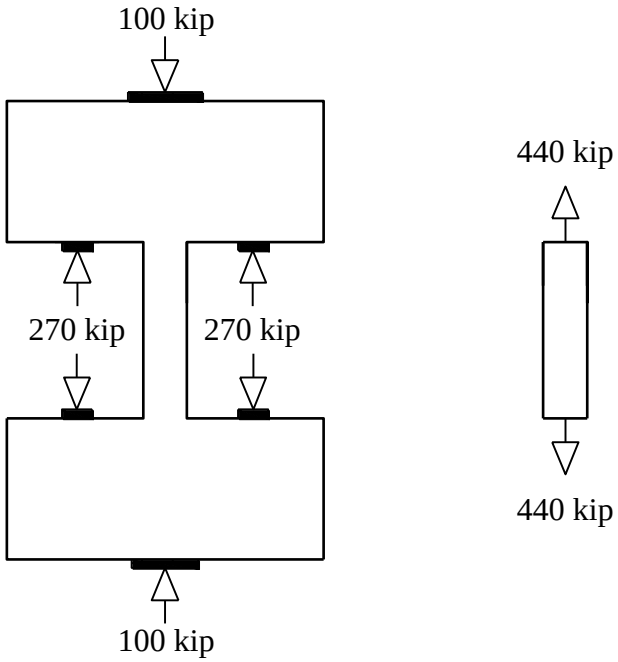

Figure 3-24: Load diagram at Load Steps 23 in TS02

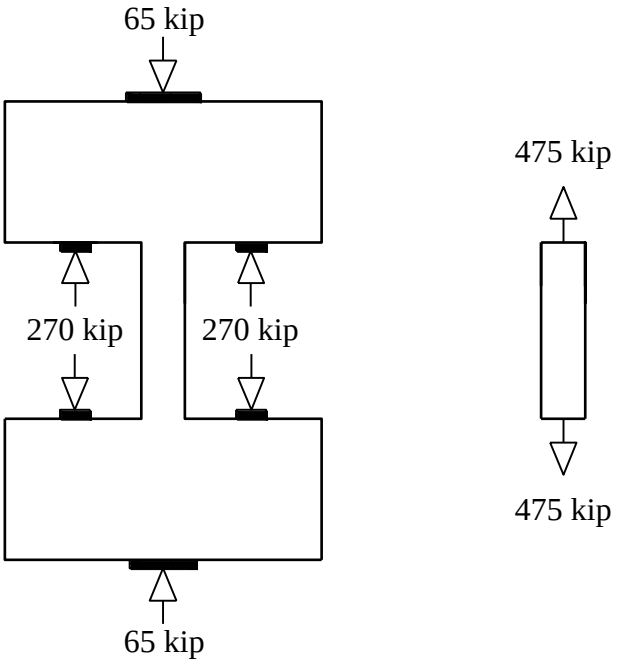

Figure 3-25: Load diagram at Load Steps 25 in TS02

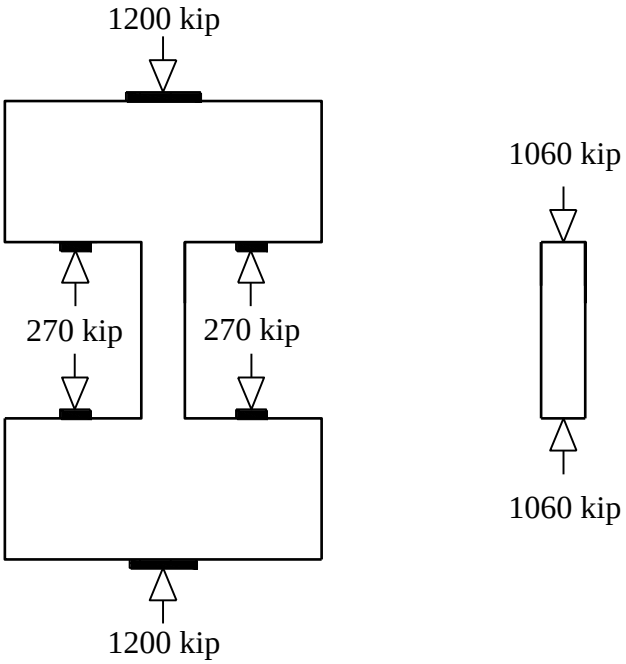

Figure 3-26: Load diagram at Load Steps 26 in TS02

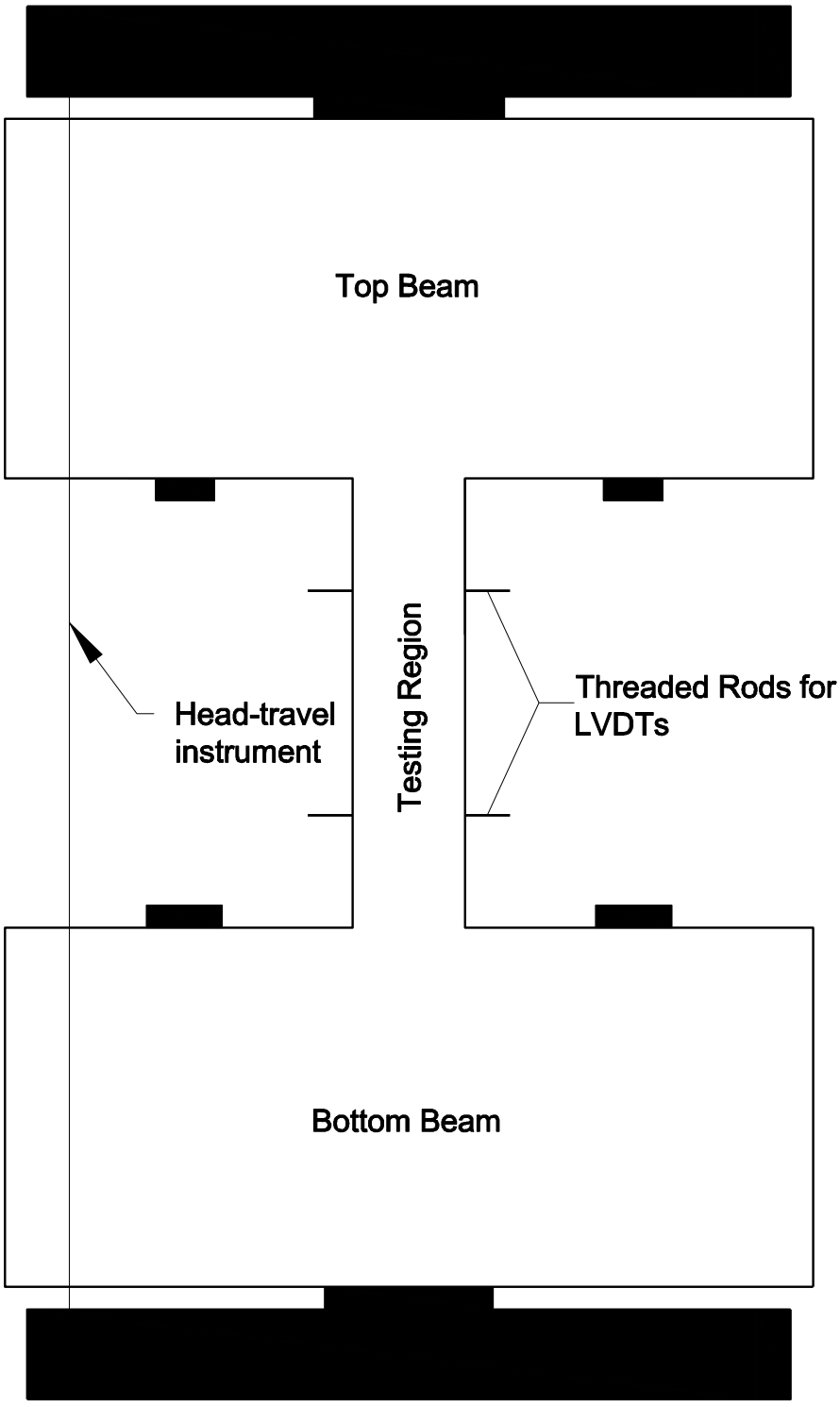

Figure 3-27: Instrumentation

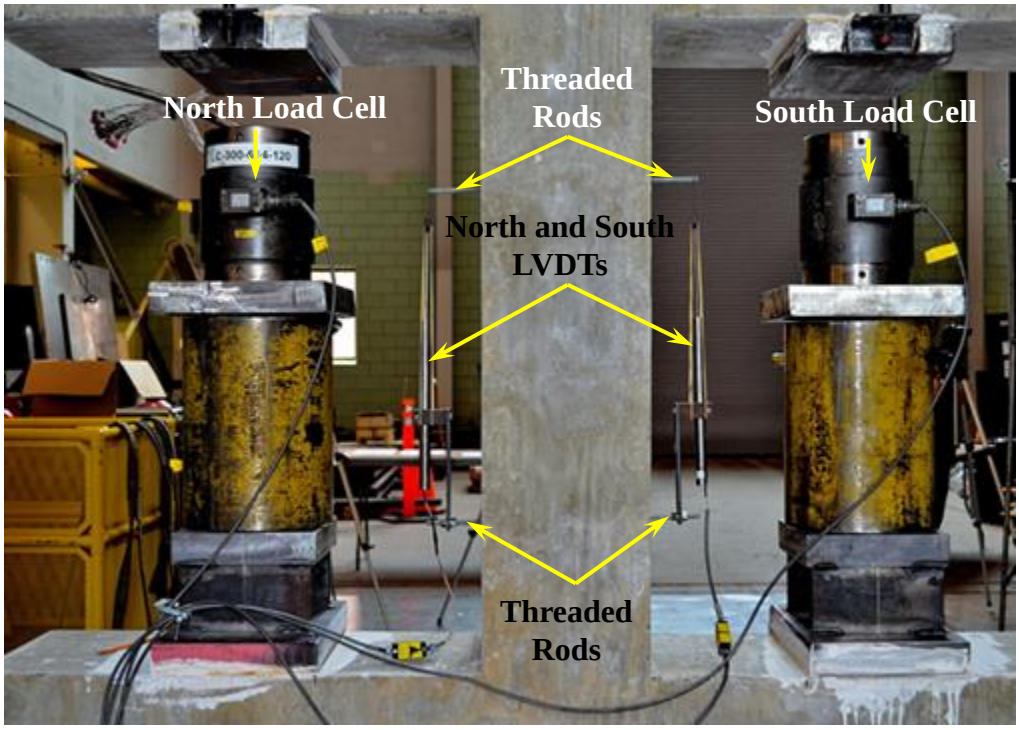

Figure 3-28: Instrumentation before loading

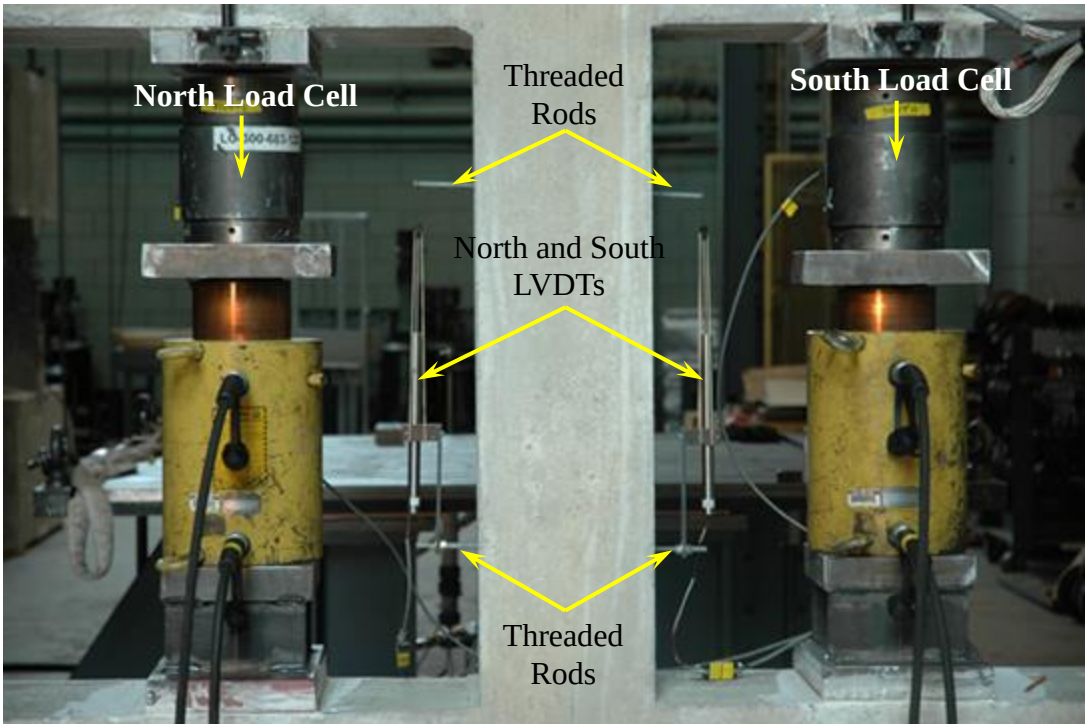

Figure 3-29: Instrumentation during loading

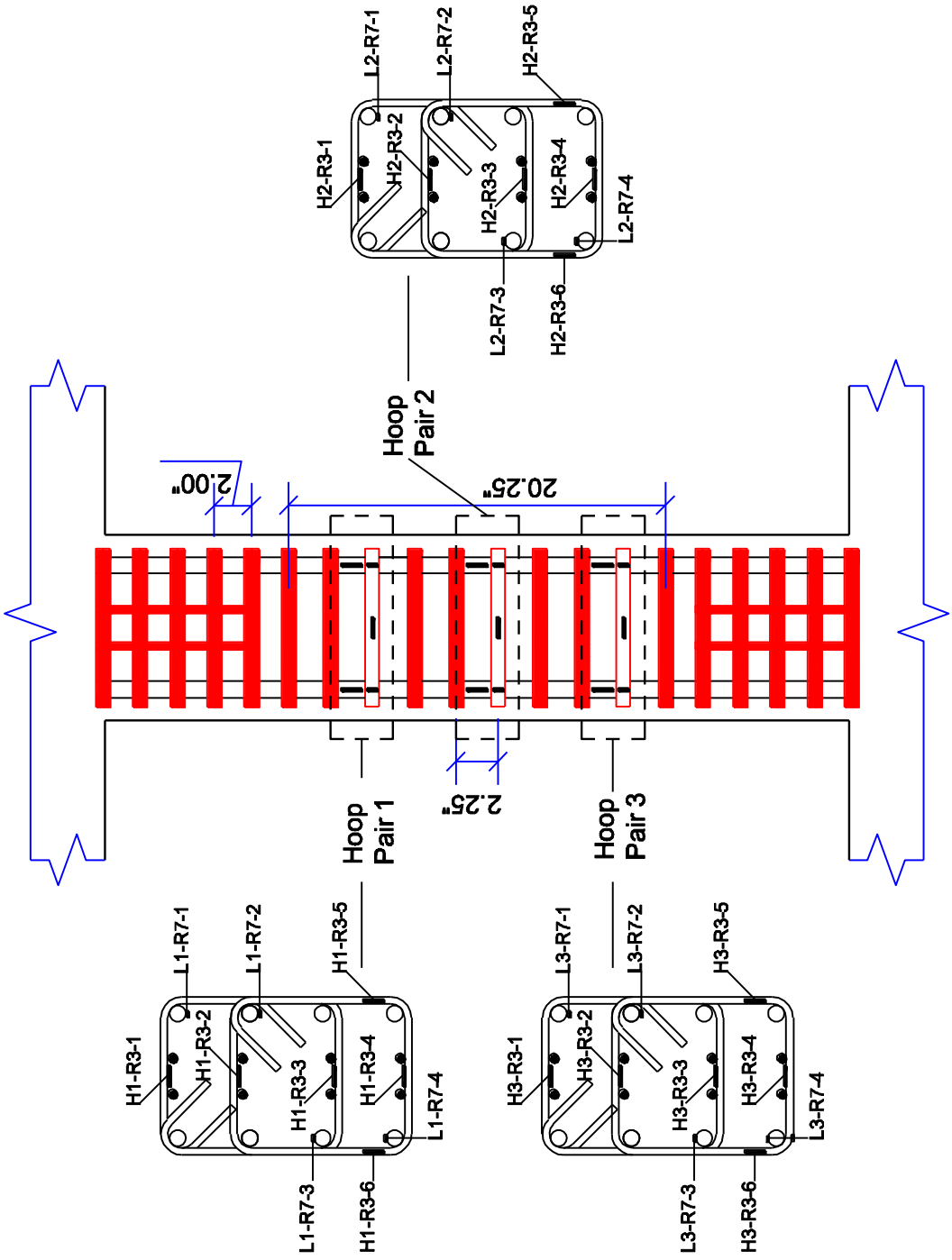

Figure 3-30: Strain gage notation in tesing region

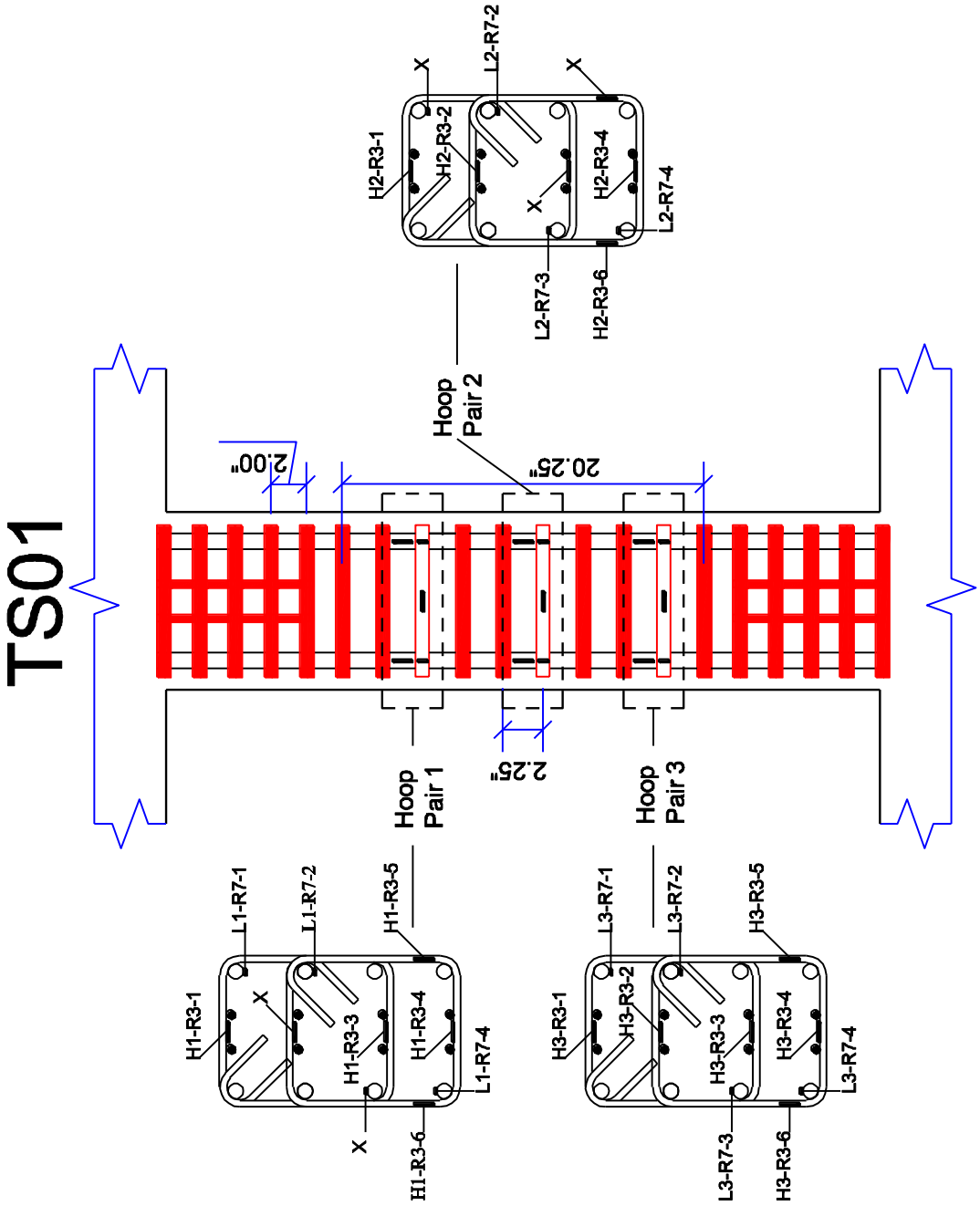

Figure 3-31: Strain gage notation for TS01

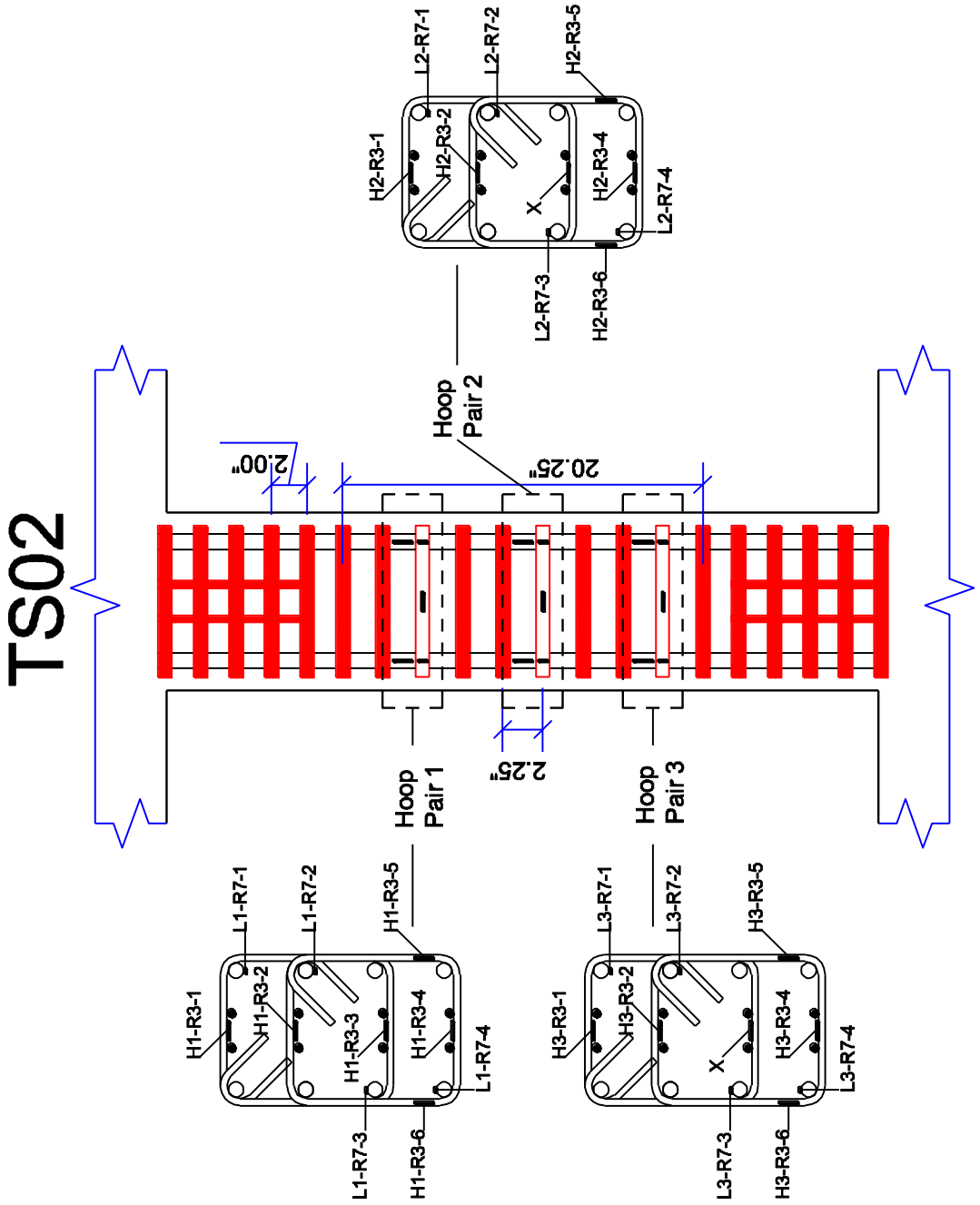

Figure 3-32: Strain gage notation for TS02

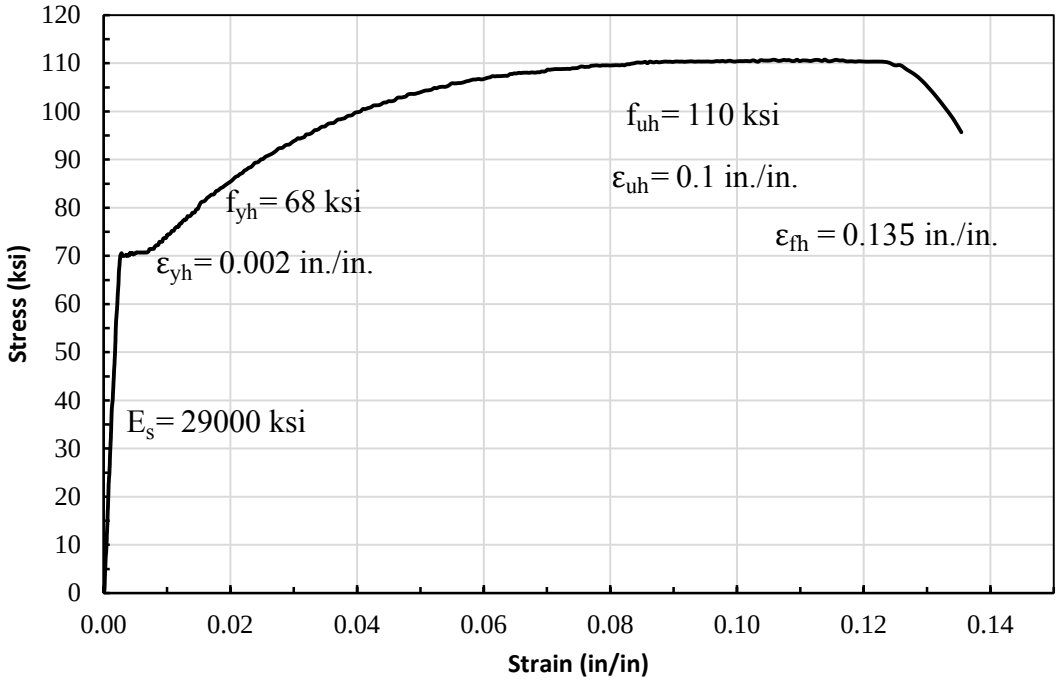

Figure 3-33: Measured stress-strain curve for confinement hoop reinforcement

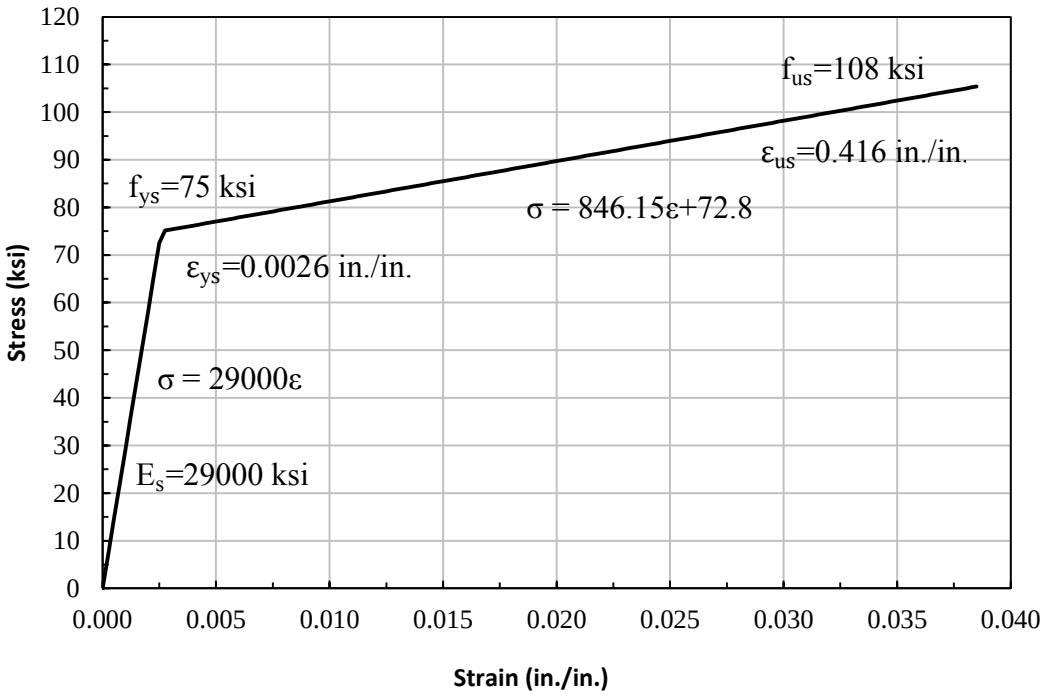

Figure 3-34: Bilinear stress-strain relation for longitudinal reinforcement bars

Figure 3-35: Reinforcement of TS01

Figure 3-36: Reinforcement of TS02

Figure 3-37: Strain gage instrumentation

Figure 3-38: Strain gage instrumentation

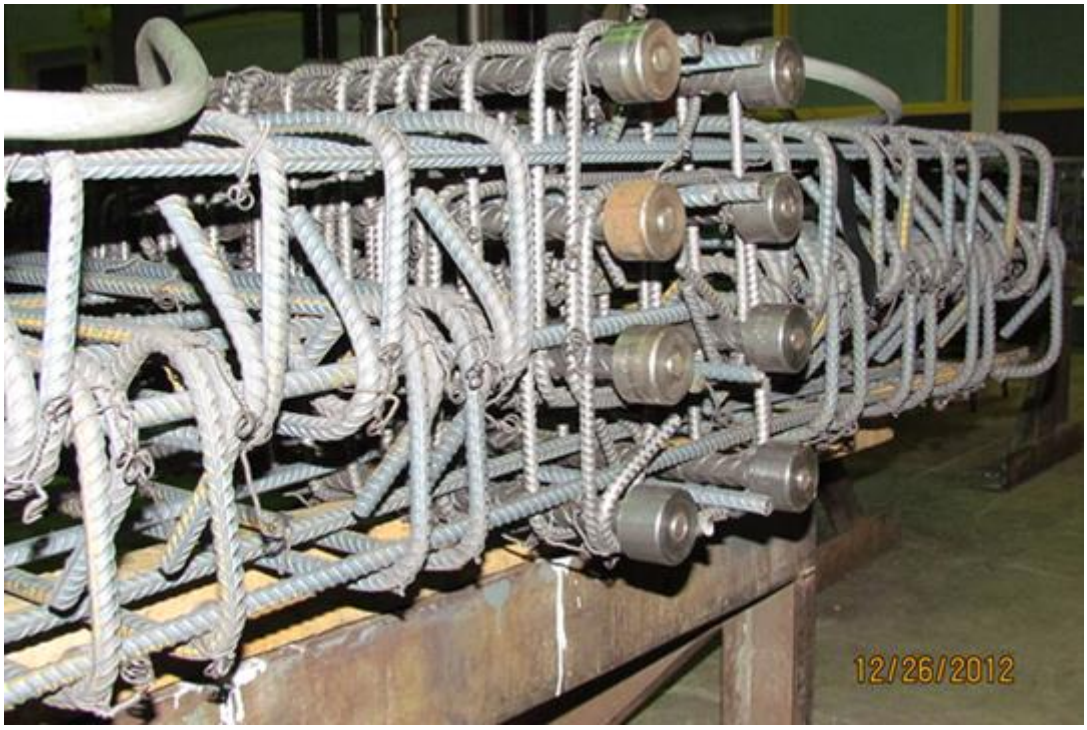

Figure 3-39: Headed bars used in confined concrete column

Figure 3-40: 90-degree hook of flexural bars

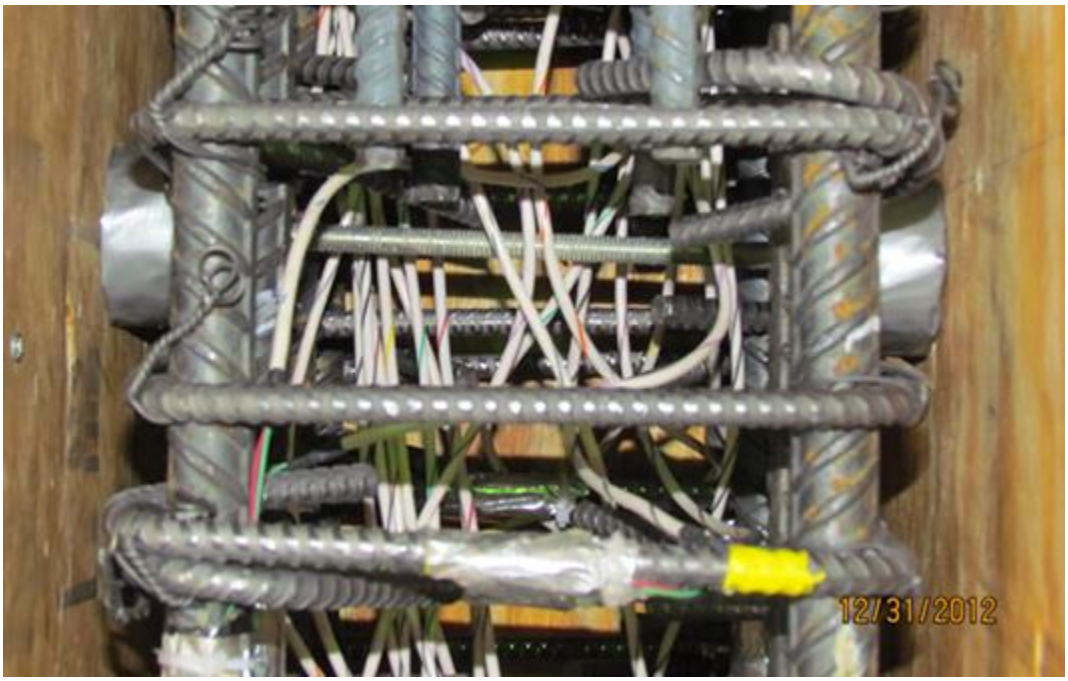

Figure 3-41: Threaded rod with polystyrene pocket

Figure 3-42: Lifting inserts installation

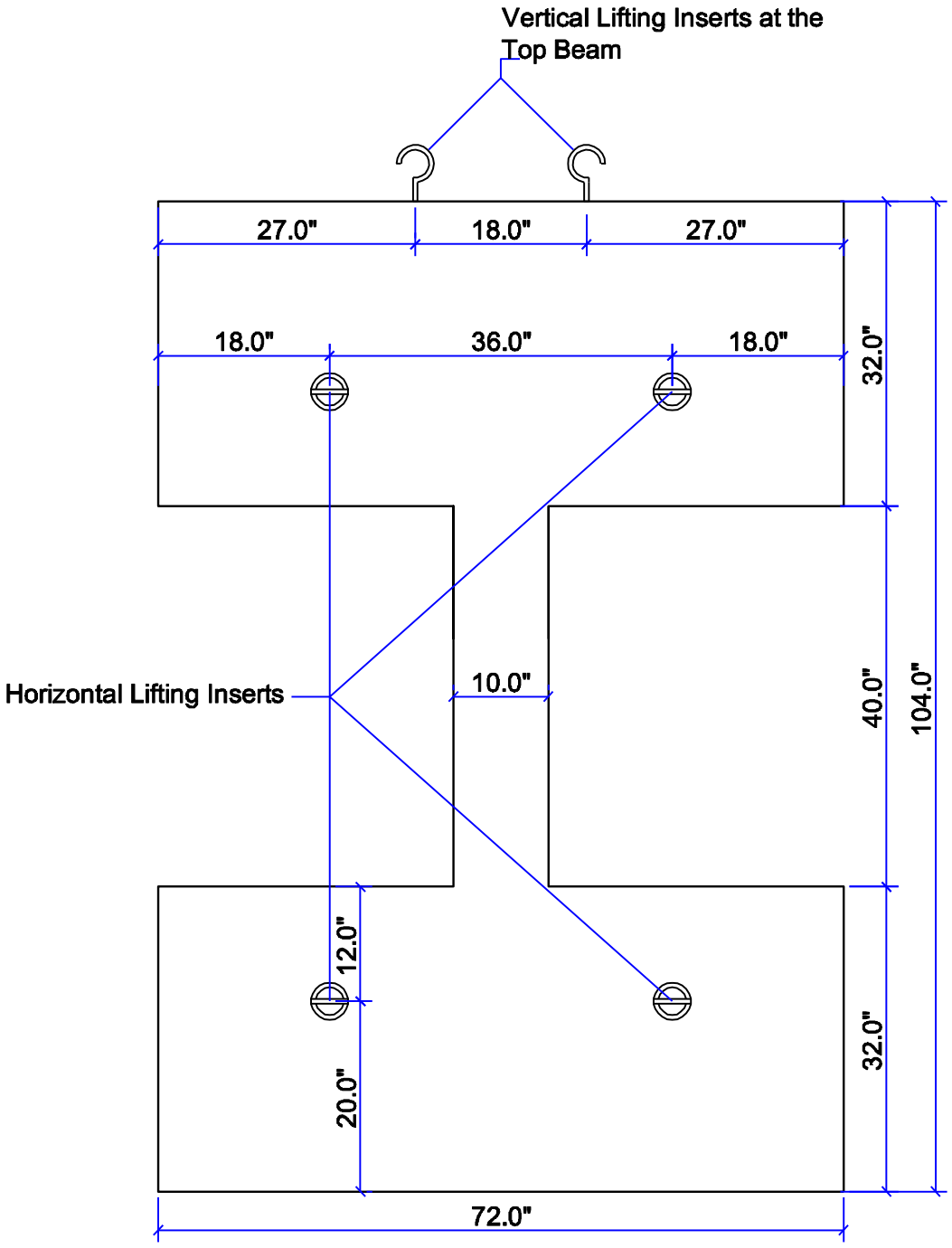

Figure 3-43: Location of lifting inserts

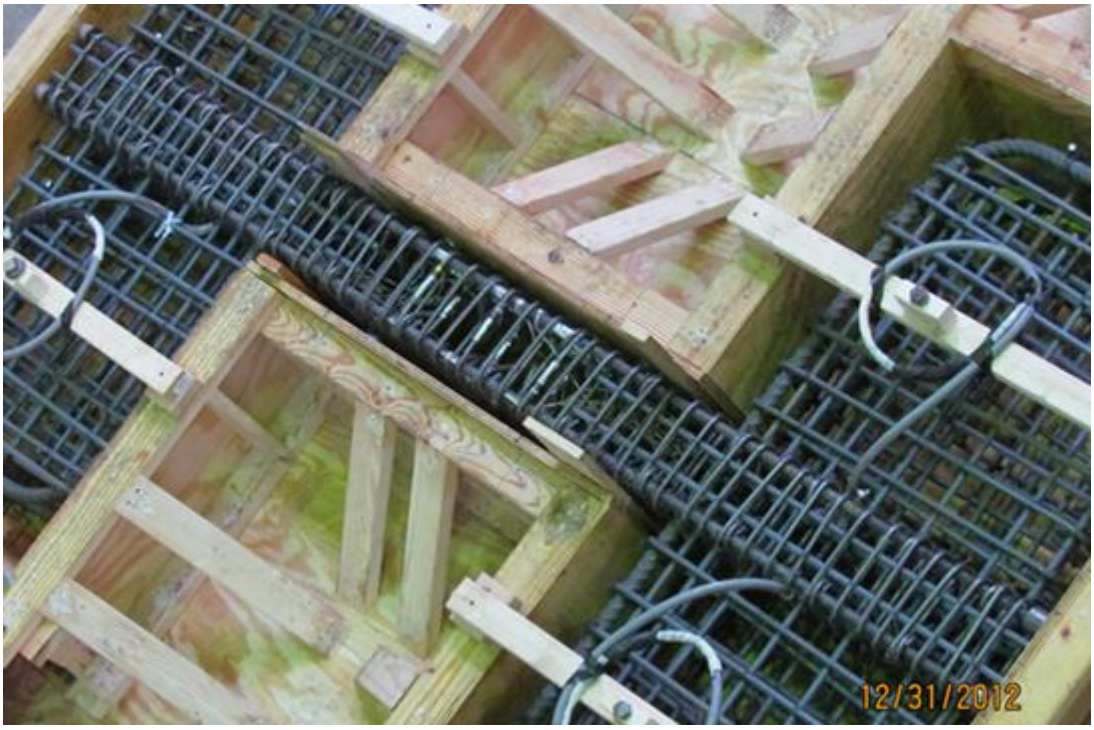

Figure 3-44: Reinforcement of confined concrete column inside the wooden form

Figure 3-45: Reinforcement of testing specimens placed inside the wooden forms

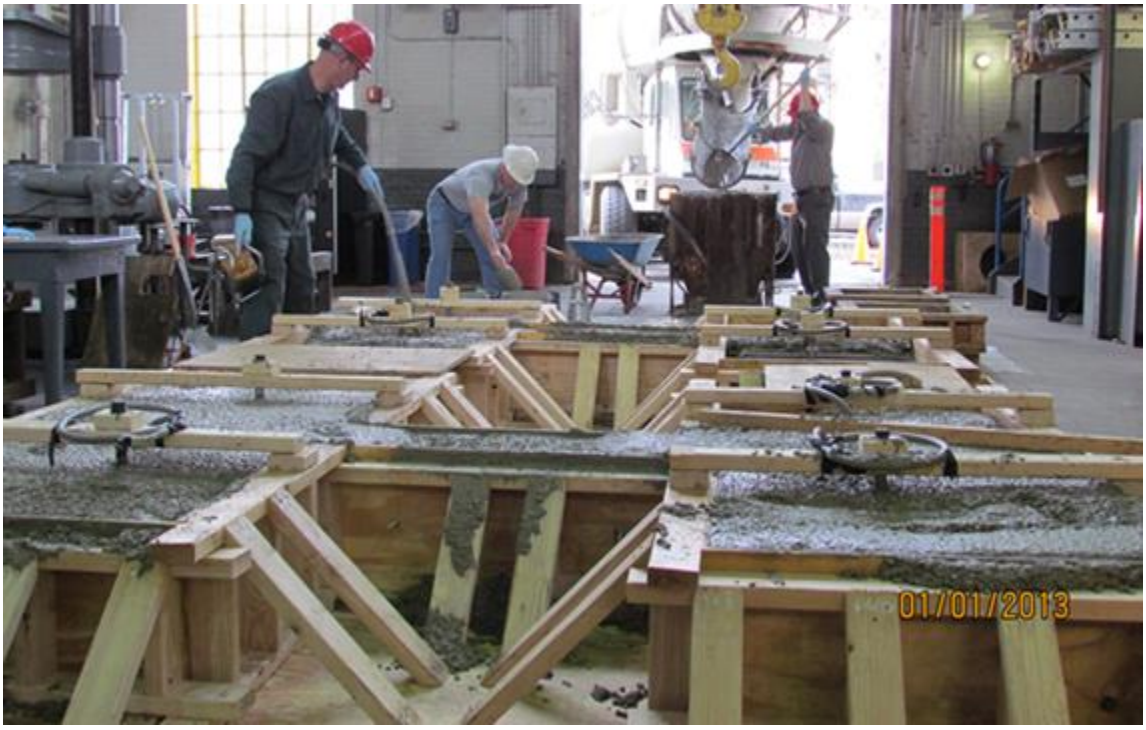

Figure 3-46: Concrete casting of test specimens

Figure 3-47: Concrete casting of test specimens

Figure 3-48: Transfering test specimens using a crane

Figure 3-49: Transfering test specimens using rollers

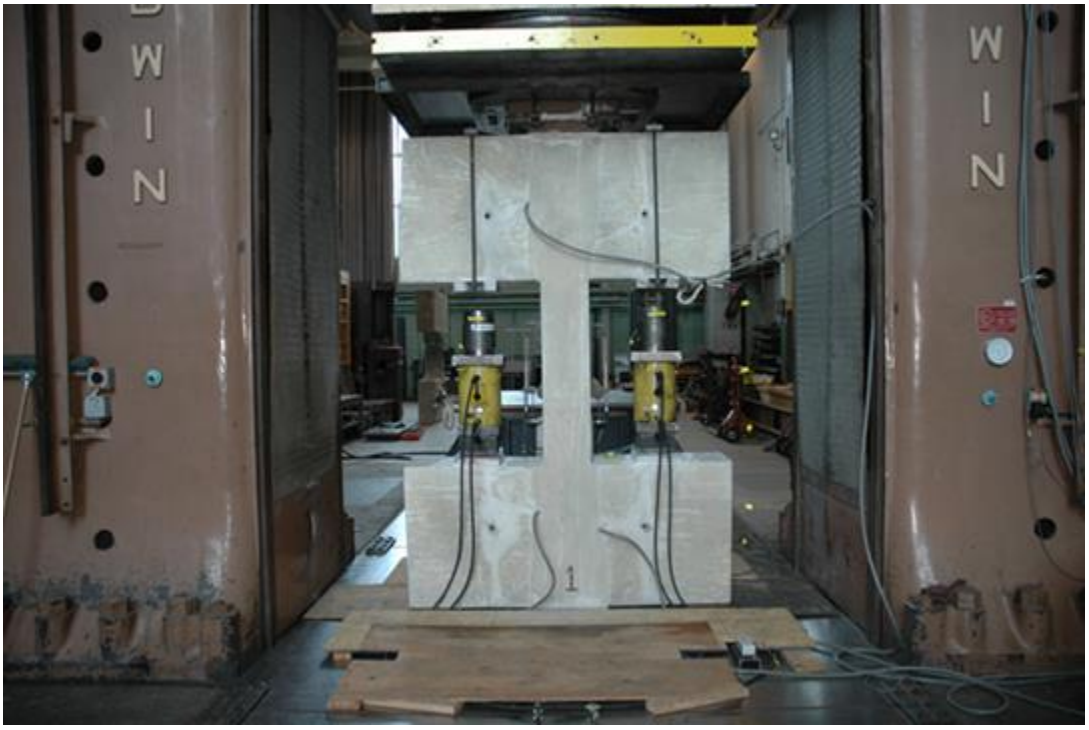

Figure 3-50: West face of TS01 before loading

Figure 3-51: West face of TS02 before loading

CHAPTER 4

EXPERIMENTAL RESULTS

4.1 INTRODUCTION

This chapter explains the experimental results. The experimental data includes the recorded data from the instrumentation, recorded sizes of cracks at load steps, and photographs at load steps. The experimental results include the deformation of testing region versus net load in testing region; average strain of testing region versus net load in testing region; deformation of test specimen versus net load in testing region; strains in longitudinal mild steel reinforcement bars versus net load in testing region; and strain in confinement hoops versus net load in testing region. In all plots, the net load in testing region is provided on the vertical axis, and strain or deformation of confined concrete column or testing region is provided on horizontal axis. All plots for the experiments are presented in terms of net load in testing region of each test specimen.

Section 4.2 explains the overall response of test specimens. Section 4.3 explains the concrete cracking in confined concrete column particularly in testing region of each test specimen recorded at the end of the load steps, and photographs of the confined concrete column at the load steps.

4.2 OVERALL RESPONSE OF TEST SPECIMENS

This section presents and explains the test data for each test. This includes: (1) explaining the behavior and deformation of test region and explaining key points on deformation plots of the test results; (2) specimen deformation plots; (3) testing region deformation plots; (5) testing region strain plots; and, (6) strain plots for strain gages of the longitudinal mild steel reinforcement and confinement hoops.

4.2.1 Behavior and Deformation of Test Specimens

As discussed in detail later for both specimens, the peak strength of testing region cross-section was reached at the initiation of cover spalling. At this stage, the confinement hoops started to restrain buckling of the longitudinal mild steel reinforcement bars inside the confined concrete. After this, the confined concrete strength started to drop. At this peak strength, on average, the tensile strain in confinement hoop reinforcement was 40-50% of their yielding strain limit.

After a small drop in strength after the initiation of cover spalling, the strength slowly increased until the ultimate strength of the confined concrete core was reached. At this point, the confinement hoops reached the maximum effective lateral stress (i.e., the confinement hoop reinforcement yielded). The load and the corresponding strain at the testing region were almost the same for the two test specimens.

After the confinement hoop reinforcement reached their yielding strain limit, the confined concrete provided significant ductility (i.e., deformation). The confined concrete load gradually decreased and the axial compression strain increased. This stage was maintained until the first confinement hoop fractured. A sudden drop of strength and

buckling of longitudinal reinforcement bars were noticed. Soon after first hoop fracture, the second and third hoops fractured. Both internal and external confinement hoops fractured.

Key Load Points on TS01 Plots

Figure 4-1 shows key points on head-travel versus testing region load plot of TS01. In TS01, the confined concrete column section was loaded to 360 kip in tension at Load Step 19 and Load Step 21 (See Table 3-2). The actual maximum tensile strain in the longitudinal mild steel reinforcement bars of the confined concrete column was $4\varepsilon_{ys}$ based on strain gages data at tension Load Step 21. The column section was stressed in compression to the peak strength and to compression failure in Load Step 24.

Cover spalling in the testing region initiated at a peak load of 1447 kip. The first confinement hoop fractured followed by buckling of longitudinal mild steel reinforcement bars at 859 kip post-peak load of testing region. The second hoop fractured at 659 kip post-peak load of testing region. The third hoop fractured at 593 kip post-peak load of testing region.

NLVDT was influenced by cover spalling at post-peak load of 957 kip and a compression deformation of 0.72 in. of testing region; therefore, leading to incorrect results after that load. SLVDT was not influenced by cover spalling during the testing; therefore, it gives correct data for the entire testing duration. The UTM loading was stopped at 476 kip post-peak load of testing region. The UTM load was unloaded at post-peak load of 450 kip. The testing load ranged from 360 kip in tension to 1447 kip in compression.

Key Load Points on TS02 Plots

Figure 4-2 shows key points on head-travel versus testing region load plot of TS02. For TS02, the confined concrete column section was loaded to 440 kip in tension (to $12\varepsilon_{ys}$ of tensile strain) at Load Step 23 and to 475 kip in tension (to $16\varepsilon_{ys}$ of tensile strain) at Load Step 25 (See Table 3-3). The column section was stressed in compression to the peak strength and to compression failure in Load Step 29.

Cover spalling in the testing region initiated at a peak load of 1384 kip. The first confinement hoop fractured followed by buckling of longitudinal mild steel reinforcement bars at 668 kip post-peak load of testing region. The second hoop fractured at 568 kip post-peak load of testing region. The third hoop fractured at 502 kip post-peak load of testing region.

NLVDT was influenced by cover spalling at post-peak load of 1076 kip and a compression deformation of 0.437 in. of testing region; therefore, leading to incorrect results after that load. SLVDT was influenced by cover spalling at post-peak load of 1127 kip and a compression deformation of 0.30 in. of testing region; therefore, leading to incorrect results after that load. The UTM loading was stopped at 504 kip post-peak load of testing region. The UTM load was unloaded at post-peak load of 454 kip. The testing load ranged from 475 kip tension to 1384 kip in compression.

4.2.2 Specimen Deformation Plots

Figure 4-3 shows the deformation of the entire test specimen recorded by head-travel instrument for TS01. Figure 4-4 shows the deformation of the test specimen recorded by head-travel instrument for TS02. The deformation of each test specimen is plotted versus net load of the testing region.

In the specimen deformation plots, the head-travel instrument accounted for some initial deformations in the steel plates that were placed between the top and bottom heads of the UTM and the test specimen. Initial deformations occurred at the initial load steps (Load Step 0 to Load Step 4, See Table 3-2 and Table 3-3) for the adjustment of each actuator's load to a constant load of 270 kip. At these load steps the actual deformation of each test specimen was very small compared to the deformation recorded by the head-travel instrument. Therefore, the deformation of head-travel instrument at Load Step 04, Δ_{ini}, was found and subtracted from the head-travel data to remove the initial deformation of the UTM machine from the head-travel record. The value of Δ_{ini} was 0.081 in. for TS01 and 0.091 in. for TS02; therefore, head-travel plot for TS01 was shifted by 0.081 in. to the left and head-travel plot for TS02 was shifted by 0.091 in. to the left.

Figure 4-5 and Figure 4-6 show the shifting illustration for TS01 and TS02, respectively.

4.2.3 Test Region Deformation Plots

Figure 4-7 and Figure 4-8 show the testing region deformation versus net load of the testing region in TS01 from NLVD and SLVDT, respectively. Figure 4-9 and Figure 4-10 show the deformation of testing region versus net load of testing region in TS02 from NLVD and SLVDT, respectively. The key loading points for the deformation plots of the LVDTs are the same as detailed in Section 4.2.1 on the head-travel versus testing region load plot for TS01 and TS02, respectively.

4.2.4 Testing Region Strain Plots

Figure 4-11 and Figure 4-12 show the average strain of the testing region record from NLVDT and SLVDT for TS01, respectively. Figure 4-13 and Figure 4-14 show the average strain of the testing region recorded from NLVDT and SLVDT in TS02, respectively. The average strain from NLVDT and SLVDT at each test specimen is plotted versus net load of the testing region.

4.2.5 Strain Plots for Strain Gages

Figure 4-15, Figure 4-16, and Figure 4-17 show the location of strain gages in longitudinal mild steel reinforcement bars at 3 hoop-pair locations, hoop-pair 1, hoop-pair 2, and hoop-pair 3, where the strains were recorded in longitudinal mild steel reinforcement.

Figure 4-18, Figure 4-19, and Figure 4-20 show longitudinal bar buckling directions; locations of hoop fractures; and locations of damaged strain gages in confinement hoop-pairs in TS01. Figure 4-21, Figure 4-22, and Figure 4-23 show longitudinal bar buckling directions; locations of hoop fractures; and locations of damaged strain gages in confinement hoop-pairs in TS02. In these figures, the triangle symbol indicates

longitudinal bar buckling; the star symbol indicates hoop fracture; and, the cross symbol indicates a damaged strain gage with "No record".

Figure 4-24 to Figure 4-76 show strain data. The strain data are plotted versus net load of testing region. First, these plots are provided for strain gages of longitudinal mild steel reinforcement bars, then for strain gages of the confinement hoops at the three hoop-pairs denoted as hoop-pair 1, hoop-pair 2, and hoop-pair 3. The original strain data was recorded in micro-strain, which was later converted to in./in.

Some of the strain gages were damaged at concrete casting as explained in Chapter 3. For several of the strain gages, a value of 10^{38} appears for the reading at some point during data recording. This indicates that the strain gage failed during testing. There is one strain gage (L3-R7-4 in TS01) where the strain data recording was discontinued, but then returned back to normal performance. If any strain gage data appears to terminate prematurely in a plot, this is an indication that the strain gage either ran out of range or failed.

4.2.6 Strain versus Load in Longitudinal Reinforcement

Figure 4-15, Figure 4-16, and Figure 4-17 show the location of strain gages in longitudinal mild steel reinforcement bars at 3 hoop-pair locations, hoop-pair 1, hoop-pair 2, and hoop-pair 3, where the strains were recorded in longitudinal mild steel reinforcement. Table 4-1 and Table 4-2 summarizes the output strains for the strain gages used in longitudinal mild steel reinforcement at each test specimen. Section 3.5.4 gives detailed explanation of strain gages instrumentation.

In TS01, strain gages L1-R7-3 and L2-R7-1 were damaged during concrete casting; therefore, no record exists for these strain gages. In TS02, all strain gages were working prior to testing; therefore, records exist for all the strain gages. The strain gages data was continuously recorded into pre-designed data sheets for the entire test duration. The strain data from the strain gages are plotted versus net load in testing region.

Strain versus Load in Longitudinal Reinforcement for TS01

In TS01, hoop-pair 1, strain gages L1-R7-1 and L1-R7-2 functioned for all load steps. The maximum tensile strain is 0.008 in./in. ($3.1\varepsilon_{ys}$) in L1-R7-1 and 0.007 in./in. ($2.7\varepsilon_{ys}$) in L1-R7-2. The maximum compression strain is 0.017 in./in. ($6.6\varepsilon_{ys}$) in L1-R7-1 and 0.032 in./in. ($12.4\varepsilon_{ys}$) in L1-R7-2. None of the longitudinal mild steel reinforcement inside hoop-pair 1 reached the ultimate strain limit. The strain gage L1-R7-2 shows that the reinforcement bar buckled before reaching the ultimate strain limit.

In TS01, hoop-pair 2, strain gages L2-R7-2 and L2-R7-4 functioned for most of the load steps. The maximum tensile strain is 0.011 in./in. ($4.2\varepsilon_{ys}$) in L2-R7-2 and 0.01 in./in. ($3.9\varepsilon_{ys}$) in L2-R7-4. The maximum compression strain is 0.054 in./in. ($20.8\varepsilon_{ys}$, which is more than the ultimate strain limit of 0.0416 in./in. of the bars) in L2-R7-2. The strain gage L2-R7-2 shows that the compression strain in reinforcement bar near hoop-pair 2 passed the ultimate strain limit.

In TS01, hoop-pair 3, all the strain gages functioned for most of the load steps. The maximum tensile strain is 0.01 in./in. ($4.2\varepsilon_{ys}$) in L3-R7-1, L3-R7-2, L3-R7-3 and 0.007 in./in. ($2.7\varepsilon_{ys}$) in L3-R7-4. The maximum compression strain is 0.022 in./in. ($8.5\varepsilon_{ys}$) in L3-R7-1 and L3-R7-2, 0.064 in./in. ($24.7\varepsilon_{ys}$) in L3-R7-3, and 0.011 in./in. ($4.2\varepsilon_{ys}$) in L3-R7-4. The strain gage L3-R7-3 shows that compression strain in reinforcement bar near hoop-pair 3 passed the ultimate strain limit.

In summary, in TS01, the data from strain gages show that, on average, the maximum tensile strain was 0.01 in./in. ($3.8\varepsilon_{ys}$), and compression strain in some of the longitudinal mild steel reinforcement bars passed the ultimate strain limit of the bars. The maximum compression strain was 0.054 in./in. ($20.8\varepsilon_{ys}$) and 0.064 in./in ($24.6\varepsilon_{ys}$). The maximum compression strain occurred at hoop-pair 2 and hoop pair 3. The maximum tensile strain occurred at hoop-pair 2, which is located at the mid-height of the testing region.

Strain versus Load in Longitudinal Reinforcement for TS02

In TS02, hoop-pair 1, the strain gage L1-R7-2 functioned for all the load steps. The maximum tensile strain is 0.041 in./in. ($15.8\varepsilon_{ys}$), and the maximum compression strain is 0.025 in./in. ($9.6\varepsilon_{ys}$, which is less than the ultimate strain of 0.0416 in./in. of the bars). The strain gage L1-R7-2 shows that the reinforcement bar reached their ultimate strain limit in tension (0.0416 in./in.). It can be inferred from strain gage L1-R7-2, that some of the bars reached their ultimate strain limit in tension. The other three strain gages failed at the first inelastic tensile loading step (Load Step 23). It is noted that the compression loading at Load Step 22(b) mistakenly happened due to an error by UTM operator who was controlling the compression loading of UTM. The compression loading at Load Step 22(b) was still in the elastic range of the confined concrete column section; therefore, it did not affect the behavior of the testing results.

In TS02, hoop-pair 2, only strain gage L2-R7-3 functioned for most of the load steps. The other strain gages failed during inelastic tensile loading steps (Load Step 23 and Load Step 25). The maximum recorded tensile strain is 0.03 in./in. ($11.5\varepsilon_{ys}$) in L1-R7-1, 0.027 in./in. ($10.4\varepsilon_{ys}$) in L2-R7-2, 0.0416 in./in. ($16.0\varepsilon_{ys}$) in L2-R7-3, and 0.033 in./in. ($12.3\varepsilon_{ys}$) in L2-R7-4. The maximum compression strain, which is only recorded in L2-R7-3, is 0.08 in./in. ($30.8\varepsilon_{ys}$). The strain gage L2-R7-3 shows that compression strain in reinforcement bar passed the ultimate strain limit of the longitudinal reinforcement bars (0.0416 in./in.) near hoop-pair 2. The confinement hoops effectively prevented the reinforcement bars from buckling. The strain data for L2-R7-1 and L2-R7-2 implies that the reversal compression strain after inelastic tensile loading was small compared to tensile strain of reinforcement bars. The reinforcement bars did not return to original position in compression after inelastic tensile loading of reinforcement bars (tensile strain is higher than compression strain at the inelastic tensile cyclic loading steps).

In TS02, hoop-pair 3, only strain gage L3-R7-1 functioned for most of the load steps. The reliable maximum tensile strain is 0.036 in./in. ($13.8\varepsilon_{ys}$) in L3-R7-1, 0.04 in./in. ($15.4\varepsilon_{ys}$) in L3-R7-2, 0.031 in./in. ($11.9\varepsilon_{ys}$) in L3-R7-3, and 0.022 in./in. ($8.5\varepsilon_{ys}$) in L3-R7-4. This shows that the longitudinal reinforcement bars were elongated closely to the ultimate strain limit of the bars ($16.0\varepsilon_{ys}$). The maximum compression strain recorded in L3-R7-1

is 0.028 in./in. (10.8ε_{ys}). The sudden failure of strain gage L3-R7-1 implies that the bar locally buckled.

In summary, in TS02, the strain gage data shows that, on average, the maximum inelastic tensile strain reached 0.0416 in./in. (16.0ε_{ys}), and compression strain in some of the longitudinal mild steel reinforcement bars passed the ultimate strain limit of the bars. The maximum tensile strain reached 16.0ε_{ys} in L2-R7-3 and L3-R7-2. The maximum tensile strain occurred at hoop-pair 2, which is located at the mid-height of the testing region. The maximum compression strain was 0.08 in./in. (30.8ε_{ys}) recorded in L2-R7-3. The maximum compression strain occurred at hoop-pair 2 and hoop pair 3.

4.2.7 Strain versus Load in Confinement Hoop-Pairs

Figure 4-15, Figure 4-16, and Figure 4-17 show the location of strain gages in three confinement hoop-pairs, hoop-pair 1, hoop-pair 2, and hoop-pair 3, where the strain gages were recorded in the confinement hoop reinforcement.

In TS01, strain gages H1-R3-2, H2-R3-3, H2-R3-5, and, in TS02, strain gages H2-R3-3 and H3-R3-3 were damaged during concrete casting. Therefore, no record exists for these strain gages. The data was continuously recorded into pre-designed data sheets for the entire test duration of each test specimen. The instrumentation details for confinement hoops strain gages are presented in Section 3.5.4. The stress-strain relation for confinement hoop reinforcement is presented in Section 3.6. The strain data from the strain gages is plotted versus net load in testing region.

Strain versus Load in Confinement Hoop-Pairs of TS01

In TS01, hoop-pair 1, strain gage H1-R3-3, which is an internal leg strain gage, displayed larger strain. The internal strain gage, H1-R3-3, has a record of 0.053 in./in. (16.5ε_{yh}) of the tensile strain at 1050 kip of the post-peak load (Load Step 24). Other strain gages failed before a strain of 0.005 in./in. in confinement hoops. The confinement hoops reinforcement reached the maximum compression load of 1447 kip in testing region at 40-50% of their yielding strain limit.

In TS01, hoop-pair 2, strain gage H2-R3-6, which is an outer leg strain gage of the confined concrete core, displayed larger strain. Strain gage H2-R3-6 recorded up to 0.0115 in./in. (5.75ε_{yh}) of tensile strain at 1160 kip compression load in testing region. Other strain gages failed before a strain of 0.005 in./in. The internal leg strain gage H2-R3-2 failed at strain of 0.0035 in./in. The confinement hoops reinforcement reached the maximum compression load of 1447 kip in testing region at 40-50% of their yielding strain limit.

In TS01, hoop-pair 3, strain gages H3-R3-1, H3-R3-5, and H3-R3-6, which are strain gages on outer legs of the confined concrete, failed before a strain of 0.0025 in./in. Strain gage H3-R3-4, which is outer leg strain gage, failed before a strain of 0.005 in./in. The internal leg strain gages, H3-R3-2 and H3-R3-3, functioned for all load steps. The maximum tensile strain is 0.0036 in./in. (1.8ε_{yh}) in H3-R3-2, and 0.0043 in./in. (2.15ε_{yh}) in H3-R3-3. This shows that the inner leg strain gages H3-R3-2 and H3-R3-3 did not

reach the ultimate strain limit of the confinement hoop reinforcement. The confinement hoop reinforcement reached the maximum compression load of 1447 kip in testing region at 40-50% of their yielding strain limit.

In summary, in hoop-pair 1, the strain in strain gage H1-R3-3 in the internal hoop leg was greater than the ultimate strain limit of the confinement hoop reinforcement (ε_{uh}). In hoop-pair 2, strain gages quickly failed because of dominant effect of cyclic loading at the mid-height of the testing region; therefore, nothing can be concluded about the internal legs of confinement hoop at H2-R3-2. In hoop-pair 3, the strain gages data from internal leg strain gages shows that strains in internal legs of hoop-pair 3 was smaller than the ultimate strain limit of the confinement hoop reinforcement (ε_{uh}).

Strain versus Load in Confinement Hoop-Pairs of TS02

In TS02, hoop-pair 1, strain gage H1-R3-3 and H1-R3-5 displayed larger strains than other stain gages. Other strain gages failed before strain of 0.002 in./in. (before reaching yielding strain limit of confinement hoop reinforcement). The maximum strain is 0.0096 in./in. ($4.8\varepsilon_{yh}$) in H1-R3-3 and 0.0135 in./in. ($6.75\varepsilon_{yh}$) in H1-R3-5. The maximum compression load at testing region was 1384 kip. The confinement hoops reinforcement reached the maximum compression load in testing region at 40-50% of their yielding strain limit.

In TS02, hoop-pair 2, the strain gages H2-R3-1, H2-R3-2 and H2-R3-6 displayed larger strains than other stain gages. The maximum strain is 0.0105 in./in. ($5.25\varepsilon_{yh}$) in H2-R3-1 and 0.054 in./in. ($27.0\varepsilon_{yh}$) in H2-R3-2. The strain in strain gage H2-R3-2 in the internal hoop leg was greater than the ultimate strain limit of the confinement hoop reinforcement (ε_{uh}). The strain gage H2-R3-6 failed at a strain of 0.003 in./in. ($1.15\varepsilon_{yh}$). Other strain gages failed before strain of 0.002 in./in. The maximum compression load at testing region is 1384 kip. The confinement hoops reinforcement reached the maximum recorded compression load in testing region at 40-50% of their yielding strain limit.

In TS02, hoop-pair 3, strain gages H3-R3-1, H3-R3-2, and H2-R3-6 displayed larger strains than other stain gages. Other strain gages failed before a strain of 0.001 in./in. The maximum strain is 0.004 in./in. in H3-R3-1, 0.0026 in./in. in H3-R3-2, and 0.0068 in./in. in H3-R3-6. Strain gages H3-R3-2 and H3-R3-6 have complete records. The strain in strain gage H3-R3-2 in the internal hoop leg was smaller than the yielding strain limit of the confinement hoop reinforcement (ε_{uh}). The maximum compression load at testing region was 1384 kip. The confinement hoops reinforcement reached the maximum compression load in testing region at 40-50% of their yielding strain limit.

In summary, the maximum strain recorded in confinement hoop of TS02 was 0.054 in./in. ($27\varepsilon_{yh}$) that occurred in hoop-pair 2. The strain in strain gages of internal hoop legs at hoop-pair 1 was less than the ultimate strain limit of the confinement hoop reinforcement (ε_{uh}). The strain in strain gage H2-R3-2 in the internal hoop leg was greater than the ultimate strain limit of the confinement hoop reinforcement (ε_{uh}). In hoop-pair 3, only strain gages H3-R3-2 and H3-R3-6 have complete records. The strain in strain gage H3-

R3-2 in the internal hoop leg was smaller than the ultimate strain limit of the confinement hoop reinforcement (ε_{uh}).

4.3 CONCRETE CRACKING

Figure 4-77 to Figure 4-106 show the measured sizes of cracks at the end of specified load step. Table 4-3 and Table 4-4 summarizes the measured sizes of cracks at the end of specified load steps in TS01 and TS02, respectively. All the cracks on each specimen were numbered based on their sequence of occurrence.

The cracks in confined concrete column and, particularly, in testing region were measured at the end of specified load steps in each test specimen. Cracks were only measured on the east face and west face of the confined concrete column of each test specimen. Crack gages were used to measure the cracks. Crack gages are transparent plastic cards with varying width lines drawn on them. The cards are placed against the concrete surface, and the line width that most closely matches the crack width is used to estimate the crack width.

The cracks were measured at the end of each tensile loading steps starting at Load Step 06. After yielding of longitudinal mild steel reinforcement bars inside the confined concrete in tension (after Load Step 19), the cracks were measured in subsequent compression loading steps too to check closures of cracks.

Figure 4-77 and Figure 4-78 show flexural shear cracks developed in top and bottom beams in TS01, respectively. Figure 4-88 and Figure 4-89 show flexural-shear cracks developed in top and bottom beams in TS02, respectively. The flexural-shear cracks developed at top and bottom beams at the column connections during each test specimen after beams were fully loaded by actuators at the end of Load Step 04.

Table 4-1: Longitudinal strain gage data for TS01

Gage #	Performance	Details	Remarks
L1-R7-1	Load Step	Step 24	Complete record
	ε_{maxt}	0.008 in./in.	
	P_{maxt}	360 kip	
	$P_{com\varepsilon 0}$	1000 kip	
	ε_{maxc}	0.017 in./in.	$6.5\varepsilon_{yh}$
	P_{maxc}	960 kip	
	ε_{maxe}	0.013 in./in.	
L1-R7-2	Load Step	Step 24	Complete record
	ε_{maxt}	0.007 in./in.	
	P_{maxt}	360 kip	
	$P_{com\varepsilon 0}$	700 kip	
	ε_{maxc}	0.032 in./in.	$12.3\varepsilon_{yh}$
	P_{maxc}	960 kip	
	ε_{maxe}	0.028 in./in.	
L1-R7-3			No record exist
L1-R7-4	Load Step	Phase 07	
	ε_{maxt}	0.008 in./in.	
	P_{maxt}	360 kip	Failed
	$P_{com\varepsilon 0}$		
	ε_{maxc}		
	P_{maxc}		
	ε_{maxe}		
L2-R7-1			No record exist
L2-R7-2	Load Step	Step 24	Complete record
	ε_{maxt}	0.011 in./in.	
	P_{maxt}	360 kip	
	$P_{com\varepsilon 0}$	1300 kip	
	ε_{maxc}	0.054 in./in.	$20.8\varepsilon_{yh}$
	P_{maxc}	600 kip	
	ε_{maxe}	0.050 in./in.	
L2-R7-3	Load Step	Phase 07	
	ε_{maxt}	0.006 in./in.	
	P_{maxt}	360 kip	Failed
	$P_{com\varepsilon 0}$		
	ε_{maxc}		
	P_{maxc}		
	ε_{maxe}		

Table 4-1 (Continued)

Gage #	Performance	Details	Remarks
L2-R7-4	Load Step	Step 24	Failed in peak compression load
	ε_{maxt}	0.01 in./in.	
	P_{maxt}	360 kip	
	$P_{com\varepsilon 0}$	1300 kip	
	ε_{maxc}	0.016 in./in.	$6.2\varepsilon_{yh}$
	P_{maxc}	1200 kip	Failed
	ε_{maxe}		
L3-R7-1	Load Step	Step 24	
	ε_{maxt}	0.01 in./in.	
	P_{maxt}	360 kip	
	$P_{com\varepsilon 0}$	1350 kip	
	ε_{maxc}	0.022 in./in.	$8.5\varepsilon_{yh}$
	P_{maxc}	1050 kip	
	ε_{maxe}	0.010 in./in.	
L3-R7-2	Load Step	Step 24	Failed in peak compression load
	ε_{maxt}	0.01 in./in.	
	P_{maxt}	360 kip	
	$P_{com\varepsilon 0}$	1100 kip	
	ε_{maxc}	0.022 in./in.	$8.5\varepsilon_{yh}$
	P_{maxc}	1150 kip	Failed
	ε_{maxe}		
L3-R7-3	Load Step	Step 24	Failed in peak compression load
	ε_{maxt}	0.01 in./in.	
	P_{maxt}	360 kip	
	$P_{com\varepsilon 0}$	1350 kip	
	ε_{maxc}	0.064 in./in.	$24.6\varepsilon_{yh}$
	P_{maxc}	1100 kip	Failed
	ε_{maxe}		
L3-R7-4	Load Step	Step 24	
	ε_{maxt}	0.007 in./in.	
	P_{maxt}	360 kip	
	$P_{com\varepsilon 0}$	1200 kip	
	ε_{maxc}	0.011 in./in.	$4.23\varepsilon_{yh}$
	P_{maxc}	1000 kip	
	ε_{maxe}	0.007 in./in.	

Table 4-2: Longitudinal strain gage data for TS02

Gage #	Performance	Details	Remarks
L1-R7-1	Load Step	Phase 08	Yield cycles
	ε_{maxt}	0.032 in./in.	
	P_{maxt}	440 kip	Failed
	$P_{com\varepsilon 0}$		
	ε_{maxc}		
	P_{maxc}		
	ε_{maxe}		
L1-R7-2	Load Step	Step 29	Complete record
	ε_{maxt}	0.041 in./in.	
	P_{maxt}	475 kip	
	$P_{com\varepsilon 0}$	1375 kip	
	ε_{maxc}	0.024 in./in.	$9.23\varepsilon_{yh}$
	P_{maxc}	1000 kip	
	ε_{maxe}	0.02 in./in.	
L1-R7-3	Load Step	Phase 08	Multiple of strain cycles
	ε_{maxt}	0.016 in./in.	
	P_{maxt}	440 kip	Failed
	$P_{com\varepsilon 0}$		
	ε_{maxc}		
	P_{maxc}		
	ε_{maxe}		
L1-R7-4	Load Step	Phase 08	Multiple of strain cycles
	ε_{maxt}	0.034 in./in.	
	P_{maxt}	440 kip	Failed
	$P_{com\varepsilon 0}$		
	ε_{maxc}		
	P_{maxc}		
	ε_{maxe}		
L2-R7-1	Load Step	Phase 08	Multiple of strain cycles
	ε_{maxt}	0.03 in./in.	
	P_{maxt}	440 kip	Failed
	$P_{com\varepsilon 0}$		
	ε_{maxc}		
	P_{maxc}	980 kip	
	ε_{maxe}		
L2-R7-2	Load step	Phase 08	Multiple of Strain Cycles
	ε_{maxt}	0.027 in./in.	
	P_{maxt}	440 kip	Failed
	$P_{com\varepsilon 0}$		
	ε_{maxc}		
	P_{maxc}	980 kip	
	ε_{maxe}		

Table 4-2 (Continued)

Gage #	Performance	Details	Remarks
L2-R7-3	Load Step	Step 24	Complete record
	ε_{maxt}	0.042 in./in.	
	P_{maxt}	475 kip	
	$P_{com\varepsilon 0}$	1300 kip	
	ε_{maxc}	0.08 in./in.	$30.8\varepsilon_{yh}$
	P_{maxc}	800 kip	Failed
	ε_{maxe}		
L2-R7-4	Load Step	Phase 08	Multiple of strain cycles
	ε_{maxt}	0.033 in./in.	
	P_{maxt}	475 kip	Failed
	$P_{com\varepsilon 0}$		
	ε_{maxc}		
	P_{maxc}	980 kip	
	ε_{maxe}		
L3-R7-1	Load Step	Step 29	
	ε_{maxt}	0.036 in./in.	
	P_{maxt}	475 kip	
	$P_{com\varepsilon 0}$	900 kip	
	ε_{maxc}	0.028 in./in.	$10.8\varepsilon_{yh}$
	P_{maxc}	1140 kip	Failed
	ε_{maxe}		
L3-R7-2	Load Step	Phase 08	Multiple of strain cycles
	ε_{maxt}	0.04 in./in.	
	P_{maxt}	475 kip	
	$P_{com\varepsilon 0}$	980 kip	Failed
	ε_{maxc}		
	P_{maxc}		
	ε_{maxe}		
L3-R7-3	Load Step	Phase 08	Multiple of strain cycles
	ε_{maxt}	0.03 in./in.	
	P_{maxt}	475 kip	Failed
	$P_{com\varepsilon 0}$		
	ε_{maxc}		
	P_{maxc}	980 kip	
	ε_{maxe}		
L3-R7-4	Load Step	Phase 08	Multiple of strain cycles
	ε_{maxt}	0.022 in./in.	
	P_{maxt}	400 kip	Failed
	$P_{com\varepsilon 0}$		
	ε_{maxc}		
	P_{maxc}	980 kip	
	ε_{maxe}		

Table 4-3: Crack record for TS01

Step #	East Side		West Side		Figure Reference
	Crack #	Crack Size (in)	Crack #	Crack Size (in)	
Step 06	1	HL			
Step 07	1	0.006			
	2	HL			
	3	HL			
	4	HL			
	6	HL			
Step 08	1	0.006			
	2	0.006			
	3	0.006			
	4	HL			
	6	HL			
Step 09	1	0.008			
	2	0.006			
	3	HL			
	4	HL			
	5	HL			
	6	HL			
Step 10	1-6	Closed			
Step 11	1	0.008			
	2	0.006			
	3	0.010			
	4	HL			
	5	HL			
	6	HL			
	7	HL			
Step 12	1-7	Closed			
Step 13	1	0.008			Figure 4-17
	2	0.010			
	3	0.006			
	4	0.006			
	5	HL			
	6	HL			
	7	HL			
Step 14	1-7	Closed			

Note: HL denotes a hair line crack with a width that is too narrow to be estimated with the crack comparator.

Table 4-3 (Continued)

Step #	East Side		West Side		Figure Reference
	Crack #	Crack Size (in)	Crack #	Crack Size (in)	
Step 15	1	0.016	1	0.012	Figure 4-18, Figure 4-19
	2	0.012	2	0.010	
	3	0.012	3	0.012	
	4	0.010			
	5	0.008			
	6	HL			
	7	HL			
	8	HL			
	9	0.006			
	10	0.006			
Step 16	1-10	Closed		Closed	
Step 17	1	0.016	1	0.014	Figure 4-20, Figure 4-21
	2	0.014	2	0.014	
	3	0.012	3	0.016	
	4	0.012	Bottom	0.012	
	5	0.010			
	6	0.006			
	7	HL			
	8	HL			
	9	0.006			
	10	0.006			
Step 18	1-10	Closed		Closed	
Step 19	1	0.024	1	0.016	Figure 4-22, Figure 4-23
	2	0.020	2	0.020	
	3	0.016	3	0.024	
	4	0.016	5	0.020	
	5	0.014			
	6	0.006			
	7	HL			
	8	HL			
	9	0.006			
	10	0.006			
	11	HL			
Step 20	1-11	Closed		Closed	

Table 4-3 (Continued)

Step #	East Side		West Side		Figure Reference
	Crack #	Crack Size (in)	Crack #	Crack Size (in)	
Step 21	1	0.036	1	0.024	Figure 4-24, Figure 4-25
	2	0.036	2	0.032	
	3	0.024	3	0.040	
	4	0.024	5+Bott	0.036	
	5	0.020			
	6	0.006			
	7	HL			
	8	HL			
	9	0.006			
	10	0.008			
	11	0.006			
	12	HL			
	13	0.008			
Step 22	1-13	Closed			
Step 23	1-13	Closed			
Step 24		To Failure			

Table 4-4: Cracks record for TS02

	East Side		West Side		
Step #	Crack #	Crack Size (in)	Crack #	Crack Size (in)	Figure Reference
Step 06	1	HL			
	2	HL			
Step 07	1	0.006			Figure 4-28
	2	HL			
Step 08	1	0.010			Figure 4-29
	2	0.008			
Step 09	0	0.020			Figure 4-30
	1	0.012			
	2	0.008			
	3	HL			
	4	0.006			
	5	0.006			
Step 10	0-5	Closed			
Step 11	0	0.032			
	1	0.014			
	2	0.006			
	3	HL			
	4	0.006			
	5	0.006			
Step 12	0	0.600			
	1-5	Closed			
Step 13	0	0.024			Figure 4-31
	1	0.014			
	2	0.008			
	3	HL			
	4	0.008			
	5	0.008			
Step 14	0	0.020			
	1-5	Closed			
Step 15	0	0.040			Figure 4-32
	1	0.020			
	2	0.016			
	3	0.006			
	4	0.014			
	5	0.014			
	6	0.006			
	7	HL			
	8	0.006			
	9	HL			

Table 4-4 (Continued)

	East Side		West Side		
Step #	Crack #	Crack Size (in)	Crack #	Crack Size (in)	Figure Reference
Step 16	0	0.140			
	1-9	Closed			
Step 17	0	0.036			Figure 4-33
	1	0.024			
	2	0.012			
	3	HL			
	4	0.016			
	5	0.016			
	6	0.008			
	7	HL			
	8	0.006			
	9	0.006			
	10	0.006			
Step 18	0	0.012			
	1-10	Closed			
Step 19	0	0.04			Figure 4-34, Figure 4-35
	1	0.032	1	0.020	
	2	0.020	2	0.018	
	3	HL	4	0.032	
	4	0.016	5	0.018	
	5	0.016			
	6	0.010			
	7	HL			
	8	0.006			
	9	0.010			
	10	0.014			
	11	0.016			
	12	HL			
	13	0.008			
Step 20	0	0.010			
	1-13	Closed			

Table 4-4 (Continued)

	East Side		West Side		
Step #	Crack #	Crack Size (in)	Crack #	Crack Size (in)	Figure Reference
Step 21	0	0.040			Figure 4-36
	1	0.050	1	0.024	
	2	0.020	2	0.032	
	3	HL	4	0.036	
	4	0.02	5	0.024	
	5	0.02			
	6	0.016			
	7	HL			
	8	0.006			
	9	0.006			
	10	0.024			
	11	0.016			
	12	HL			
	13	0.006			
	14	0.008			
Step 22	0	0.008			
	1-4	Closed			
Step 23	0	NR*			Figure 4-37, Figure 4-38
	1	0.240	1	0.080	
	2	0.200	2	0.080	
	3	HL	4	0.080	
	4	0.160	5	0.080	
	5	0.200			
	6	0.200			
	7	HL			
	8	0.006			
	9	0.006			
	10	0.068			
	11	0.14			
	12	HL			
	13	0.066			
	14	0.036			
	15	0.032			
	16	0.024			

*NR denotes “no record exists”.

Table 4-4 (Continued)

	East Side		West Side		
Step #	Crack #	Crack Size (in)	Crack #	Crack Size (in)	Figure Reference
Step 24	0	0.012			
	1	0.008			
	2	HL			
	3	HL			
	4	0.006			
	5	HL			
	6	HL			
	7	HL			
	8	HL			
	9	HL			
	10	HL			
	11	0.01			
	12	HL			
	13	HL			
	14	HL			
	15	HL			
	16	HL			
Step 25	0	0.060			Figure 4-39, Figure 4-40
	1	0.240	1	0.120	
	2	0.140	2	0.080	
	3	HL	4	0.120	
	4	0.120	5	0.120	
	5	0.160			
	6	0.140			
	7	HL			
	8	0.032			
	9	HL			
	10	0.140			
	11	0.200			
	12	HL			
	13	0.066			
	14	0.020			
	15	0.060			
	16	0.060			

Table 4-4 (Continued)

	East Side		West Side		
Step #	Crack #	Crack Size (in)	Crack #	Crack Size (in)	Figure Reference
Step 26	0	0.008			Figure 4-41
	1	0.016			
	2	0.008			
	3	HL			
	4	0.036			
	5	HL			
	6	HL			
	7	HL			
	8	HL			
	9	HL			
	10	HL			
	11	0.016			
	12	HL			
	13	HL			
	14	0.036			
	15	HL			
	16	0.006			
Step 29		To Failure			Figure 4-44

Note: HL denotes a hair line crack with a width that is too narrow to be estimated with the crack comparator.

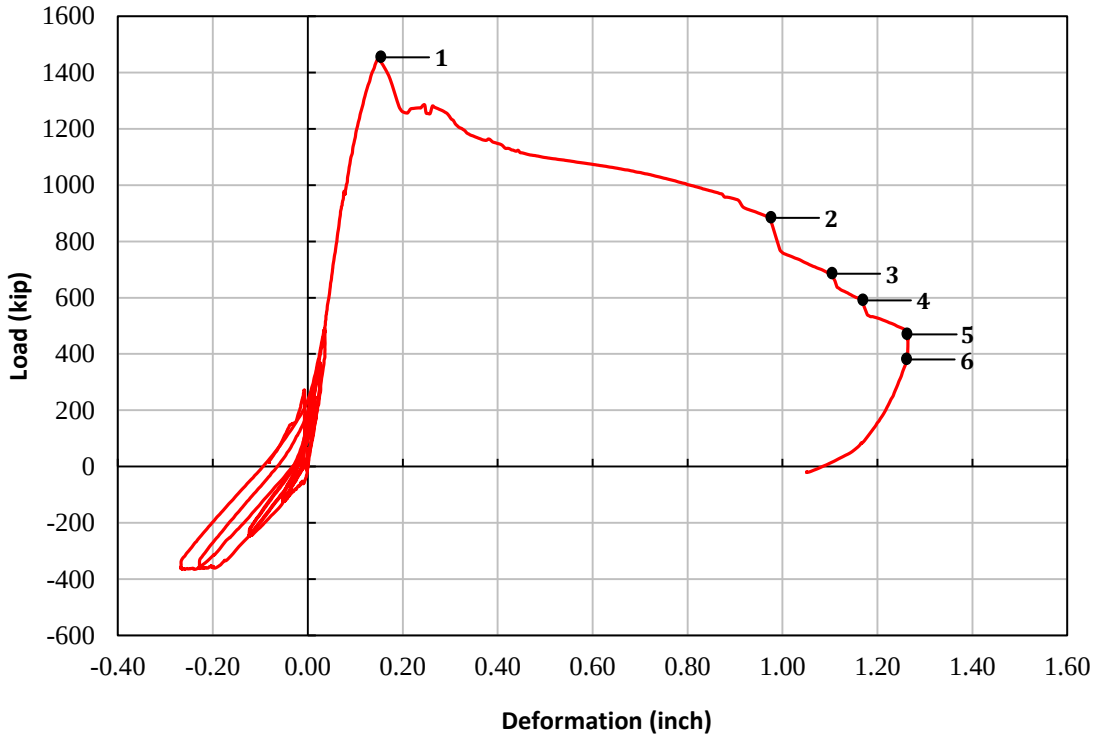

Figure 4-1: Key points of head-travel record for TS01

(1) 1447 kip: Initiation of concrete cover spalling
(2) 858 kip: First hoop fracture, longitudinal rebar buckling
(3) 658 kip: Second hoop fracture
(4) 593 kip: Third hoop fracture
(5) 476 kip: Stopping Universal Testing Machine loading
(6) 450 kip: Unloading the Universal Testing Machine

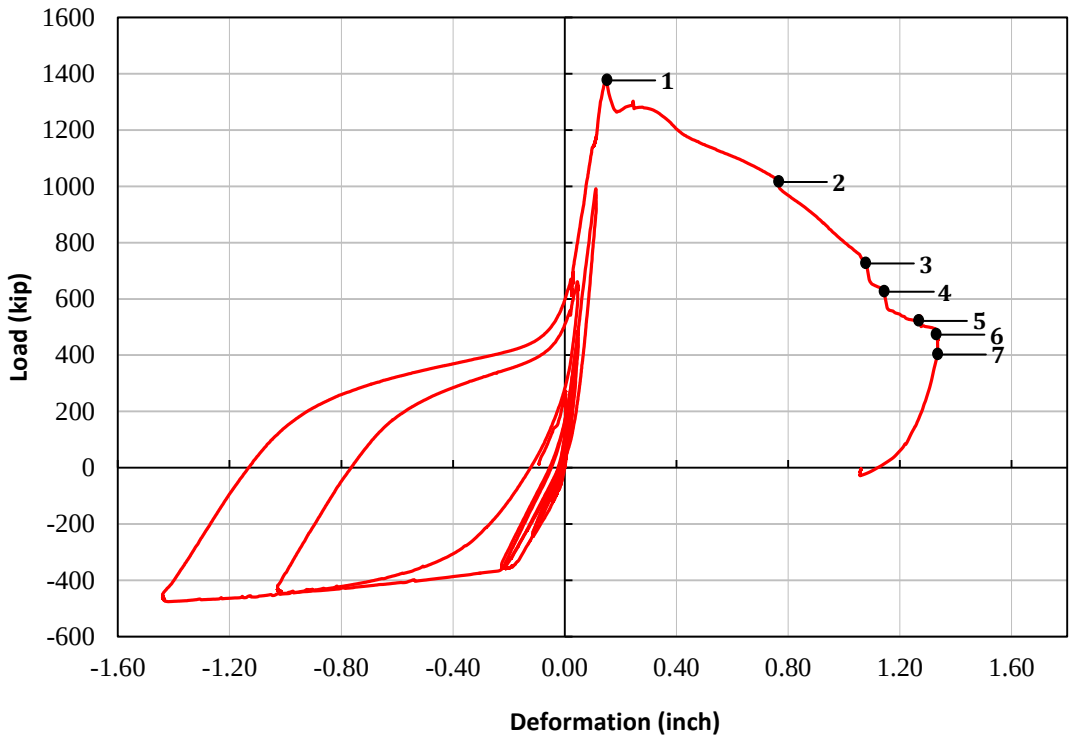

Figure 4-2: Key points of head-travel record for TS02

(1) 1383 kip: Initiation of concrete cover spalling
(2) 1010 kip: Minor local buckling
(3) 668 kip: First hoop fracture, longitudinal rebar buckling
(4) 568 kip: Second hoop fracture
(5) 502 kip: Third hoop fracture
(6) 504 kip: Stopping Universal Testing Machine loading
(7) 454 kip: Unloading the Universal Testing Machine

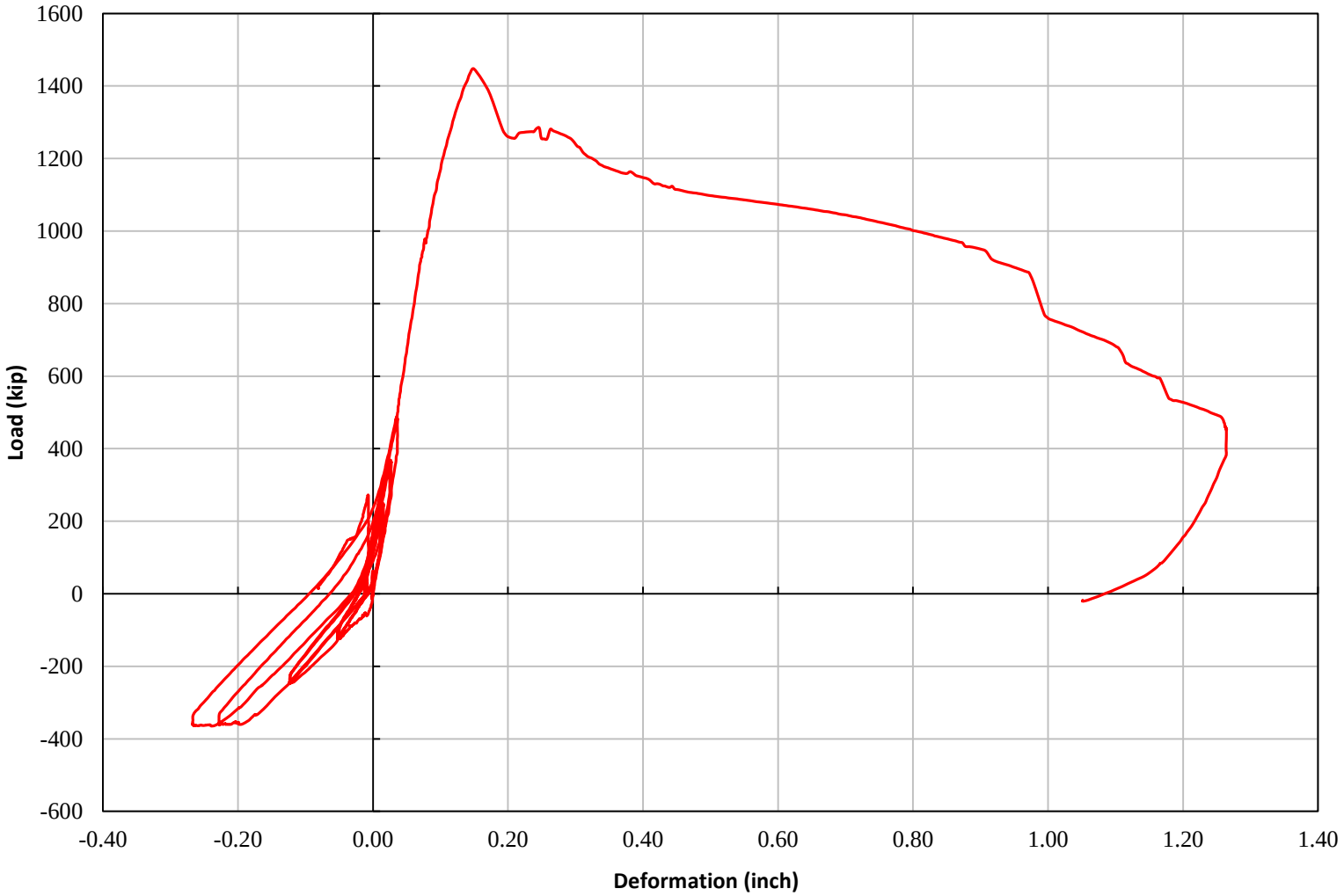

Figure 4-3: Head-travel for TS01

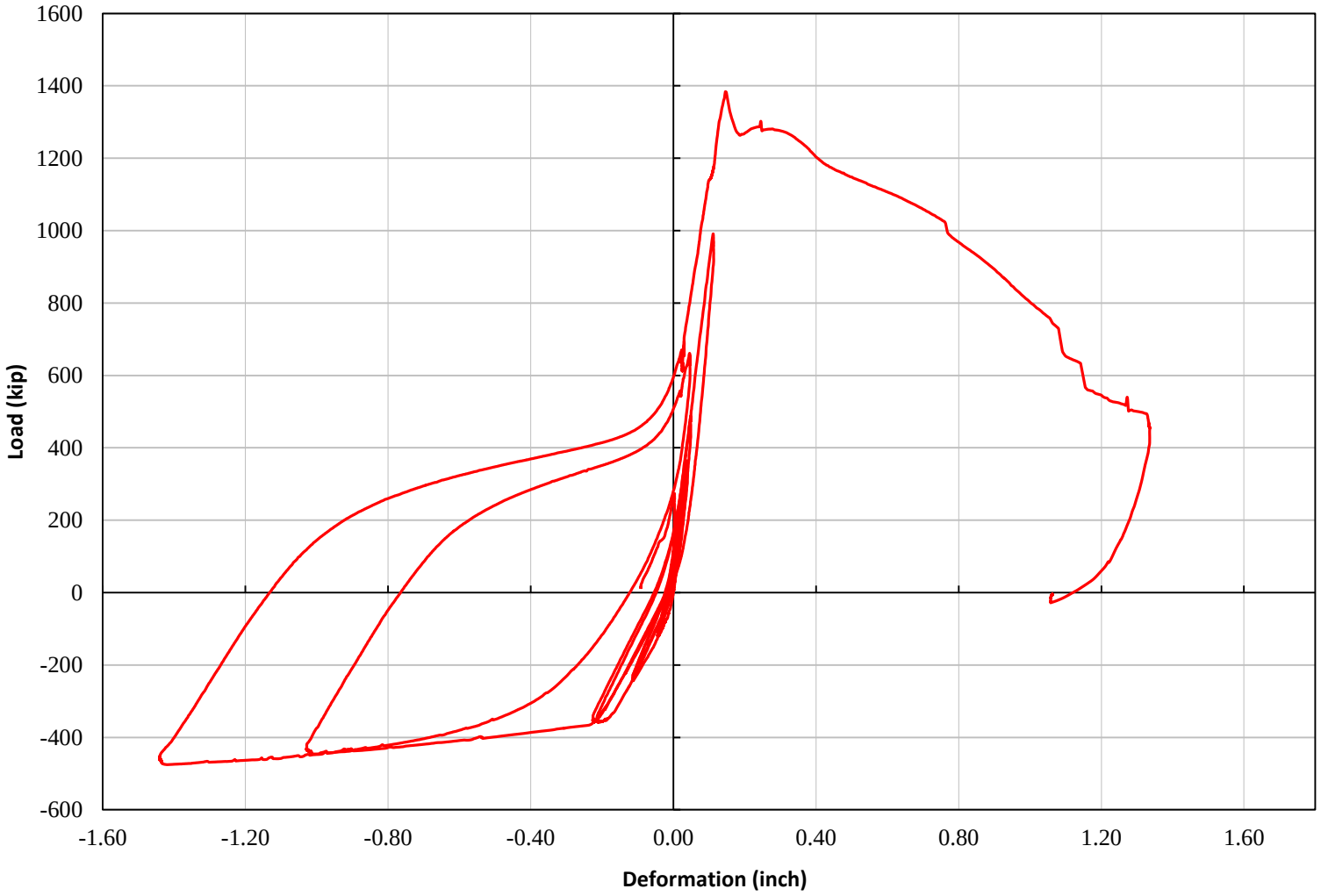

Figure 4-4: Head-travel for TS02

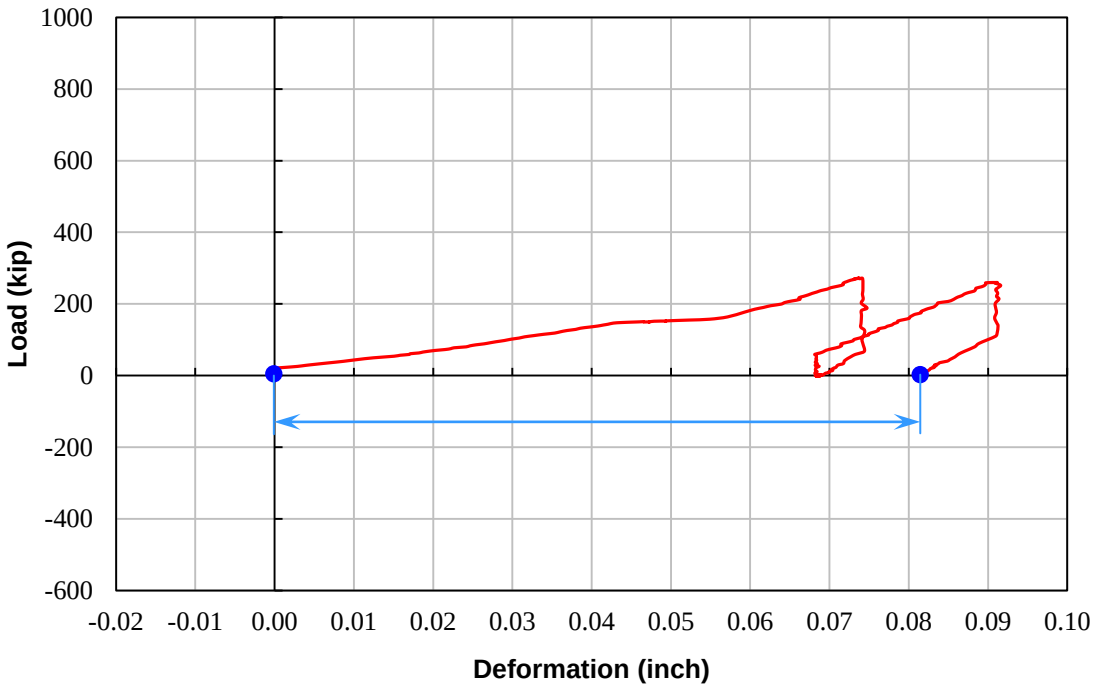

Figure 4-5: Head-travel at the end of Load Step 04 for TS01

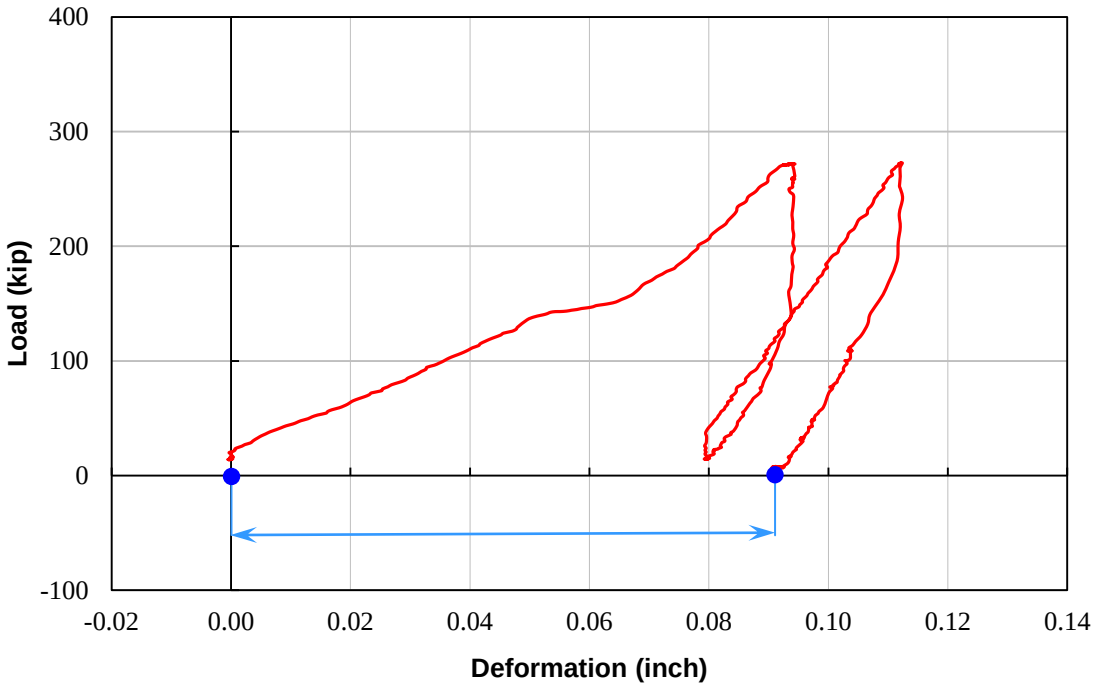

Figure 4-6: Head-travel at the end of Load Step 04 for TS02

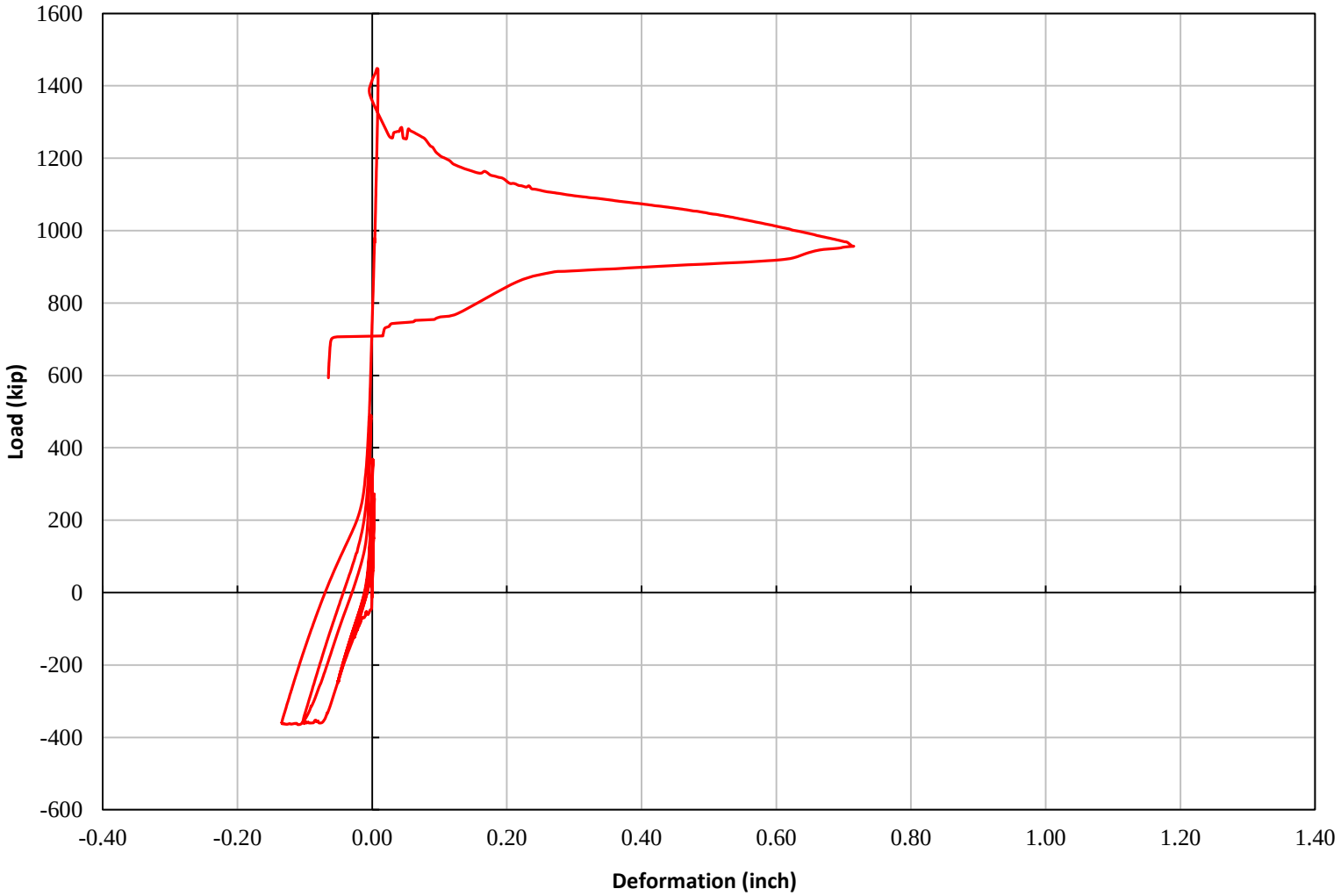

Figure 4-7: NLVDT deformation for TS01

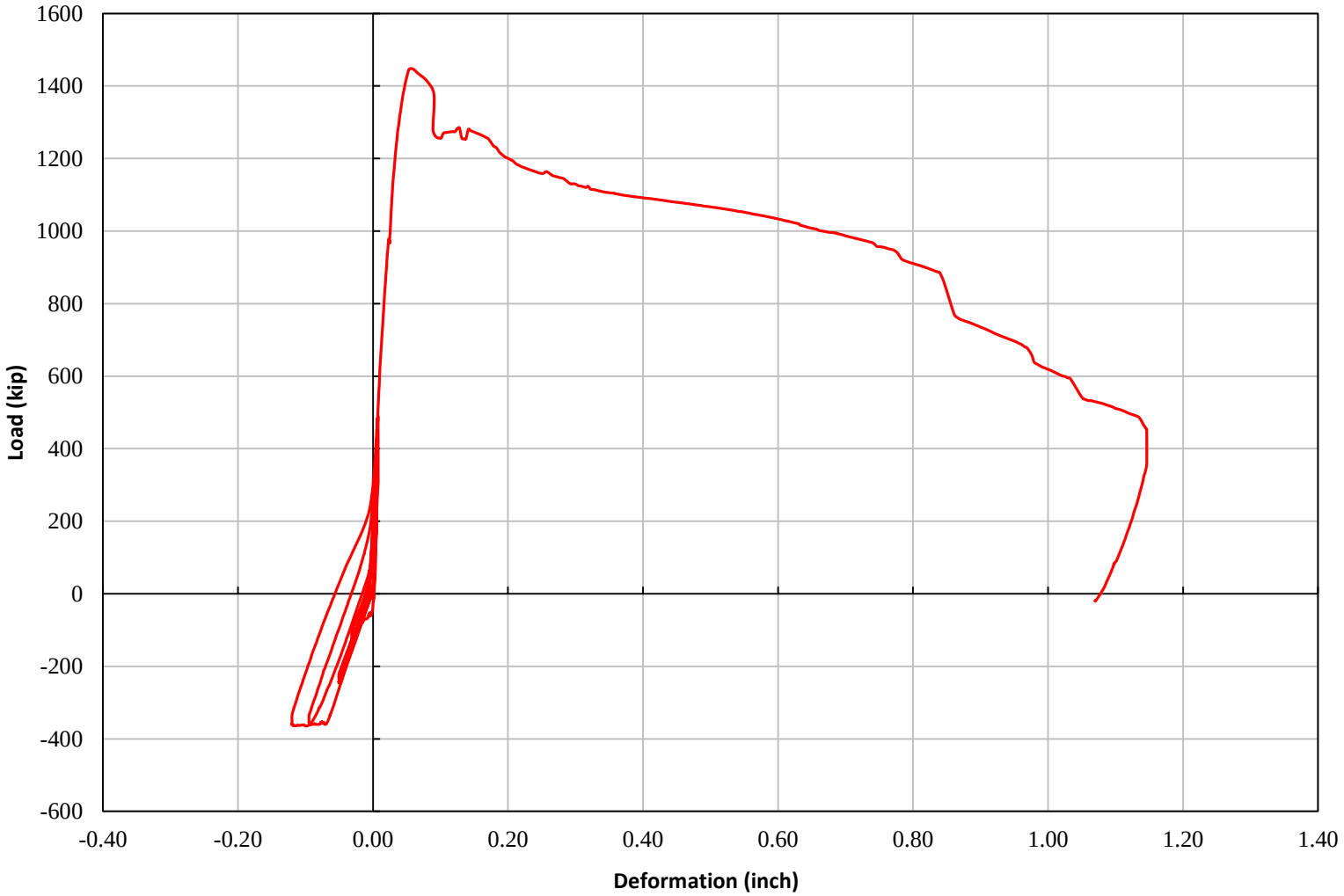

Figure 4-8: SLVDT deformation for TS01

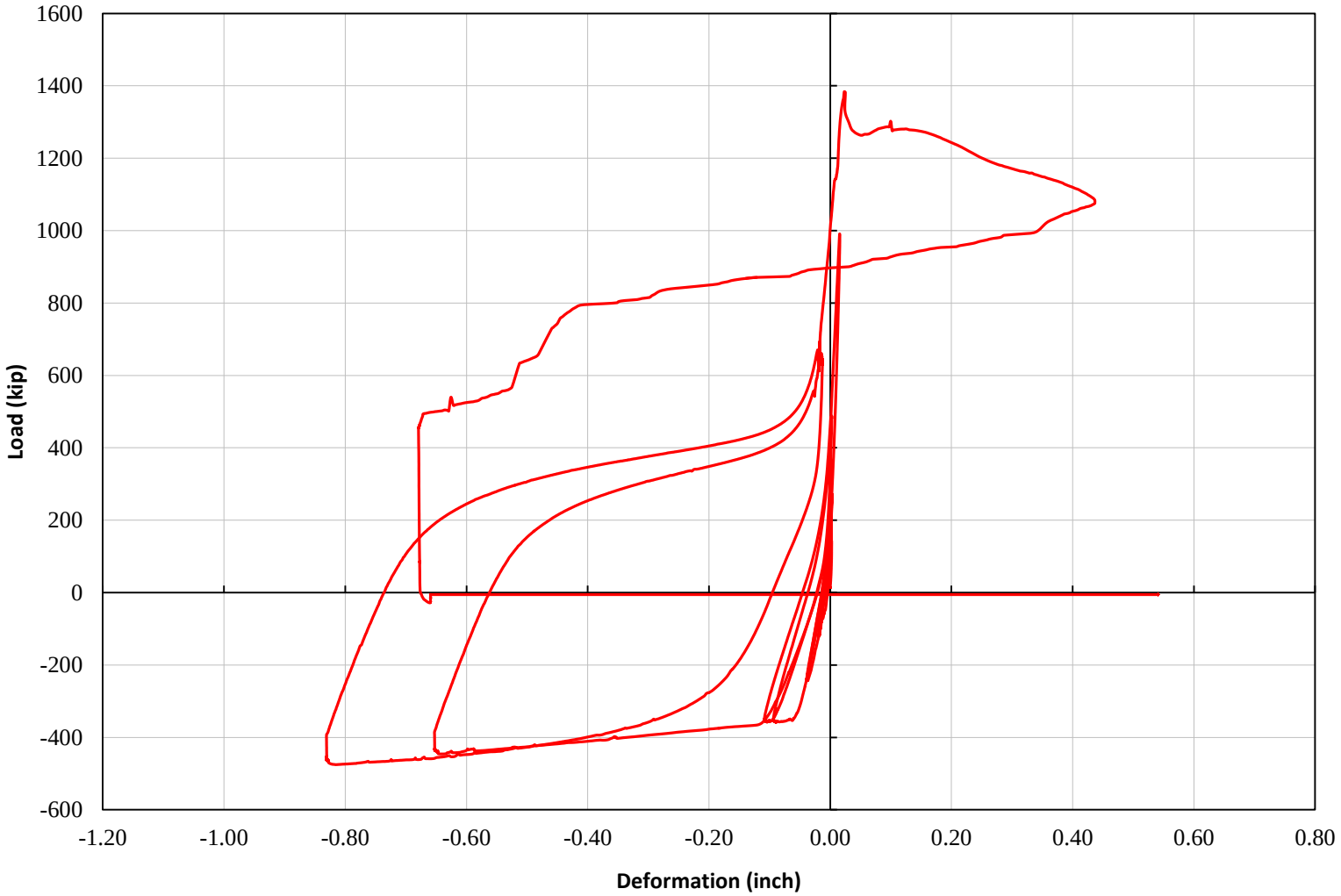

Figure 4-9: NLVDT deformation for TS02

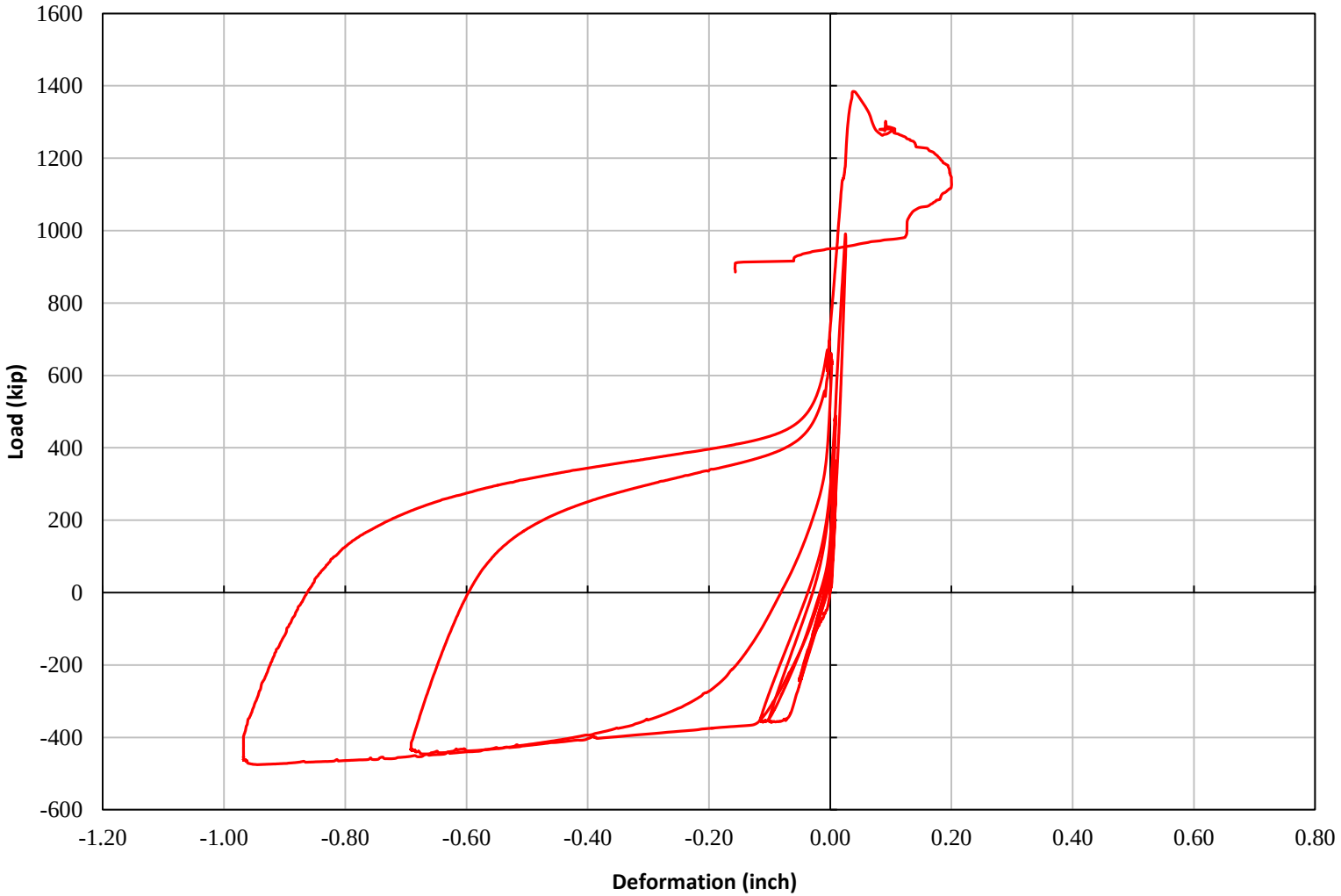

Figure 4-10: SLVDT deformation for TS02

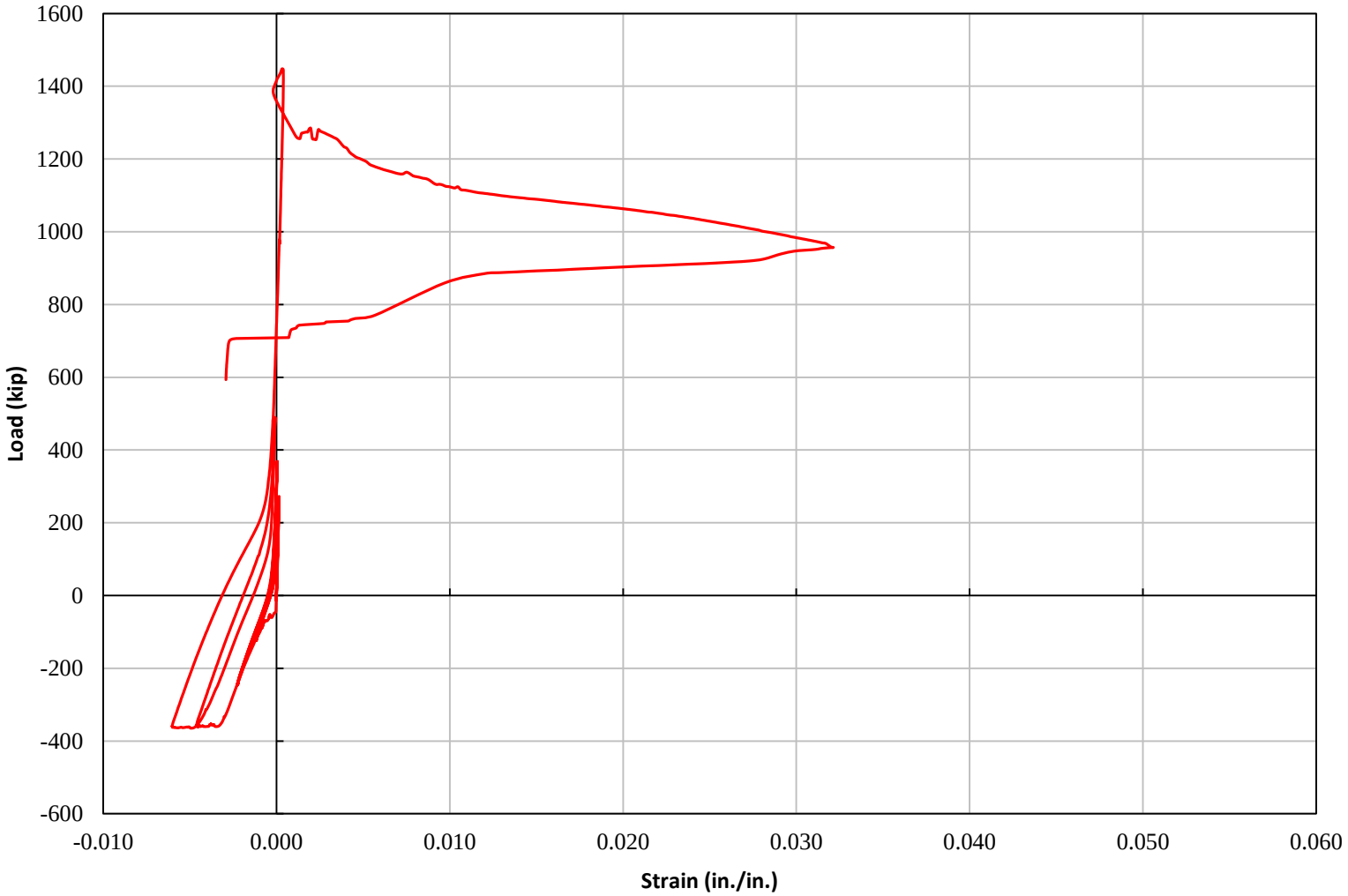

Figure 4-11: Strain from NLVDT for TS01

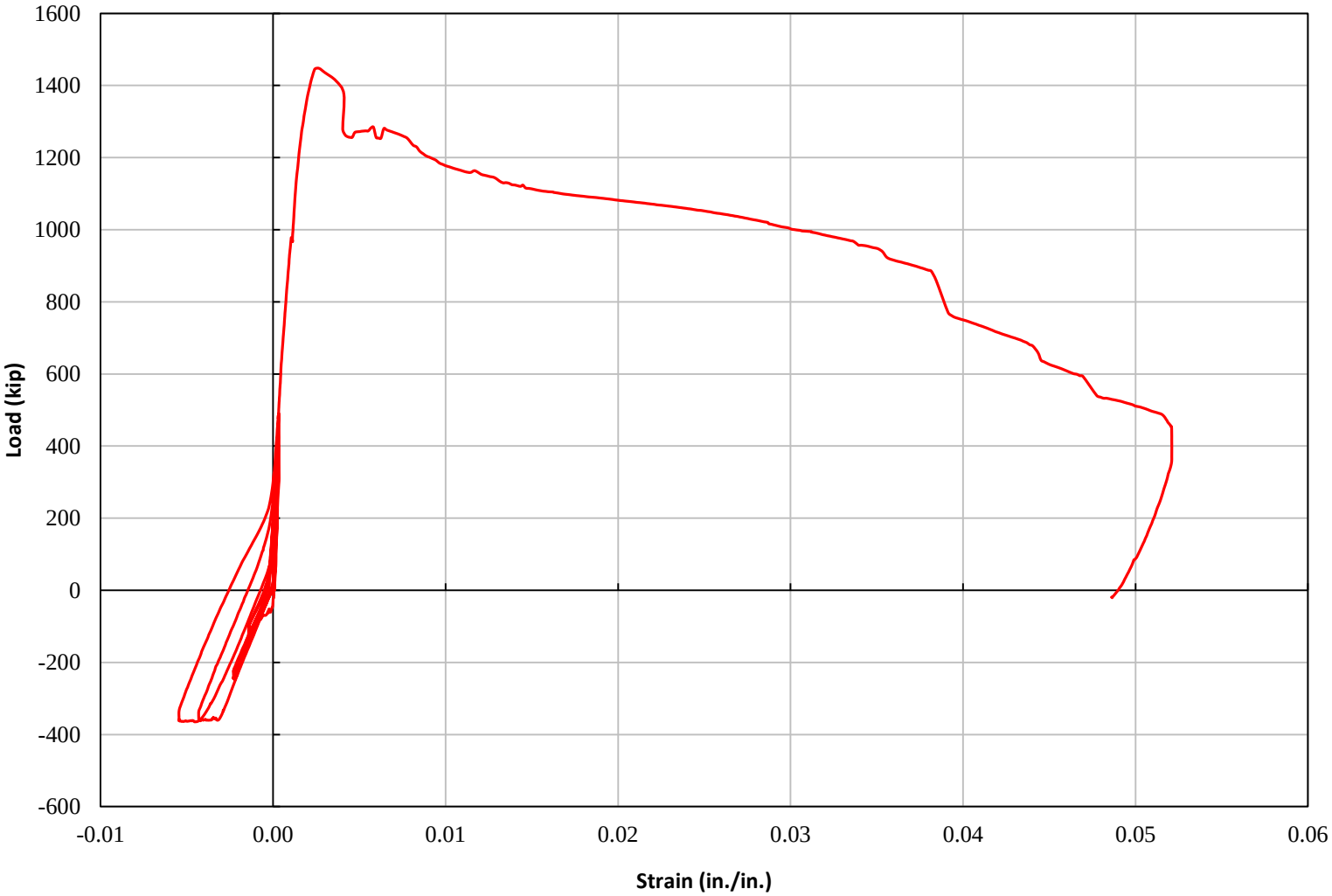

Figure 4-12: Strain from SLVDT for TS01

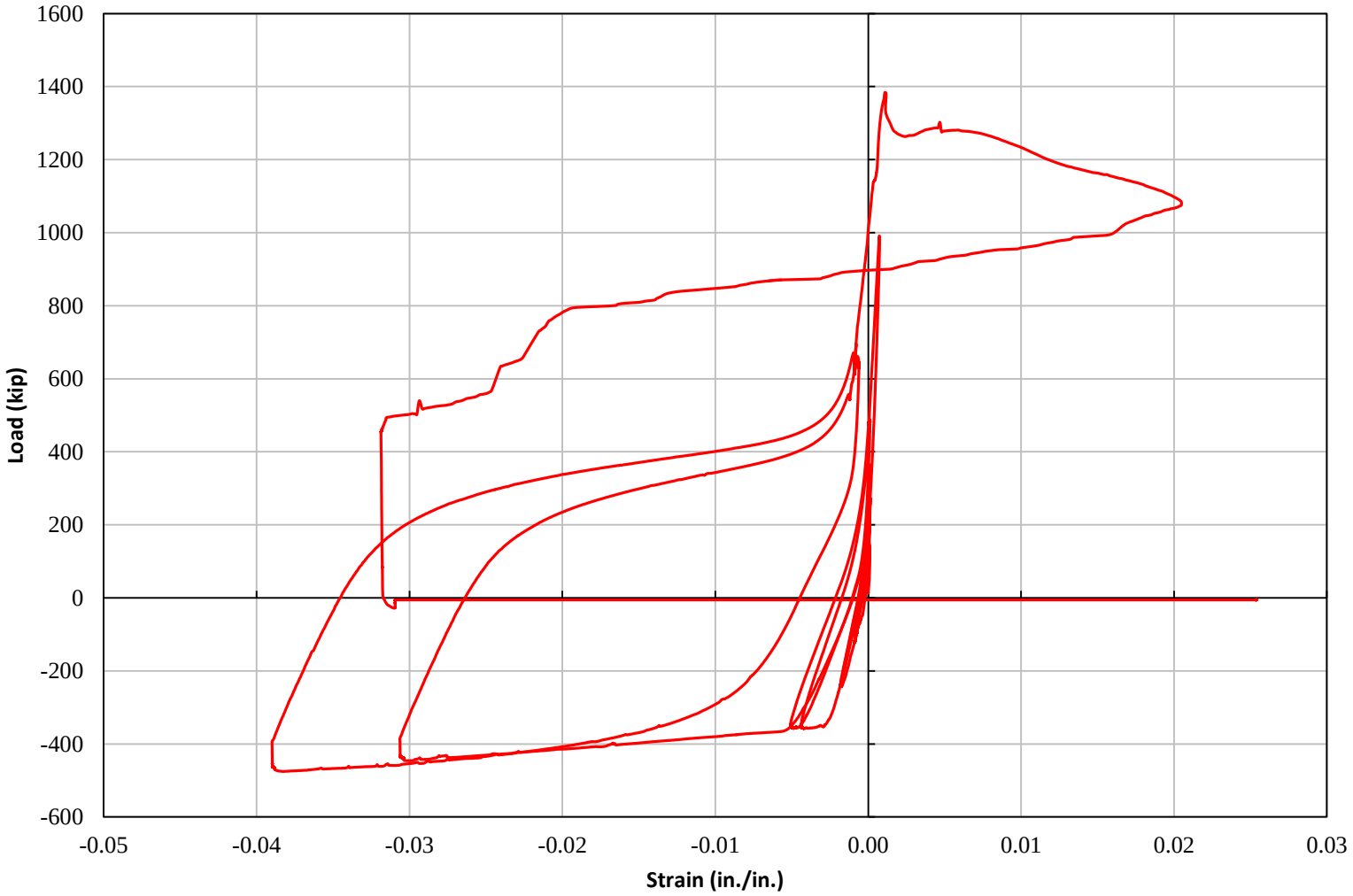

Figure 4-13: Strain from NLVDT for TS02

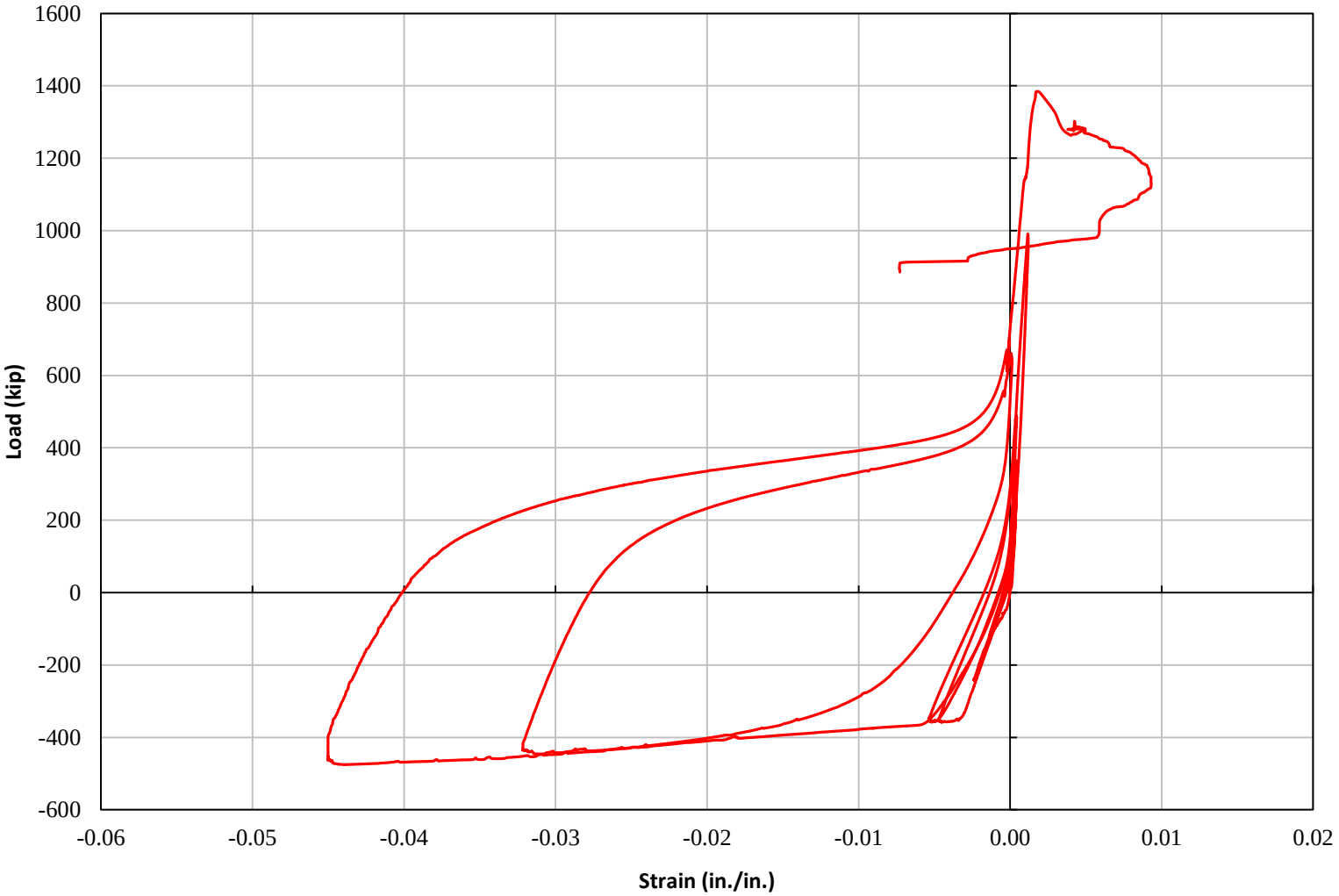

Figure 4-14: Strain from SLVDT for TS02

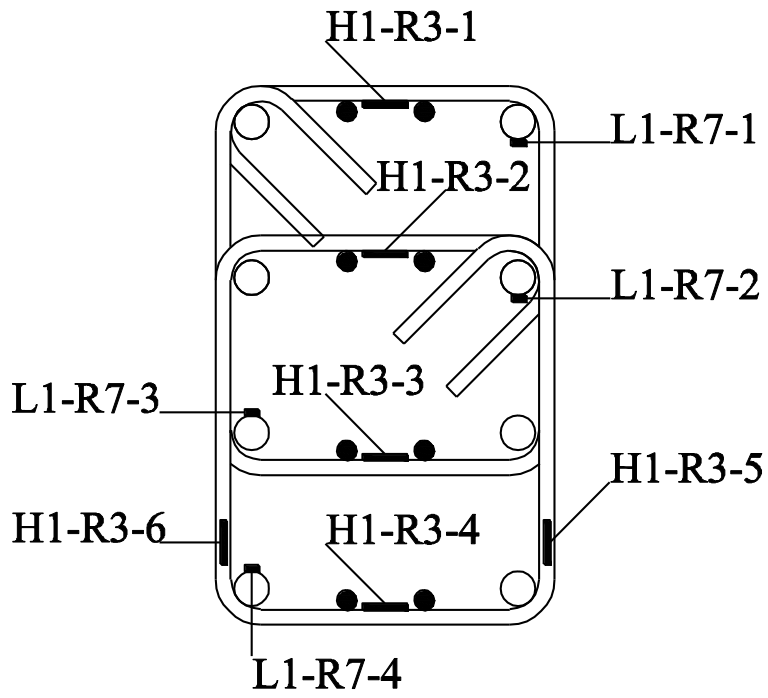

Figure 4-15: Strain gage notation in confinement hoop-pair 1

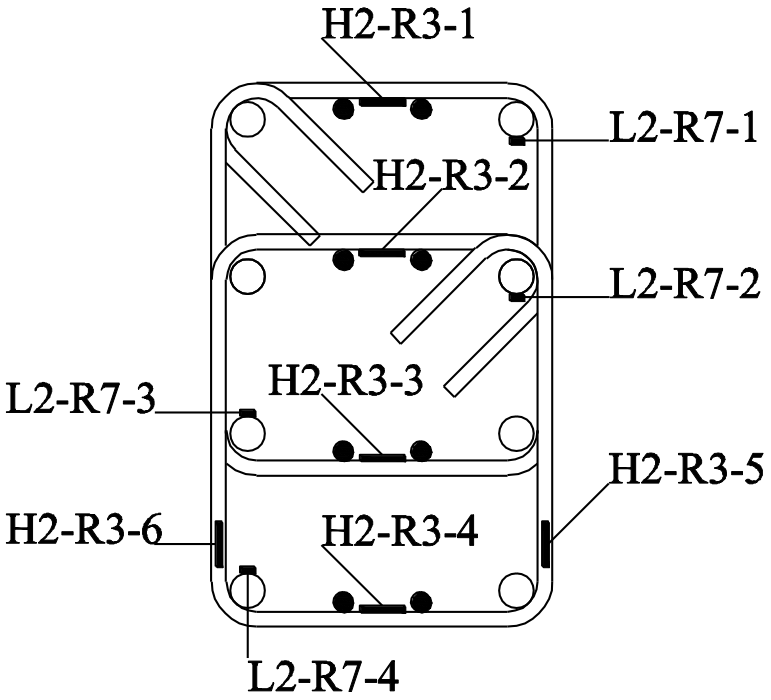

Figure 4-16: Strain gage notation in confinement hoop-pair 2

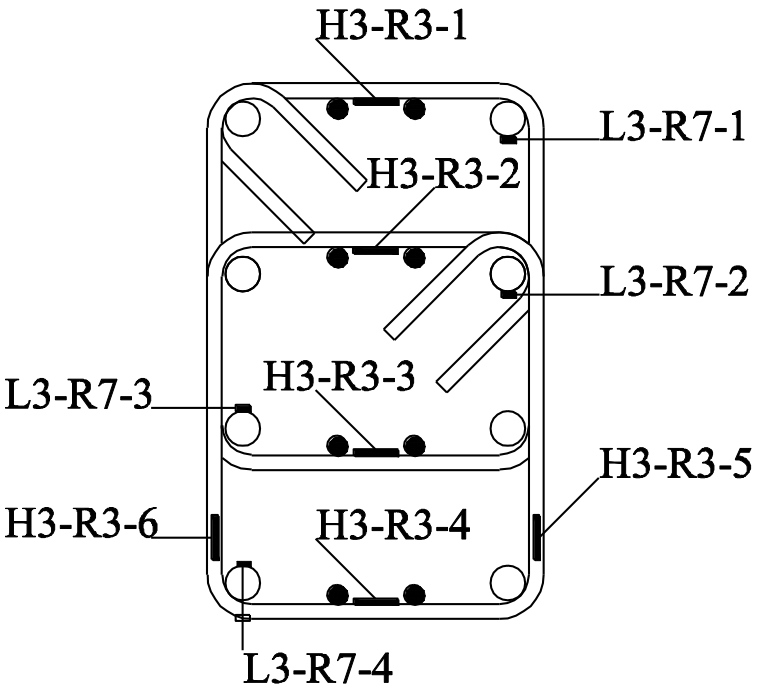

Figure 4-17: Strain gage notation in confinement hoop-pair 3

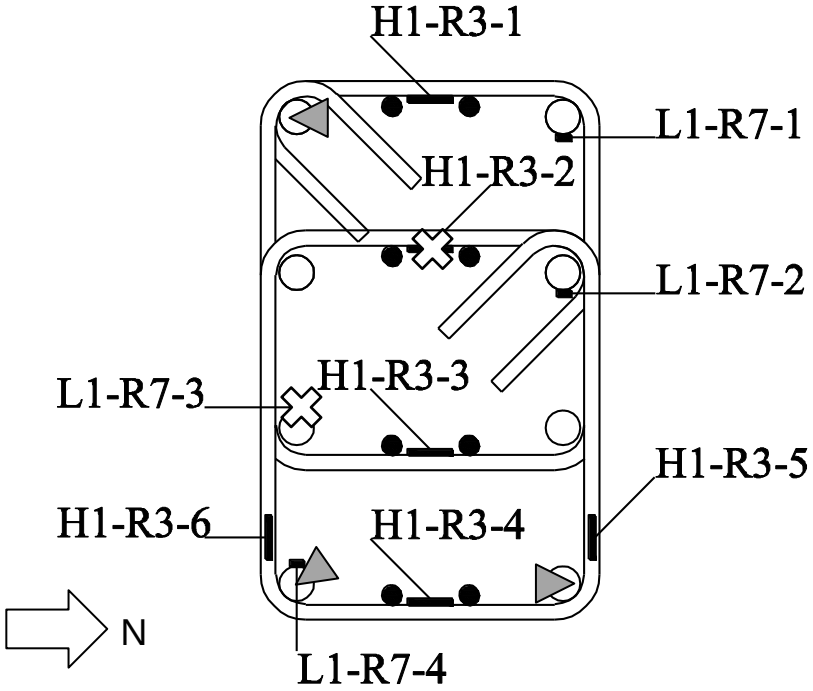

Figure 4-18: Condition of strain gage in confinement hoop-pair 1 in TS01

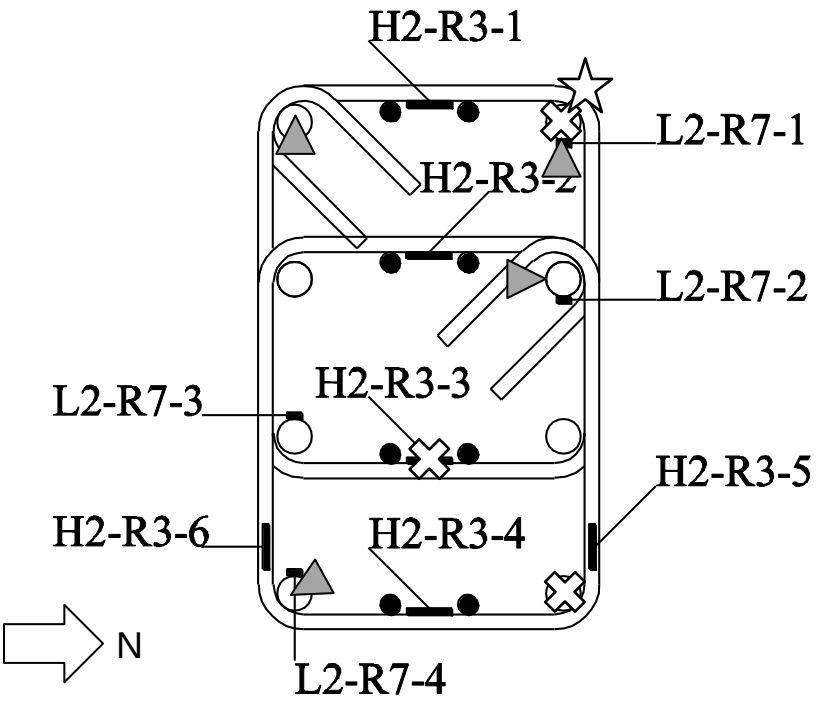

Figure 4-19: Condition of strain gage in confinement hoop-pair 2 in TS01

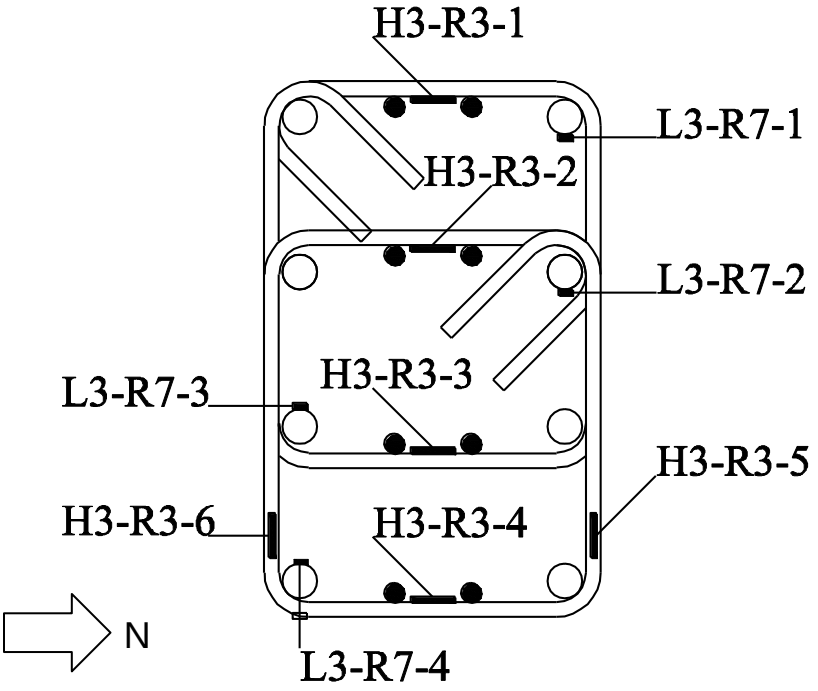

Figure 4-20: Condition of strain gage in confinement hoop-pair 3 in TS01

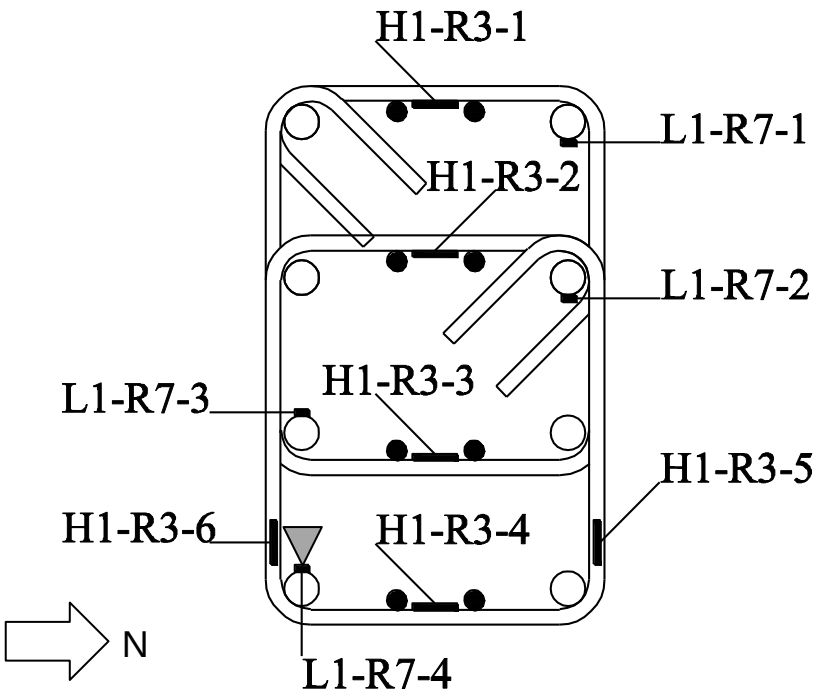

Figure 4-21: Condition of strain gage in confinement hoop-pair 1 in TS02

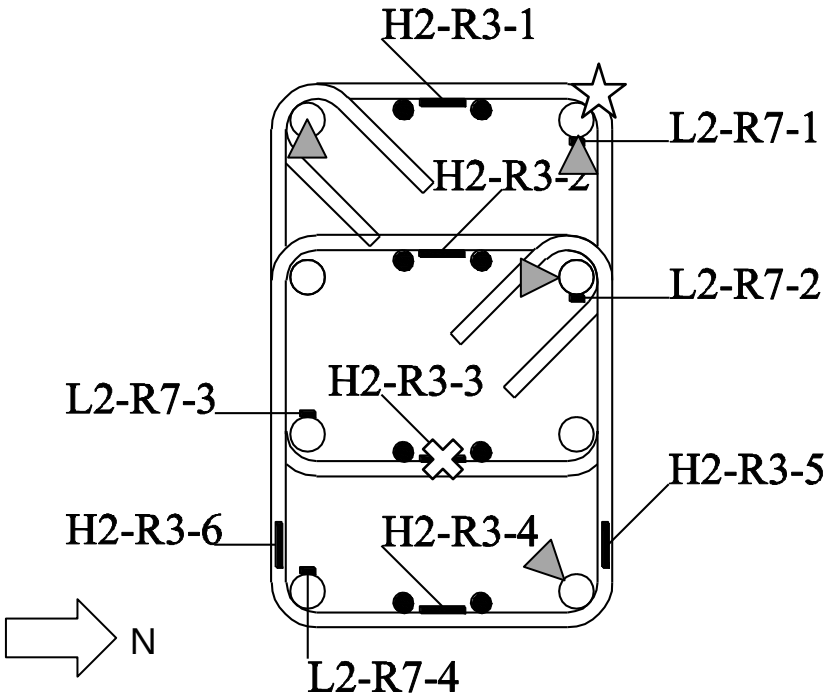

Figure 4-22: Condition of strain gage in confinement hoop-pair 2 in TS02

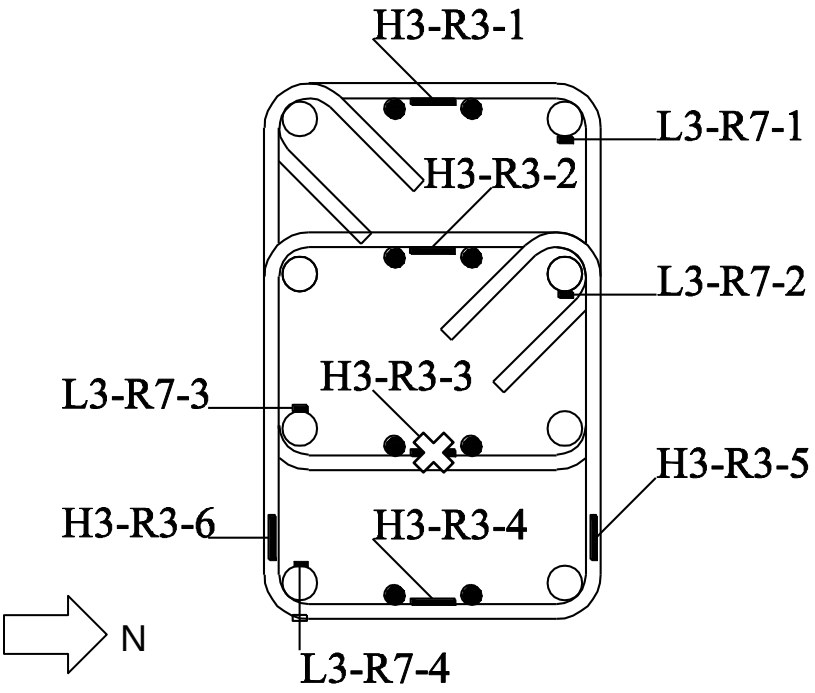

Figure 4-23: Condition of strain gage in confinement hoop-pair 3 in TS02

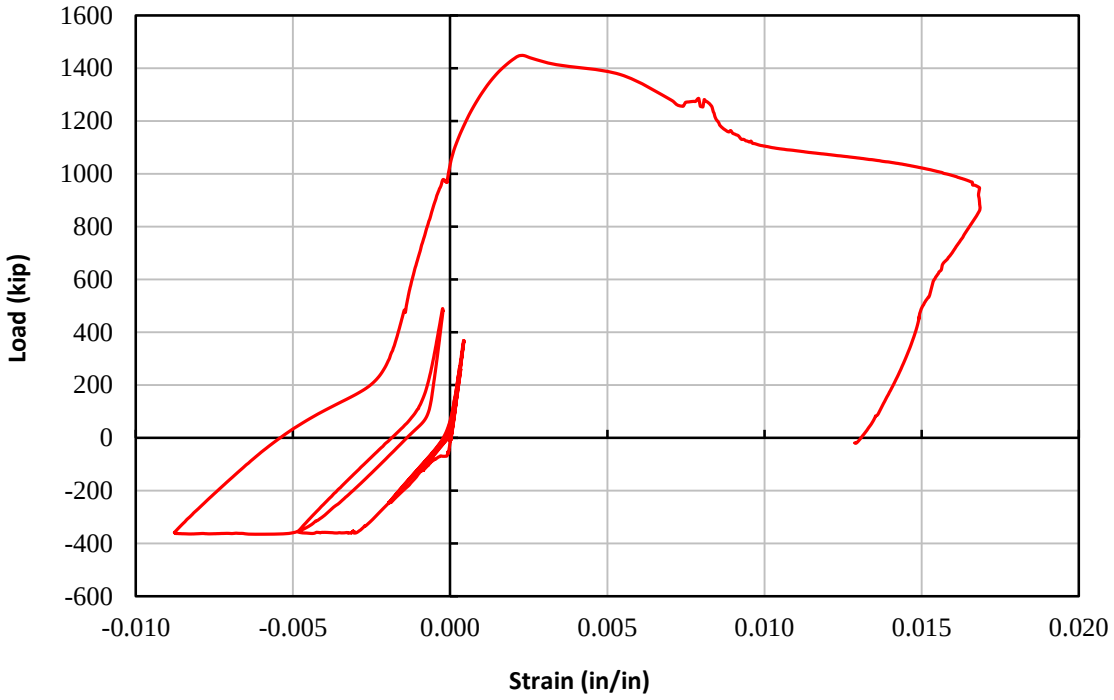

Figure 4-24: Strain gage L1-R7-1 for TS01

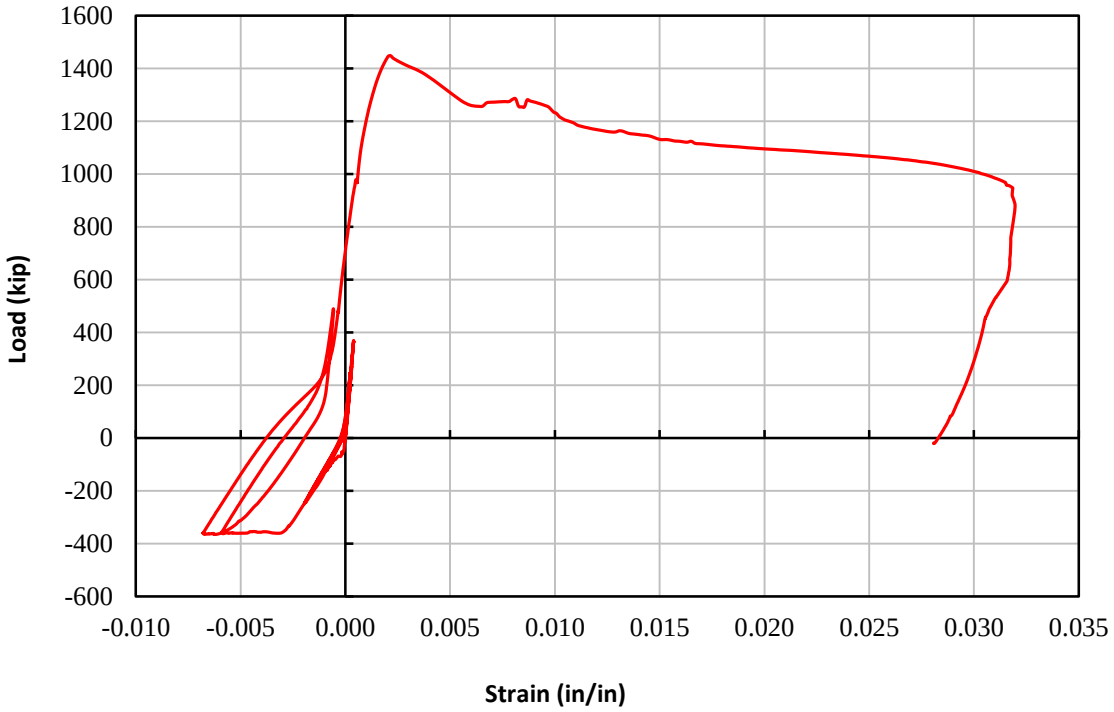

Figure 4-25: Strain gage L1-R7-2 for TS01

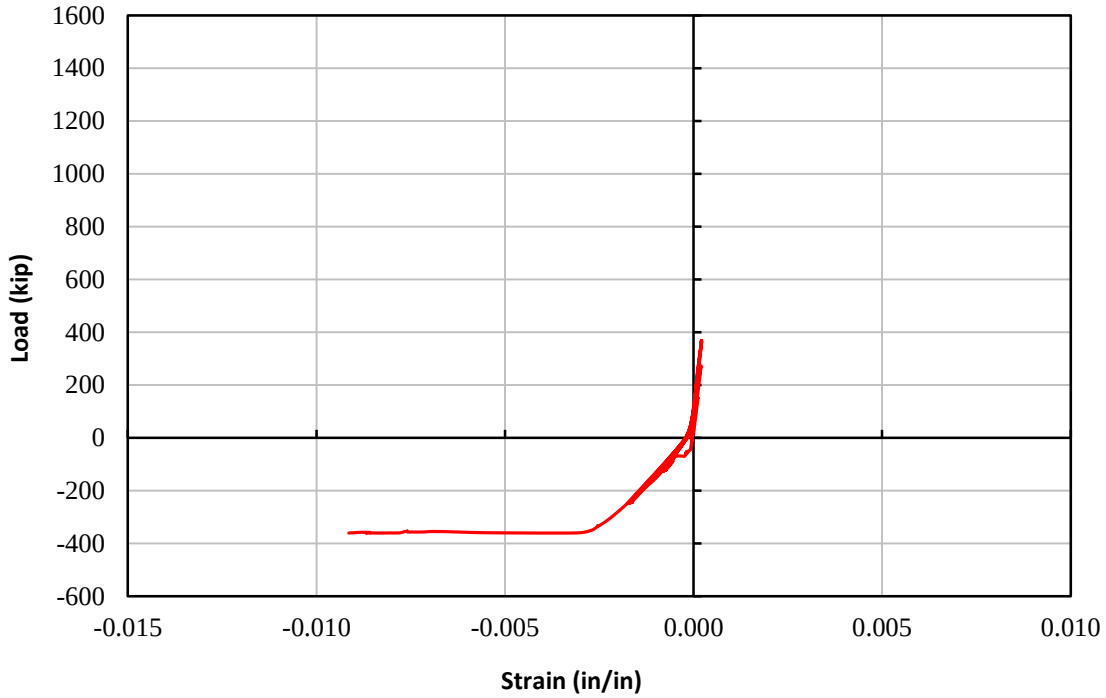

Figure 4-26: Strain gage L1-R7-4 for TS01

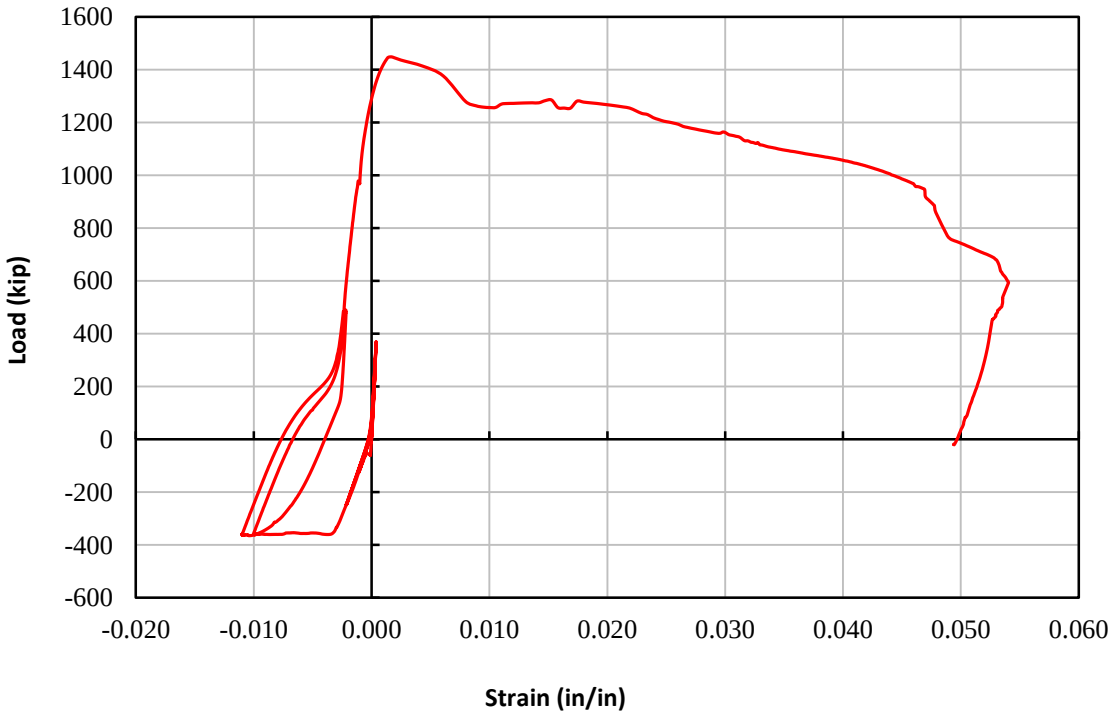

Figure 4-27: Strain gage L2-R7-2 for TS01

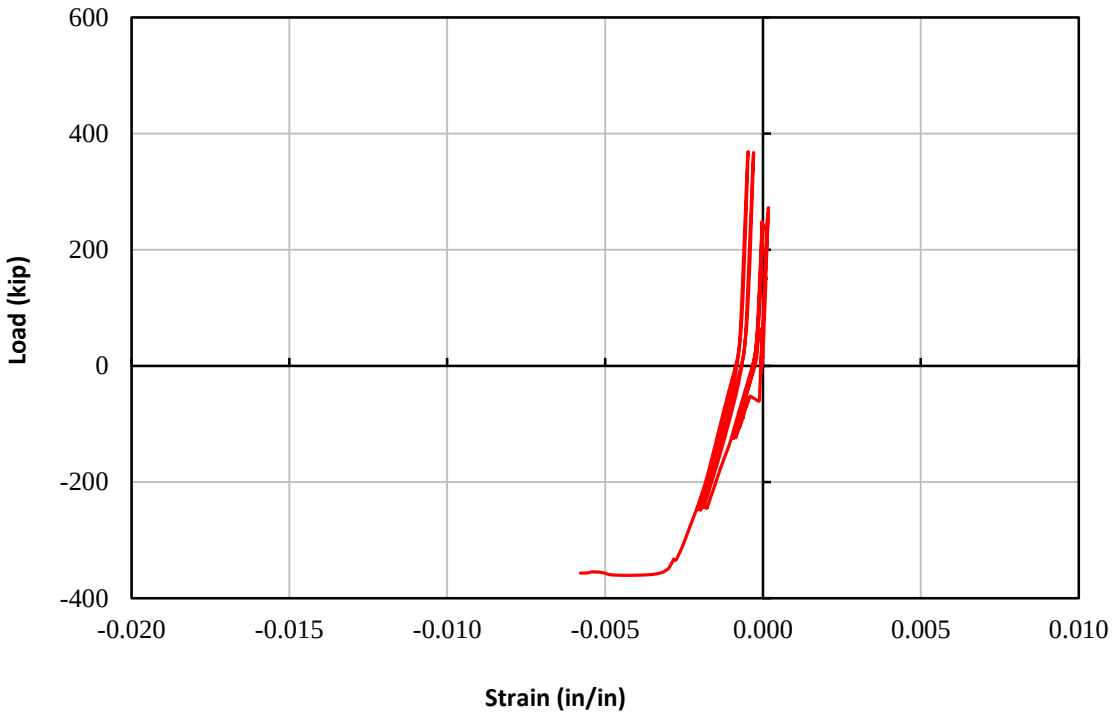

Figure 4-28: Strain gage L2-R7-3 for TS01

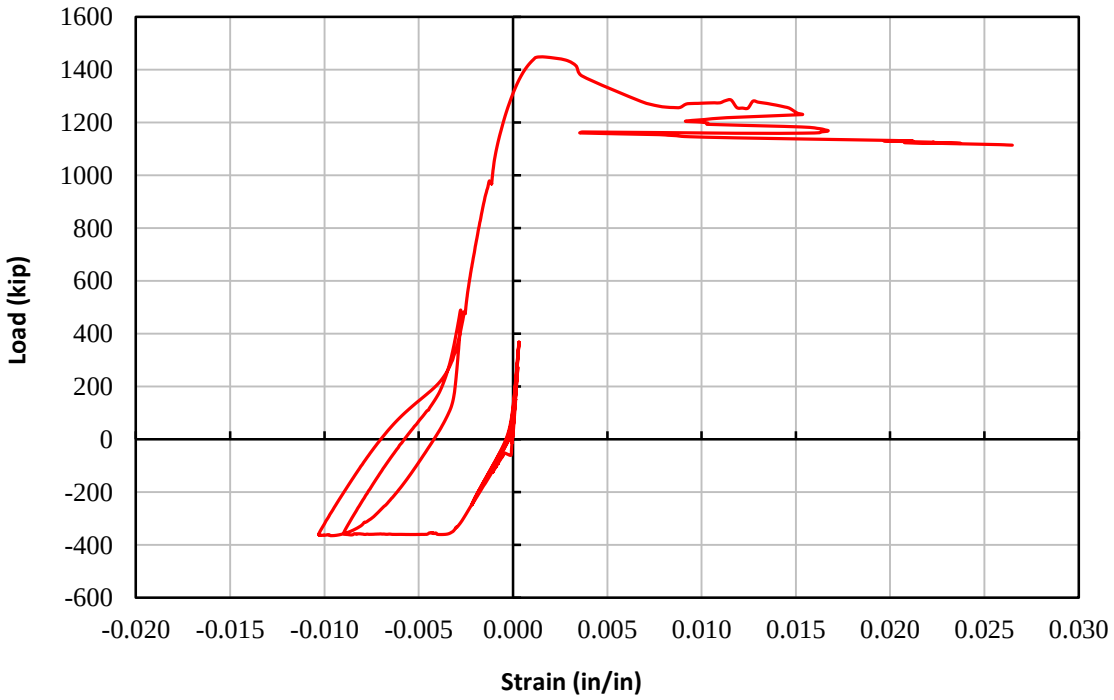

Figure 4-29: Strain gage L2-R7-4 for TS01

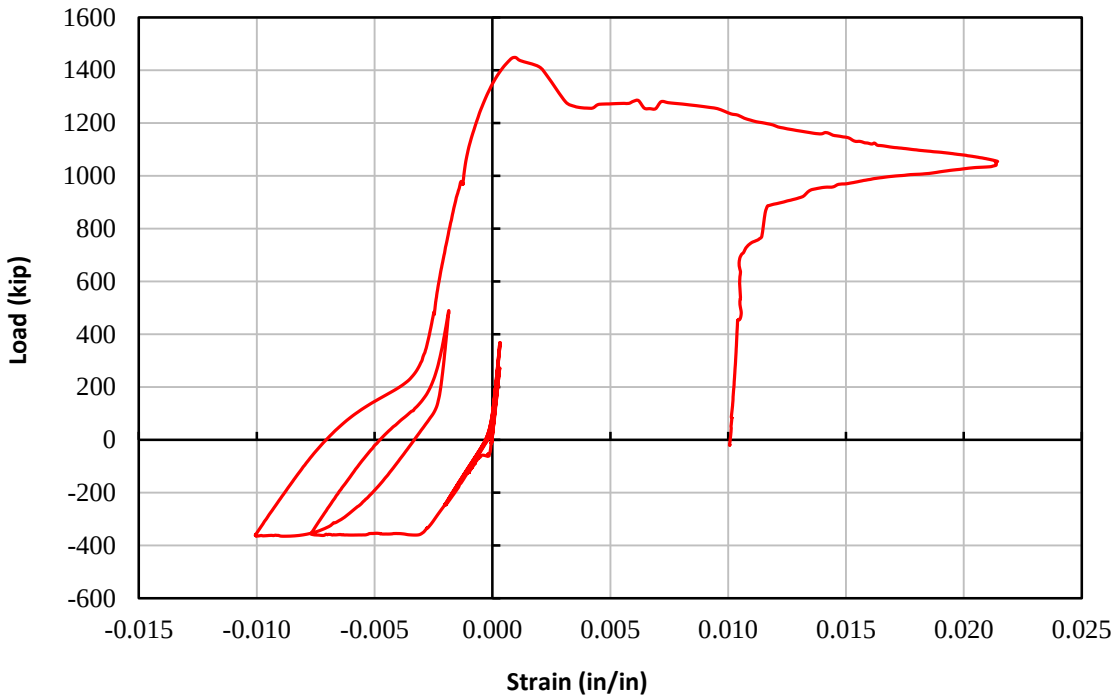

Figure 4-30: Strain gage L3-R7-1 for TS01

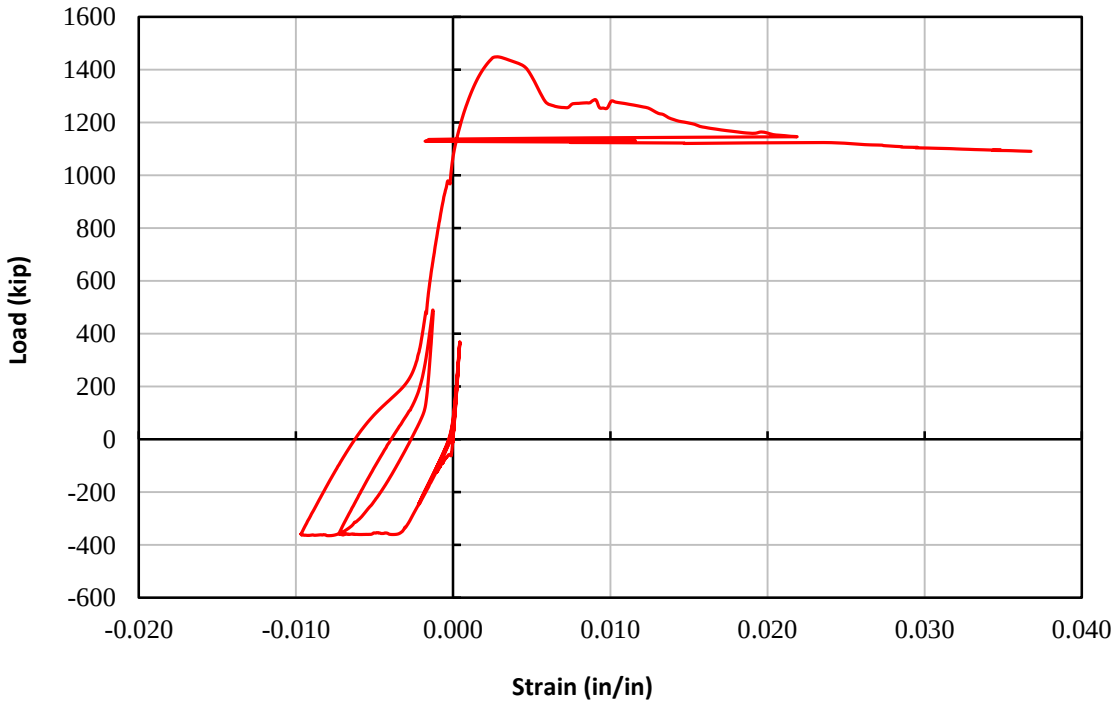

Figure 4-31: Strain gage L3-R7-2 for TS01

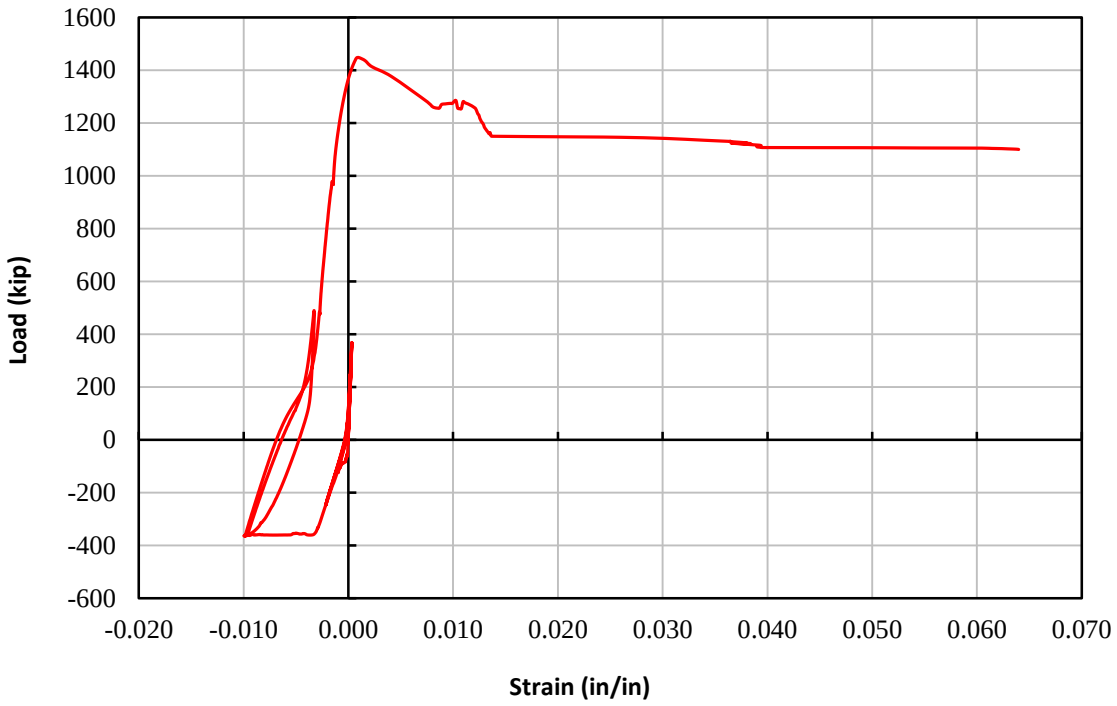

Figure 4-32: Strain gage L3-R7-3 for TS01

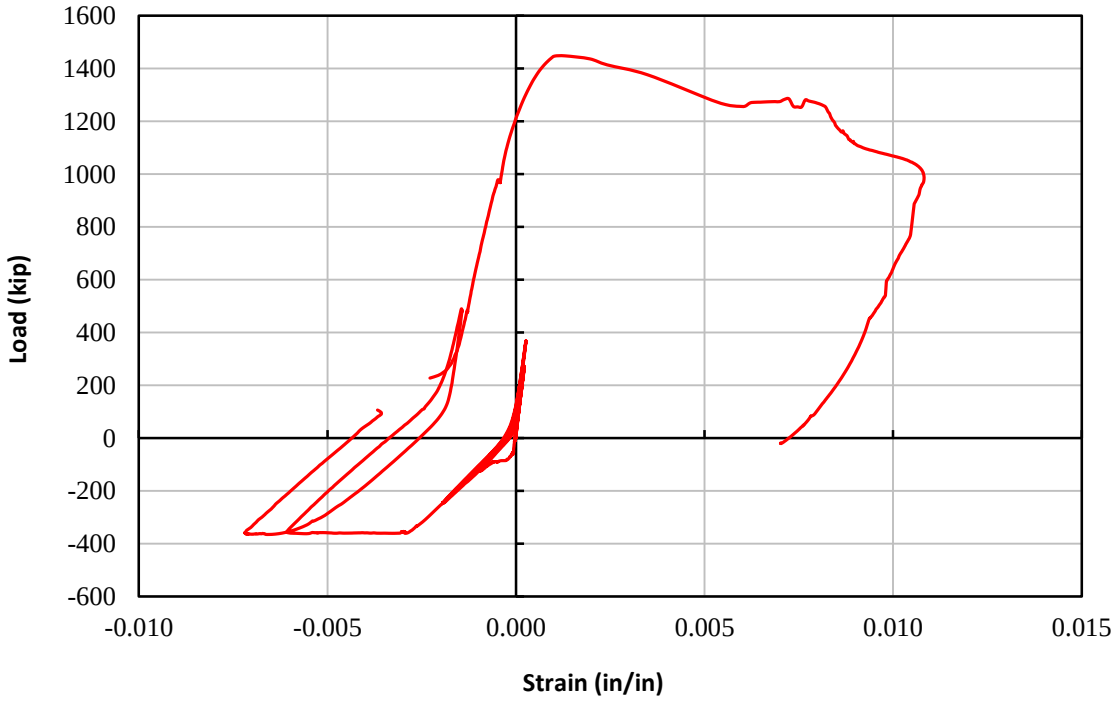

Figure 4-33: Strain gage L3-R7-4 for TS01

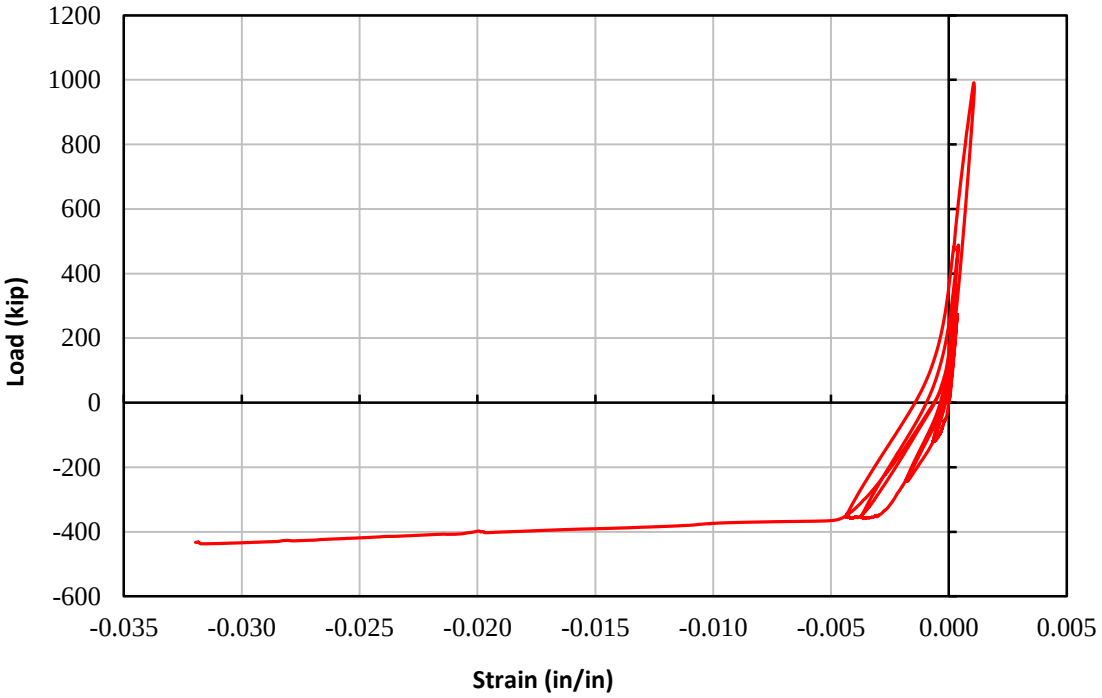

Figure 4-34: Strain gage L1-R7-1 for TS02

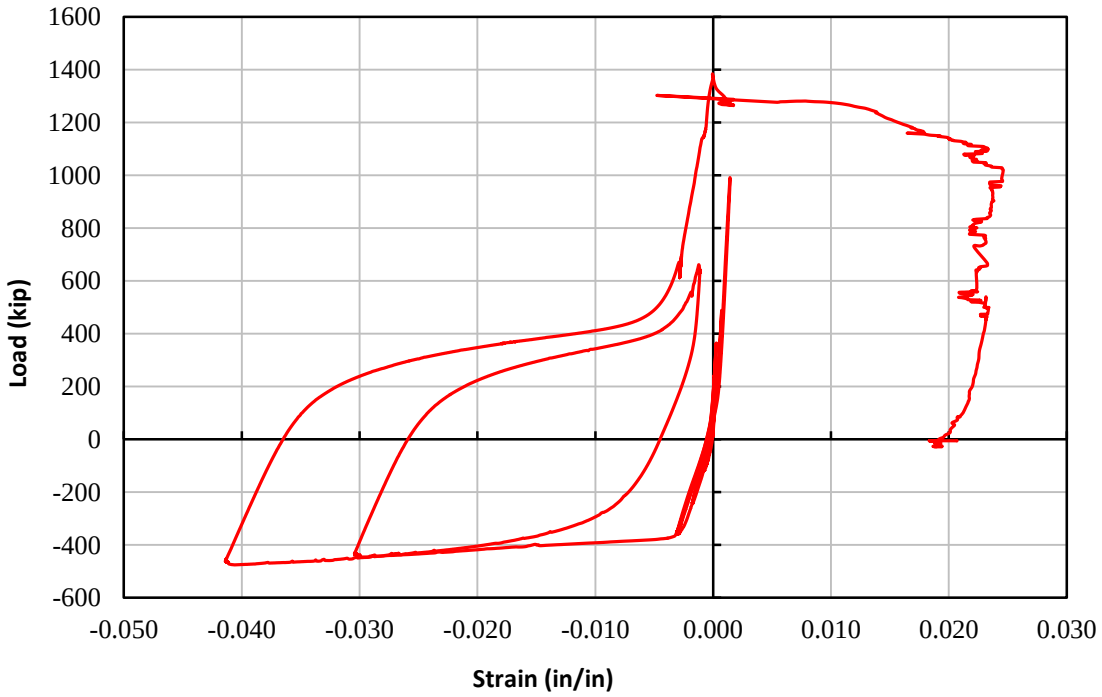

Figure 4-35: Strain gage L1-R7-2 for TS02

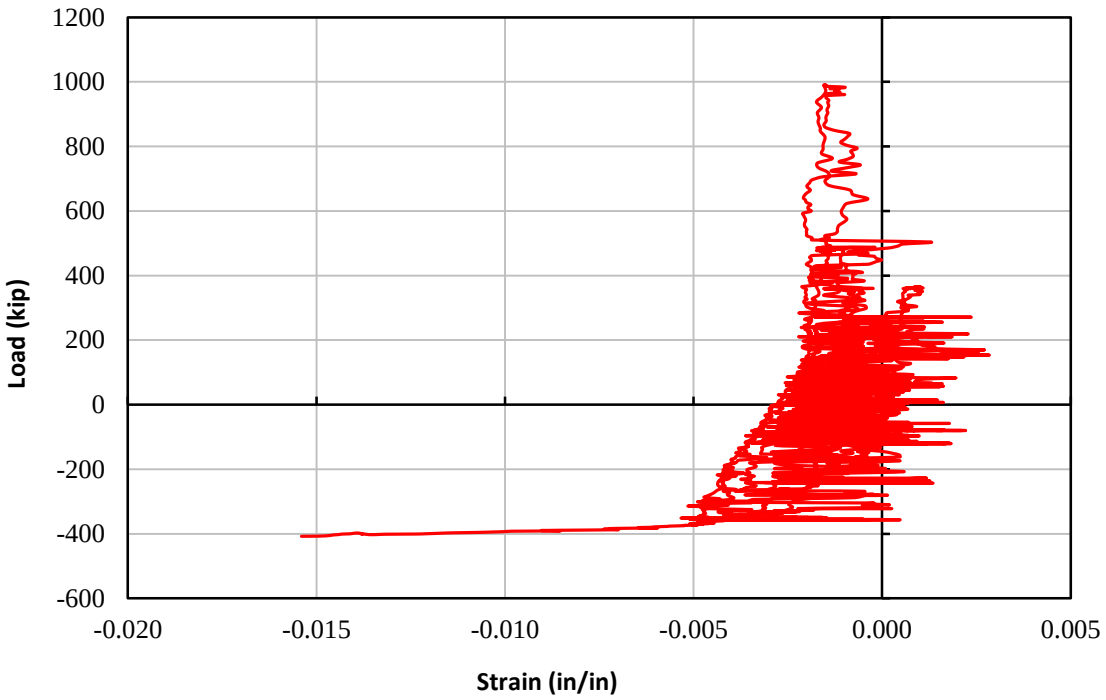

Figure 4-36: Strain gage L1-R7-3 for TS02

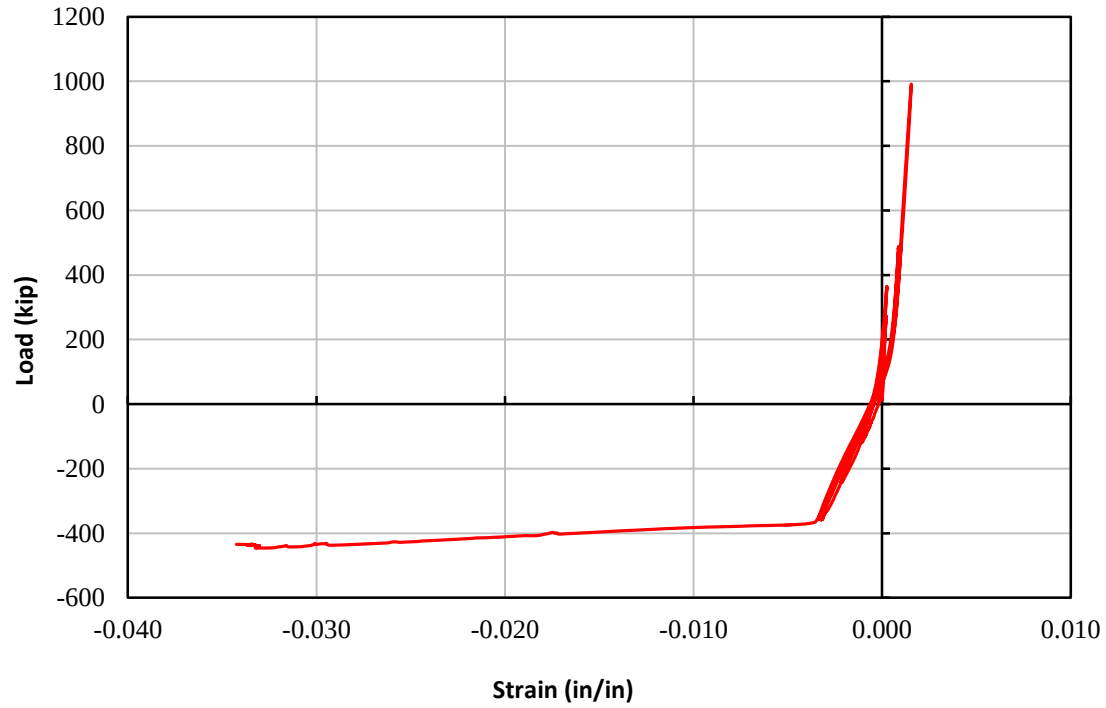

Figure 4-37: Strain gage L1-R7-4 for TS02

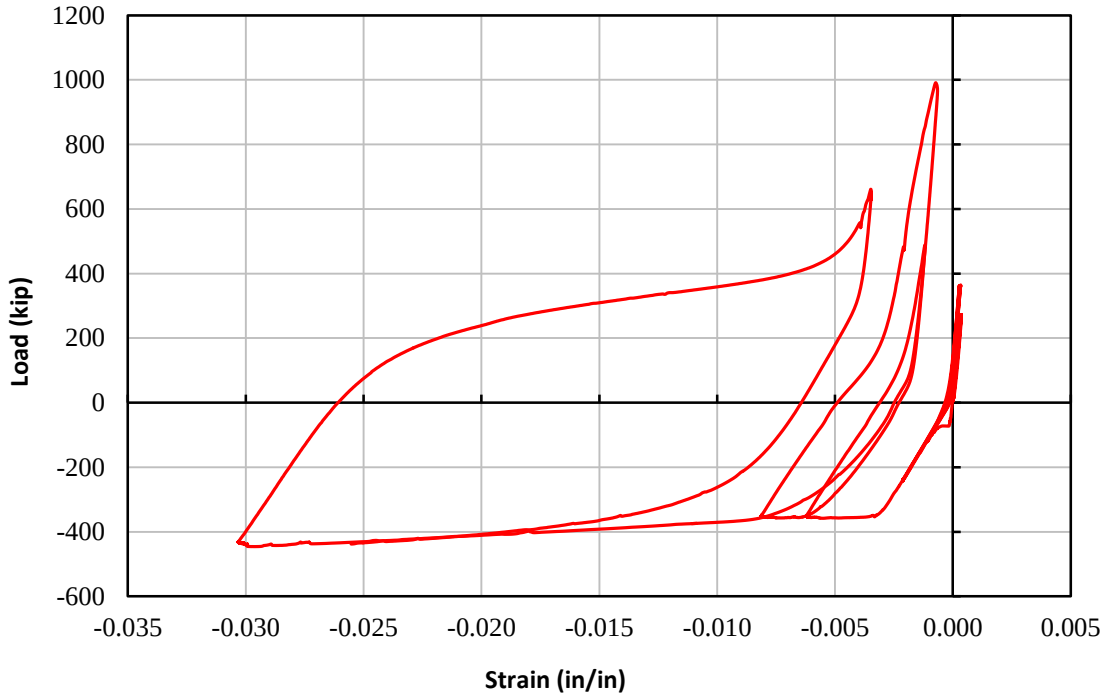

Figure 4-38: Strain gage L2-R7-1 for TS02

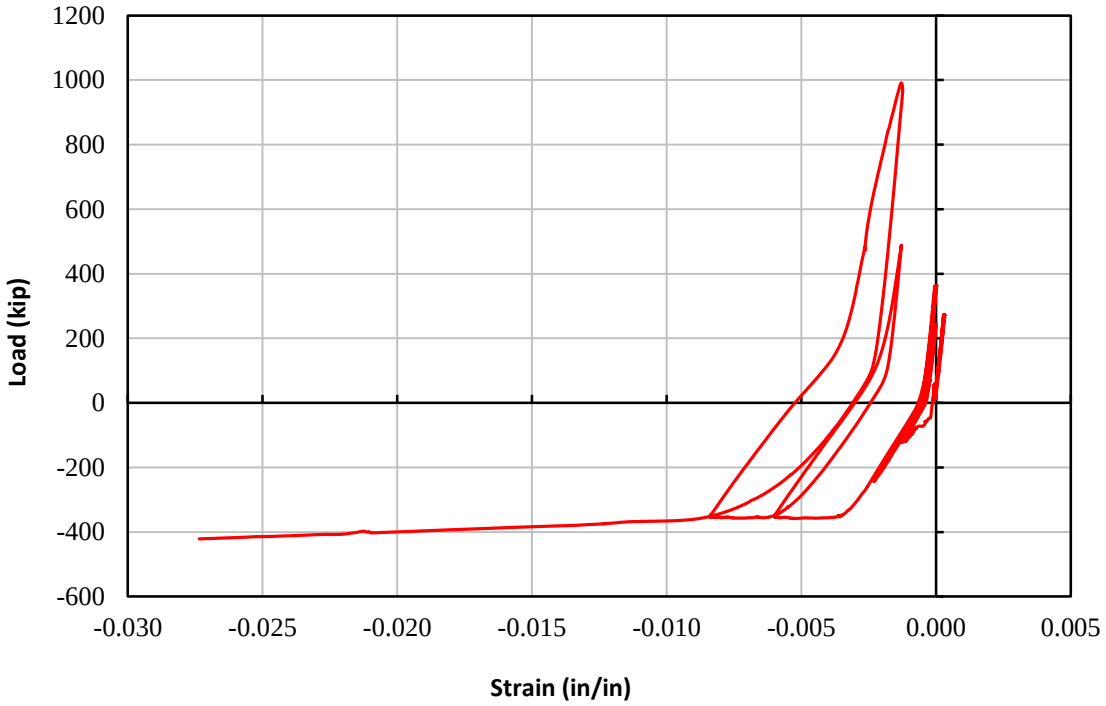

Figure 4-39: Strain gage L2-R7-2 for TS02

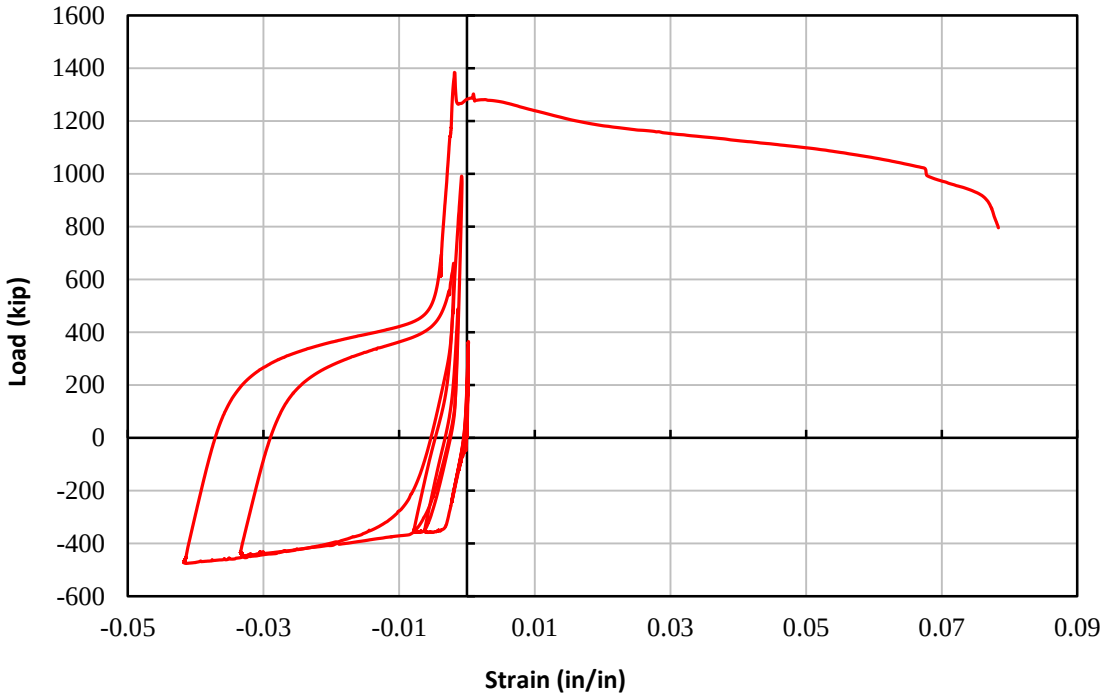

Figure 4-40: Strain gage L2-R7-3 for TS02

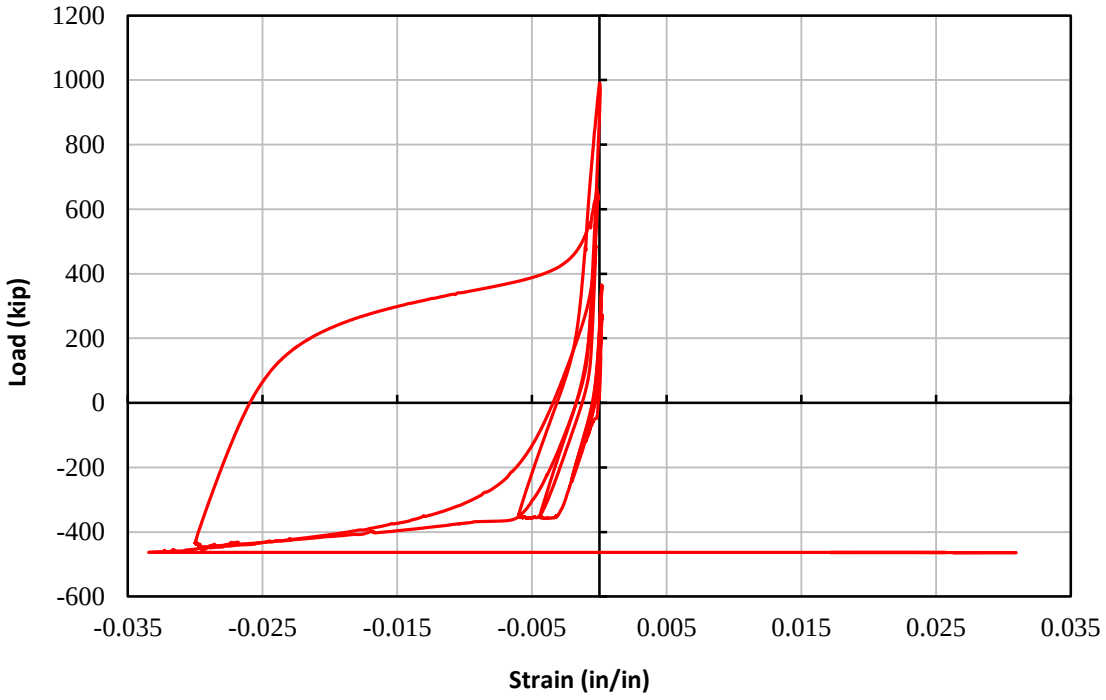

Figure 4-41: Strain gage L2-R7-4 for TS02

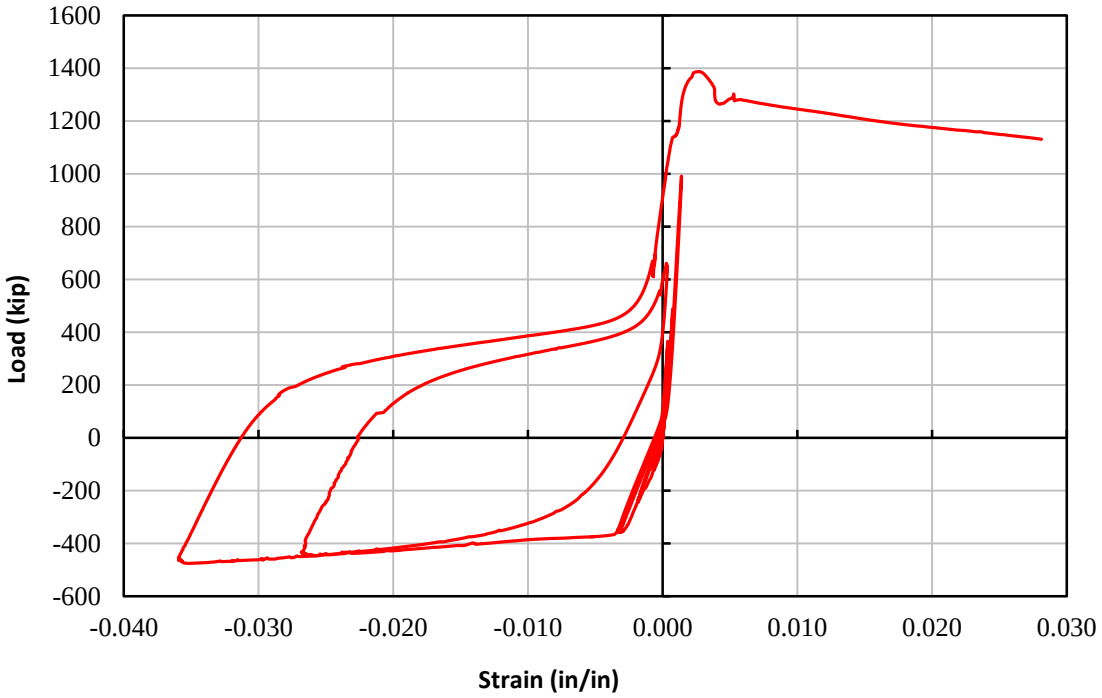

Figure 4-42: Strain gage L3-R7-1 for TS02

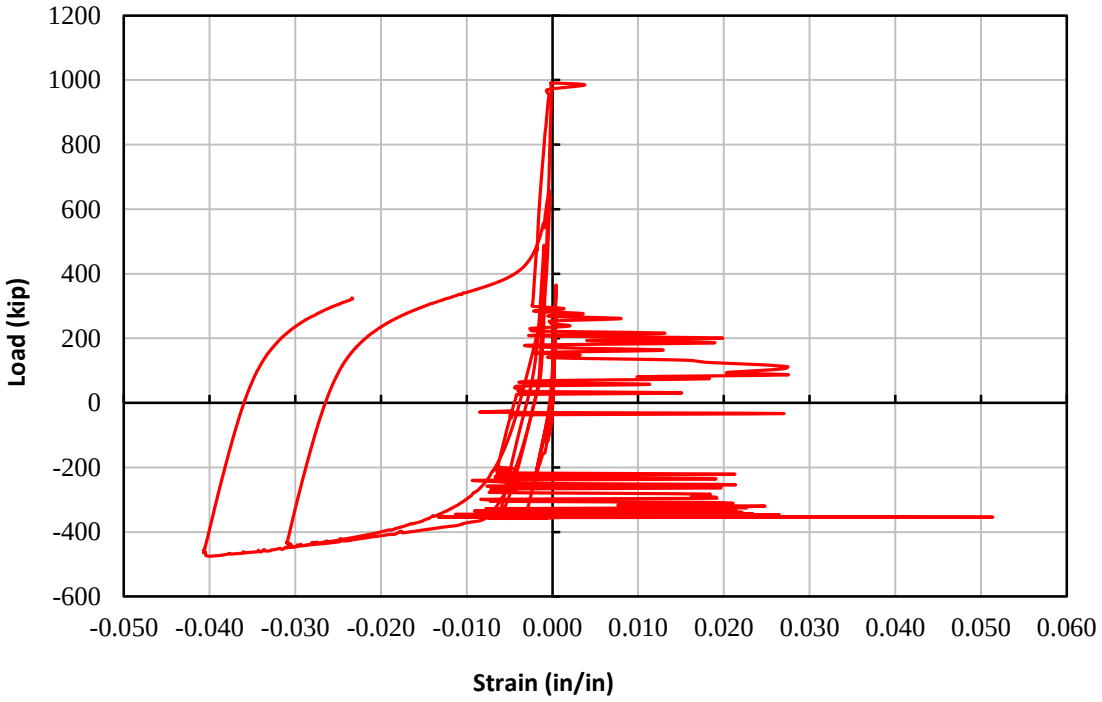

Figure 4-43: Strain gage L3-R7-2 for TS02

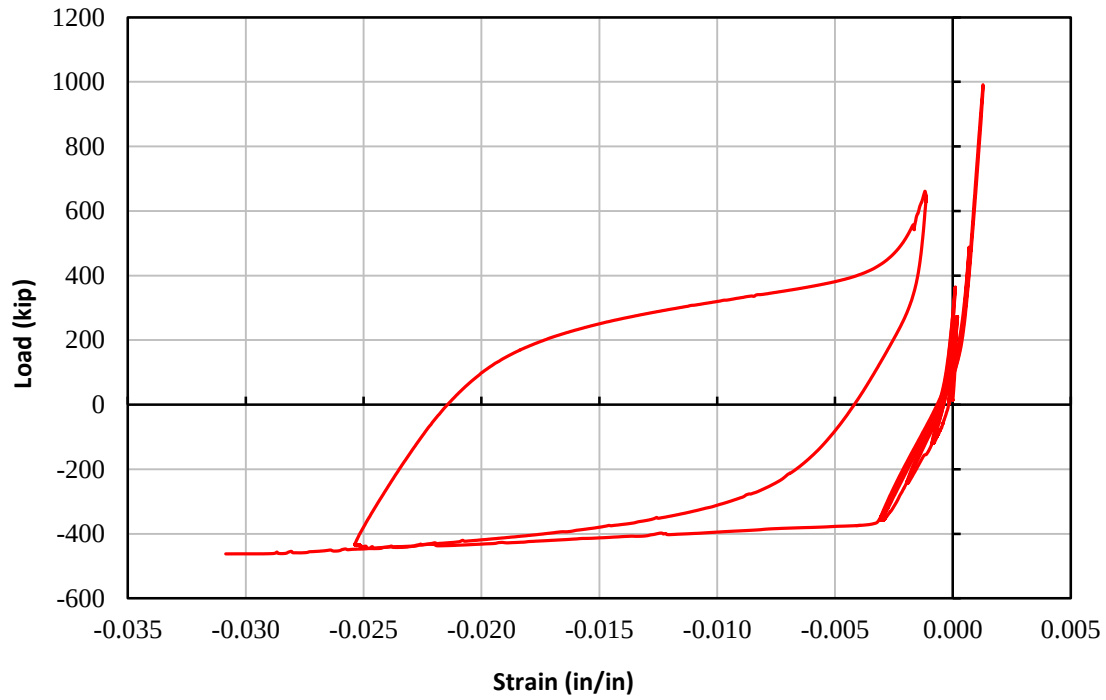

Figure 4-44: Strain gage L3-R7-3 for TS02

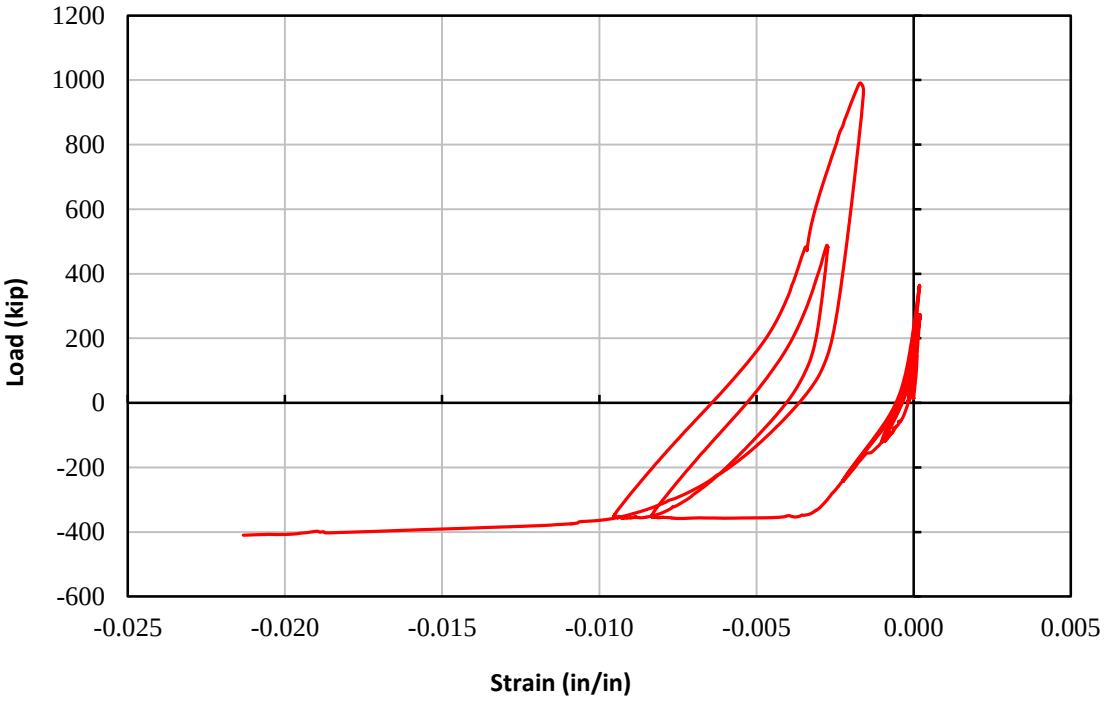

Figure 4-45: Strain gage L3-R7-4 for TS02

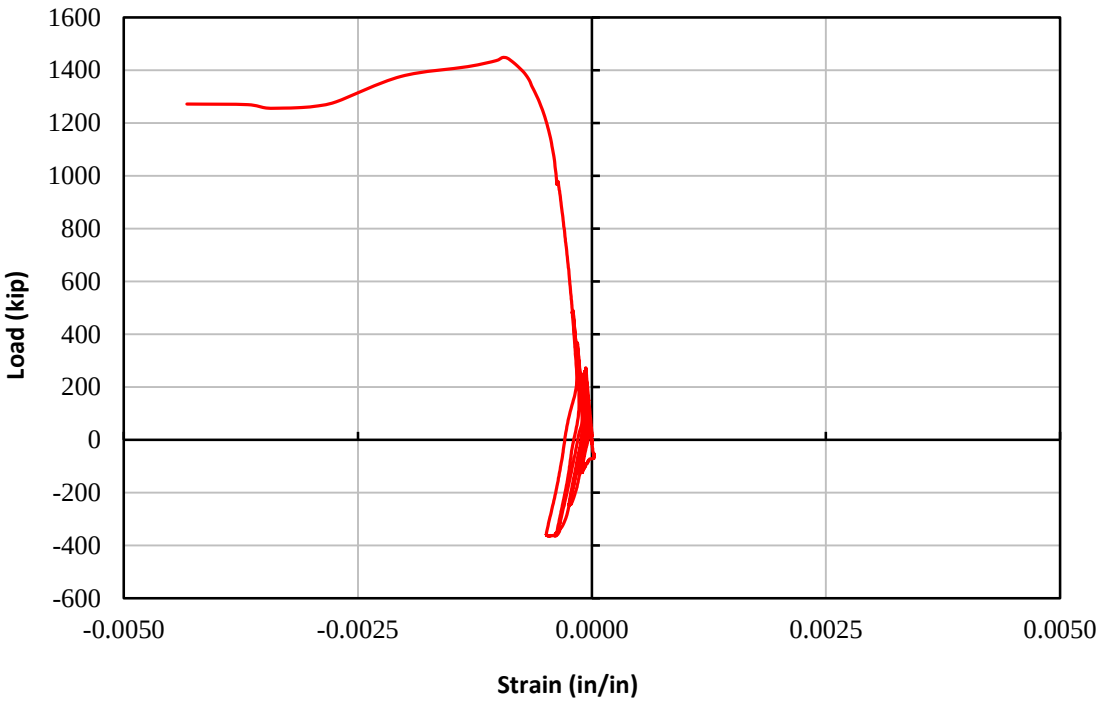

Figure 4-46: Strain gage H1-R3-1 for TS01

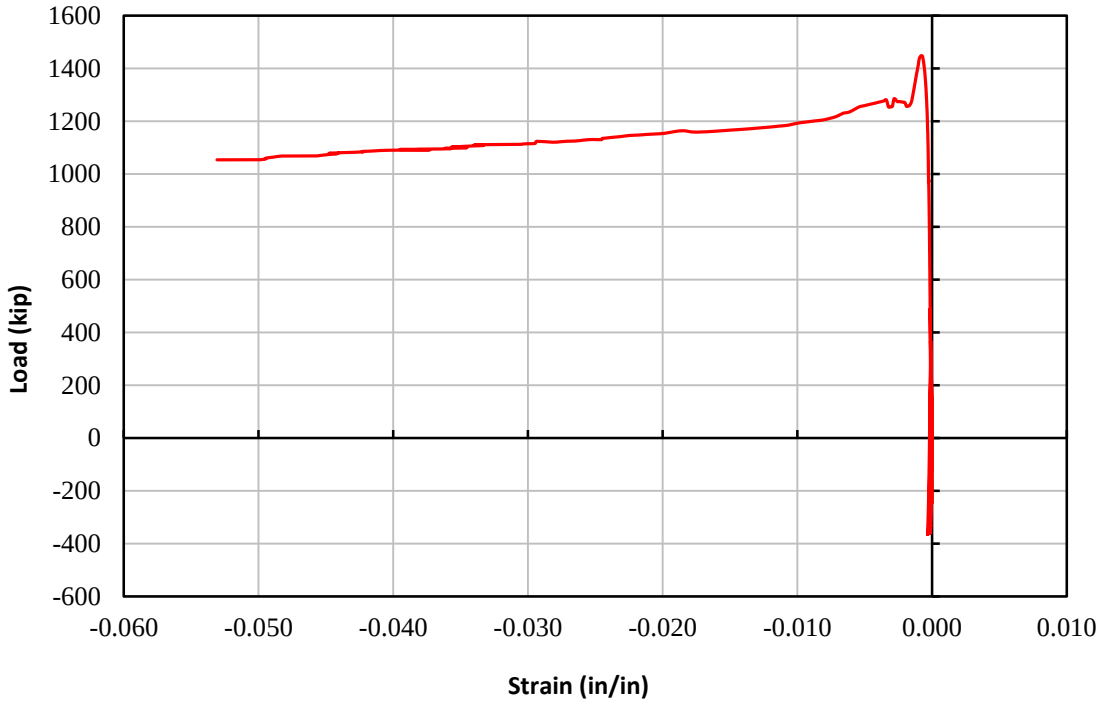

Figure 4-47: Strain gage H1-R3-3 for TS01

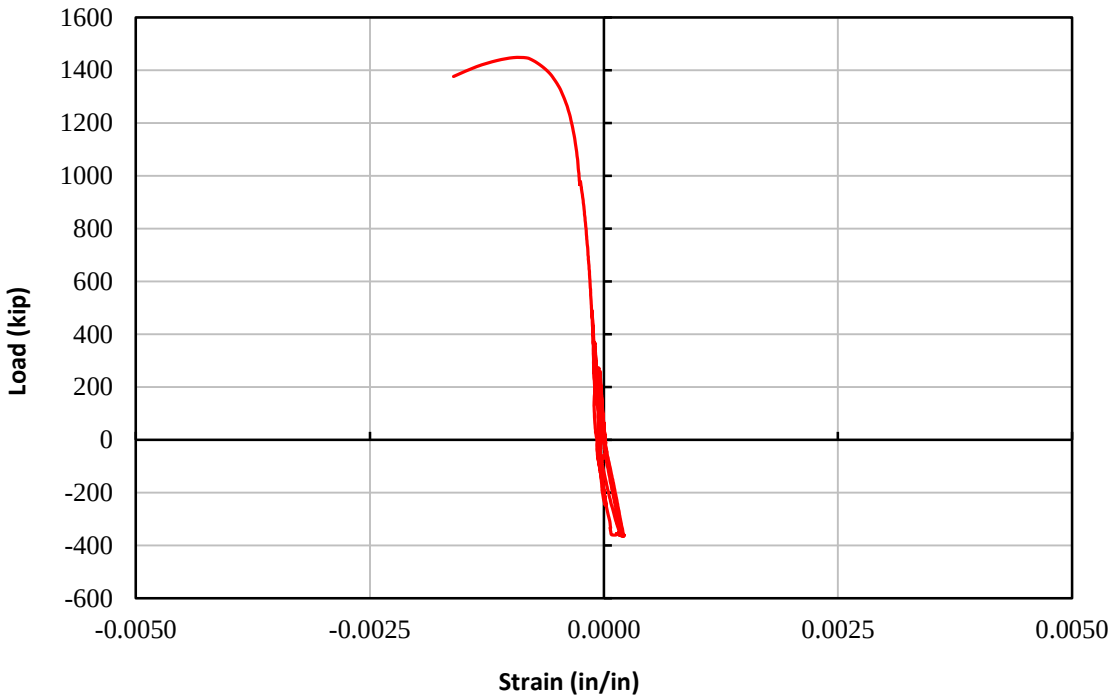

Figure 4-48: Strain gage H1-R3-4 for TS01

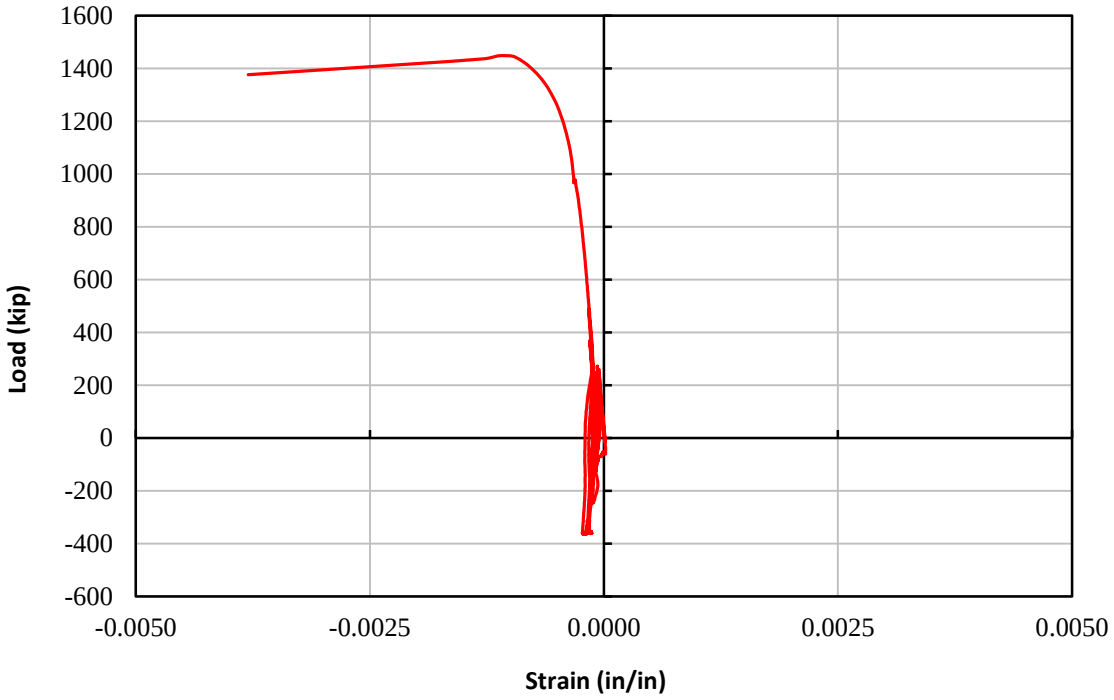

Figure 4-49: Strain gage H1-R3-5 for TS01

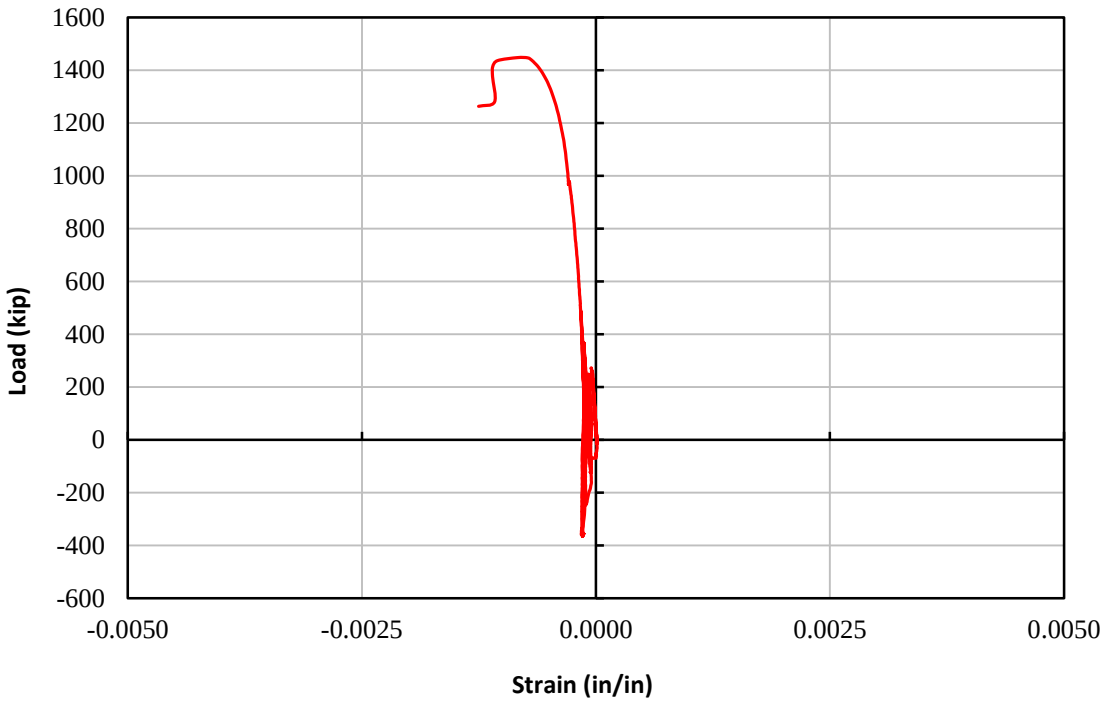

Figure 4-50: Strain gage H1-R3-6 for TS01

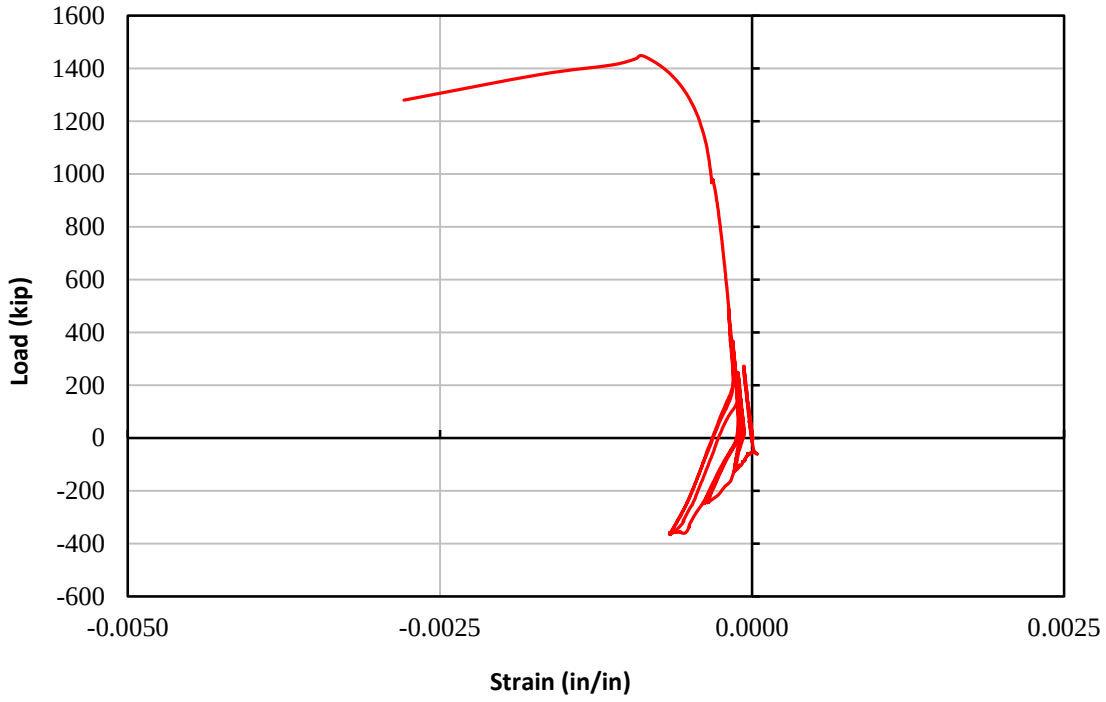

Figure 4-51: Strain gage H2-R3-1 for TS01

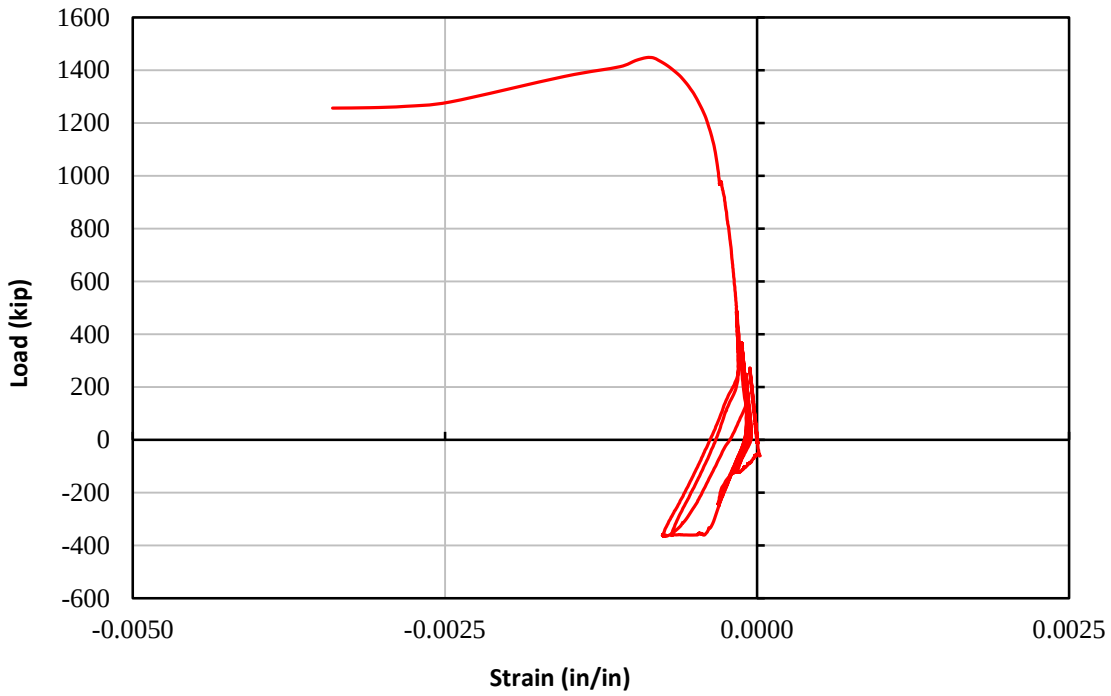

Figure 4-52: Strain gage H2-R3-2 for TS01

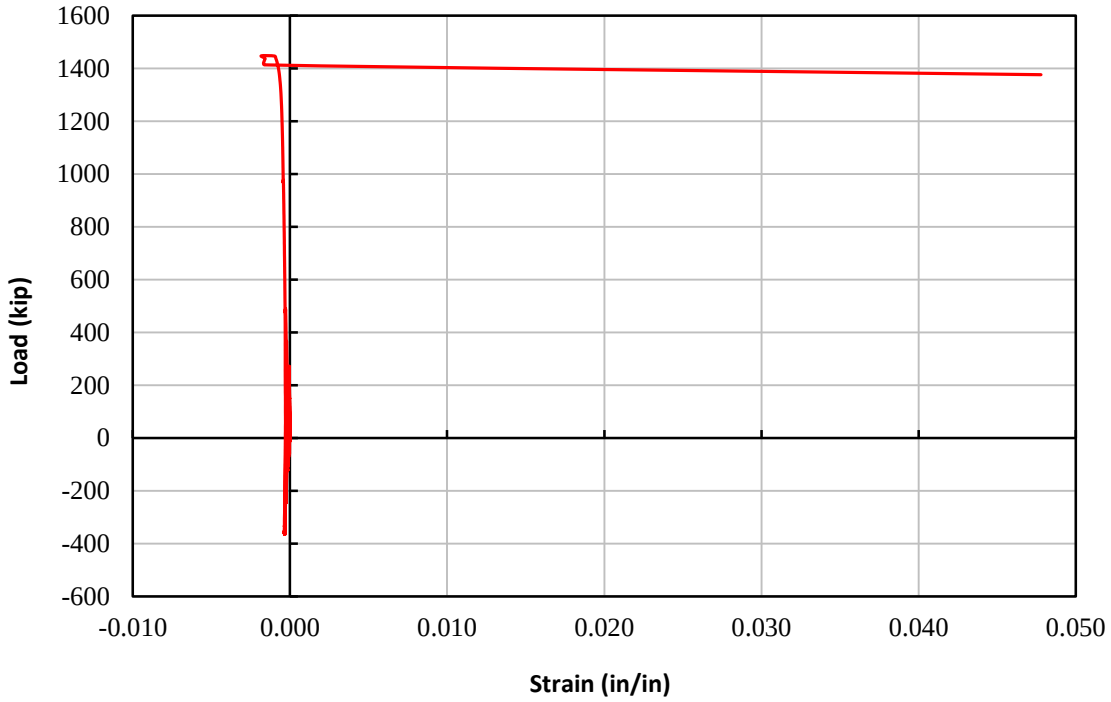

Figure 4-53: Strain gage H2-R3-4 for TS01

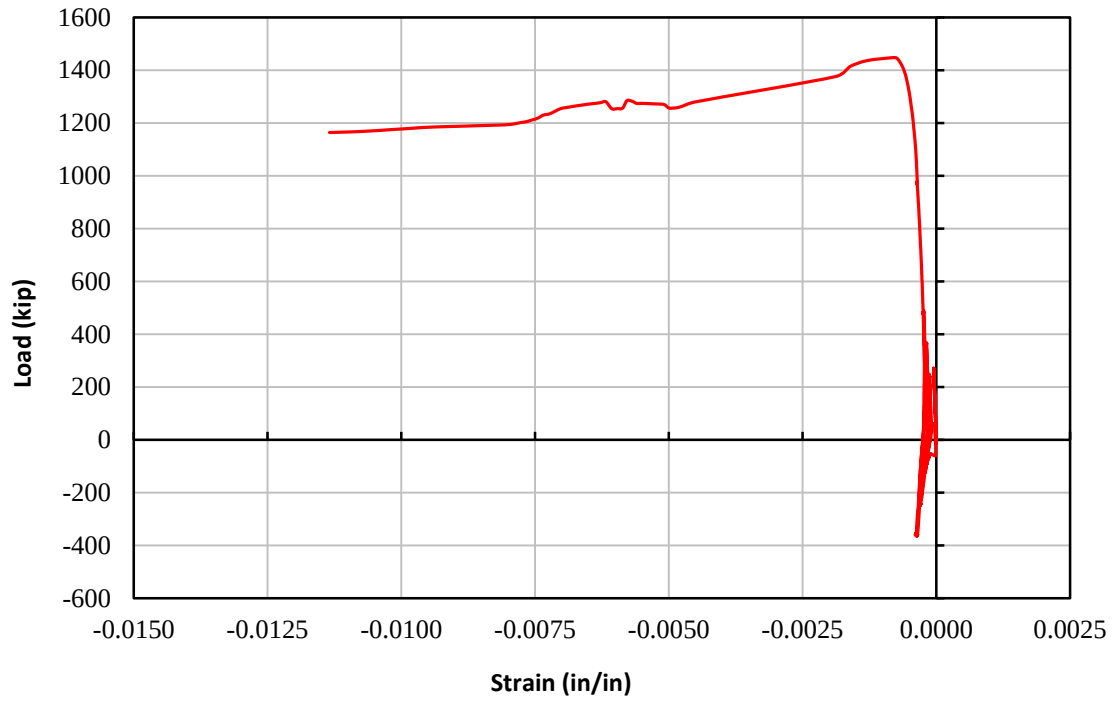

Figure 4-54: Strain gage H2-R3-6 for TS01

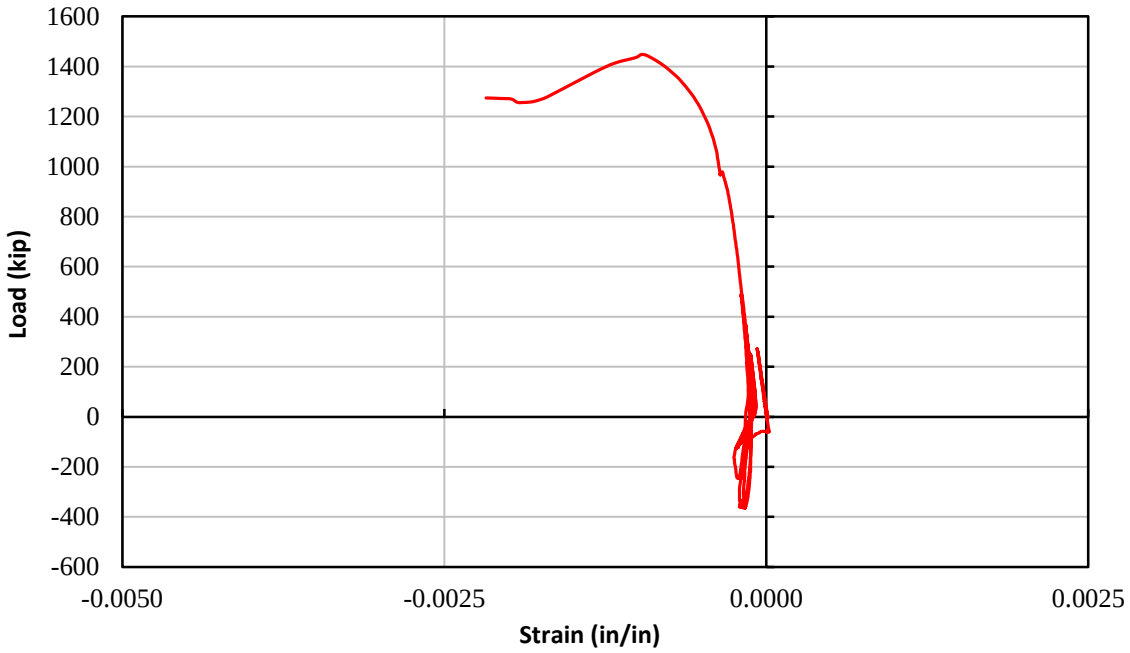

Figure 4-55: Strain gage H3-R3-1 for TS01

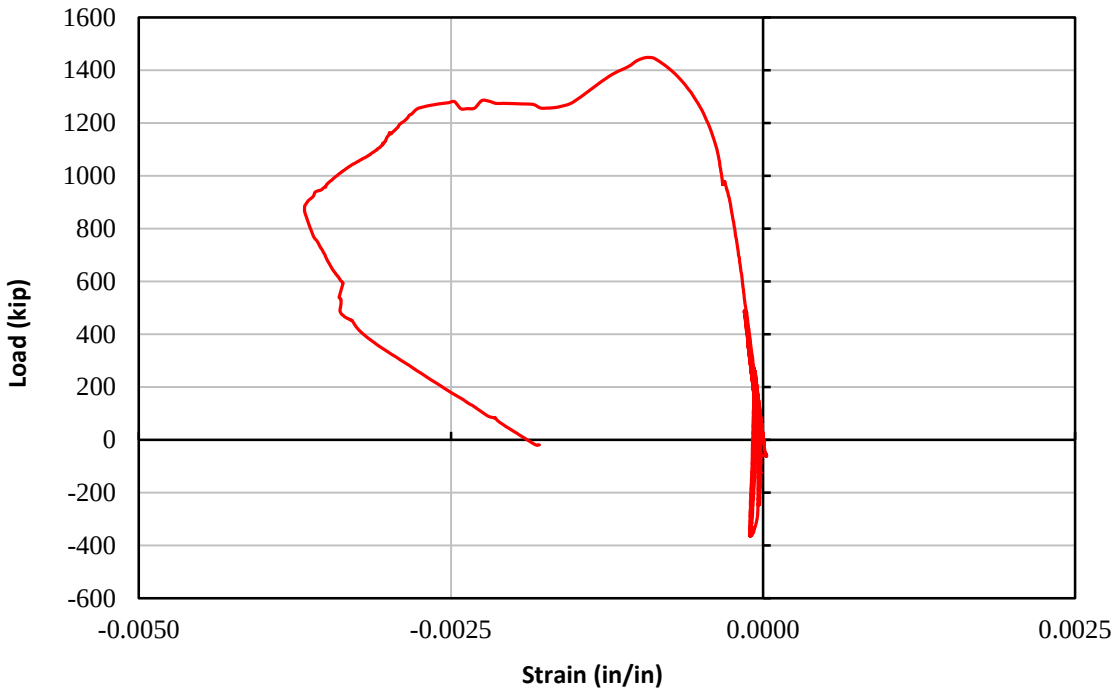

Figure 4-56: Strain gage H3-R3-2 for TS01

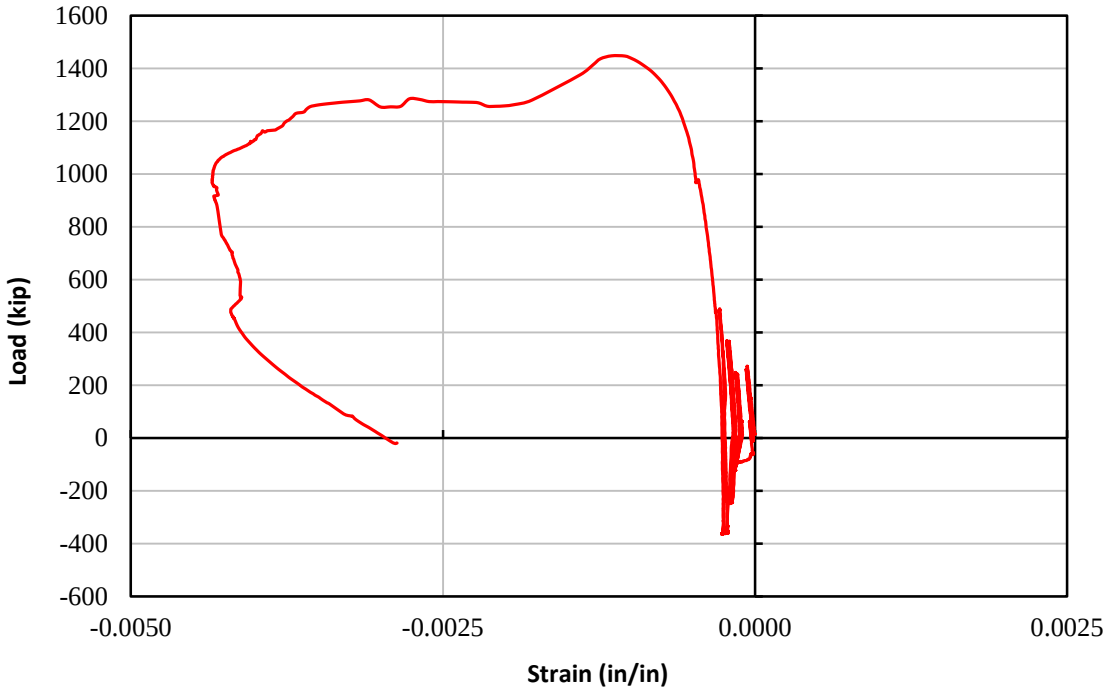

Figure 4-57: Strain gage H3-R3-3 for TS01

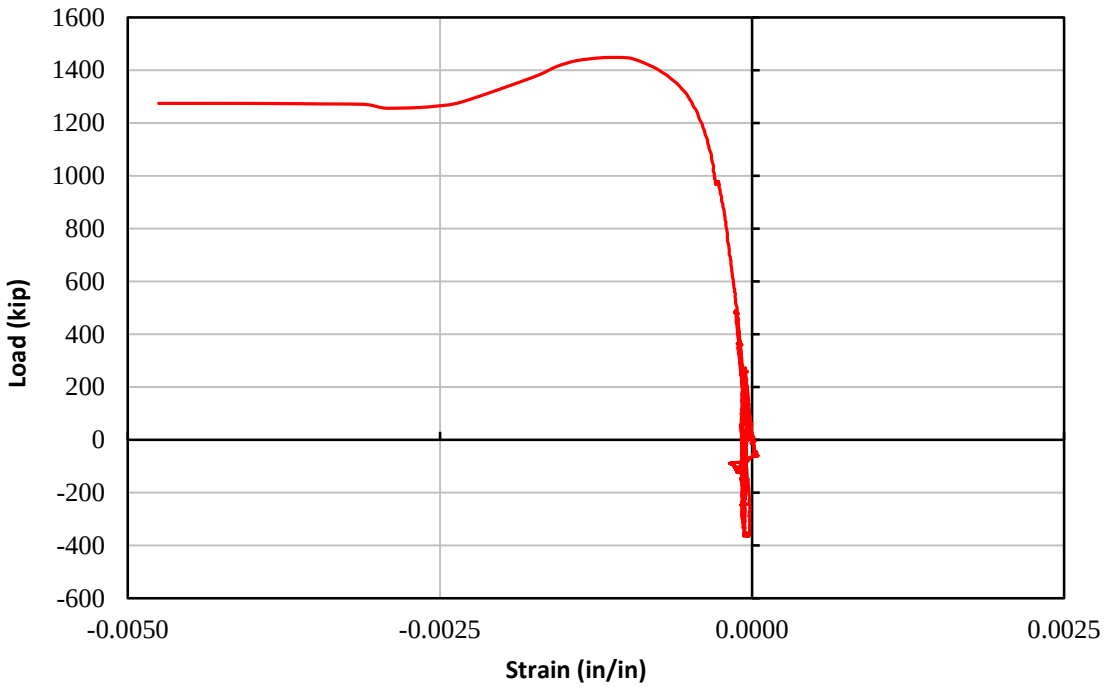

Figure 4-58: Strain gage H3-R3-4 for TS01

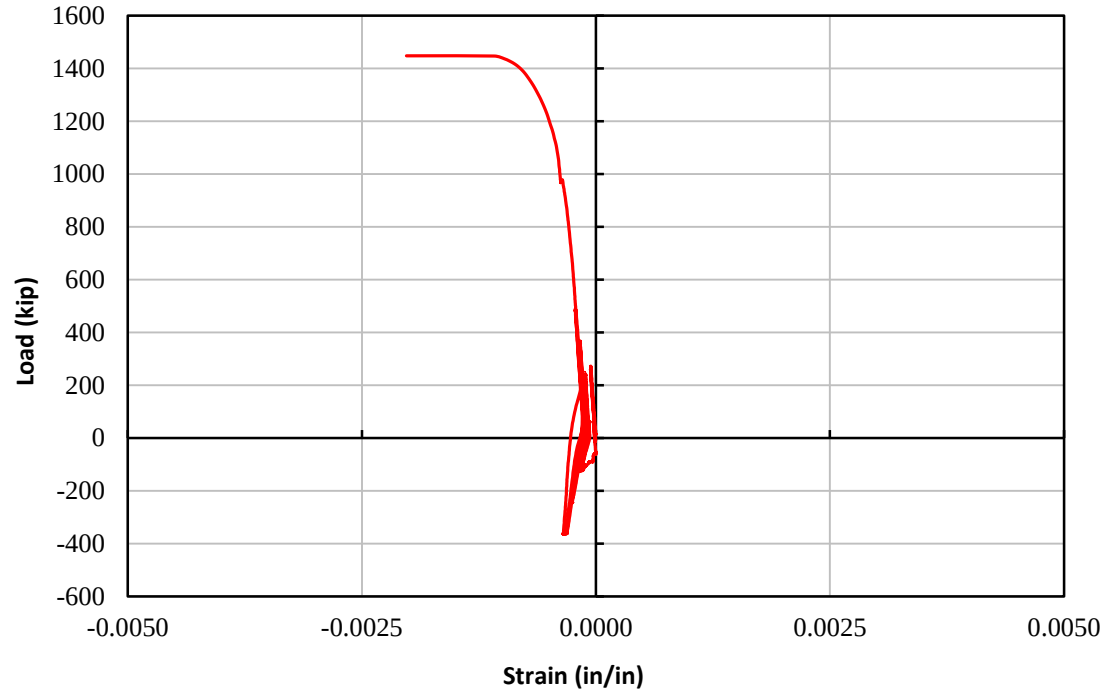

Figure 4-59: Strain gage H3-R3-5 for TS01

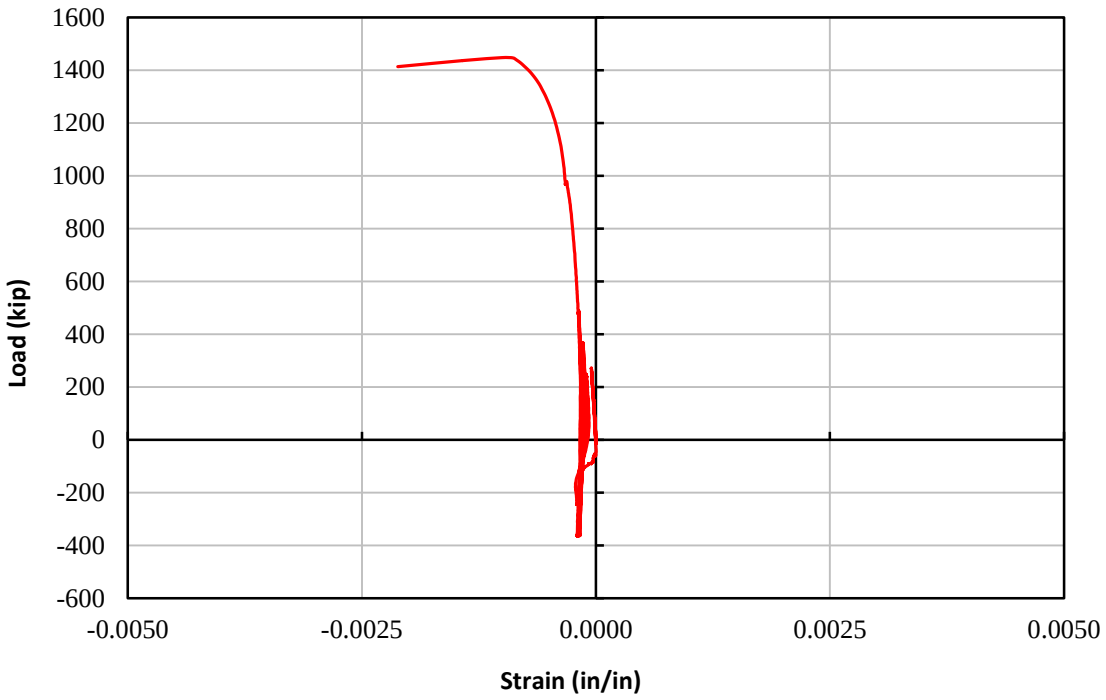

Figure 4-60: Strain gage H3-R3-6 for TS01

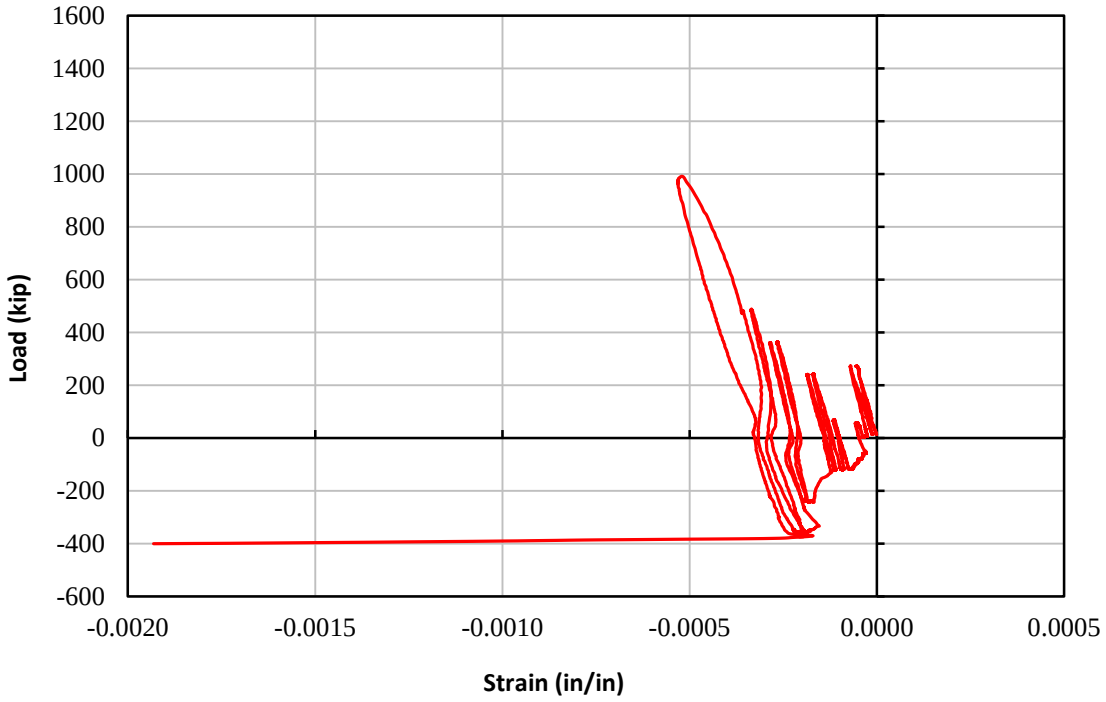

Figure 4-61: Strain gage H1-R3-1 for TS02

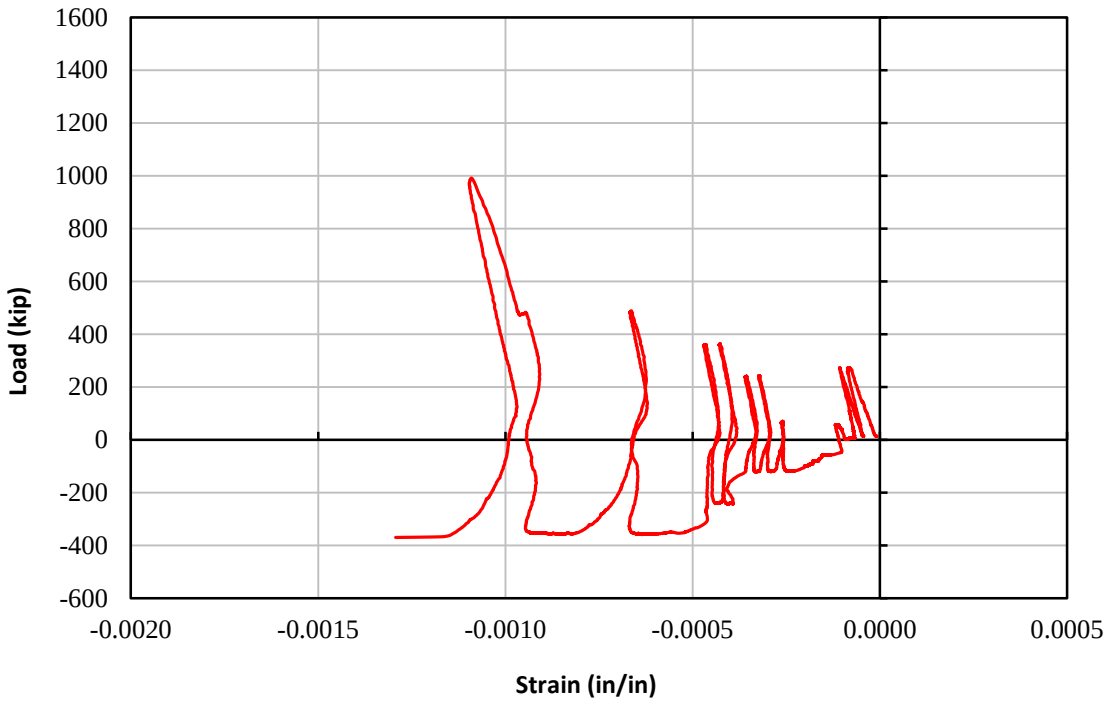

Figure 4-62: Strain gage H1-R3-2 for TS02

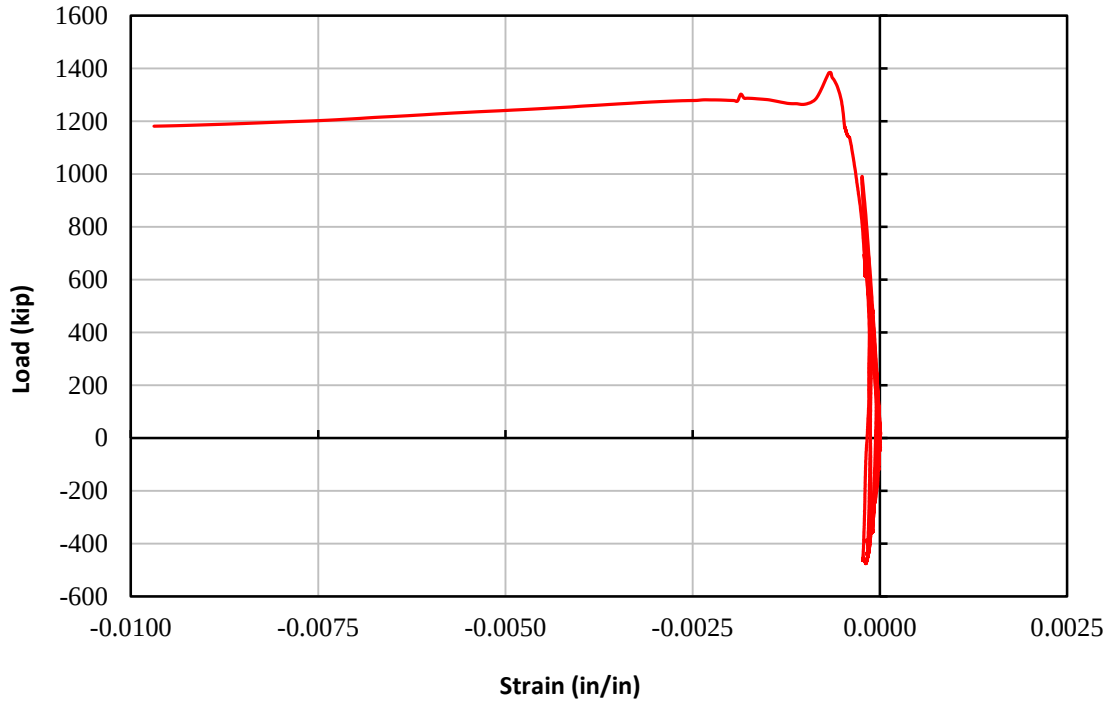

Figure 4-63: Strain gage H1-R3-3 for TS02

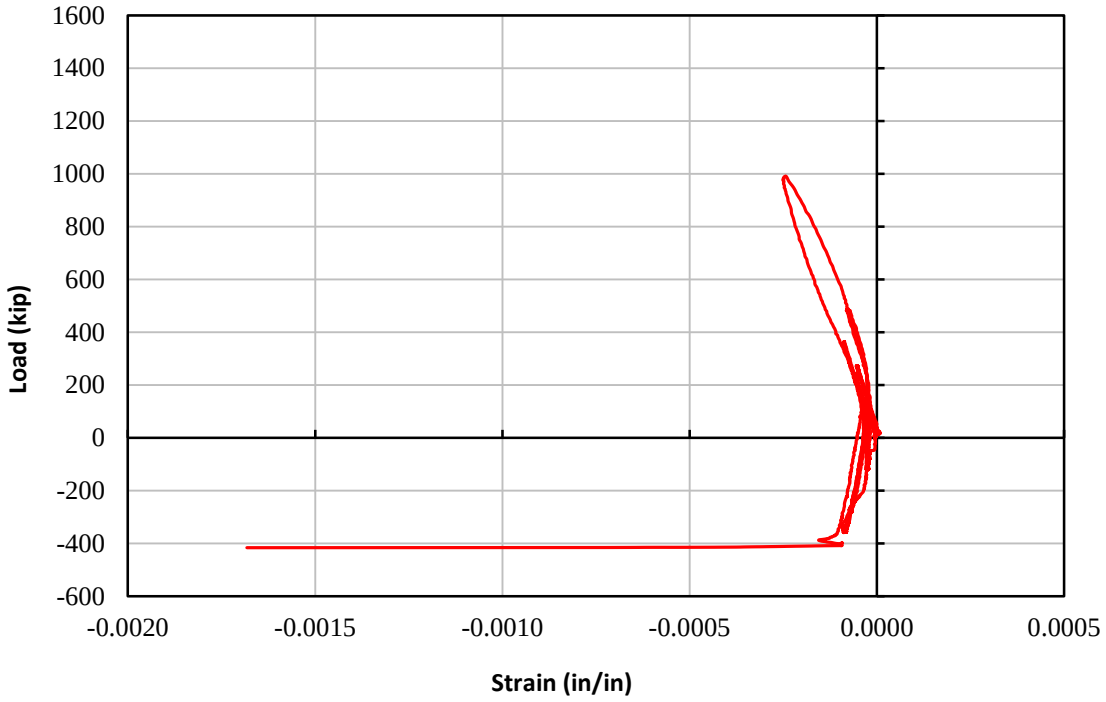

Figure 4-64: Strain gage H1-R3-4 for TS02

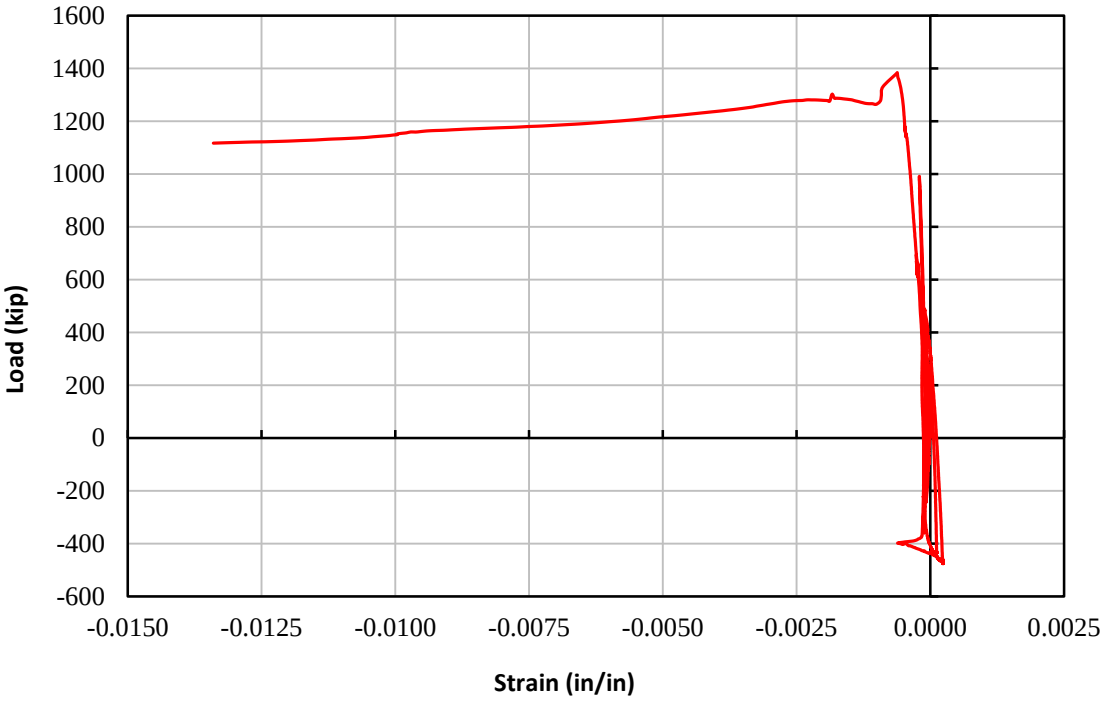

Figure 4-65: Strain gage H1-R3-5 for TS02

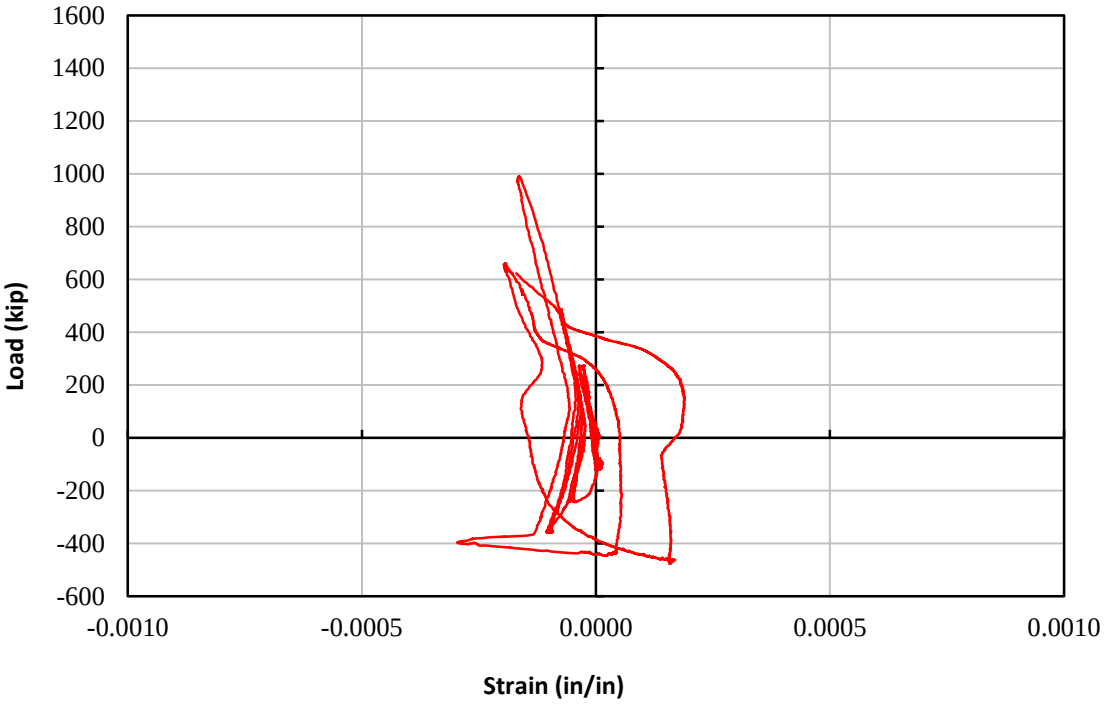

Figure 4-66: Strain gage H1-R3-6 for TS02

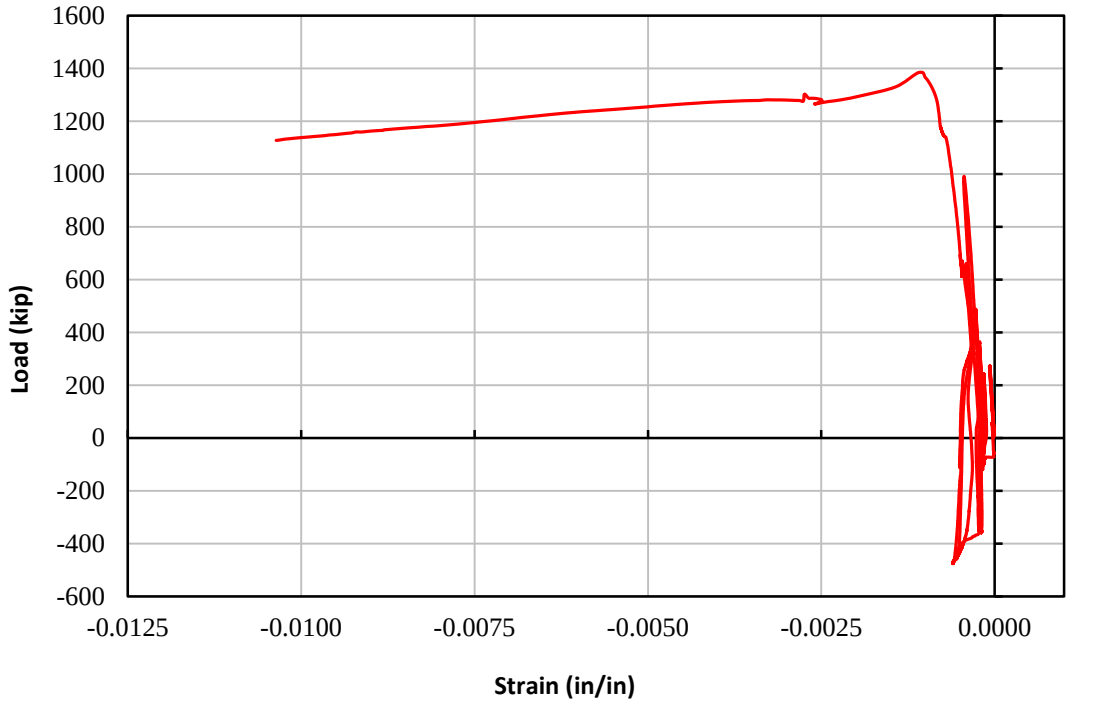

Figure 4-67: Strain gage H2-R3-1 for TS02

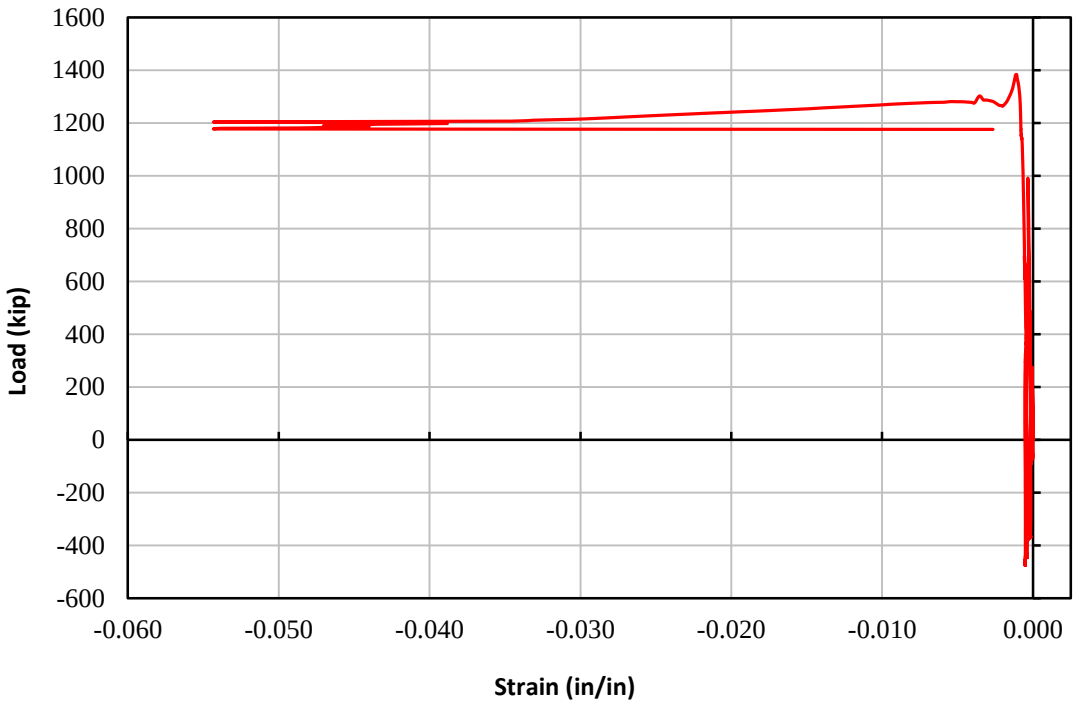

Figure 4-68: Strain gage H2-R3-2 for TS02

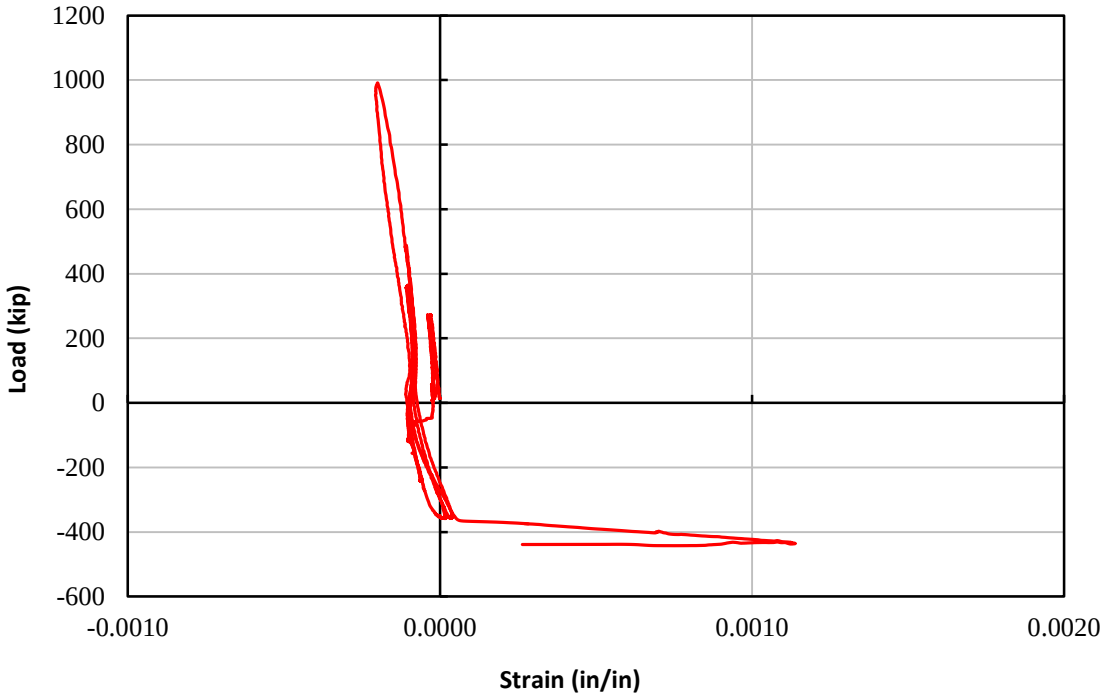

Figure 4-69: Strain gage H2-R3-4 for TS02

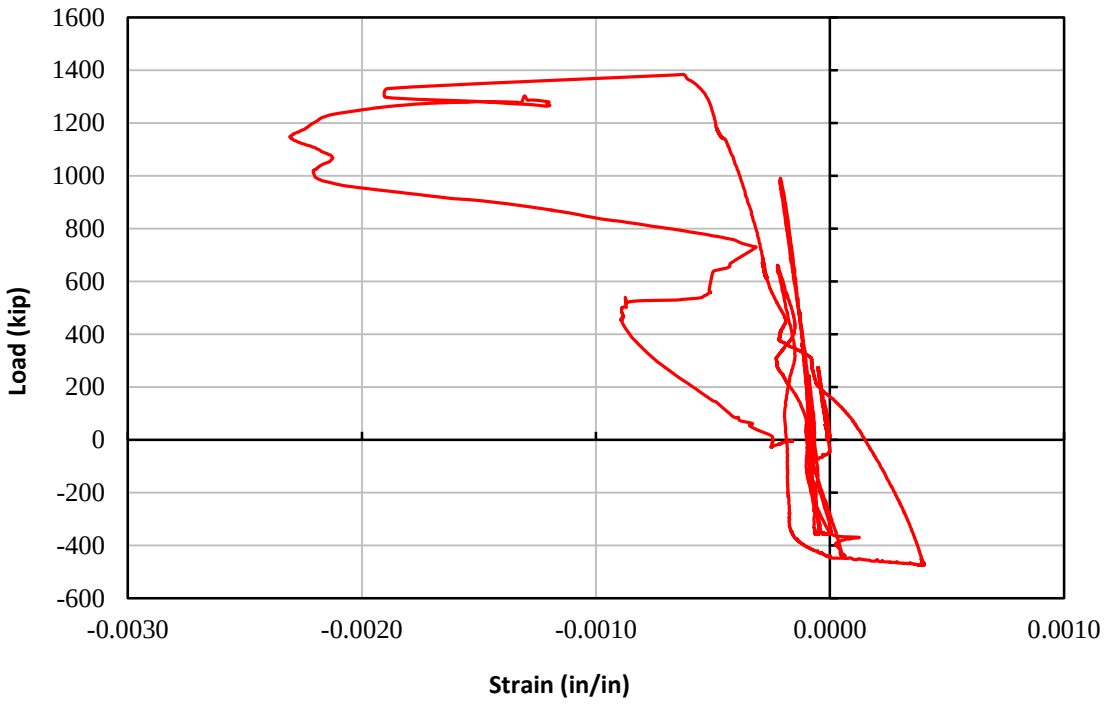

Figure 4-70: Strain gage H2-R3-5 for TS02

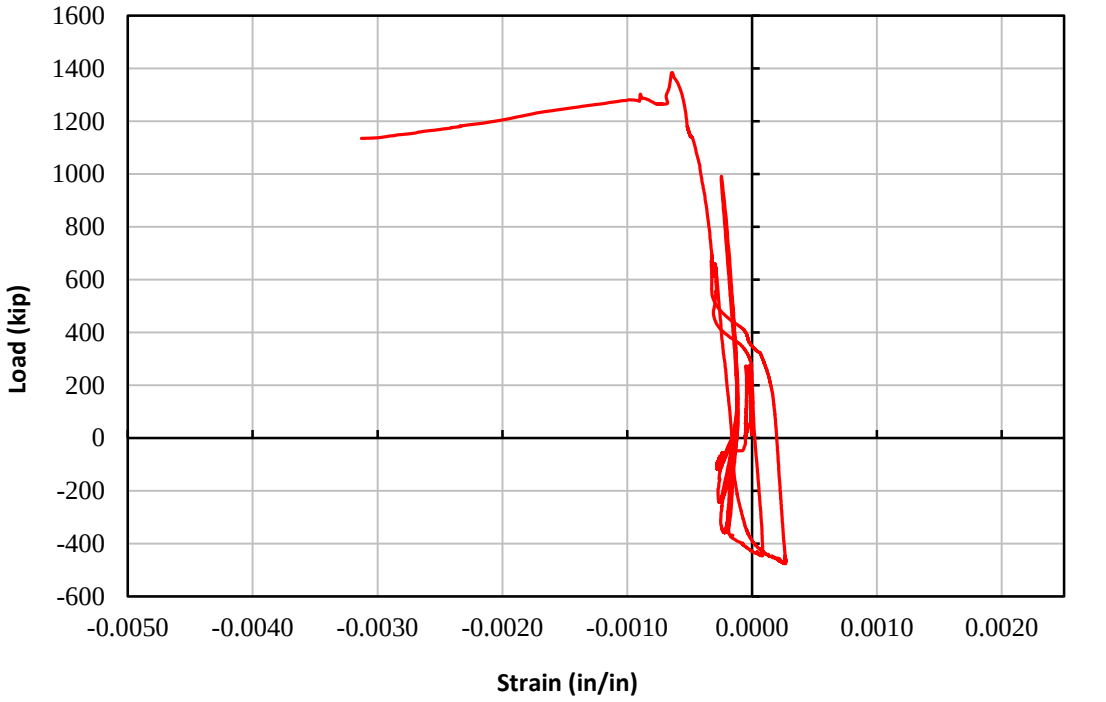

Figure 4-71: Strain gage H2-R3-6 for TS02

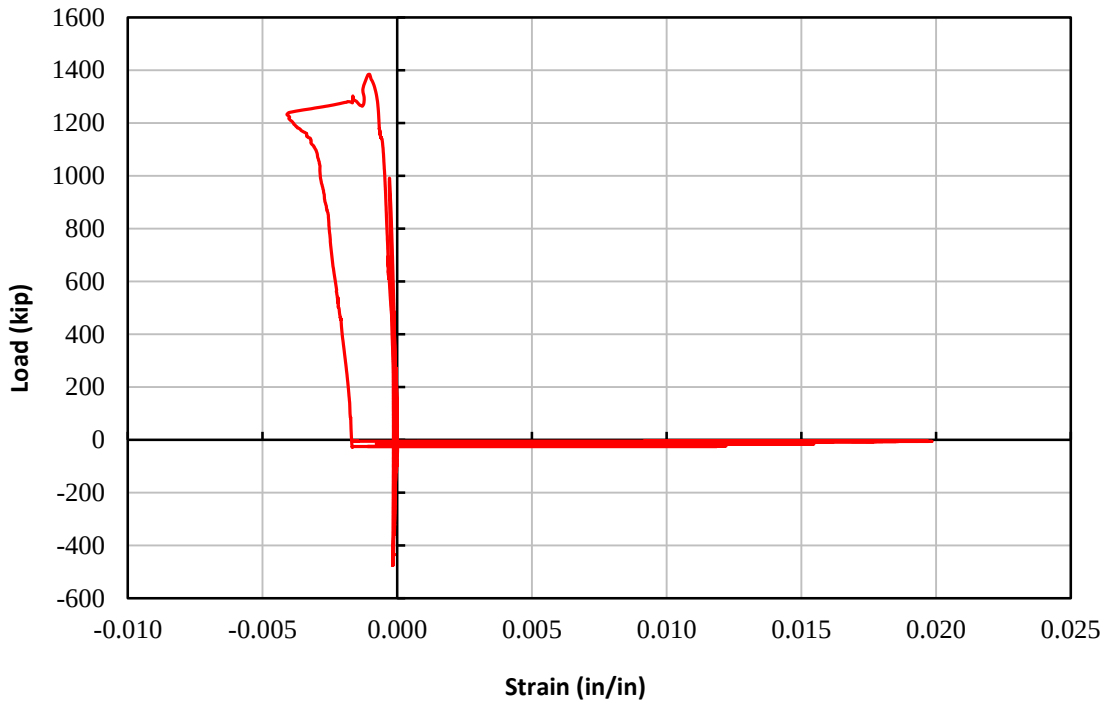

Figure 4-72: Strain gage H3-R3-1 for TS02

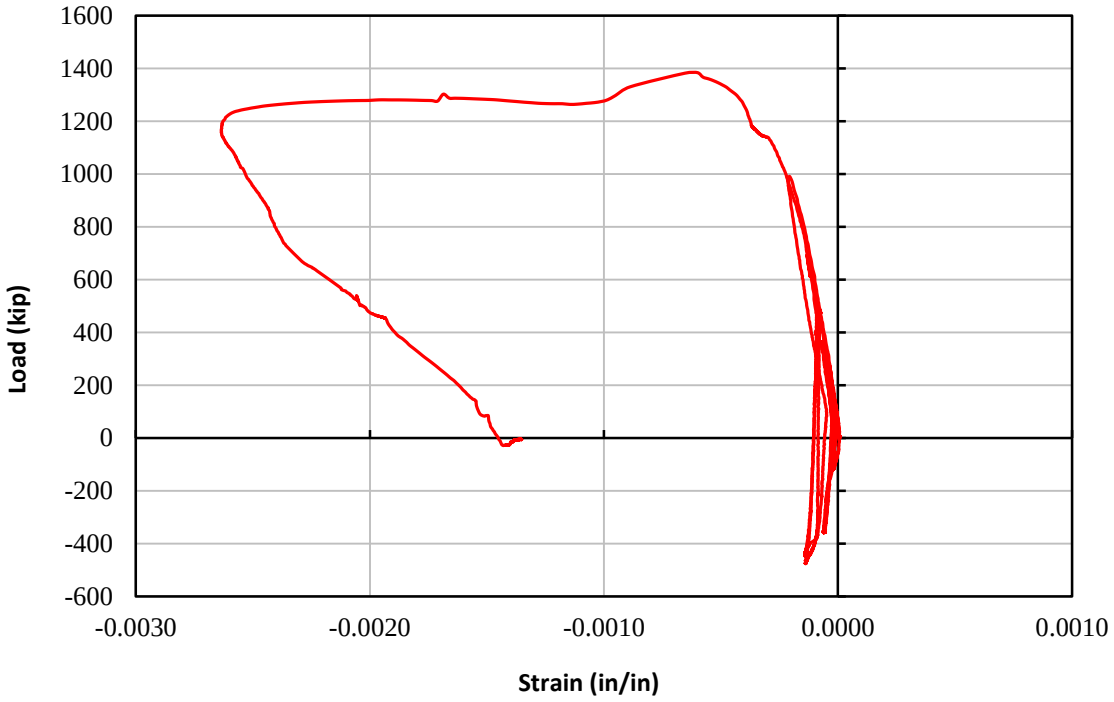

Figure 4-73: Strain gage H3-R3-2 for TS02

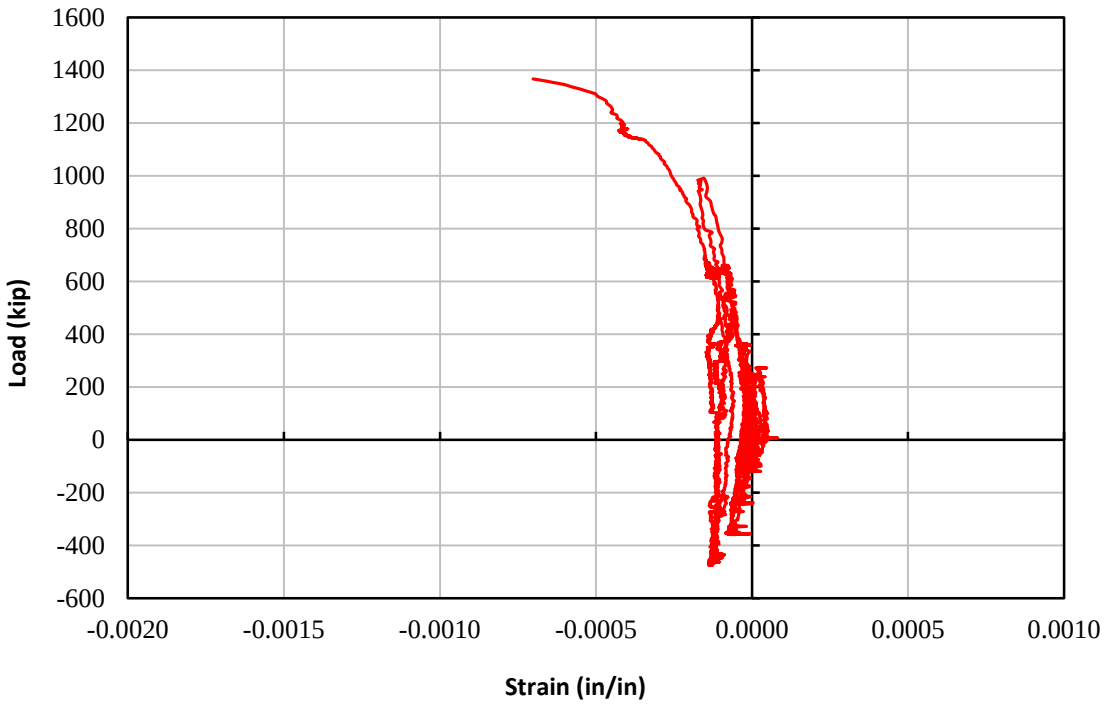

Figure 4-74: Strain gage H3-R3-4 for TS02

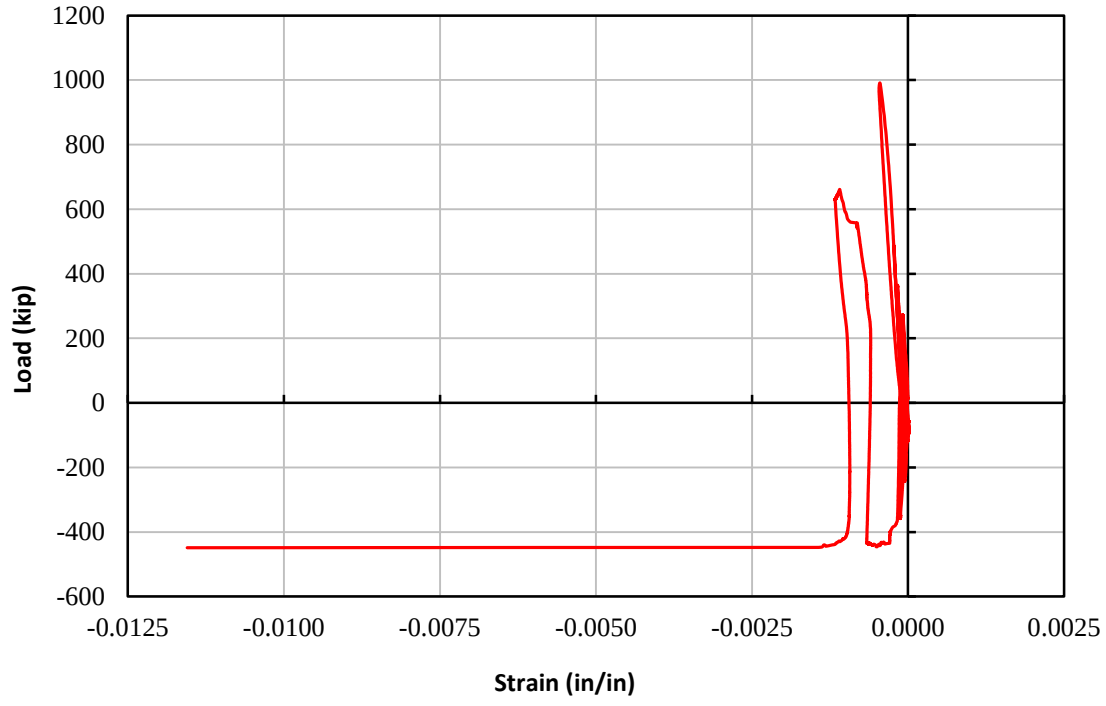

Figure 4-75: Strain gage H3-R3-5 for TS02

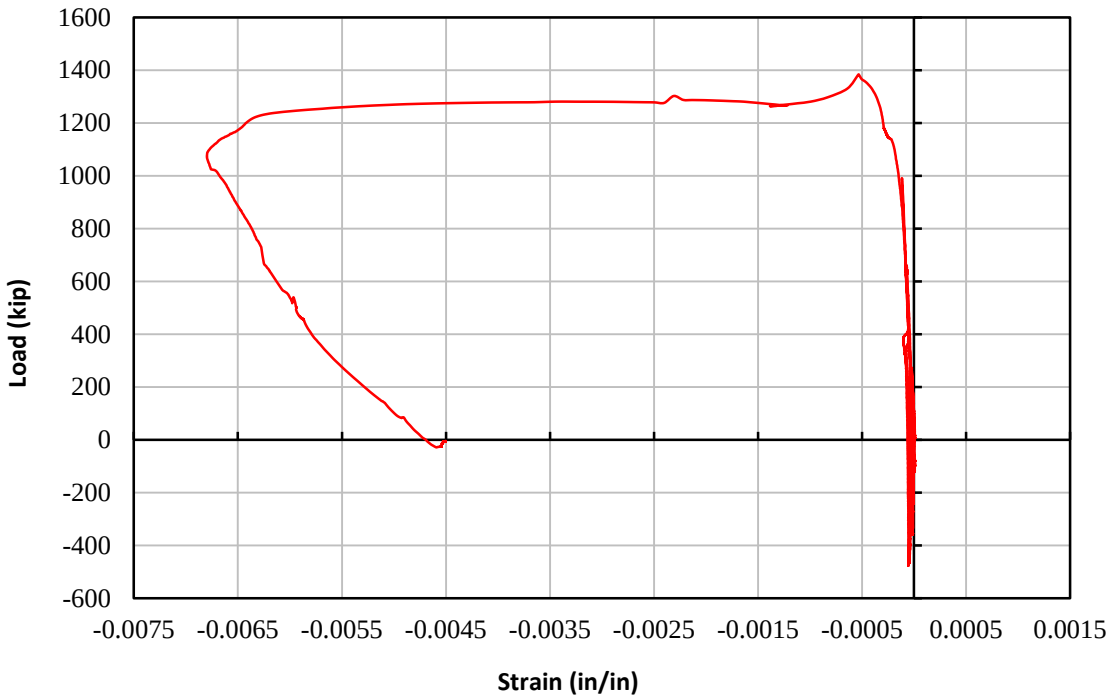

Figure 4-76: Strain gage H3-R3-6 for TS02

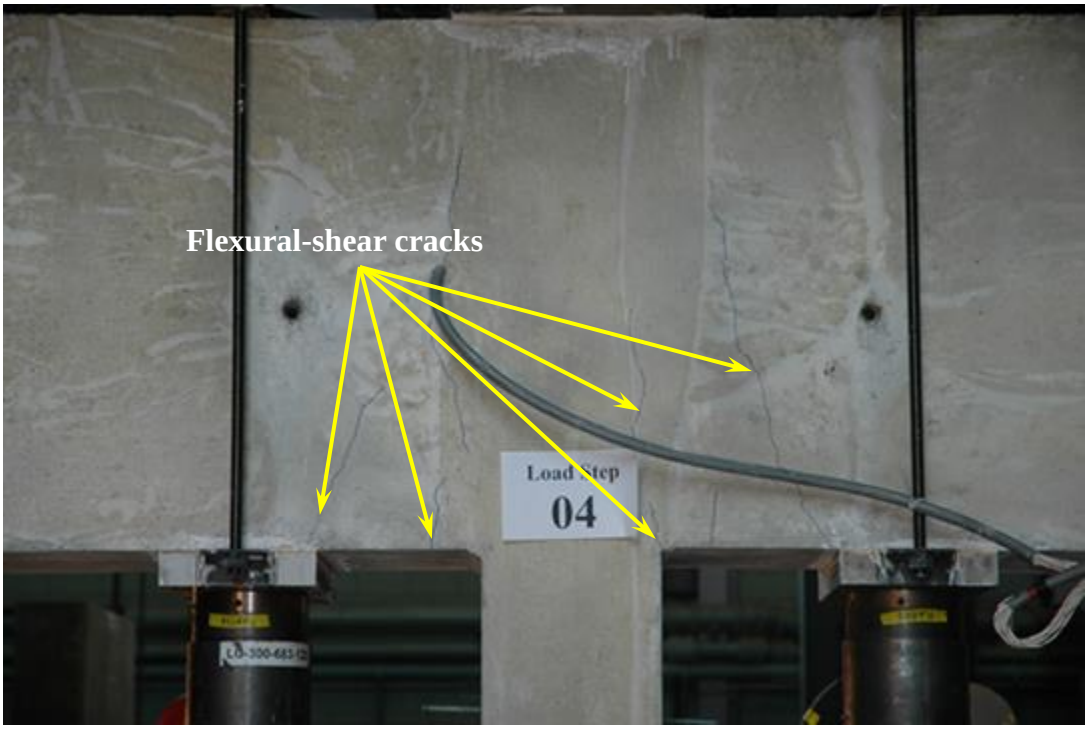

Figure 4-77: Flexural-shear cracks in top beam of TS01

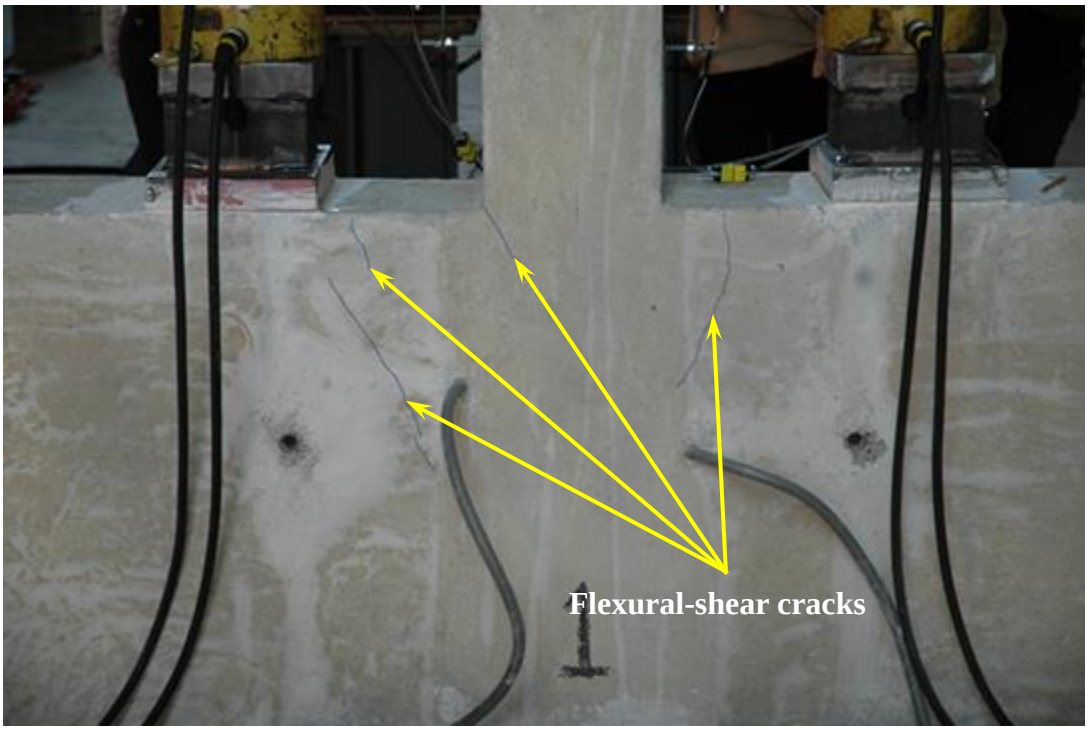

Figure 4-78: Flexural-shear cracks in bottom beam of TS01

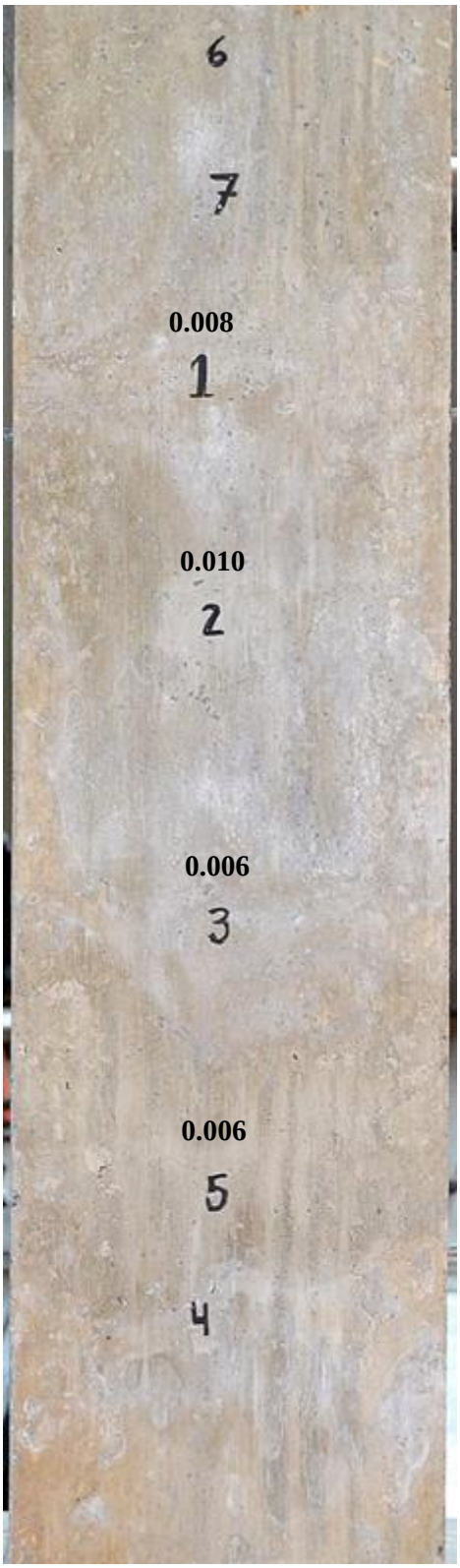

Figure 4-79: Cracks on east face of TS01 at Load Step 13

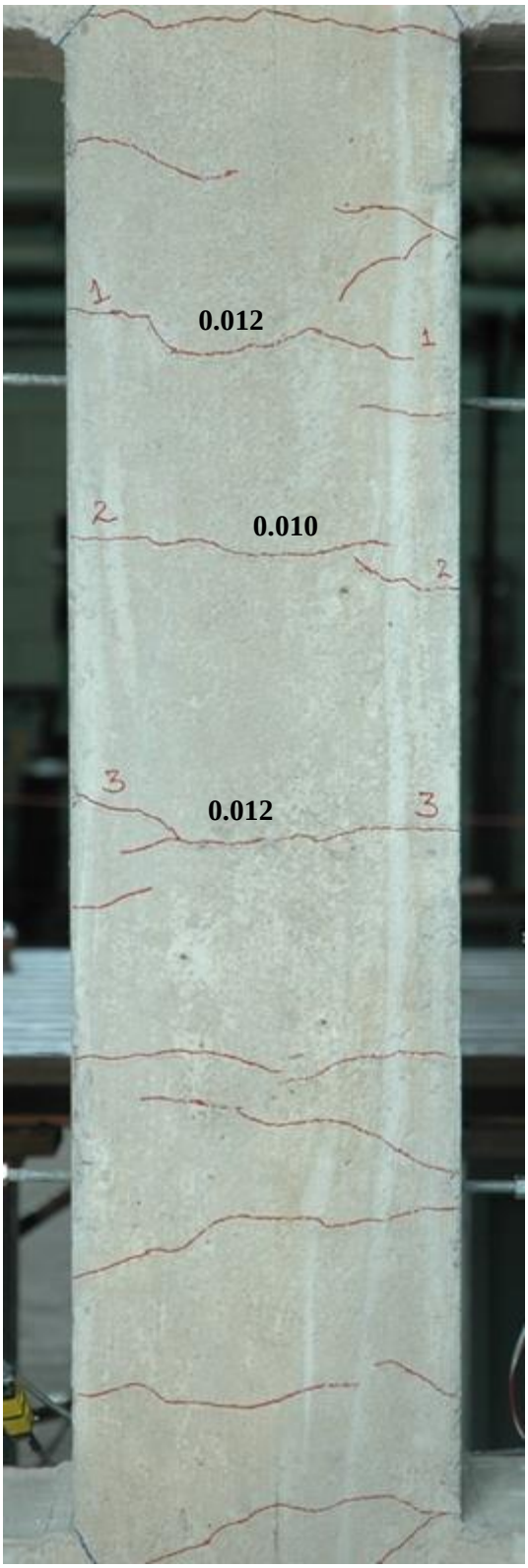

Figure 4-80: Cracks on west face of TS01 at Load Step 15

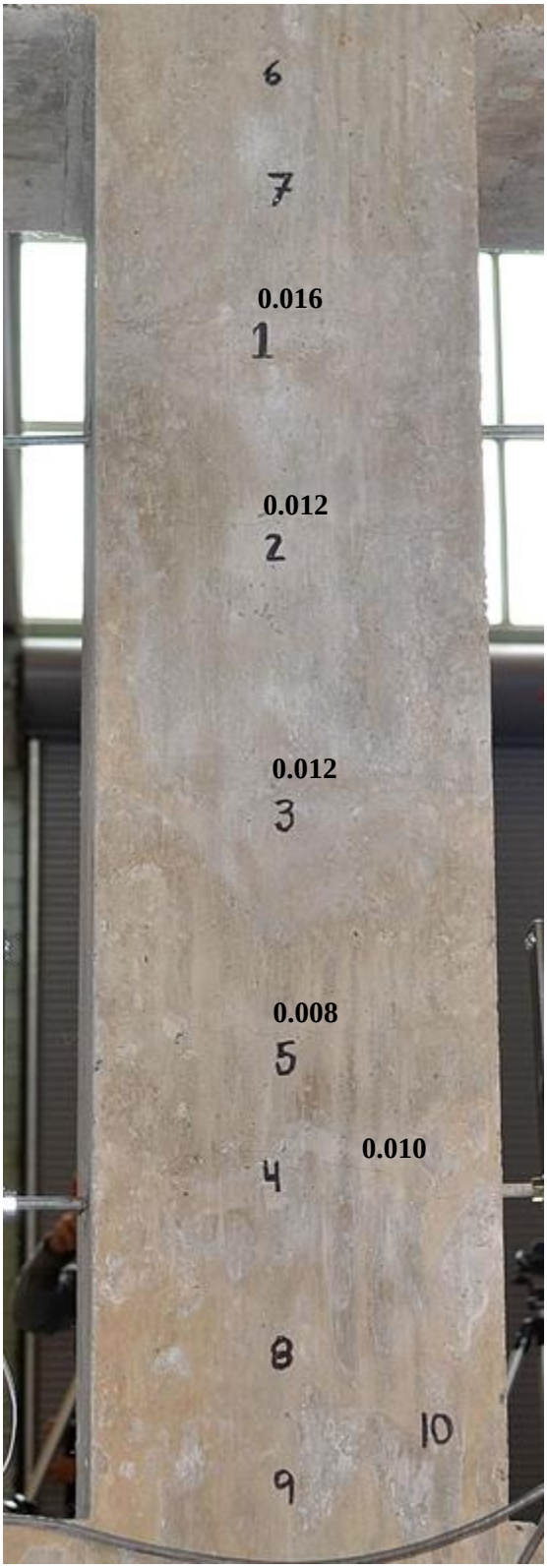

Figure 4-81: Cracks on east face of TS01 at Load Step 15

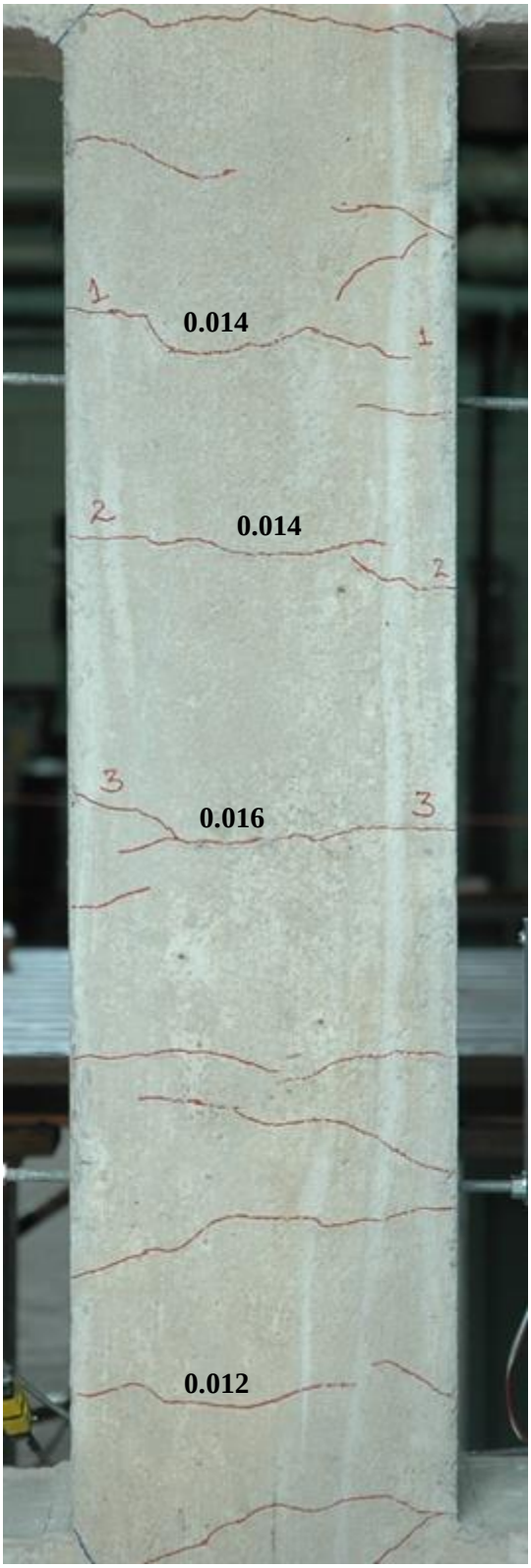

Figure 4-82: Cracks on west face of TS01 at Load Step 17

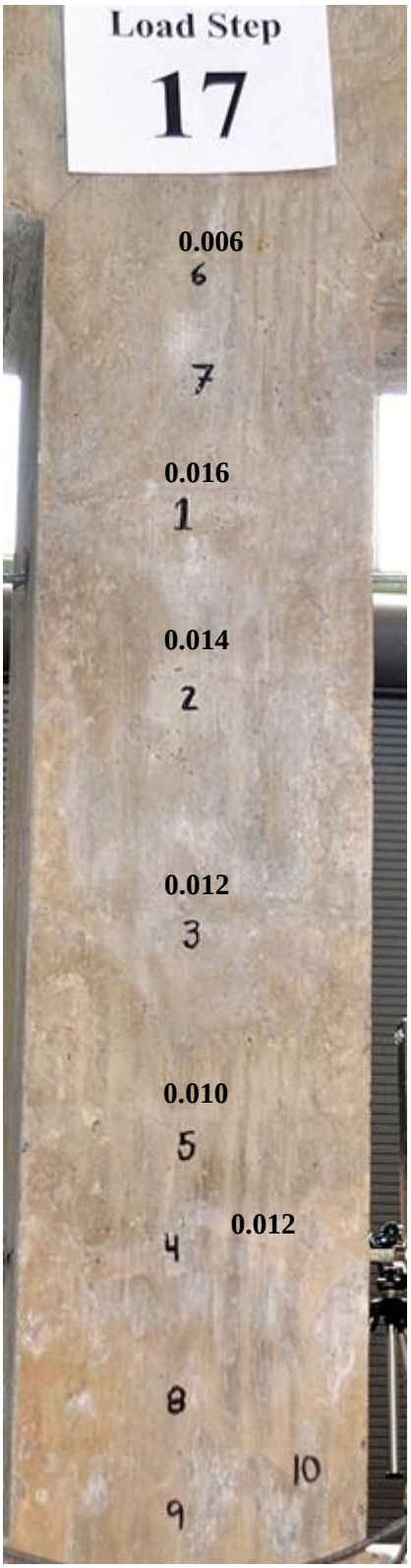

Figure 4-83: Cracks on east face of TS01 at Load Step 17

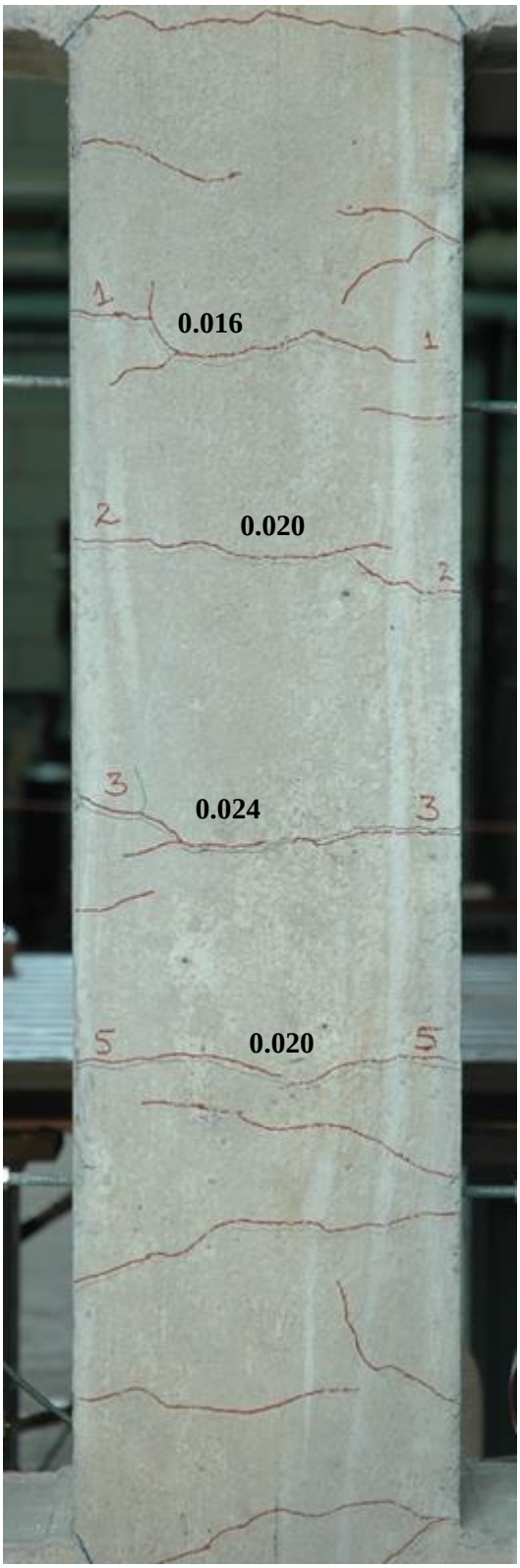

Figure 4-84: Cracks on west face of TS01 at Load Step 19

Figure 4-85: Cracks on east face of TS01 at Load Step 19

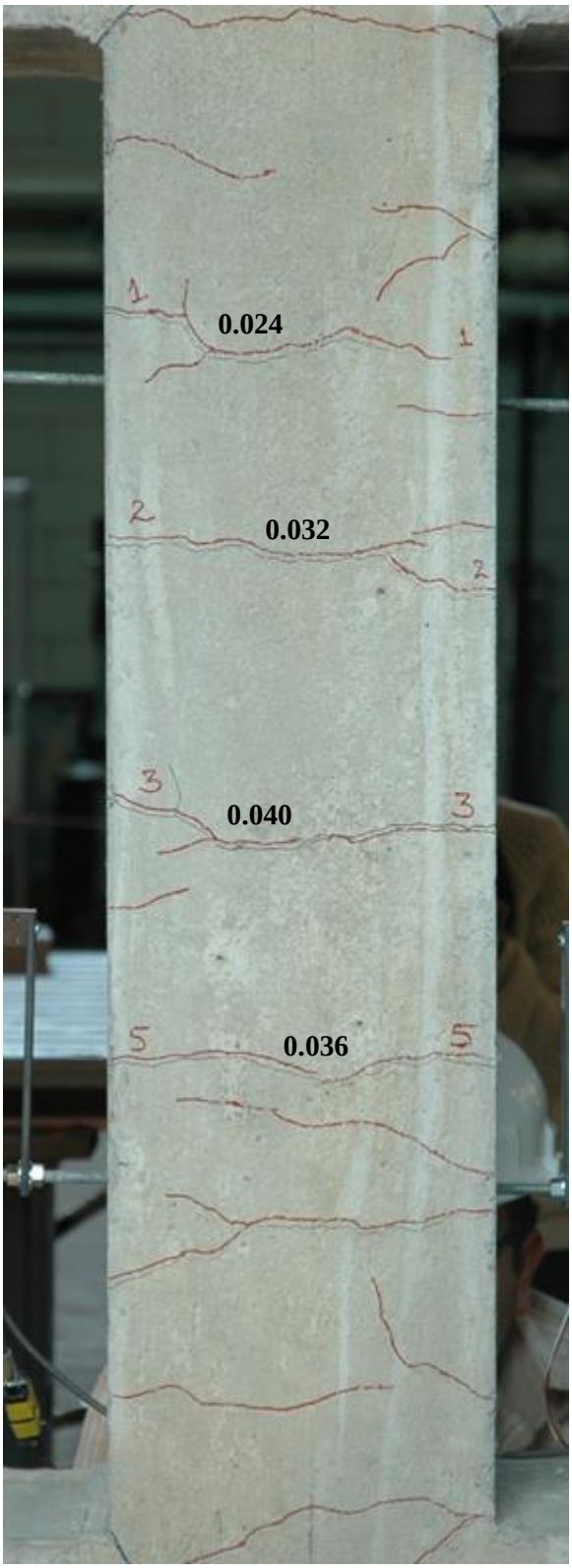

Figure 4-86: Cracks on west face of TS01 at Load Step 21

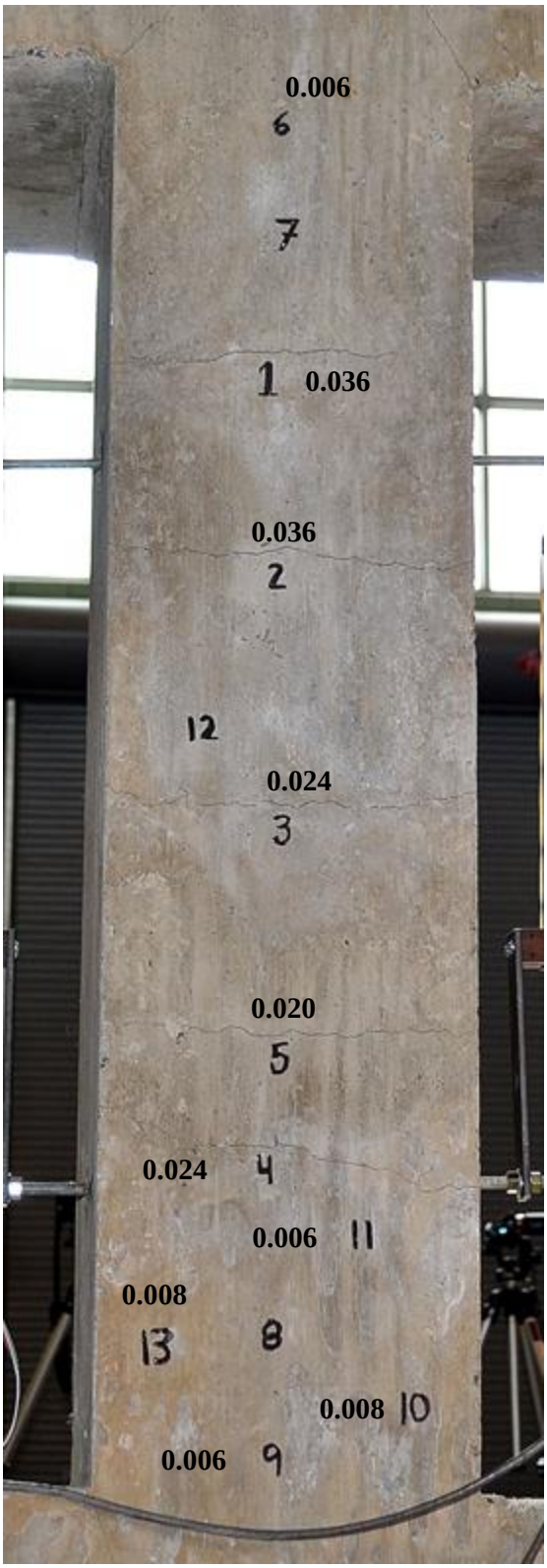

Figure 4-87: Cracks on east face of TS01 at Load Step 21

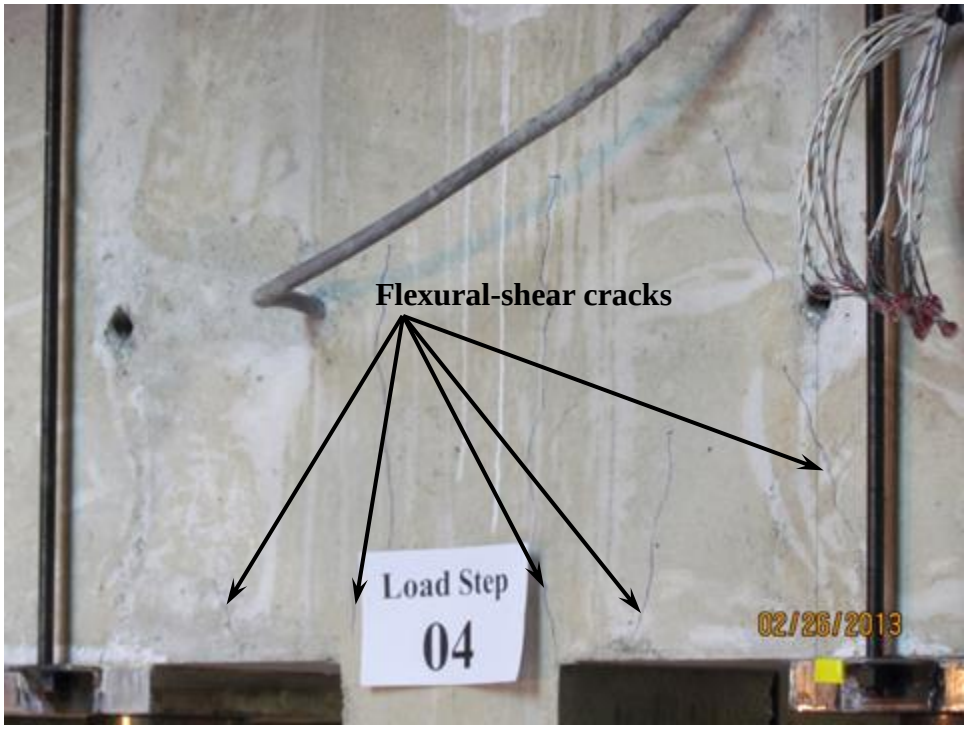

Figure 4-88: Flexural-shear cracks in top beam of TS02

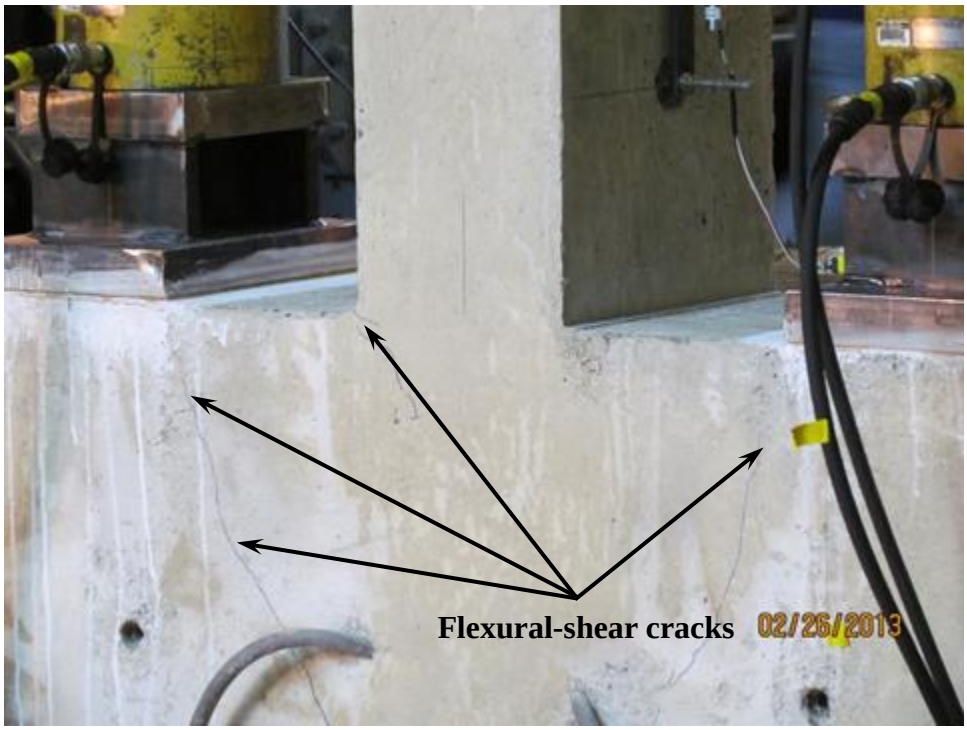

Figure 4-89: Flexural-shear cracks in bottom beam of TS02

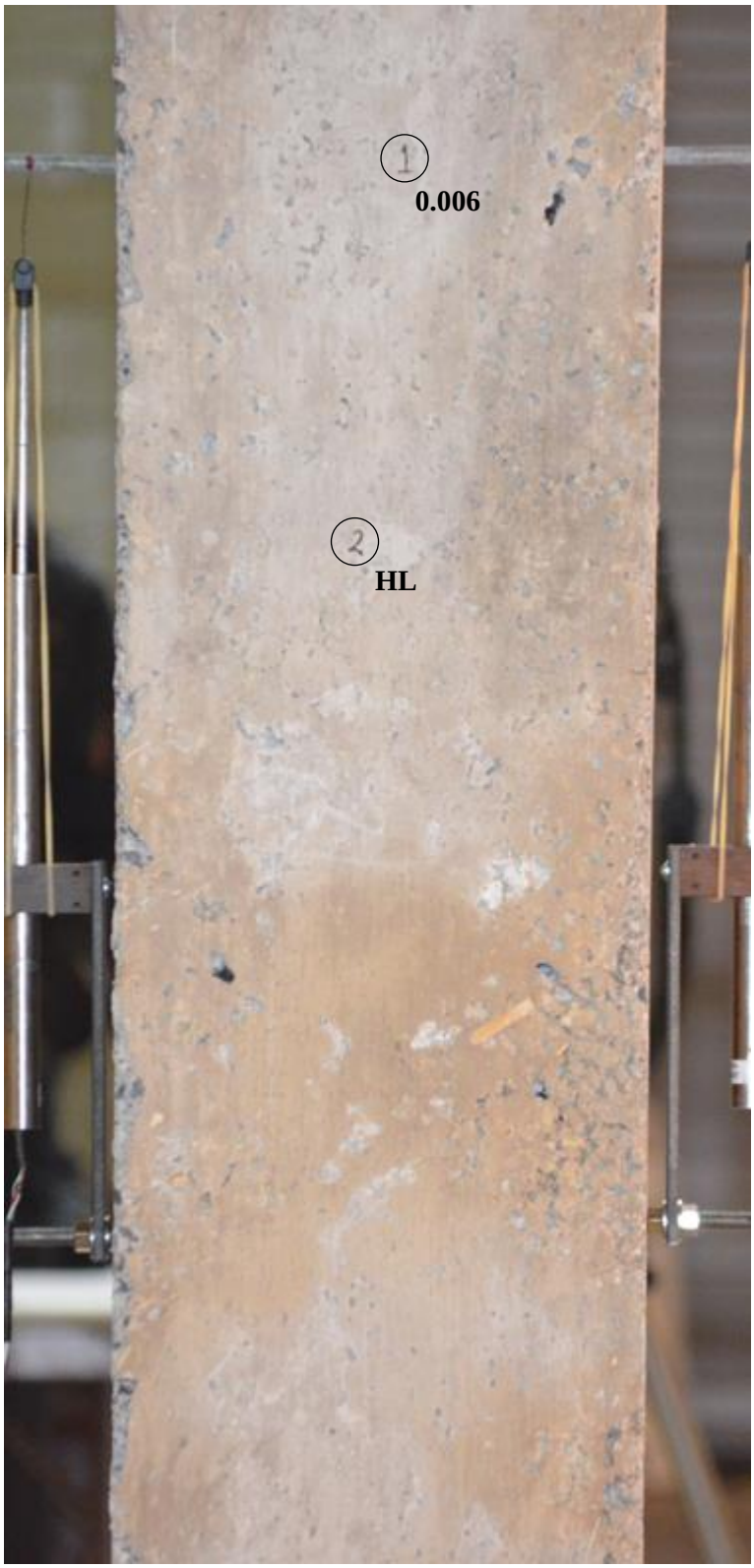

Figure 4-90: Cracks on west face of TS02 at Load Step 07

Figure 4-91: Cracks on east face of TS02 at Load Step 08

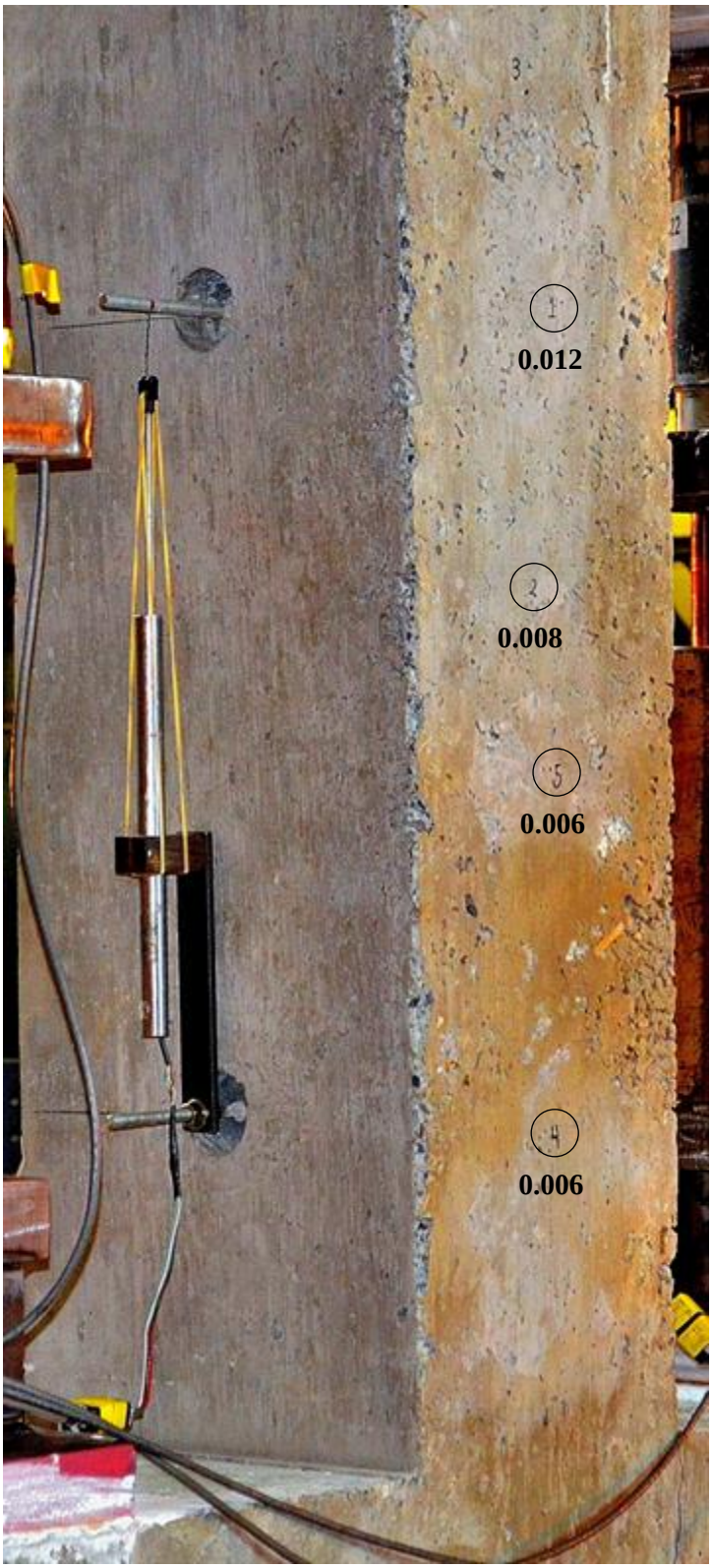

Figure 4-92: Cracks on west face of TS02 at Load Step 09

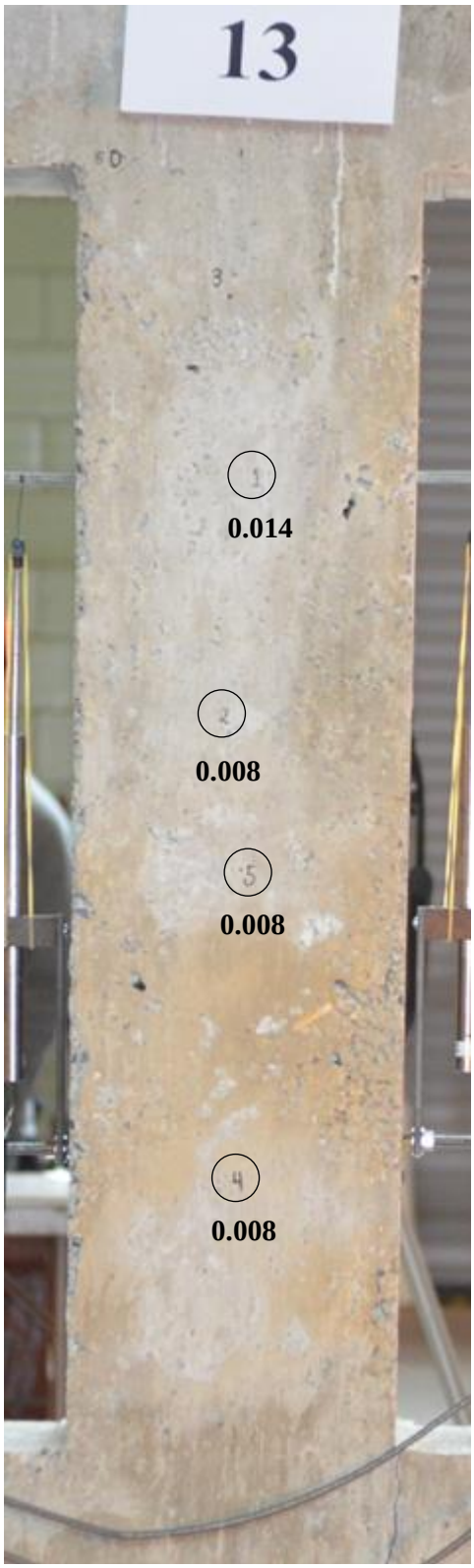

Figure 4-93: Cracks on east face of TS02 at Load Step 13

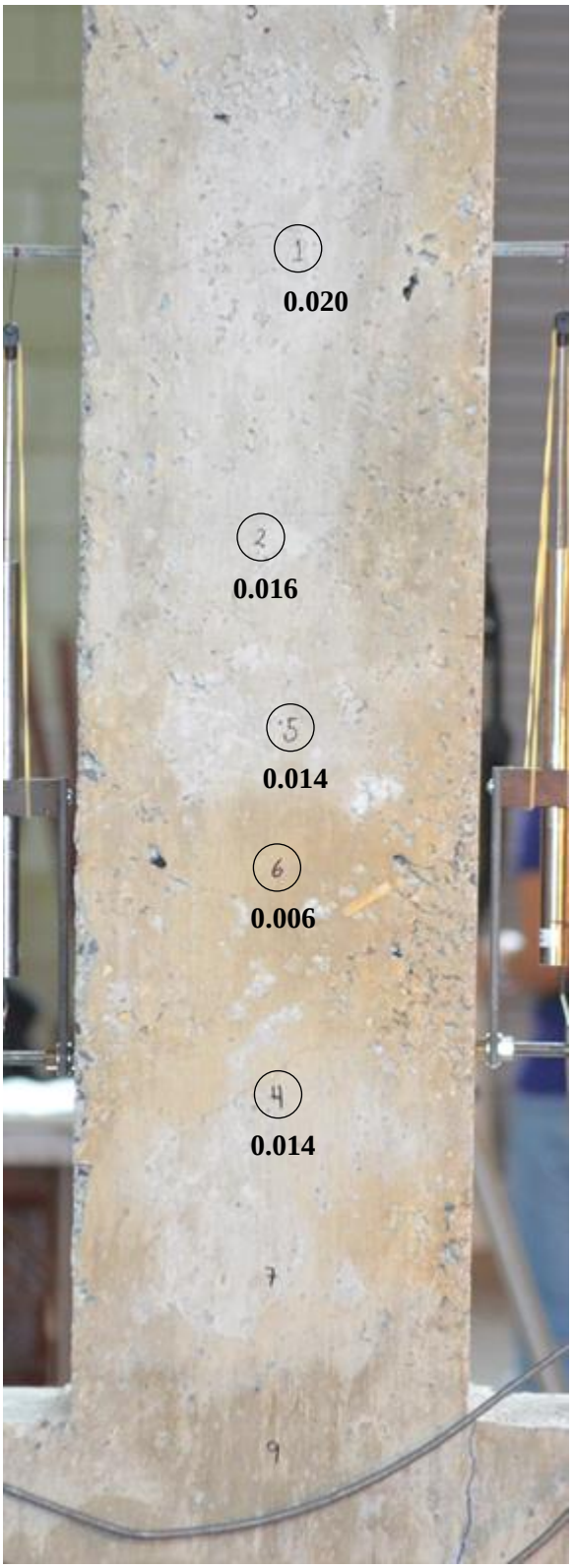

Figure 4-94: Cracks on east face of TS02 at Load Step 15

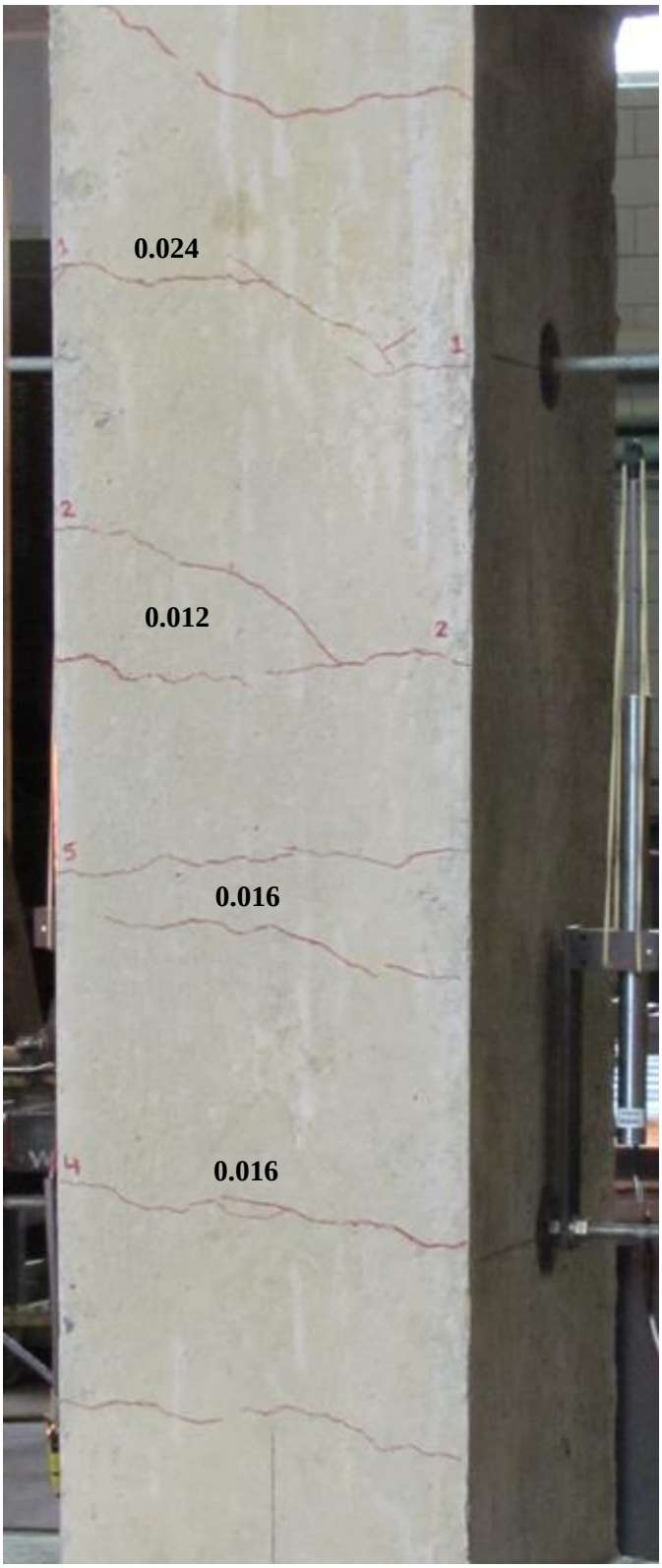

Figure 4-95: Cracks on west face of TS02 at Load Step 17

Figure 4-96: Cracks on east face of TS02 at Load Step 19

Figure 4-97: Cracks on west face of TS02 at Load Step 19

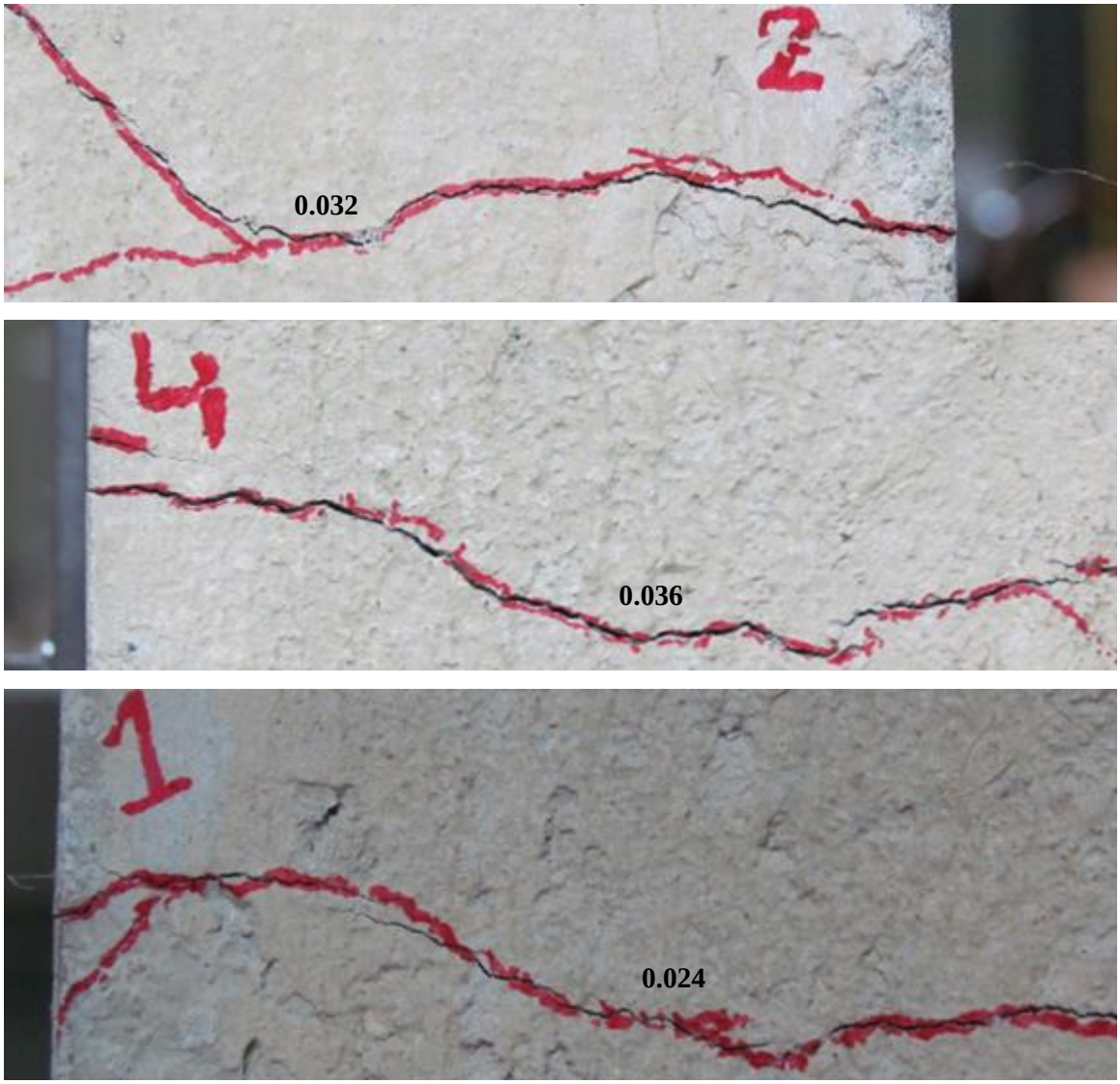

Figure 4-98: Cracks on west face of TS02 at Load Step 21

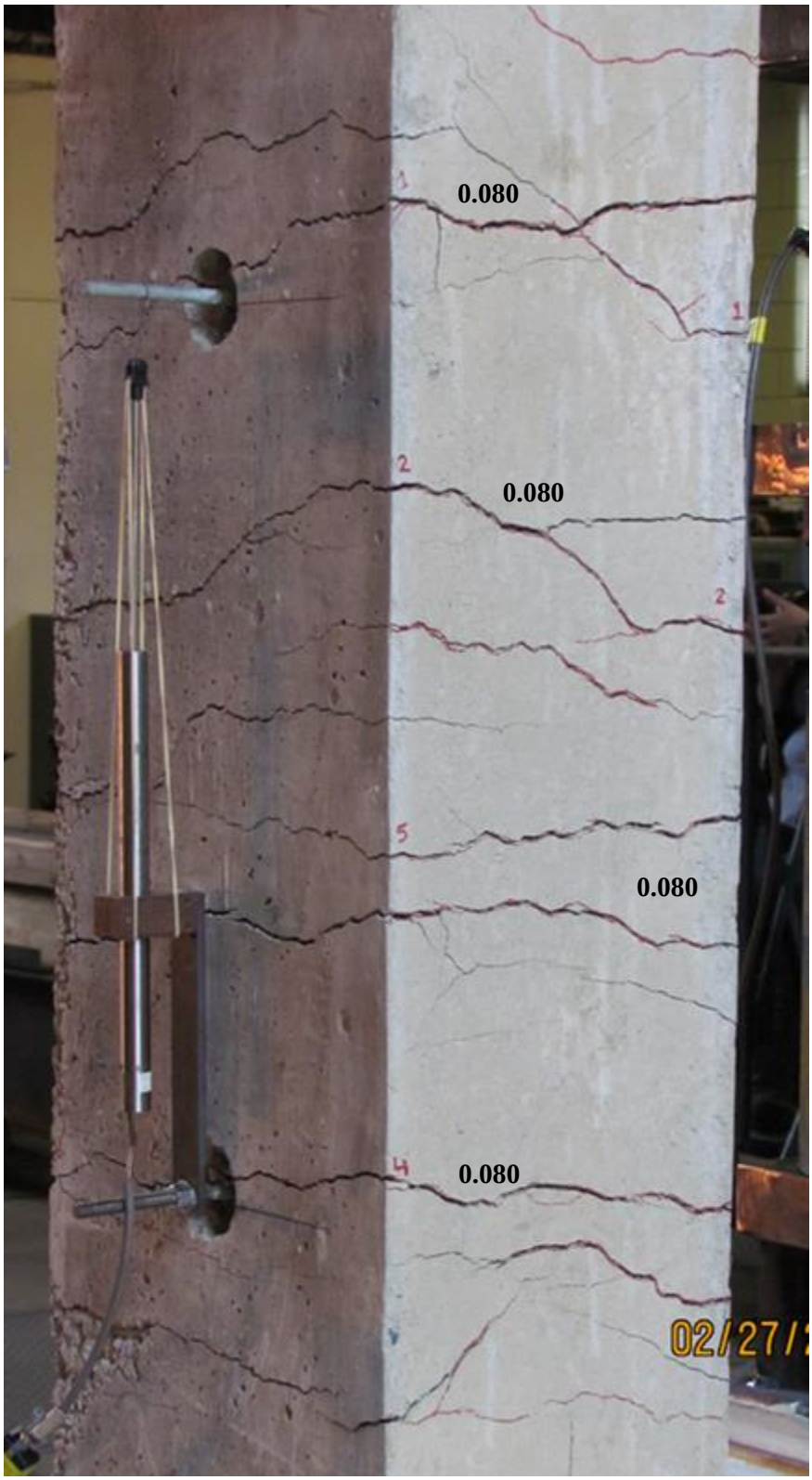

Figure 4-99: Cracks on north-west face of TS02 at Load Step 23

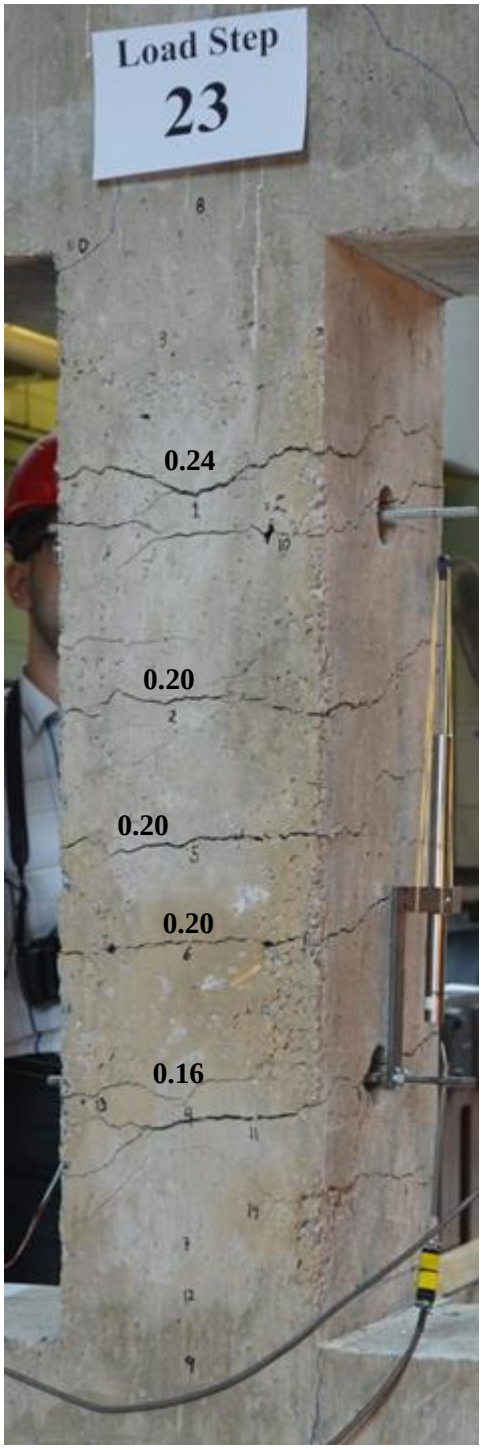

Figure 4-100: Cracks on north-west face of TS02 at Load Step 23

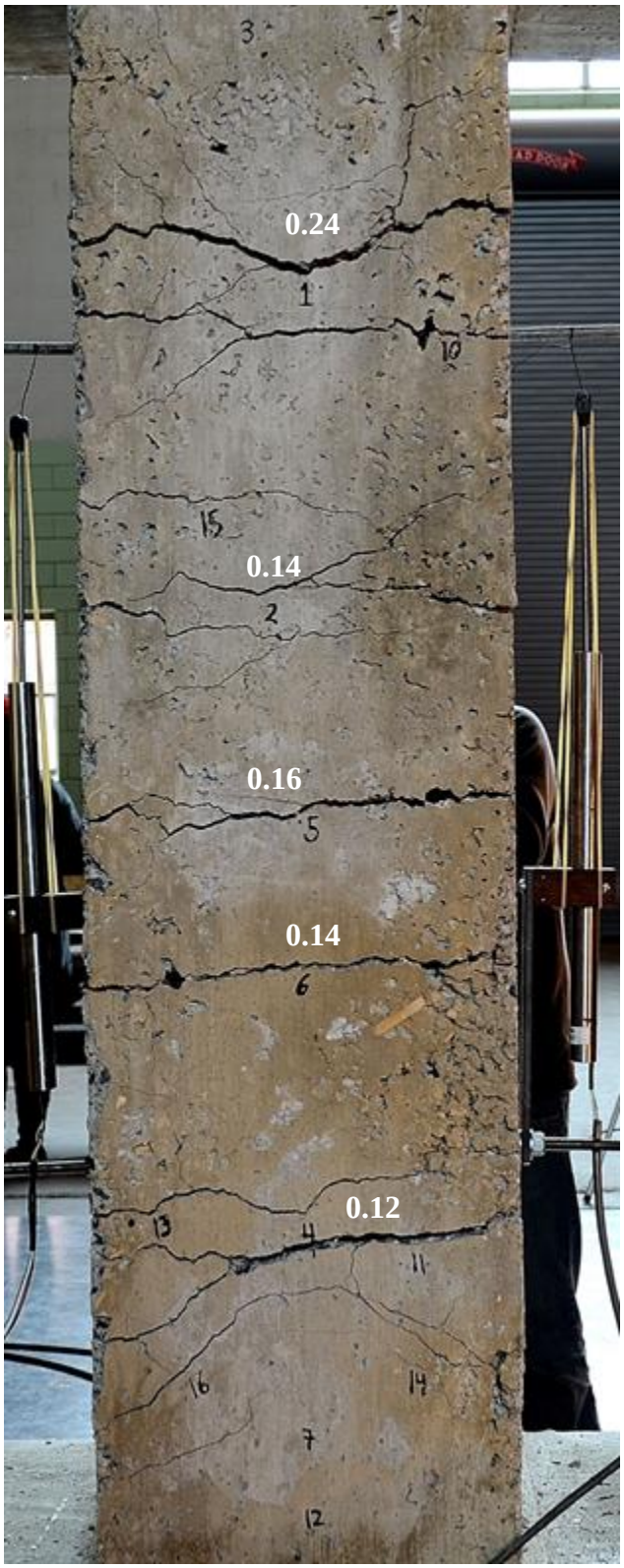

Figure 4-101: Cracks on east face of TS02 at Load Step 25

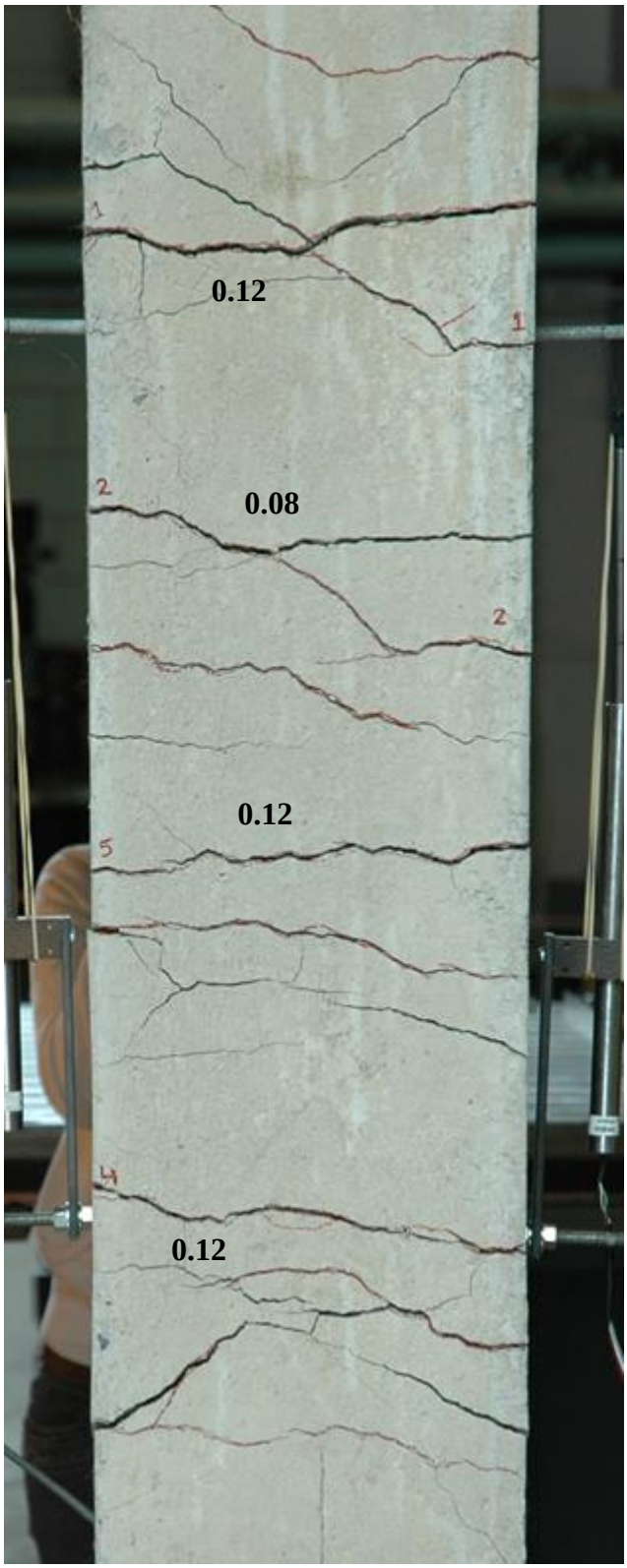

Figure 4-102: Cracks on west face of TS02 at Load Step 25

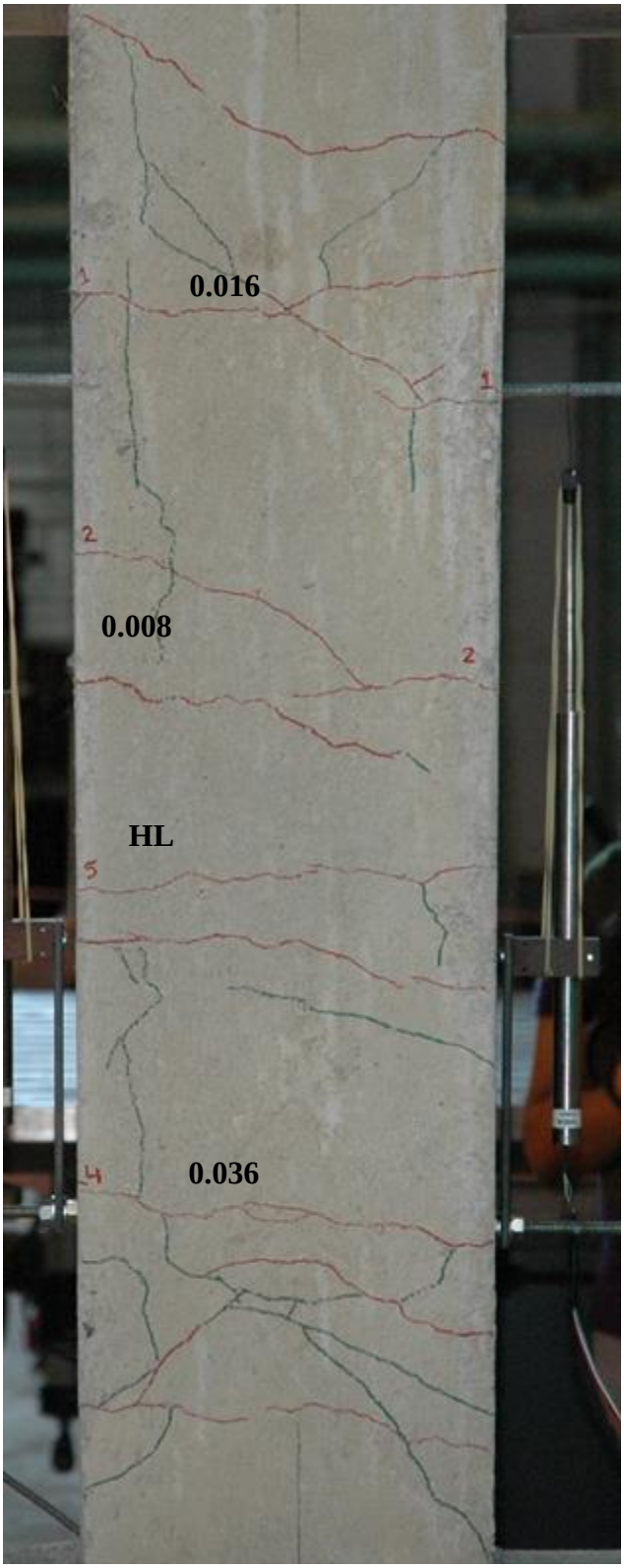

Figure 4-103: Cracks on west face of TS02 at Load Step 26

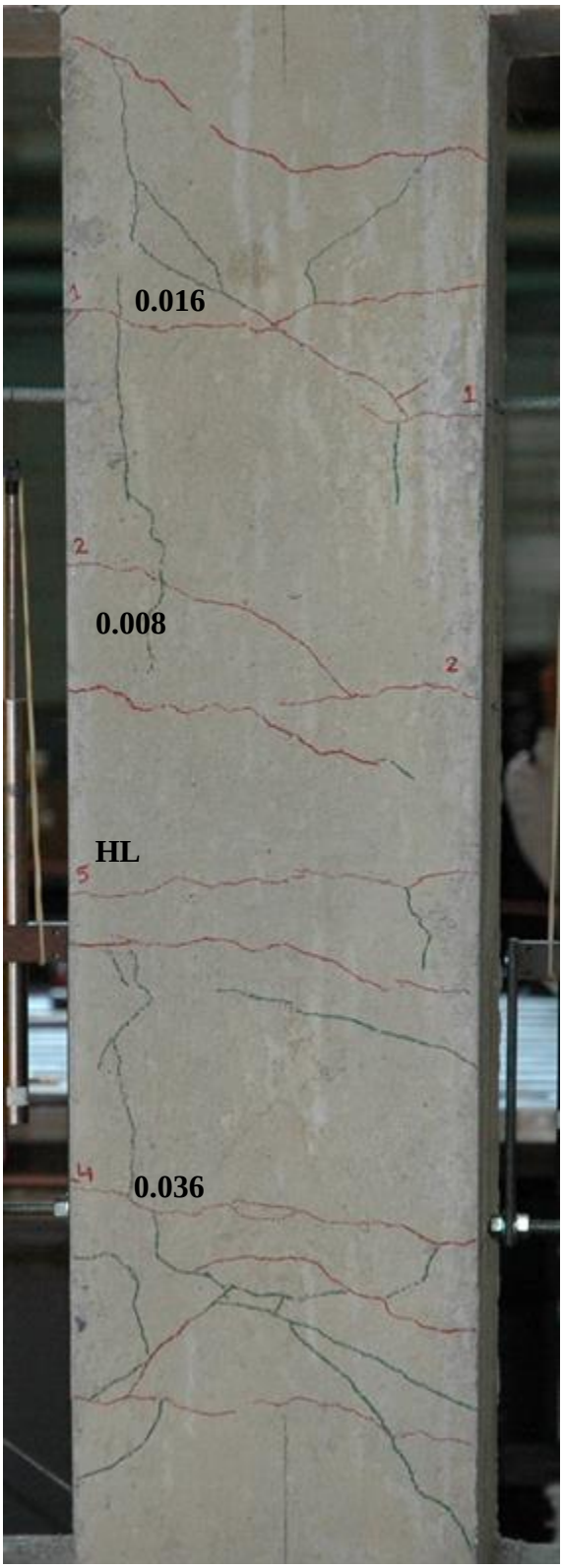

Figure 4-104: Cracks on west face of TS02 at Load Step 28

Figure 4-105: Cracks on east face of TS02 at Load Steps 26-28

Figure 4-106: TS02 at the end of the test

CHAPTER 5

DISCUSSION

5.1 INTRODUCTION

This chapter discusses the experimental results. The results for the two test specimens are compared to observe the effects of different levels of inelastic tensile cyclic loading of the longitudinal mild steel reinforcement bars inside the confined concrete. Also included in this chapter is the comparison of the test results with results from previously developed theoretical confined concrete models under monotonic compression loading. The comparison focuses on the effects of tensile loading on the compression behavior, strength, and ductility of confined concrete.

Section 5.2 compares and discusses the average test data for the two LVDTs in each test specimen. Section 5.3 presents an approach developed to convert the head-travel (test specimen deformation) to testing region deformation. Section 5.4 discusses the testing region tensile deformation (cracks) and gradual crack closure effects under reversed compression loading. Section 5.5 discusses ultimate concrete compression strain based on test results and theoretical formulas from other researchers. Section 5.6 discusses theoretical stress-strain models for confined concrete under monotonic compression loading from other researchers. Section 5.7 presents details about compression behavior, strength and ductility of confined concrete under different levels of inelastic tensile cyclic loading of the longitudinal mild steel reinforcement bars. Section 5.8 presents a comparison of compression behavior, strength, and ductility of confined concrete test results with results from previously developed confined concrete models under monotonic compression loading. Finally, Section 5.9 summarizes the findings of the test results presented in Chapter 4 and the comparisons made in Chapter 5.

5.2 AVERAGE OF LVDTs DATA PLOTS

Figure 5-1 and Figure 5-2 show the average deformation in testing region of TS01 and TS02, respectively. Figure 5-3 and Figure 5-4 show the average strain in testing region of TS01 and TS02, respectively.

The average of LVDTs data in each test specimen is the average of the data recorded by NLVDT and SLVDT in each test specimen. This includes the average deformation and average strain of testing region. Both average deformation and average strain of testing region is plotted versus net load in testing region. After cover spalling initiation in each test specimen, one or both of LVDTs were influenced by cover spalling. Therefore, after that point the corresponding LVDT provides incorrect data, and the data from the LVDT is ignored. Before initiation of cover spalling, all LVDTs provide useful data.

TS01

In TS01, NLVDT was influenced by cover spalling at post-peak axial load of 957 kip of testing region at a compression deformation of 0.715 in. Therefore, it gives incorrect data after this point. SLVDT was not influenced by cover spalling or testing operation, therefore, it gives complete data for the entire test duration. For the average of LVDTs

plots, until post-peak load of 957 kip the average data of NLVDT and SLVDT is plotted. This point is shown by a black dot on the average of LVDT plots. After post-peak load of 957 kip only SLVDT represents the average plots.

TS02

In TS01, SLVDT was influenced by cover spalling at post-peak axial load of 1127 kip of testing region at a compression deformation of 0.294 in. Therefore, it gives incorrect data after this point. NLVDT was altered by cover spalling at post-peak axial load of 1076 kip of testing region at a compression deformation of 0.437 in. Therefore, it gives incorrect results beyond this point. For the average of LVDTs plots, until post-peak load of 1127 kip (deformation of 0.29 in.), the average of NLVDT and SLVDT is plotted. This point is shown by a black dot on the average of LVDT plots. After post-peak load 1127 kip (deformation of 0.29 in.) and before post-peak load of 1076 kip, only NLVDT represents the average plots. After post-peak load of 1076 kip, no deformation or average strain data exist for the testing region in TS02.

5.3 CONVERTING HEAD-TRAVEL TO TESTING REGION DEFORMATION

This section presents the procedure used to obtain the testing region deformation data from the head-travel data (test specimen deformation data). This procedure was applied to the test specimen data because the LVDTs did not provide useful data for the entire test. Figure 5-5 and Figure 5-6 show the average of LVDTs deformation plot and head-travel plots for TS01 and TS02, respectively. In compression, the head-travel plots exhibit less stiffness compared to average of LVDTs plots for deformation. This is because the complete test specimen has more flexibility compared to testing region only. To obtain the testing region deformation data from head-travel data, the deformations of other parts of the test specimen, outside of the testing region, need to be removed from the head-travel data.

The conversion is needed to: (1) check the accuracy of testing region deformation data from LVDTs; and, (2) approximate the incomplete testing region deformation data recorded by LVDTs. The accuracy of deformation (or average strain) data for the testing region, recorded by NLVT and SLVDT in each test specimen, was affected by: (1) cover spalling that was initiated at the peak-strength of testing region section at the compression failure load step in each specimen; and, (2) rotation of threaded rods at the testing region to which the LVDTs were attached.

The following assumptions were made to convert the head-travel data to the testing region deformation data: (1) outside of the testing region, the concrete cover remains intact in other parts of the confined concrete column of the test specimen; (2) outside of the testing region, the specimen remains linear elastic; (3) the cover concrete was stressed into the non-linear elastic range, but the effects of this nonlinearity is negligible; (4) outside of the testing region, full compatibility exists between longitudinal mild steel reinforcement bars and concrete during the test; (5) the effective cross-section area of the confined concrete column inside the beams is chosen 16 in. x 15 in. (240 in^2) compared to the 10 in. x 15 in. (150 in^2) cross-section area of the confined concrete column (or testing region); and, (6) the conversion of head-travel data to testing region deformation

is made for compression loading only (in tensile loading there were also cracks in other parts of the confined concrete column. Therefore, this conversion was not applied to the confined concrete column in tension loading).

Figure 5-7 shows the division of test specimen into five parts for conversion purposes. In formulation given below, the deformation of other parts of the test specimens, outside of the testing region, is subtracted from the head-travel data to obtain the testing region deformation data.

The force-deformation behavior of the other parts of the test specimens is:

$$P = k_i \Delta_i \quad (5\text{-}1)$$

The axial stiffness of each part is:

$$k_i = \frac{A_i E_i}{L_i} \quad (5\text{-}2)$$

The total stiffness of the other parts of the test specimens is as follows:

$$\frac{1}{k_0} = \frac{1}{k_1} + \frac{1}{k_2} + \frac{1}{k_1} + \frac{1}{k_2} \quad (5\text{-}3)$$

$$\frac{1}{k_0} = 2\frac{1}{k_1} + 2\frac{1}{k_2} \quad (5\text{-}4)$$

$$k_0 = \frac{k_1 k_2}{2(k_1 + k_2)} \quad (5\text{-}5)$$

The effective modulus of elasticity for each cross-section, A_i, can be estimated using the transformed section formula, where A_i equals the sum of the steel area, A_s, and the concrete area, A_c.

$$P = P_c + P_s \quad (5\text{-}6)$$

$$\frac{\Delta}{L} EA = \frac{\Delta}{L} E_c A_c + \frac{\Delta}{L} E_s A_s \quad (5\text{-}7)$$

$$E_i = \frac{E_c A_c + E_s A_s}{A_c + A_s} \quad (5\text{-}8)$$

Δ_0, equal to $2\Delta_1 + 2\Delta_2$, is the deformation of the other parts of the test specimen. This is used to find the testing region deformation data from the head-travel data as follows.

$$\Delta_0 = \Delta_1 + \Delta_1 + \Delta_2 + \Delta_2 \quad (5\text{-}9)$$

$$\Delta_t = \Delta_h - \Delta_0 \quad (5\text{-}10)$$

$$\Delta_t = \Delta_h - \frac{P}{k_0} \quad (5\text{-}11)$$

where, P is the axial load in the test specimen.

The same formulation applies for each test specimen. Eq. (5-11) gives the testing region deformation plots from the head travel plots.

Figure 5-8 and Figure 5-9 show the results of Eq. (5-11) from head-travel data and the average of LVDTs for TS01 and TS02, respectively. Figure 5-10, Figure 5-11, and Figure 5-12 show the average of LVDTs, NLVT, and SLVDT deformation plots from the tests with the plot generated from the conversion of head-travel data to the testing region

deformation data at Load Step 24 for TS01. Figure 5-13, Figure 5-14, and Figure 5-15 show the average of LVDTs, NLVDT, and SLVDT deformation plots from the tests with the plot generated from the conversion of head-travel data to the testing region deformation data at Load Step 29 for TS02.

The total axial load in confined concrete column of the test specimen is the summation of load in steel bars, load in cover concrete, and load in confined concrete. The total longitudinal reinforcement steel area was 6.4 in^2 in confined concrete column sections except in the testing region where it was 4.8 in^2. The actual confined concrete column cross-section area in testing region was 155.8 in^2 in TS01 and 156.5 in^2 in TS02. The elastic modulus of actual testing region cross-section area was estimated 6066 ksi in TS01 and 6058 ksi in TS02. The elastic modulus of confined concrete column cross-section area inside the beams was estimated 5718 ksi in TS01 and TS02. The stiffness k_1 was estimated 21442 kip/in. in TS01 and TS02, and the stiffness k_2 was estimated 47223 kip/in. in TS01 and 47403 kip/in. in TS02, respectively. Using Eq. (5-11), the value of k_0 was estimated 14755 kip/in. for TS01 and TS02.

5.4 TENSILE DEFORMATION

This section presents information regarding tensile deformation (cracks) in the confined concrete column particularly in testing region of the test specimens due to tensile cyclic loading, including information on crack closures at the end of the reversing compression load steps after the application of inelastic tensile loading to the longitudinal mild steel reinforcement inside the confined concrete column. Information on the design cracking capacity of testing region, and the actual cracking capacity of testing region is also presented.

During the test, the confined concrete column at the testing region started to crack at 100 kip of tension load based on visual observation. The section was considered to be fully cracked at 120 kip of tension load based on visual observations. Figure 5-16 to Figure 5-21 of the strain gage data from longitudinal reinforcement bars implies that the concrete section in testing region cracked between 60-70 kip load following the cracking limit of $4.5\sqrt{f'_c(\text{psi})}$ to $5\sqrt{f'_c(\text{psi})}$ which is presented in Nilson and Dolan (2010). The design cracking load for testing region of confined concrete column was estimated 83 kip (0.535 ksi) based on $6\sqrt{f'_c(\text{psi})}$ formula from Paulay and Priestley (1992), and Chang and Mander (1994).

TS01

TS01 was visually considered cracked under tensile loading at Load Step 09. To make certain that the specimen was fully cracked, the cracking cycles of 120 kip were applied two more times during Load Phase 05. The maximum tension crack size was 0.01 in. at Load Phase 05 in cracks number 2 and 3. The longitudinal reinforcement bars were stressed to 2/3 of their tensile yielding strain limit at Load Phase 06. The maximum tension crack size was 0.016 in. in the crack number 1.

The longitudinal reinforcement bars were stressed to their tensile yielding strain limit at Load Steps 19 and Load Step 21. The maximum tension crack size was 0.036 in. in crack

number 1. The cracks appeared to be closed in subsequent compression load steps (Load Step 20 and Load Step 22), but the strain gage data from longitudinal bars implies that the cracks at the testing region at Load Step 20 and Load Step 22 were not completely closed. In other words, after yielding the longitudinal mild steel reinforcement inside the confined concrete column in Load Step 19 and Load Step 21, the deformation in longitudinal reinforcement bars at the end of the compression load steps (Load Step 20 and Load Step 22) was not zero. Based on the strain gage data, the actual strain in longitudinal reinforcement bars inside the confined concrete core at the end of Load Step 19 and Load Step 21 was $4.0\varepsilon_{ys}$ instead of the intended ε_{ys}.

TS02

TS02 was considered cracked at the end of Load Step 09. To make certain that the specimen was fully cracked, the cracking cycles of 120 kip were applied two more times during Load Phase 05. The maximum tension crack size was 0.014 in. at Load Phase 05 in crack number 1. The longitudinal reinforcement bars were stressed to 2/3 of their tensile yielding strain limit at Load step 15 and Load Step 17. The maximum tension crack size was 0.024 in. in the crack number 1.

The longitudinal reinforcement bars were stressed to their tensile yielding strain limit at Load Step 19 and Load Step 21. The maximum tension crack size was 0.05 in. in crack number 1. The crack appeared to be completely closed in subsequent compression load steps (Load Step 20 and Load Step 22), but the strain gage data from longitudinal bars implies that the cracks at the testing region at Load Step 20 and Load Step 22 were not completely closed. In other words, after yielding the longitudinal mild steel reinforcement inside the confined concrete column in Load Step 19 and Load Step 21, the deformation in longitudinal reinforcement bars at the end of the compression load steps (Load Step 20 and Load Step 22) was not zero.

The longitudinal reinforcement bars inside the confined concrete core were stressed to $12\varepsilon_{ys}$ and $16\varepsilon_{ys}$ in Load Step 23 and Load Step 25. The maximum tension crack size was 0.24 in. in crack number 1 at each load step. The cracks were not completely closed in the subsequent compression load steps (Load Step 24 and Load Step 26). There was a maximum crack opening of 0.01 in. in crack number 11 at the end of Load Step 24. There was a maximum crack opening of 0.036 in. in crack number 4 at the end of Load Step 25. The LVDTs deformation data implies greater tensile deformation (cracks) in the testing region then the strain gage tensile deformation (cracks) data.

5.5 ULTIMATE CONCRETE COMPRESSION STRAIN

Concrete confinement increases the compression ductility of concrete. To study the effect of inelastic tensile cyclic loading of the longitudinal mild steel reinforcement inside the confined concrete core on the compression ductility of confined concrete core, the theoretical ultimate concrete compression strain limit is estimated and compared with the actual ultimate concrete compression strain limit from the experimental data. The confined concrete is considered effective until the first confinement hoop is fractured. The axial compression strain of the confined concrete corresponding to the first confinement hoop fracture is called the ultimate concrete compression strain.

The ultimate strain of ASTM A615 Grade 60 #3 steel reinforcement used for confinement hoop, ε_{uh}, is 0.1 in/in. Based on Mander (1988) model, the ultimate concrete compression strain for the two directions of the testing region of the confined concrete column in each test specimen are:

$$\varepsilon_{cux} = 0.004 + \frac{1.4\,\rho_s f_{yh}\varepsilon_{uh}}{f'_{ccx}} = 0.028 \quad (5\text{-}12)$$

and,

$$\varepsilon_{cuy} = 0.004 + \frac{1.4\,\rho_s f_{yh}\varepsilon_{uh}}{f'_{ccy}} = 0.027 \quad (5\text{-}13)$$

The ultimate concrete compression strain for the testing region of confined concrete column based on proposed equation in Oh (2002) is:

$$\varepsilon_{cu} = 0.008 + 0.1\phi_c = 0.016 \quad (5\text{-}14)$$

Based on the test results, the ultimate concrete compression strain was recorded at 0.0385 in./in.

In all confined concrete models for the testing region, the ultimate concrete compression strain from the test results is used as the maximum strain limit on strain (or deformation) axis.

5.6 THEORETICAL STRESS-STRAIN MODELS FOR CONFINED AND UNCONFINED CONCRETE

In this section, theoretical stress-strain models for the testing region of the confined concrete column under monotonic compression loading based on Mander (1988), Chang and Mander (1994), and Oh (2002) models are developed. The theoretical models are later used for comparison with the test results to find out the effects of inelastic tensile cyclic loading on the behavior, strength, and ductility of confined concrete.

Unless given an exact formula in each individual approach for the stress-strain models, the following values and parameters are used in each approach:

(1) The strain at the peak stress for unconfined concrete is based on the following simplified equation of Sulayfani and Lamirault (1987).

$$\varepsilon'_{cc} = 0.00025 f_c'^{0.25} = 0.0023 \quad (5.15)$$

(2) The elastic modulus of unconfined concrete is based on equation from ACI 318-11 Code.

$$E_c = 57000\sqrt{f'_c} = 5080 \text{ ksi} \quad (5.16)$$

(3) For simplicity, bilinear stress-strain relationship is defined for the longitudinal mild steel reinforcement bars. The modulus of elasticity is taken as 29000 ksi for strain up to yield strain limit, $\varepsilon_{ys} = 0.0026$, corresponding to a yielding stress of 75 ksi (See Section 3.6). The post yield modulus is taken as 846 ksi between the yielding strain limit and the ultimate strain limit, $\varepsilon_{us} = 0.0416$, corresponding to

an ultimate stress of 108 ksi. The stress-strain relationships for the two intervals can be defined as follows:

$\sigma = 29000\varepsilon$ ksi (5.17)

$\sigma = 846\varepsilon + 72.8$ ksi (5.18)

(4) The area of the effectively confined concrete core, A_e, is based on the formula given in Mander (1988):

$$A_e = \left(A_c - 2\frac{w_y'}{6} - 6\frac{{w_x'}^2}{6}\right)\left(1 - \frac{s'}{2b_c}\right)\left(1 - \frac{s'}{2d_c}\right) = 69.9 \text{ in}^2 \quad (5\text{-}19)$$

(5) The area of confined concrete core within the centerlines of the hoops for each specimen is:

$$A_{cc} = b_c d_c - A_{st} = 106.6 \text{ in.}^2 \quad (5\text{-}20)$$

(6) The lateral confinement pressure for rectangular sections have different values in each direction, x and y (i.e., a three dimensional state of stress). The lateral pressure for each direction (x and y) is calculated as:

$$f_{lx}' = k_e \rho_x f_{yh} = 0.62 \text{ ksi} \quad (5\text{-}21)$$

$$f_{ly}' = k_e \rho_y f_{yh} = 0.77 \text{ ksi} \quad (5\text{-}22)$$

where,

$\rho_y = \frac{A_{sx}}{sd_c}$ and $\rho_x = \frac{A_{sy}}{sb_c}$

and,

$k_e = \frac{A_e}{A_{cc}}$

The smaller value of lateral confinement pressure is used in developing models for comparison.

5.6.1 Mander (1988) Stress-Strain Model

Figure 5-23 shows plots of the monotonic compression stress-strain models for the confined concrete and unconfined concrete based on Mander (1988) for the testing region of the confined concrete column. These plots are generated as explained below.

Unconfined Concrete

Figure 5-22 shows plot of the monotonic compression stress-strain models for unconfined concrete plotted until a compression strain of 0.01. In the Mander (1988) model, for unconfined concrete, the secant modulus at peak stress is found using the following equation:

$$E_{sec} = \frac{f_c'}{\varepsilon_c'} = 3452.2 \text{ ksi} \quad (5\text{-}23)$$

The *r*-parameter that controls the slope of both the ascending and descending regions of the stress-strain function is found using the following equation:

$$r = \frac{E_c}{E_c - E_{sec}} = 3.121 \quad (5\text{-}24)$$

The equation to describe the monotonic compression stress-strain curve for unconfined concrete is given below:

$$f_c(\varepsilon) = \frac{f'_c \left(\frac{\varepsilon}{\varepsilon'_c}\right) r}{r - 1 + \left(\frac{\varepsilon}{\varepsilon'_c}\right)^r} \quad (5\text{-}25)$$

Confined Concrete

The Mander (1988) model for the stress-strain curve of confined concrete under monotonic compression loading is found using the following equations:

$$f'_{ccx} = f'_c \left(-1.254 + 2.254\sqrt{1 + \frac{7.94 f'_{lx}}{f'_c}} - 2\frac{f'_{lx}}{f'_c} \right) = 11.58 \text{ ksi} \quad (5\text{-}26)$$

$$f'_{ccy} = f'_c \left(-1.254 + 2.254\sqrt{1 + \frac{7.94 f'_{ly}}{f'_c}} - 2\frac{f'_{ly}}{f'_c} \right) = 12.30 \text{ ksi} \quad (5\text{-}27)$$

The minimum of the two confined concrete stresses $f'_{ccx} = 11.58$ ksi is used for the confined concrete model.

$$\varepsilon'_{ccx} = \varepsilon'_c \left[1 + 5 \left(\frac{f'_{ccx}}{f'_c} - 1 \right) \right] = 0.0075 \quad (5\text{-}28)$$

$$\varepsilon'_{ccy} = \varepsilon'_c \left[1 + 5 \left(\frac{f'_{ccy}}{f'_c} - 1 \right) \right] = 0.0086 \quad (5\text{-}29)$$

where, ε'_{ccx} and ε'_{ccy} are the strains at maximum stress along the x- and y-directions, respectively.

$$r_x = \frac{E_c}{E_c - E_{sec}} = 1.431 \text{ and } r_y = \frac{E_c}{E_c - E_{sec}} = 1.39 \quad (5\text{-}30)$$

and,

$$E_{secx} = \frac{f'_{ccx}}{\varepsilon'_{ccx}} = 1529 \text{ ksi} \quad (5\text{-}31)$$

$$E_{secy} = \frac{f'_{ccy}}{\varepsilon'_{ccy}} = 1427 \text{ ksi} \quad (5\text{-}32)$$

E_{secx} and E_{secy} are the secant moduli of confined concrete at peak stress in x- and y-directions, respectively.

The stress-strain functions are plotted using the equations below:

$$f_{cx}(\varepsilon) = \frac{f'_{ccx}\left(\frac{\varepsilon}{\varepsilon'_{cc}}\right) r_x}{r_x - 1 + \left(\frac{\varepsilon}{\varepsilon'_{cc}}\right)^{r_x}} \quad (5\text{-}33)$$

$$f_{cy}(\varepsilon) = \frac{f'_{ccy}\left(\frac{\varepsilon}{\varepsilon'_{cc}}\right) r_y}{r_y - 1 + \left(\frac{\varepsilon}{\varepsilon'_{cc}}\right)^{r_y}} \quad (2\text{-}34)$$

The smaller of the two confined concrete stress-strain functions ($f_{cx}(\varepsilon)$) is used for the confined concrete model.

5.6.2 Chang and Mander (1994) Stress-Strain Model

Figure 5-24 shows plots of the monotonic compression stress-strain models for confined concrete and unconfined concrete based on Chang and Mander (1994) for the testing region of the confined concrete column. These plots are generated as explained below.

Unconfined Concrete

Figure 5-22 shows plot of the monotonic compression stress-strain model for unconfined concrete plotted until a compression strain of 0.01. The modulus of elasticity of concrete recommended by Chang and Mander (1994) is:

$$E_c = 185 f_c'^{3/8} = 5365 \text{ ksi} \quad (5\text{-}35)$$

The strain at the peak stress is:

$$\varepsilon_c' = \frac{f_c'^{1/4}}{4000} = 0.0023 \quad (5\text{-}36)$$

The equation to describe the monotonic compression stress-strain curve for unconfined concrete is based on Tsai's equation (Chang and Mander, 1994):

$$f_c(\varepsilon) = \frac{n\left(\frac{\varepsilon}{\varepsilon_c'}\right)}{1+\left(n-\frac{r}{r-1}\right)\left(\frac{\varepsilon}{\varepsilon_c'}\right)+\frac{\left(\frac{\varepsilon}{\varepsilon_c'}\right)^r}{r-1}} f_c' \quad (5\text{-}37)$$

where the n-parameter and r-parameter control the shape of the curve.

$$r = \frac{f_c'}{750} - 1.9 = 8.687 \quad (5\text{-}38)$$

and,

$$n = \frac{46}{f_c'^{3/8}} = 1.586 \quad (5\text{-}39)$$

Confined Concrete

Chang and Mander (1994) provide a simplified approach for calculating the peak stress and the corresponding strain values of the Mander (1988) confined concrete stress-strain model.

The modulus of elasticity is 5365 ksi and the strain at peak stress of the unconfined concrete is 0.0023 in./in. as given in the unconfined concrete model section. The peak stress and the corresponding peak strain values for the confined concrete are found as follows:

$$f_{cc}' = f_c'(1 + k_1 x') = 11.86 \text{ ksi} \quad (5\text{-}40)$$

$$k_1 = A\left(0.1 + \frac{0.9}{1+Bx'}\right) = 5.656 \quad (5\text{-}41)$$

$$x' = \frac{f'_{lx}+f'_{ly}}{2f'_c} = 0.087 \quad (5\text{-}42)$$

$$A = 6.886 - (0.6069 + 17.275q)e^{-4.989q} = 6.628 \quad (5\text{-}43)$$

$$B = \frac{4.5}{\frac{5}{A}(0.9849 - 0.6306e^{-3.8939r}) - 0.1} - 5 = 2.228 \quad (5\text{-}44)$$

$$q = \frac{f'_{lx}}{f'_{ly}} = 0.808 \quad (5\text{-}45)$$

where, $f'_{ly} \geq f'_{lx}$

$$\varepsilon'_{cc} = \varepsilon'_c[1 + k_2 x'] = 0.0057 \quad (5\text{-}46)$$

where,

$k_2 = 5k_1$ for $f_{ys} \leq 6$ksi

and, $k_2 = 3k_1$ for $f_{ys} > 6$ksi. Here it is $k_2 = 16.97$.

The ascending branch of the Chang and Mander (1994) model is the same as the Mander (1988) model but the descending region of the two models are different due to: (1) different formulation for peak-stress and the corresponding strain; and, (2) different formulation for modulus of elasticity of unconfined concrete.

$$E_{secx} = \frac{f'_{ccx}}{\varepsilon'_{ccx}} = 2078 \text{ ksi} \quad (5\text{-}47)$$

and,

$$r_x = \frac{E_c}{E_c - E_{sec}} = 1.632 \quad (5\text{-}48)$$

5.6.3 Oh (2002) Stress-Strain Model

Figure 5-25 shows plots of the monotonic compression stress-strain models for confined concrete and unconfined concrete based on Oh (2002) for the testing region of the confined concrete column. These plots are generated as explained below.

Unconfined Concrete

Figure 5-22 shows plot of the monotonic compression stress-strain model for unconfined concrete plotted until a compression strain of 0.01.

In the Oh (2002) model, the stress-strain relations for the linear elastic branch, which lies between 0-30 percent of the peak stress of unconfined concrete, can be presented using the following equation:

$$f_{ci} = c_i f'_c = 2.38 \text{ ksi} \quad (5\text{-}49)$$

where, $c_i = 0.3$

The corresponding strain at the linear elastic limit is:

$$\varepsilon_{ci} = \frac{f_{ci}}{E_c} = 0.000469 \quad (5\text{-}50)$$

The stress-strain relationship in the linear elastic region, $0 \leq \varepsilon \leq \varepsilon_{ci}$, is:

$$f_c(\varepsilon) = E_c\varepsilon \quad (5\text{-}51)$$

The function for the ascending branch of the stress-strain curve, $\varepsilon_{ci} \le \varepsilon \le \varepsilon_c'$, is obtained by modifying the Popovics model (Oh, 2002).

$$f_c(\varepsilon) = (f_c' - f_{ci})\omega_u \frac{r_{au}}{r_{au} - 1 + \omega_u^{r_{au}}} + f_{ci} \quad (5\text{-}52)$$

where,

$$\omega_u(\varepsilon) = \frac{\varepsilon - \varepsilon_{ci}}{\varepsilon_c' - \varepsilon_{ci}} \quad (5\text{-}53)$$

$$r_{au} = \frac{E_c}{E_c - E_{au}} = 2.485 \quad (5\text{-}54)$$

$$E_{au} = \frac{f_c' - f_{ci}}{\varepsilon_c' - \varepsilon_{ci}} = 3035 \text{ ksi} \quad (5\text{-}55)$$

The function for the descending branch is defined over an axial strain in the range $\varepsilon_c' \le \varepsilon \le \varepsilon_{cu}$. In contrast to the Mander (1988) model, the descending region in the Oh (2002) model is defined using a different *r*-parameter then the ascending region. This gives the descending branch independent behavior than the ascending branch.

$$f_c(\varepsilon) = f_c'\left(\frac{\varepsilon}{\varepsilon_c'}\right)\frac{r_{du}}{r_{du} - 1 + \left(\frac{\varepsilon}{\varepsilon_c'}\right)^{r_{du}}} \quad (5\text{-}56)$$

where,

$$r_{du} = 0.58 + 0.32f_c' + 0.077f_c'^2 = 7.975 \quad (5\text{-}57)$$

Confined Concrete

The empirical stress-strain model for monotonic compression of confined concrete developed by Oh (2002) is a plasticity model. This formulation needs a predetermined value of lateral confining pressure, f_{lx}' and f_{ly}'. The Oh (2002) model is a triaxial compression model. The smaller value of lateral confining pressure, $f_{lx}' = 0.62$ ksi, is used here. The following steps summarize the model.

The peak stress of the confined concrete and the corresponding strain is found as follows:

$$f_{cc}' = \left(f_c' + 4.1\frac{f_{lx}'}{f_c'}\right) = 10.482 \text{ ksi} \quad (5\text{-}58)$$

$$\varepsilon_{cc}' = \varepsilon_c'\left[1 + 5\left(\frac{f_{cc}'}{f_c'} - 1\right)\right] = 0.00598 \quad (5\text{-}59)$$

The stress-strain relationship in the linear elastic branch, $0 \le \varepsilon \le \varepsilon_{ci}$, is:

$$f_{cc}(\varepsilon) = E_c\varepsilon \quad (5\text{-}60)$$

where,

$$f_{ci} = (0.3 + 2\phi_c)f_c' = 3.622 \text{ ksi} \quad (5\text{-}61)$$

$$\varepsilon_{ci} = \frac{(0.3 + 2\phi_c)f_c'}{E_c} = 0.000713 \quad (5\text{-}62)$$

where,

$$\phi_c = \frac{f_{lx}'}{f_c'} = 0.078 \quad (5\text{-}63)$$

The function for the ascending branch of the stress-strain curve, $\varepsilon_{ci} \leq \varepsilon \leq \varepsilon'_{cc}$, is:

$$f_{cc}(\varepsilon) = (f'_c - f_{ci})\omega_a \frac{r_a}{r_a - 1 + \omega_a{}^{r_a}} + f_{ci} \quad (5\text{-}64)$$

where,

$$\omega_u(\varepsilon) = \frac{\varepsilon - \varepsilon_{ci}}{\varepsilon'_{cc} - \varepsilon_{ci}} \quad (5\text{-}65)$$

$$r_a = \frac{E_c}{E_c - E_{ac}} = 1.345 \quad (5\text{-}66)$$

$$E_{ac} = \frac{f'_{cc} - f_{ci}}{\varepsilon'_{cc} - \varepsilon_{ci}} = 1302 \text{ ksi} \quad (5\text{-}67)$$

The function for the descending branch is defined over an axial strain in the range $\varepsilon'_{cc} \leq \varepsilon \leq \varepsilon_{cu}$. In contrast to the Mander (1988) model, the descending branch is defined using a function and r-parameter different than the ascending branch, which gives the descending branch independent behavior.

$$f_c(\varepsilon) = f'_{cc}\left(\frac{\varepsilon}{\varepsilon'_{cc}}\right) \frac{r_d}{r_d - 1 + \left(\frac{\varepsilon}{\varepsilon'_{cc}}\right)^{r_d}} \quad (5\text{-}68)$$

where,

$$r_d = \frac{E_c}{E_c - E_{sc}} g(\phi_c) = 3.53 \quad (5\text{-}69)$$

and,

$$E_{sc} = \frac{f'_{cc}}{\varepsilon'_{cc}} = 1752 \quad (5\text{-}70)$$

The function $g(\phi_c)$ reflects the effect of confining pressure. Based on Oh's observations, the *r*-parameter from Mander (1988) model provides reasonable values for $\phi_c > 0.5$, but for $\phi_c \leq 0.5$, the r-factor from the Mander (1988) model overestimates the post-peak strength. That is, the descending region slope is too flat. Therefore, Oh developed criteria to rectify this difference.

Based on Oh's model, when:

$\phi_c = 0$, then $r_d = \left(1 - \frac{E_{su}}{E_c}\right) r_{du}$

when $0 < \phi_c \leq 0.5$, then;

$$g(\phi_c) = \left(1 - \frac{E_{su}}{E_c}\right) r_{du}(1 - 2\phi_c) + 2\phi_c = 2.31 \quad (5\text{-}71)$$

When $\phi_c > 0.5$, then r_d equals to the r factor from Mander (1988). That is, the value of $g(\phi_c) = 1$. The details are discussed in Chapter 2. In this test program, this values lies between $0 < \phi_c \leq 0.5$. Therefore, a value of 2.31 is used.

5.6.4 Mander (1988) Stress-Strain Model with Peak Stress and the Corresponding Strain Values from Oh (2002) Stress-Strain Model

Figure 5-26 shows plot of the monotonic compression stress-strain model for confined concrete based on Mander (1988) model with peak stress and the corresponding strain values from Oh (2002) model for confined concrete. This plot is generated as explained below.

In this model, the peak stress and the corresponding strain values of confined concrete in testing region is estimated based on formulation proposed in Oh (2002) model for confined concrete. The peak stress and the corresponding peak strain values are substituted in the Mander (1988) confined concrete model.

The peak stress of the confined concrete and the corresponding strain values are found as follow:

$$f'_{cc} = \left(f'_c + 4.1\frac{f'_{lx}}{f'_c}\right) = 10.48 \text{ ksi} \quad (5\text{-}72)$$

$$\varepsilon'_{cc} = \varepsilon'_c\left[1 + 5\left(\frac{f'_{cc}}{f'_c} - 1\right)\right] = 0.006 \quad (5\text{-}73)$$

The rest of the stress-strain function for confined concrete is following the Mander (1988) model. For the unconfined concrete, model from Mander (1988) is used.

5.6.5 Comparison of Stress-Strain Models

Figure 5-27 shows the plotted models for comparison. In this section, the stress-strain models for testing region based on Mander (1988), Chang and Mander (1994), Oh (2002), and Mander (1988) with peak stress and the corresponding strain values from Oh (2002) models are compared.

All the confined concrete models are similar to each other in the ascending branch. The peak stress in Chang and Mander (1994) and Oh (2002) models are reached earlier than in the Mander (1988) model. In other words, the Chang and Mander (1994) and Oh (2002) models reach the peak stress at a smaller strain then the Mander (1988) model.

In the descending branch of the models, the Mander (1988) model is flatter than the other models. The Oh (2002) model exhibits the steepest descending branch. Chang and Mander (1994) and Mander (1988) with f'_{cc} and ε'_{cc} values from Oh (2002) models fall between the Mander (1988) and Oh (2002) models. The Chang and Mander (1994) model shows higher strength compared to Mander (1988) with f'_{cc} and ε'_{cc} values from Oh (2002) model.

For unconfined concrete, all the models are similar to each other. The Mander (1988) model shows a more gradual descending branch than the other two models. The Chang and Mander (1994) and Oh (2002) models are very close to each other in the descending branch too.

5.7 COMPARISON OF TEST RESULTS BETWEEN THE TEST SPECIMENS

This section compares the test results for the two test specimens to observe the effects of different levels of inelastic tensile cyclic loading of the longitudinal mild steel reinforcement bars inside the confined concrete. The comparison focuses on the effects of tensile loading on the behavior, strength, and ductility of confined concrete under compression loading.

The first specimen was tested under increasing tensile cyclic loading up to 4 times the tensile yielding strain of the longitudinal mild steel reinforcement bars inside the confined concrete. The second specimen was tested under increasing tensile cyclic loading up to 16 times the tensile yielding strain of the longitudinal mild steel reinforcement bars of the confined concrete. Both of the specimens were then tested to failure under compression loading.

Figure 5-28 shows test specimens load-deformation response for the two test specimens based on head-travel data. Figure 5-29 shows the testing region load-deformation response for the two specimens obtained by converting the head-travel data to testing region deformation. Figure 5-30 shows the testing region load-deformation response for the two specimens based on the average value of NLVDT and SLVDT in each test specimen.

5.7.1 Comparison of Behavior and Strength

Figure 5-28, Figure 5-29 and Figure 5-30 show that the compression behavior of the two test specimens was similar. Figure 5-28 shows that the compression axial load-deformation responses for the two test specimens were similar. Figure 5-29 and Figure 5-30 show that the compression axial load-deformation responses for the testing region of the two test specimens were similar. The difference in peak compression strength between the two test specimens was 4.5%. The peak compression strength of TS01 was 1447 kip, and the peak compression strength of TS02 was 1384 kip.

The peak compression strength of the confined concrete core was reached after the peak compression strength of the entire testing region cross-section at each test specimen. The peak compression strength of confined concrete core was 1284 kip in TS01 and 1302 kip in TS02. The peak compression strength of the confined concrete core occurred at the yielding strain limit of the confinement hoop reinforcement.

5.7.2 Comparison of Compression Ductility

After reaching the peak strength of the confined concrete of the testing region in each test specimen (1284 kip in TS01 and 1302 kip in TS02), the axial load-deformation plots started to decline at increasing compression deformation. Figure 5-28 and Figure 5-29 show that compression ductility was similar for the two test specimens with two different peak inelastic tensile strains. The numbers of hoop fractures were the same. Finally, the locations of fractures on the external legs of the confinement hoops were the same.

5.7.3 Comparison of Compression Stiffness

The slope of the ascending branch of axial load-deformation plots of the testing region of the two test specimens were the same. Thus, the stiffness of the specimens was not affected by different levels of inelastic tensile cyclic loading. The ascending branches of the deformation plots of the two test specimens rise almost linearly up to the peak strength of the testing region in compression. However, near the peak strength, there is a small deviation from the line in TS02. The stiffness of the specimen can be estimated from the axial load-deformation plots in the linear ascending branch.

$$P = k_3 \Delta_t \qquad (5\text{-}74)$$

where, P is the net axial load in testing region of the confined concrete column, k_3 is the stiffness of the testing region section, and Δ_t is the deformation of the testing region. The value of k_3 is 44090 kip/in. in TS01 and 46070 kip/in. in TS02. The difference is 4.3%.

5.8 COMPARISON OF THEORETICAL MODELS AND EXPERIMENTAL RESULTS OF CONFINED CONCRETE

In this section, the theoretical stress-strain models of the testing region presented in Section 5.6 are converted to axial load-deformation models. An exact stress-strain plot cannot be presented from the test results for comparison with the theoretical stress-strain models as there was no stress data record for the testing region from the tests. Therefore, the theoretical stress-strain models for the testing region are converted to theoretical load-deformations models, and then compared with the load-deformation results from the tests. The components of testing region include: (1) cover concrete; (2) confined concrete; and, (3) longitudinal mild steel reinforcement inside the confined concrete. Section 5.8.1 discusses the conversion process. Section 5.8.2 compares the theoretical models for the testing region with the test results for the testing region.

5.8.1 Converting Theoretical Stress-Strain Models to Load-Deformation Models

The theoretical load-deformation models for the testing region of the test specimens are developed by: (1) converting the theoretical stress-strain models of the three testing region components to theoretical load-deformation models; and, (2) combining the load-deformation models of the individual testing region components. The three components of the testing region includes: (1) cover concrete; (2) confined concrete; and, (3) longitudinal mild steel reinforcement.

The theoretical stress-strain model for the longitudinal mild steel reinforcement bars inside the confined concrete core is presented in Section 3.6. The stress-strain models for cover concrete and confined concrete are presented in Section 5.6. The same longitudinal mild steel reinforcement model is used in all theoretical axial load-deformation models.

The following steps summarize the procedure to develop theoretical load-deformation models for the testing region of test specimens:

1. In developing the theoretical load-deformation plots, the axial strain (or deformation) of the testing region is considered as independent variable. Strain

increments are defined at an interval of 0.0001 in./in. starting from zero and ending at ε_{cu}.

2. The strain values were multiplied to the initial average center-to-center spacing of the threaded rods at the testing region to which the LVDTs were attached. This value is 22.05 in. for TS01 and 21.41 in. for TS02. This multiplication converts the strain to deformation.

3. Based on the test results, the first confinement hoop at the testing region fractured at a strain of 0.0385 in./in.; therefore, all the theoretical axial load-deformation models are plotted in this strain range (up to $\varepsilon_{cu} = 0.0385$ in./in.).

4. The stress values of the individual models of the testing region components were multiplied by cross-section area of each component to convert the axial stress to axial load at each structural component.

5. Axial load of individual components of testing region were added to obtain the axial load of testing region at each strain (deformation) interval.

The testing region cross-section area was 155.8 in.^{2} in TS01 and 156.5 in.^{2} in TS02. The confined concrete area, including the longitudinal reinforcement, was 106.6 in.^{2} in TS01 and TS02. The cover concrete cross-section area was 49.2 in.^{2} in TS01 and 49.9 in.^{2} in TS02. The area of longitudinal mild steel reinforcement inside the confined concrete in testing region was 4.8 in.^{2}. The average center-to-center distance between top and bottom threaded rods at the testing region to which the LVDTs were attached was 22.05 in. in TS01 and 21.41 in. in TS02.

5.8.2 Comparison of Theoretical Load-Deformation Models with Test Results

Figure 5-31 and Figure 5-32 shows the theoretical axial load-deformation models for the testing region plotted with the test results (testing region deformation plots from average of LVDTs data) for TS01 and TS02, respectively.

Based on comparison of the theoretical models with the test results, strength of the test specimens was smaller compared to any of the theoretical models for the testing region. In TS01, the strength reduction was 16% compared to Mander (1988) model, 16% compared to Chang and Mander (1994) model, and 12% compared to Oh (2002) model. In TS02, the strength reduction was 20% compared to Mander (1988) model, 20% compared to Chang and Mander (1994) model, and 16% compared to Oh (2002) model. This comparison is made at the peak strength where the cover spalling was initiated in the test.

Assuming that the field-cured concrete cylinders correctly represented the in situ compression strength of the concrete in the test specimens, it can be inferred from the comparison of the test results for the testing region with theoretical models for monotonic compression loading for the testing region that the inelastic tensile cyclic loading of the

longitudinal mild steel reinforcement caused reduction in the compression strength of the testing region.

Next, to suggest an appropriate model for the behavior of the test specimens using the theoretical models for monotonic compression loading, the theoretical models were tried with different strength reductions for the confined concrete component of the testing region. It was determined that from among the four theoretical models for the testing region, the Chang and Mander (1994) and Mander (1988) with f'_{cc} and ε'_{cc} values from Oh (2002) models with 20% strength reduction of the confined concrete component closely follow the behavior of the test results.

Figure 5-33 and Figure 5-34 shows the Chang and Mander (1994) and the Mander (1988) with f'_{cc} and ε'_{cc} values from Oh (2002) theoretical models for the testing region with the 20% strength reduction of the confined concrete component. The theoretical models are plotted with the average of LVDTs data for each test specimen.

It should be noted that the results in this section are based on the assumption that the field-cured concrete cylinders correctly represented the in-situ compression strength of the concrete in the test specimens.

5.9 SUMMARY OF FINDINGS

This section summarizes the findings from the test results that were presented in Chapter 4 and comparisons that were made in Chapter 5.

Comparing the Two Test Specimens:

The overall compression behavior, strength, and ductility of the two test specimens were similar. The difference in peak compression strength was only 4.5%. The axial force versus axial deformation curves for the two test specimens were similar to each other.

Comparison of Theoretical Models with Test Results:

Based on comparison of the test results with the theoretical models for monotonic compression loading, the compression stiffness and ductility of the confined concrete were not affected by inelastic tensile cyclic loading of the longitudinal mild steel reinforcement inside the confined concrete.

Assuming that the field-cured concrete cylinders correctly represented the in situ compression strength of the concrete in the test specimens, it can be inferred from the comparison of the test results for the testing region with theoretical models for monotonic compression loading for the testing region that the inelastic tensile cyclic loading of the longitudinal reinforcement reduced the compression strength of the testing region. On average, there was a compression strength reduction of 18% in the testing region compared to the Mander (1988) model; 18% compared to the Chang and Mander (1994) model; and 14% compared to the Oh (2002) model.

The results for the Mander (1988) theoretical model for the testing region with f'_{cc} and ε'_{cc} values from Oh (2002) model is closer to the test results then the results from the other theoretical models presented in the report. Also, this result suggests that the Mander (1988) model is very sensitive to the peak-stress and the corresponding strain values.

Remarks on the Theoretical Confined Concrete Models:

Based on the testing region models for both test specimens, it was determined that the Mander (1988) model for confined concrete overestimates the strength of confined concrete in the descending region of the curve. The Mander (1988) model curve was too flat in the descending region.

In comparison with the test results, it was determined that the Chang and Mander (1994) model gives better results than Mander (1988) model. The Chang and Mander (1994) model uses different formulas for the peak-stress and the corresponding strain values than Mander (1988) model. The Chang and Mander (1994) model gives greater strength for the confined concrete at a smaller strain compared to the Mander (1988) model.

In comparison with the test results, it was determined that the Oh (2002) model underestimates the strength of confined concrete in the descending region.

It was determined that Chang and Mander (1994) and Mander (1988) models give higher strengths compared to Oh (2002) model for confined concrete, but Chang and Mander

(1994) model reaches the peak strength sooner (i.e., in a smaller strain value) than the other two models.

It was determined that the formula provided in Oh (2002) for estimating the ultimate concrete compression strain of the confined concrete underestimates the ultimate concrete compression strain of the confined concrete.

Cracking Behavior:

Based on the average of LVDTs data in test specimens, the total testing region tensile deformation (cracks) in TS02 were seven times greater than the testing region tensile deformation (cracks) in TS01 in the maximum inelastic tensile load steps. In the reversing compression load steps, the testing region cracks in TS02 were greater in size then the cracks in TS01. The cracks in TS02 were completely closed at 870 kip compression loading while the cracks in TS01 were completely closed at 455 kip compression loading.

At tensile loads smaller than the tensile yielding limit of the longitudinal mild steel reinforcement inside the confined concrete, the cracks in the concrete were completely closed in the reversing compression loading. After inelastic tensile cyclic loading of the longitudinal reinforcement inside the confined concrete, large cracks developed in confined concrete. The size of the cracks due to inelastic tensile deformation of the longitudinal mild steel reinforcement in TS02 was 4 times greater than in TS01. At the end of the reversed compression loading after the maximum inelastic tensile loading, the average size of cracks in TS02 was 2 times greater than in TS01 (i.e., 0.1 in. in TS02 compared to 0.05 in. in TS01).

The strain gage data for longitudinal reinforcement bars indicates that the strain in compression was less than the strain in tension in reversing compression load steps of the inelastic tensile load steps of the longitudinal mild steel reinforcement. The compression strains were zero in a compression load that was 2.5 times greater than the quantity of the maximum tension load of the longitudinal mild steel reinforcement bars.

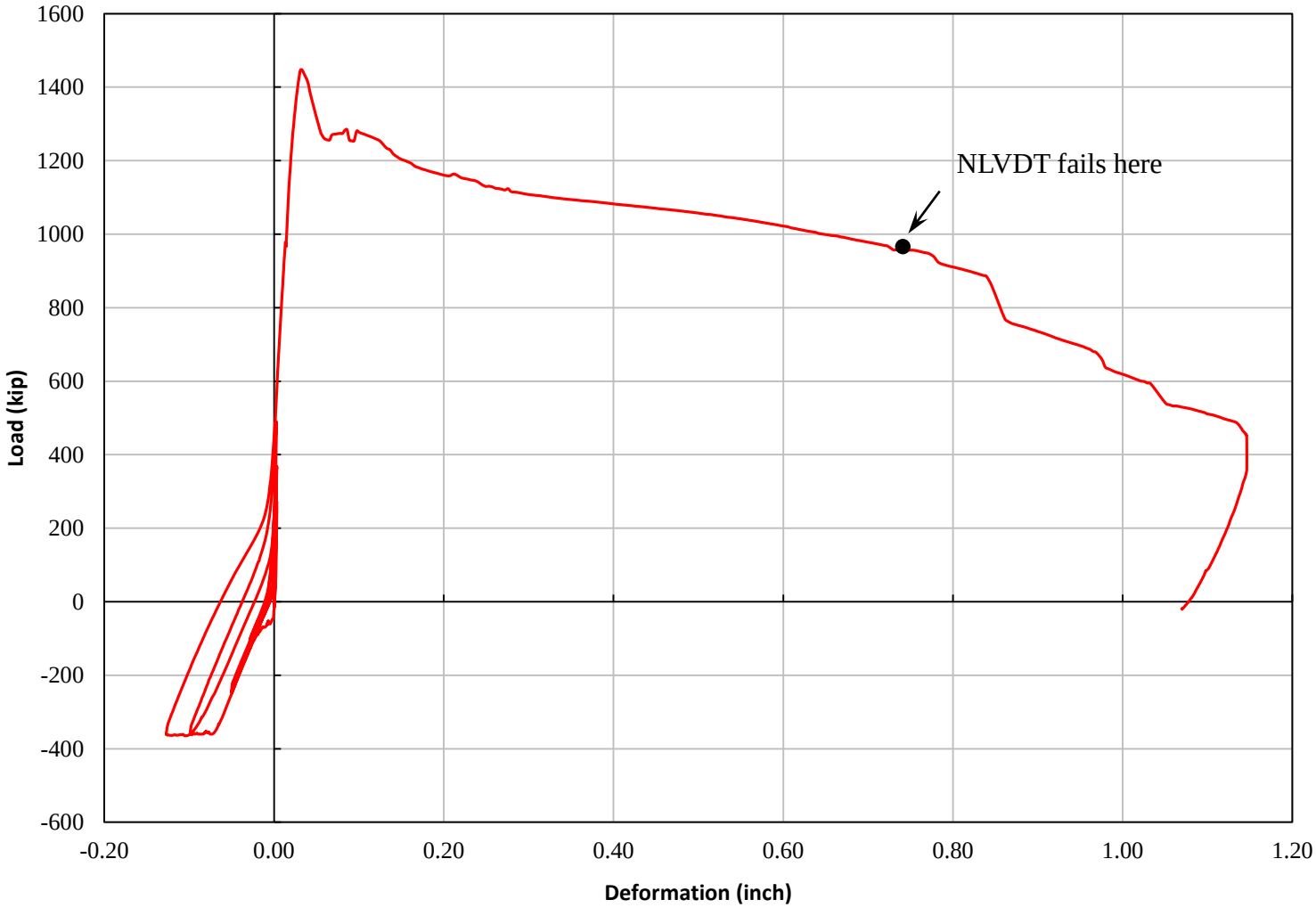

Figure 5-1: Average deformation of LVDTs for TS01

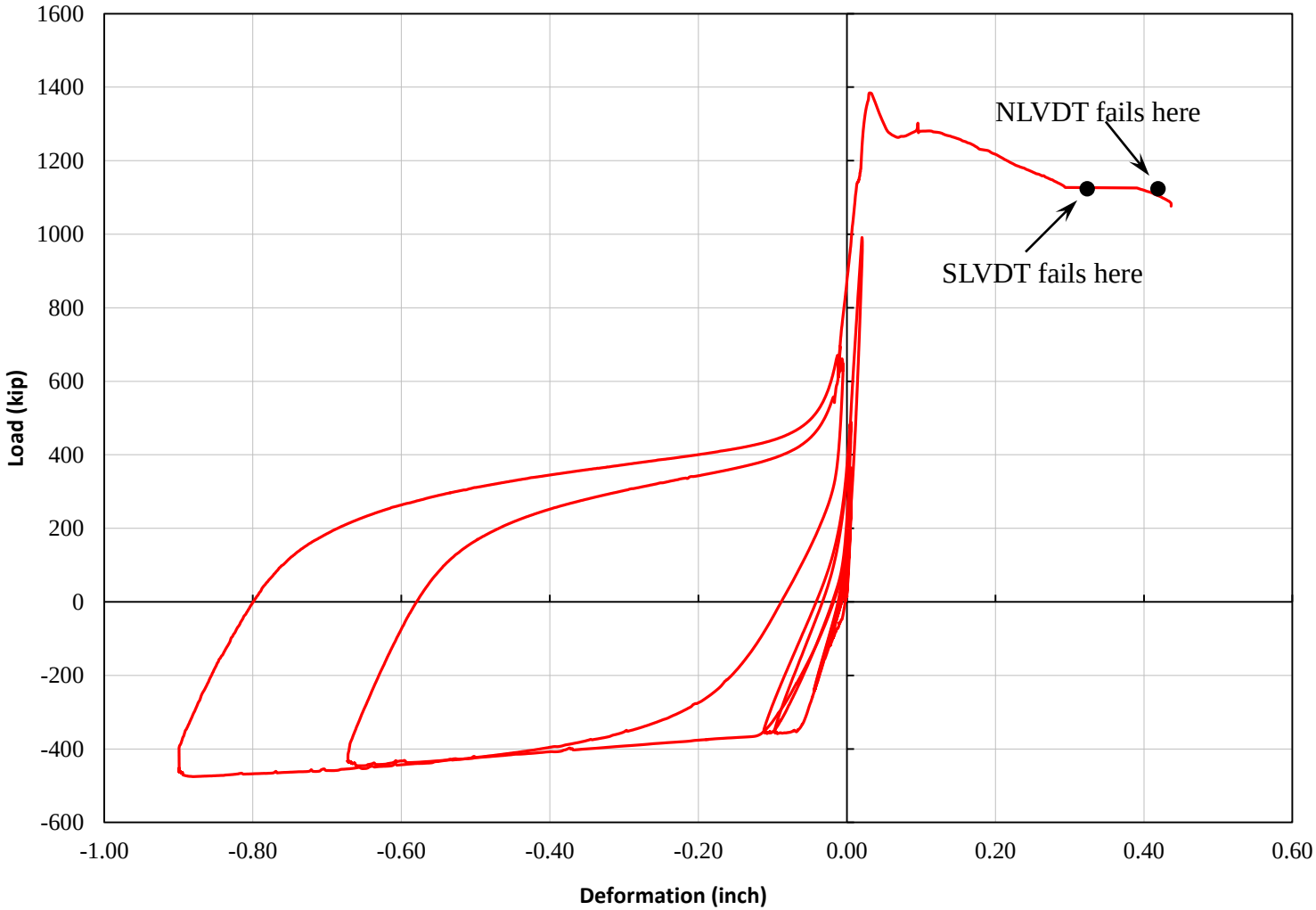

Figure 5-2: Average deformation of LVDTs for TS02

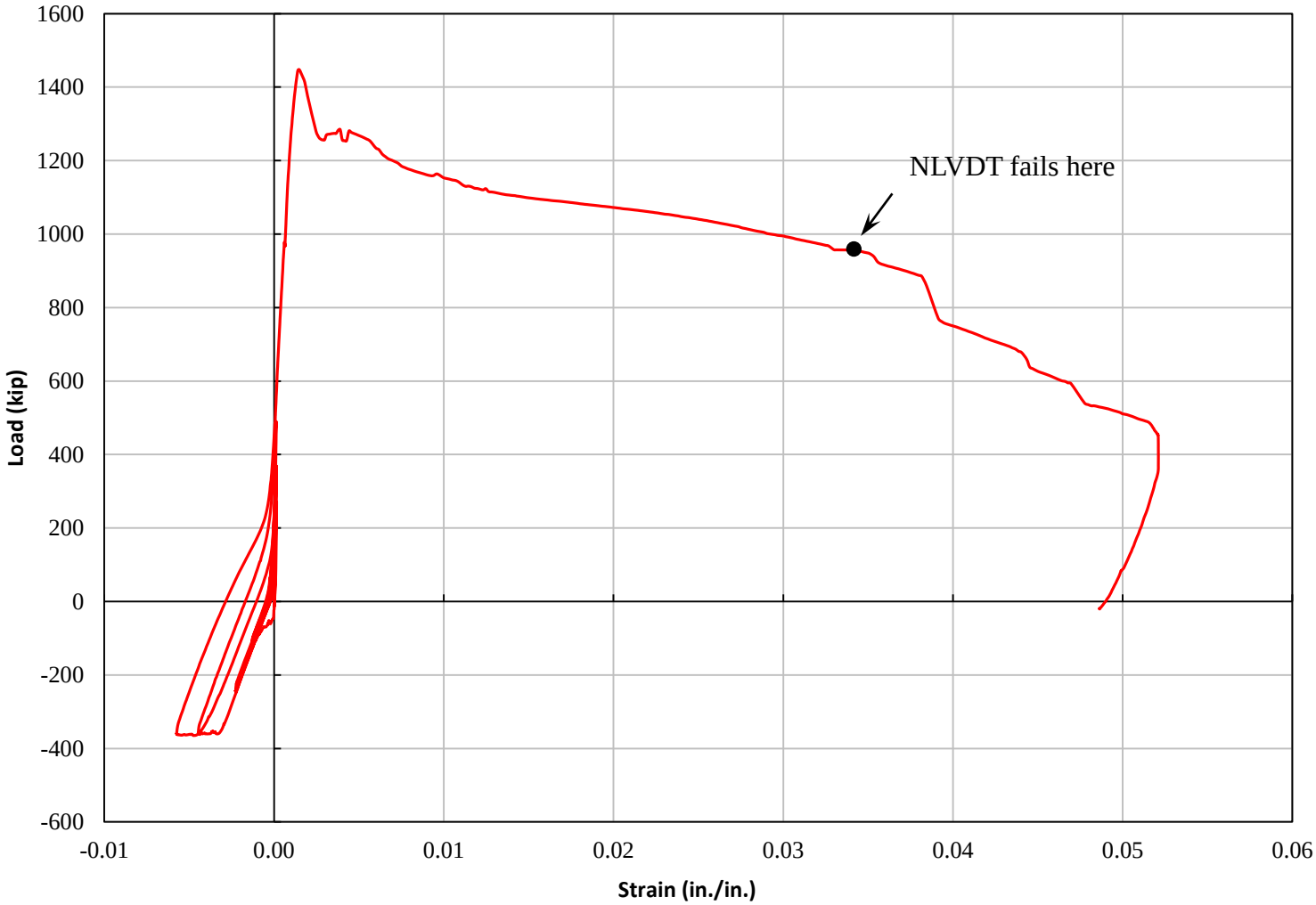

Figure 5-3: Average strain of LVDTs for TS01

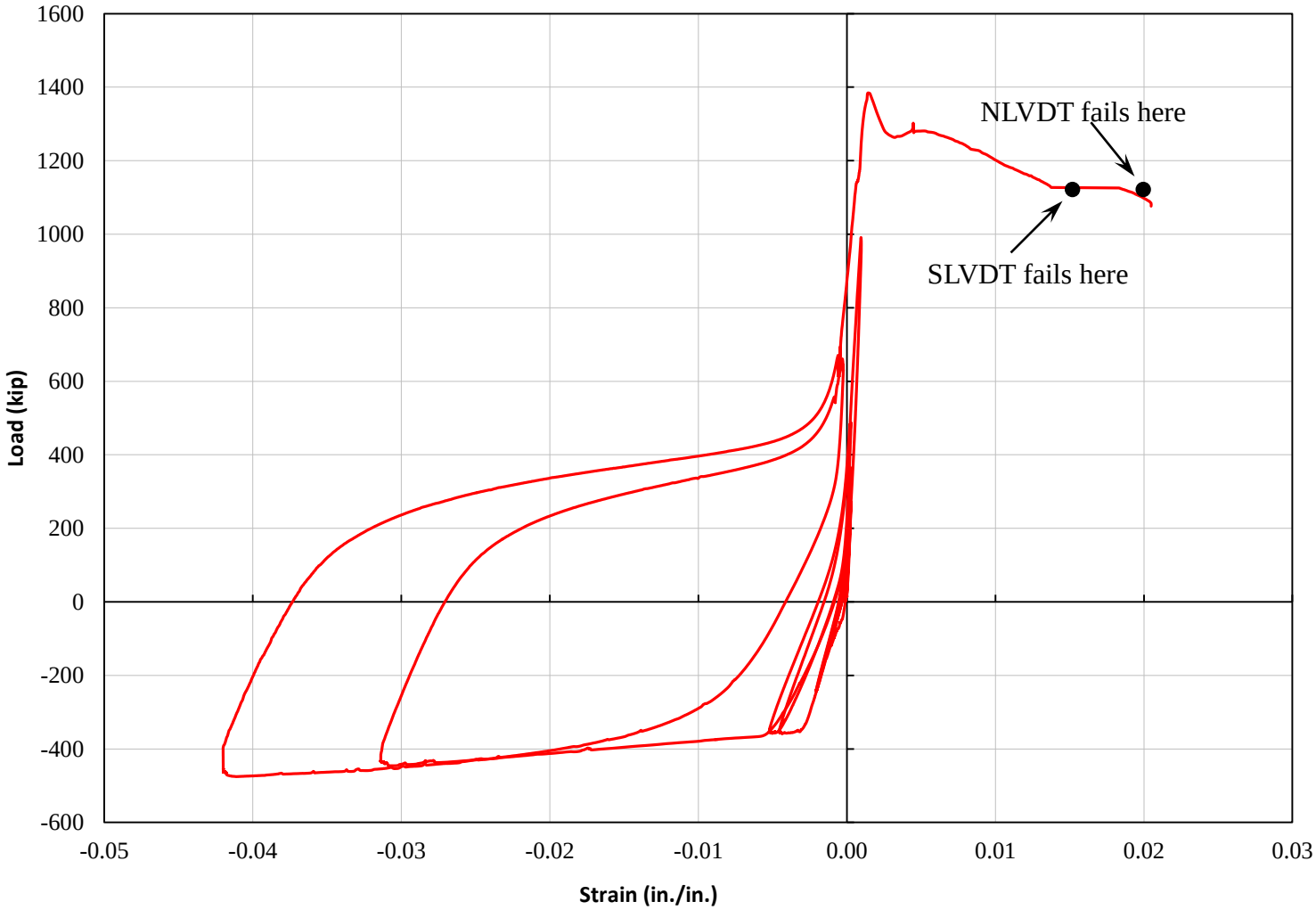

Figure 5-4: Average strain of LVDTs for TS02

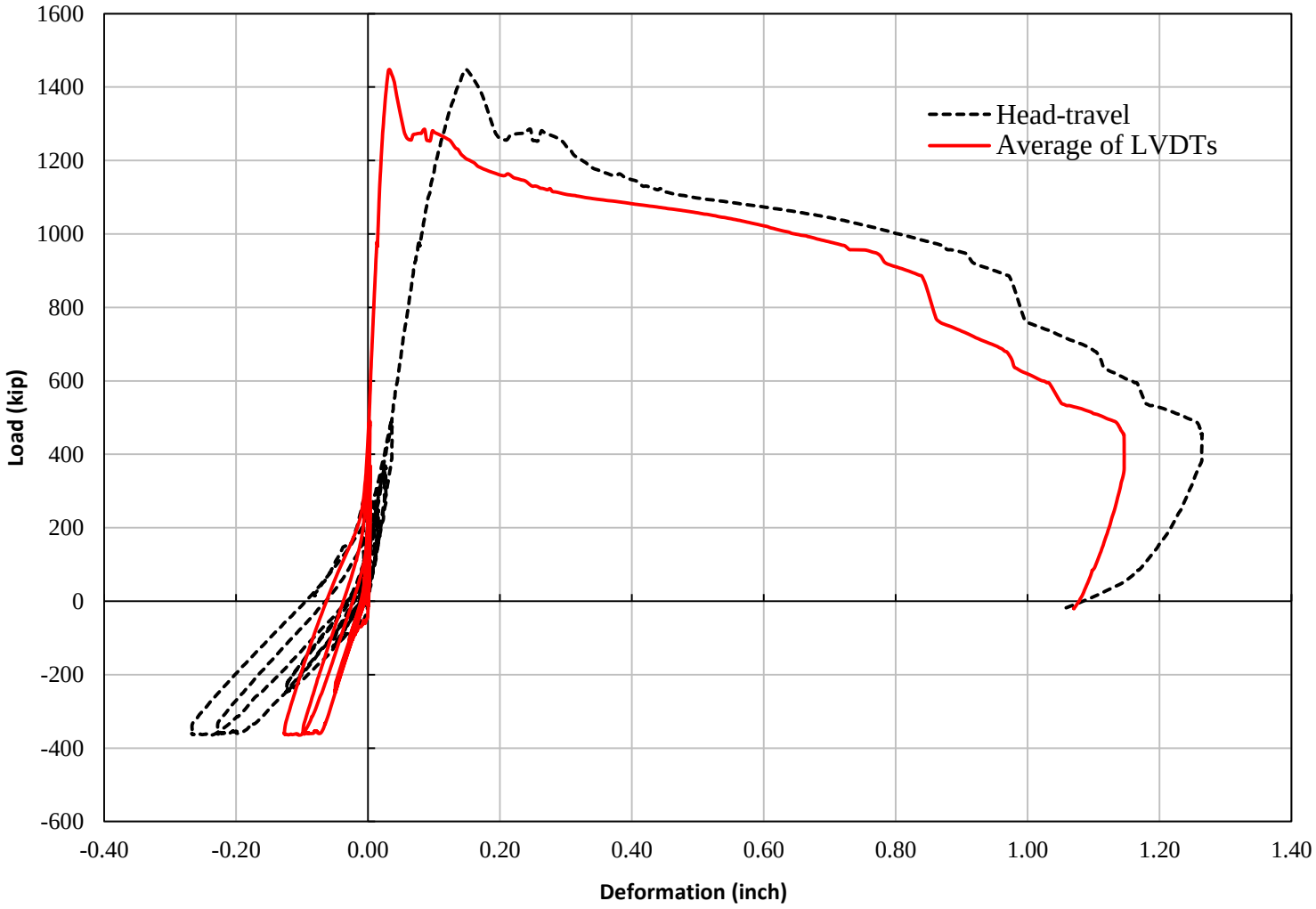

Figure 5-5: Average of LVDTs and head-travel for TS01

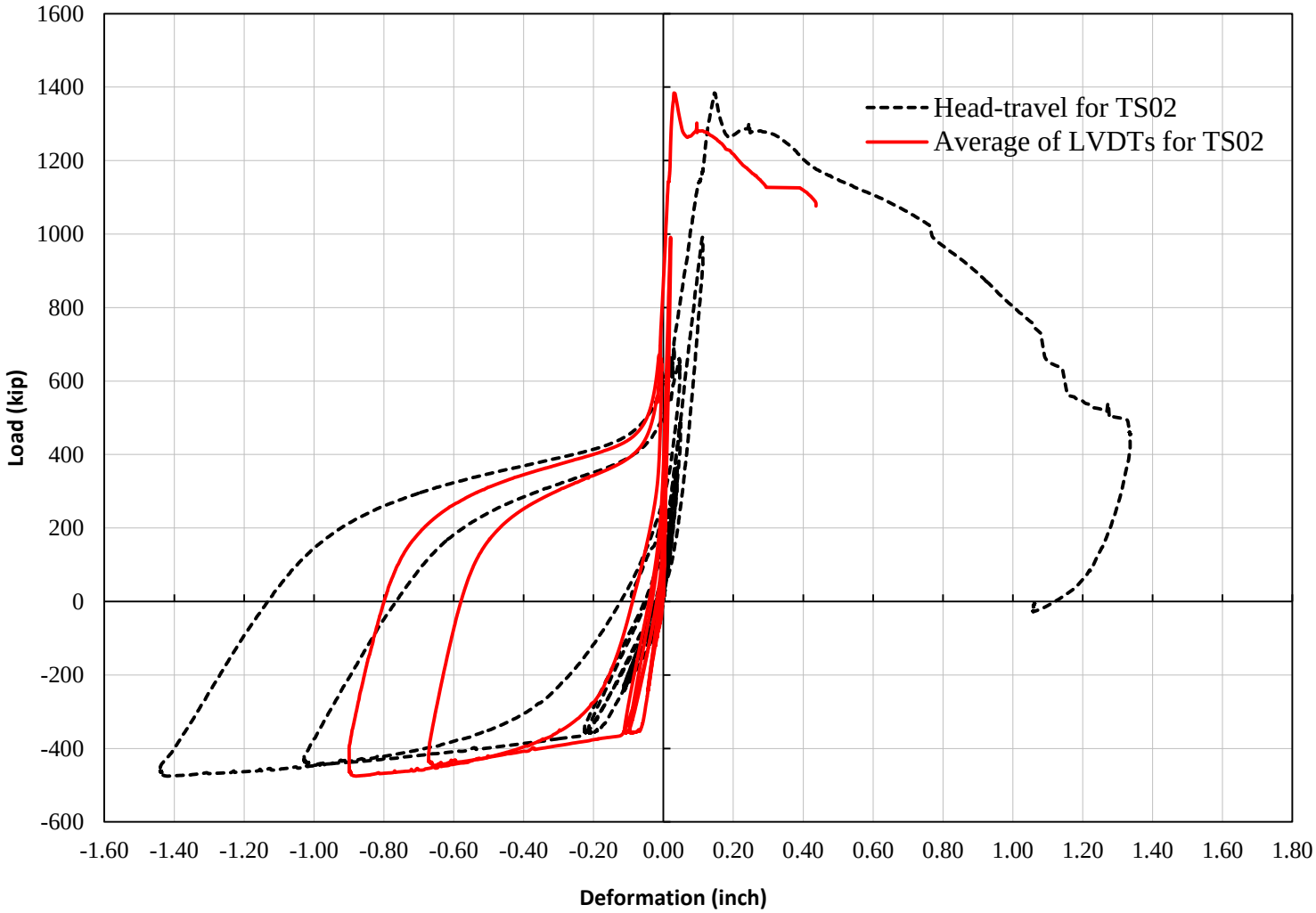

Figure 5-6: Average of LVDTs and head-travel for TS02

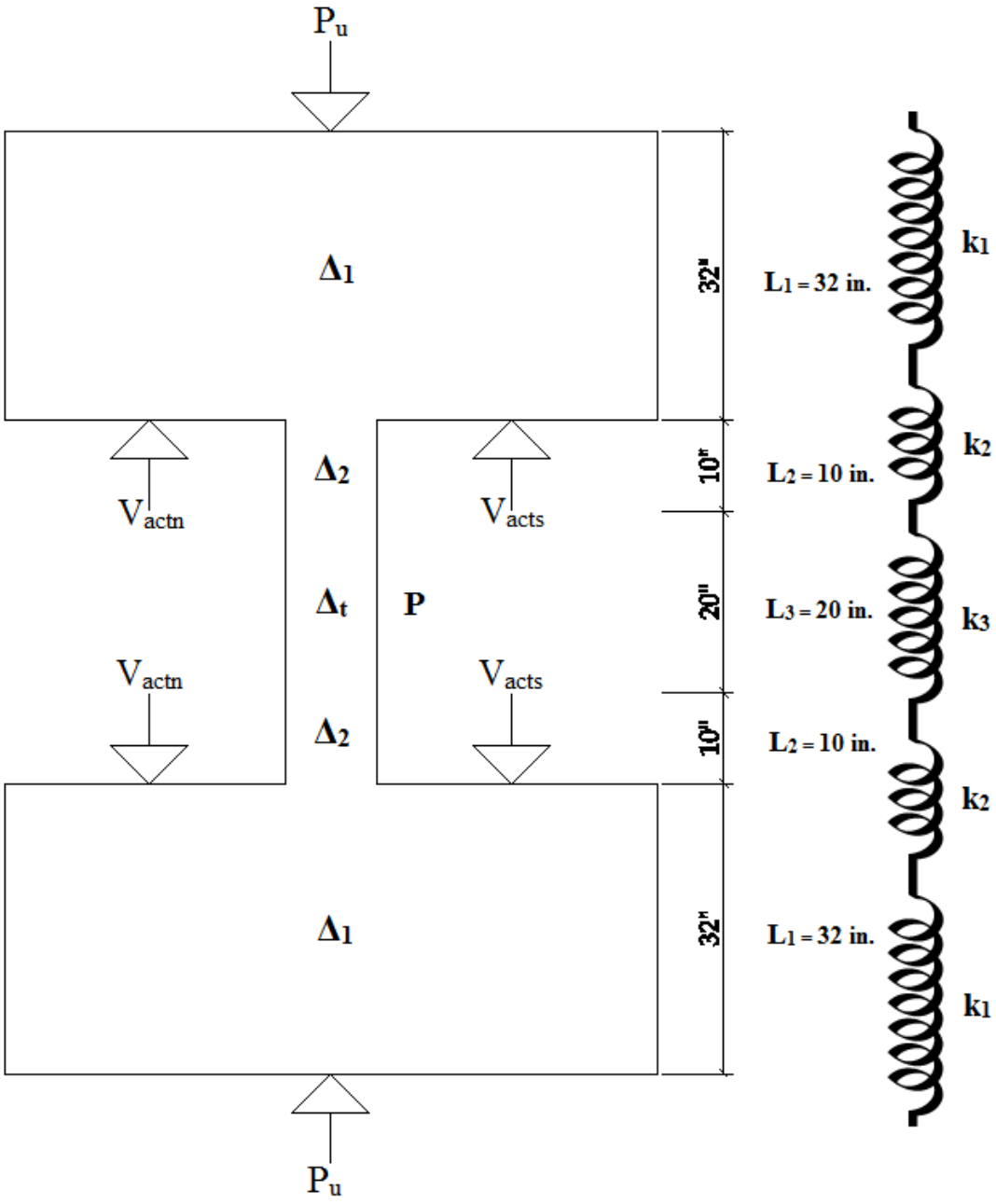

Figure 5-7: Stiffness definition and notation of test specimen

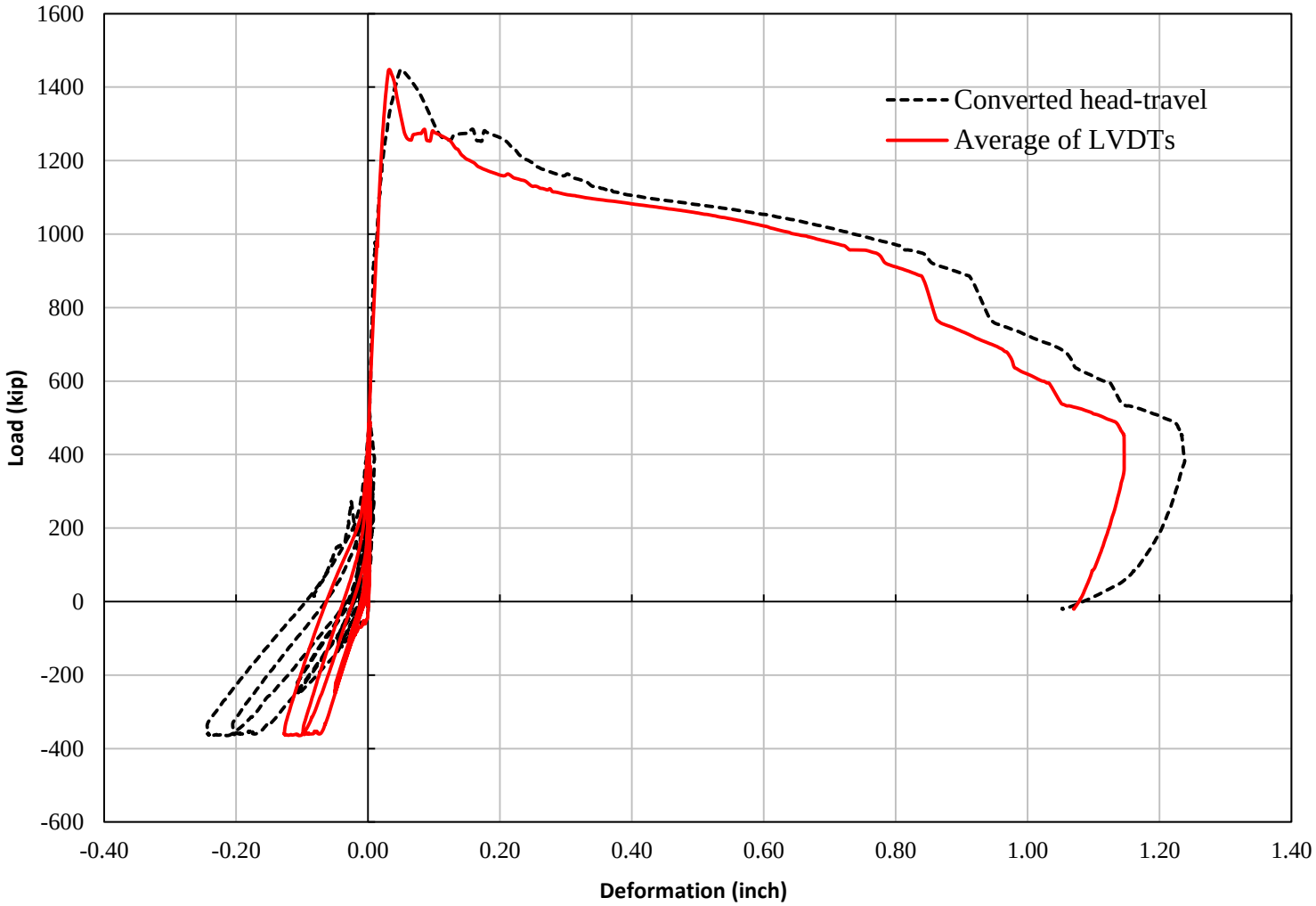

Figure 5-8: Average of LVDTs and converted head-travel for TS01

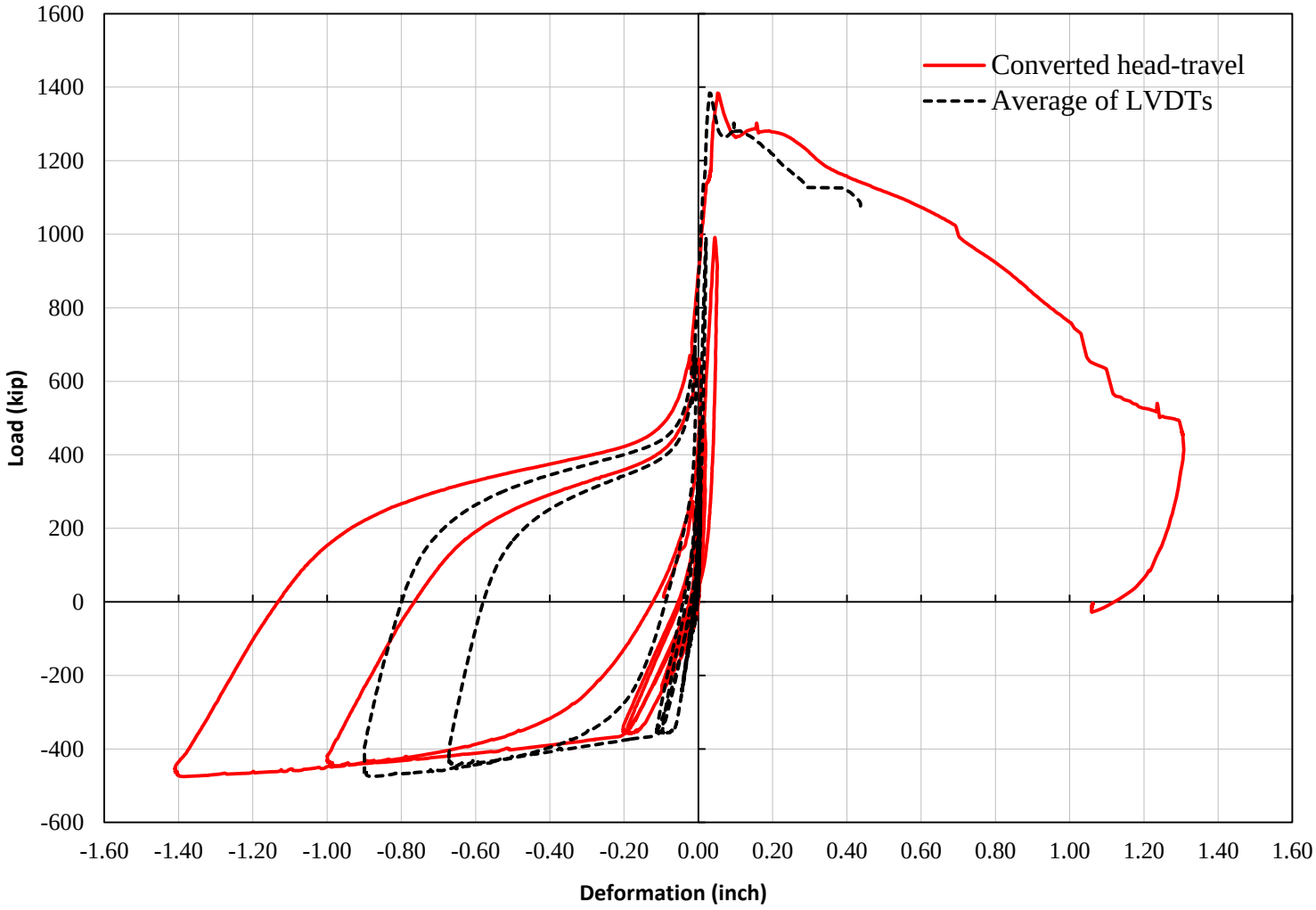

Figure 5-9: Average of LVDTs and converted head-travel for TS02

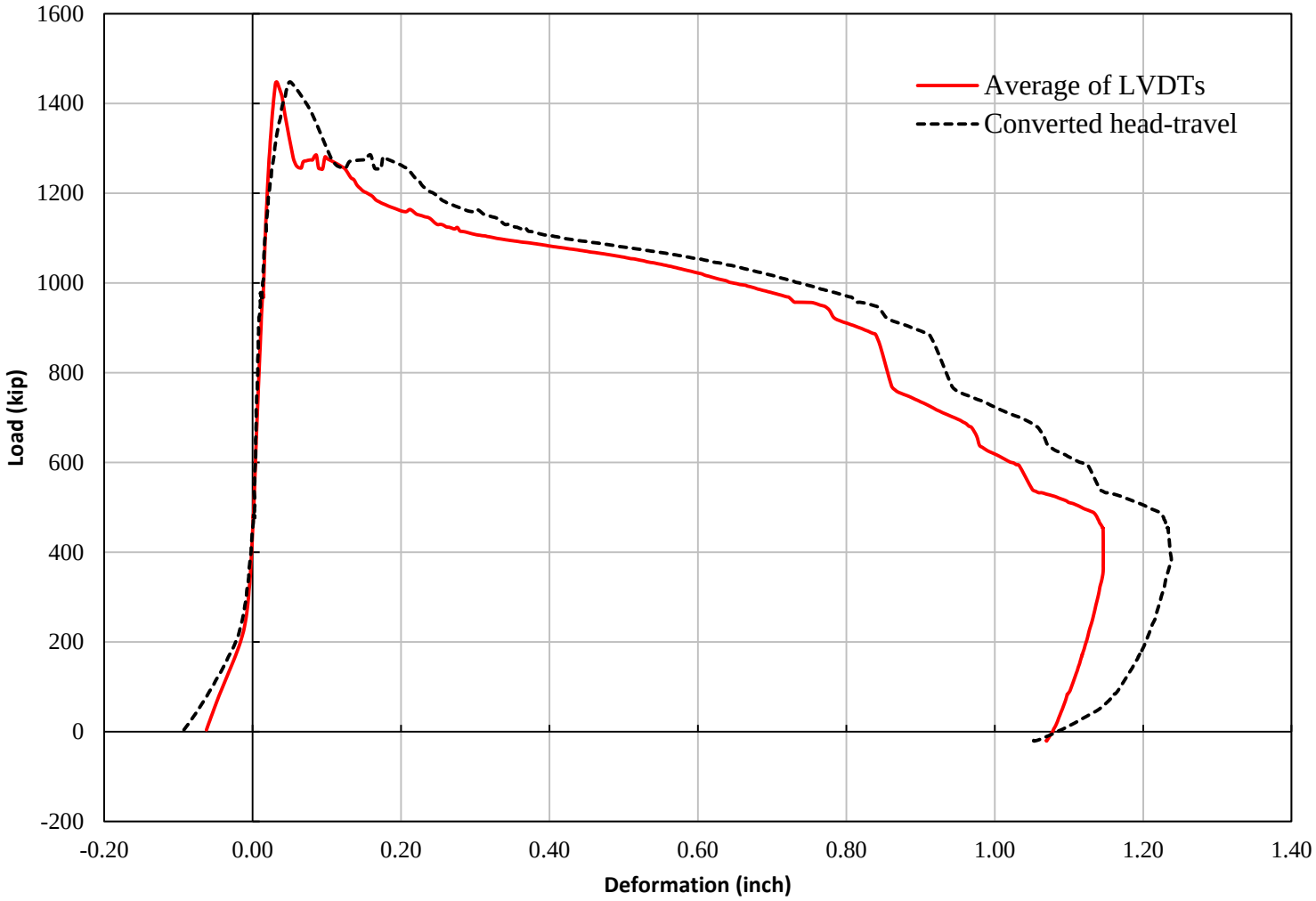

Figure 5-10: Average of LVDTs and converted head-travel for TS01 (Load Step 24)

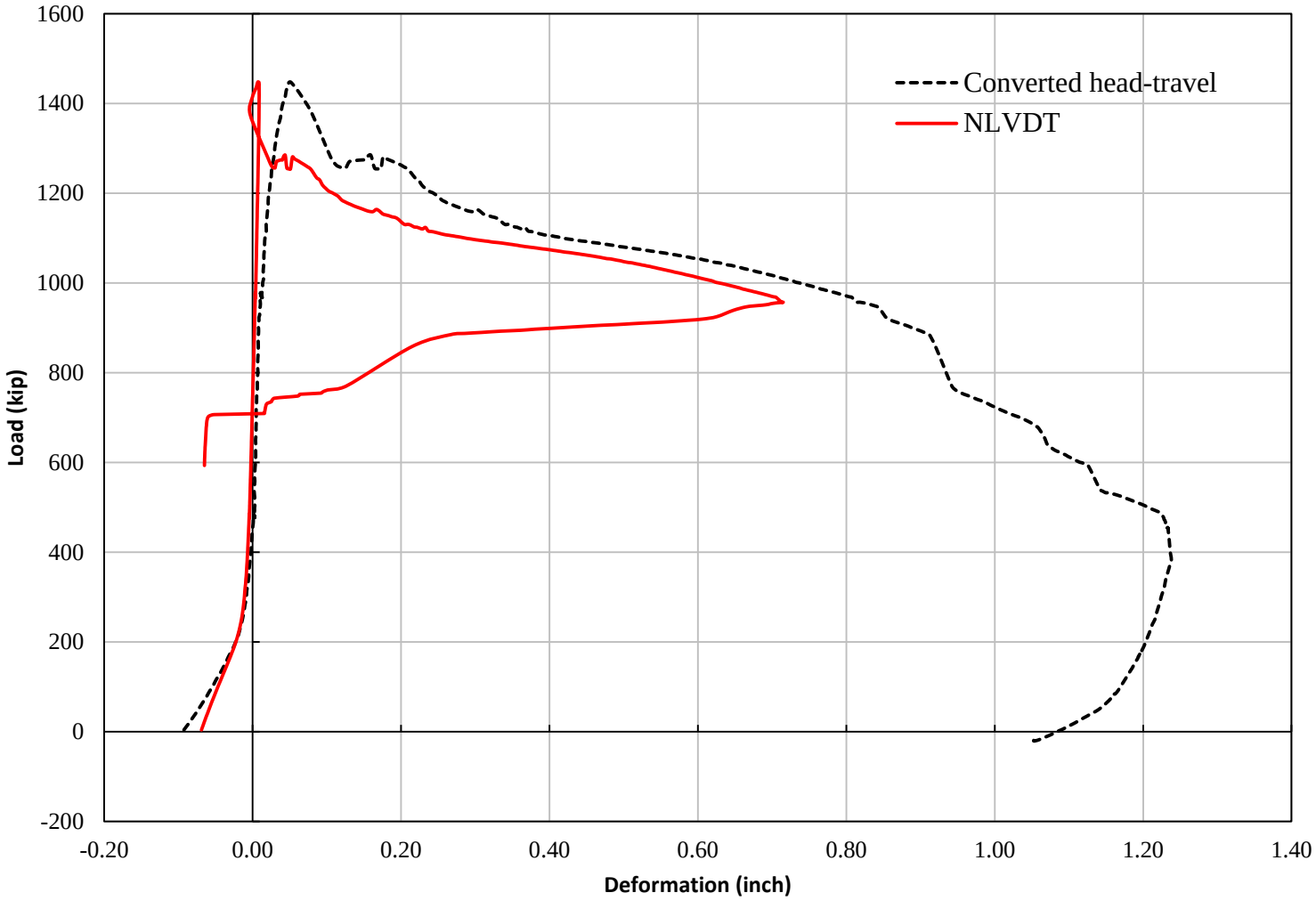

Figure 5-11: NLVDT and converted head-travel for TS01 (Load Step 24)

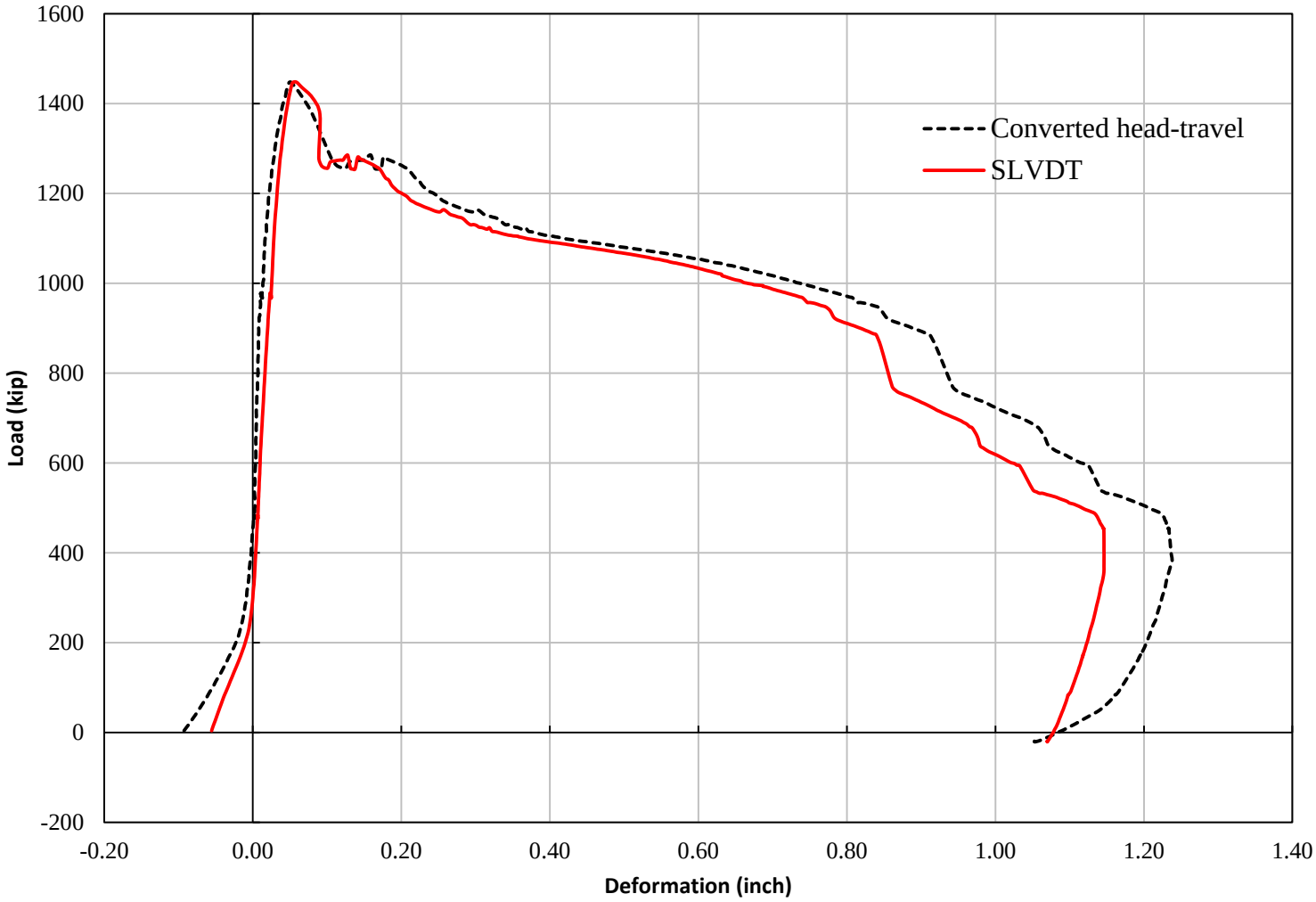

Figure 5-12: SLVDT and converted head-travel for TS01 (Load Step 24)

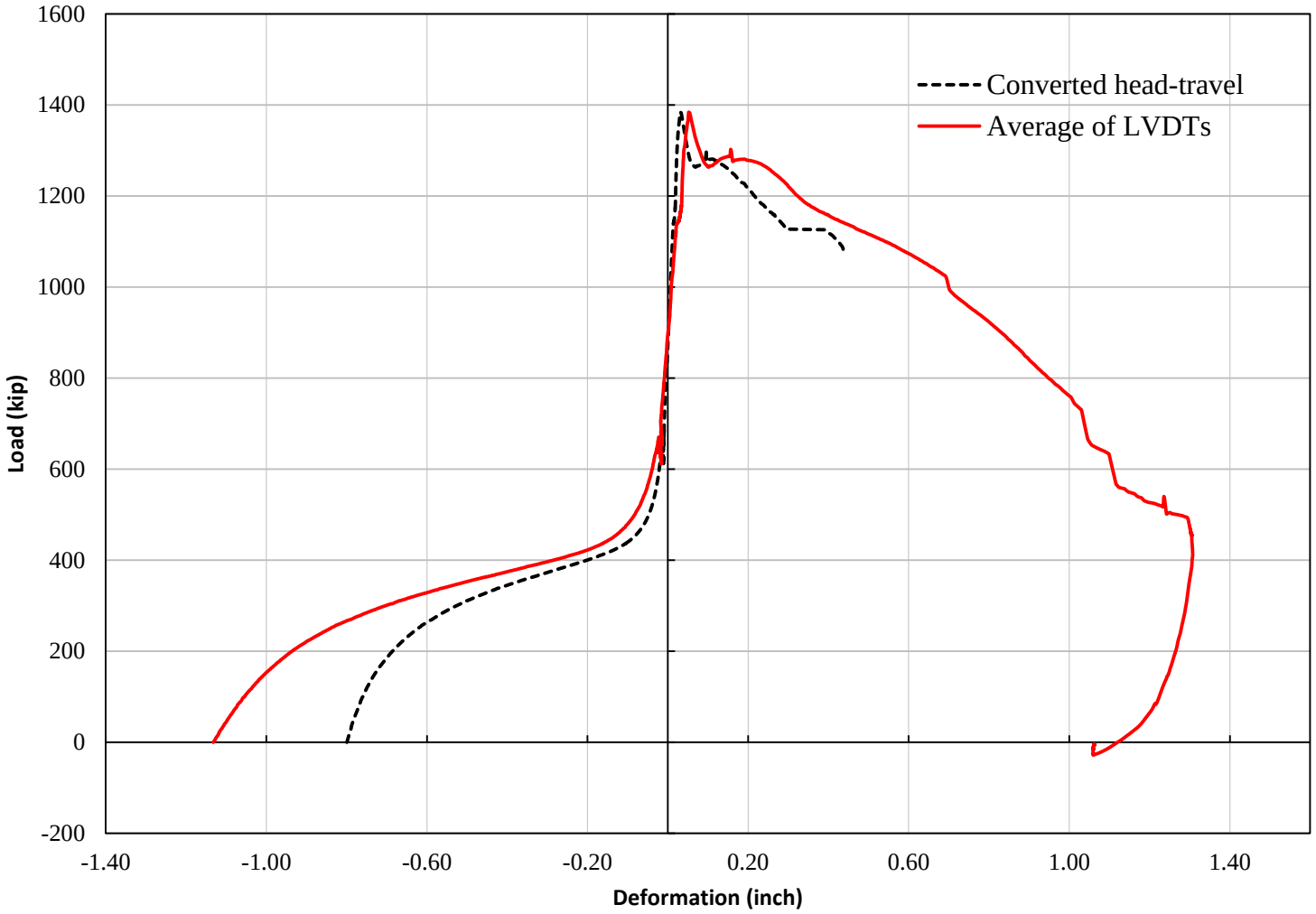

Figure 5-13: Average of LVDTs and converted head-travel for TS02 (Load Step 29)

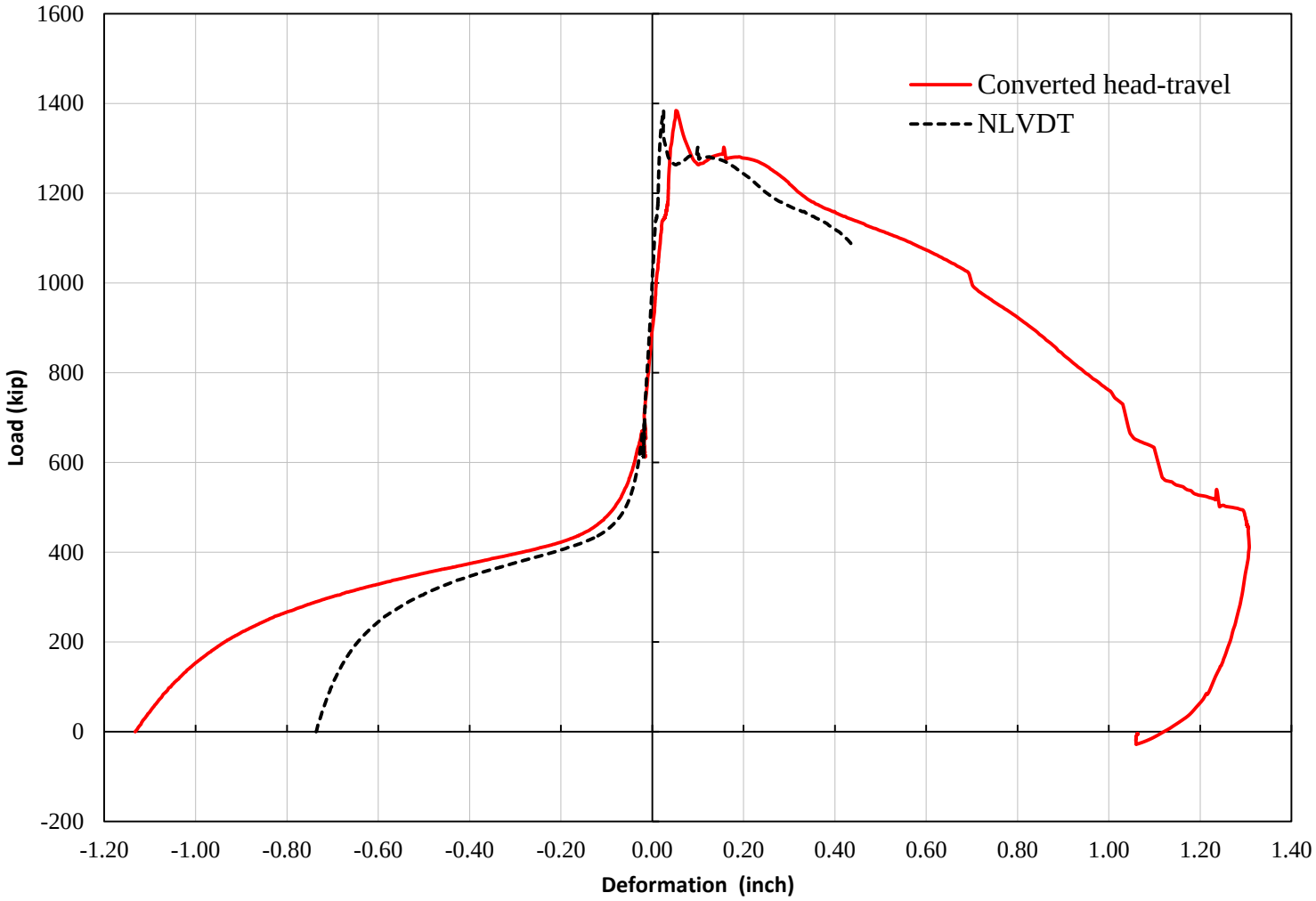

Figure 5-14: NLVDT and converted head-travel for TS02 (Load Step 29)

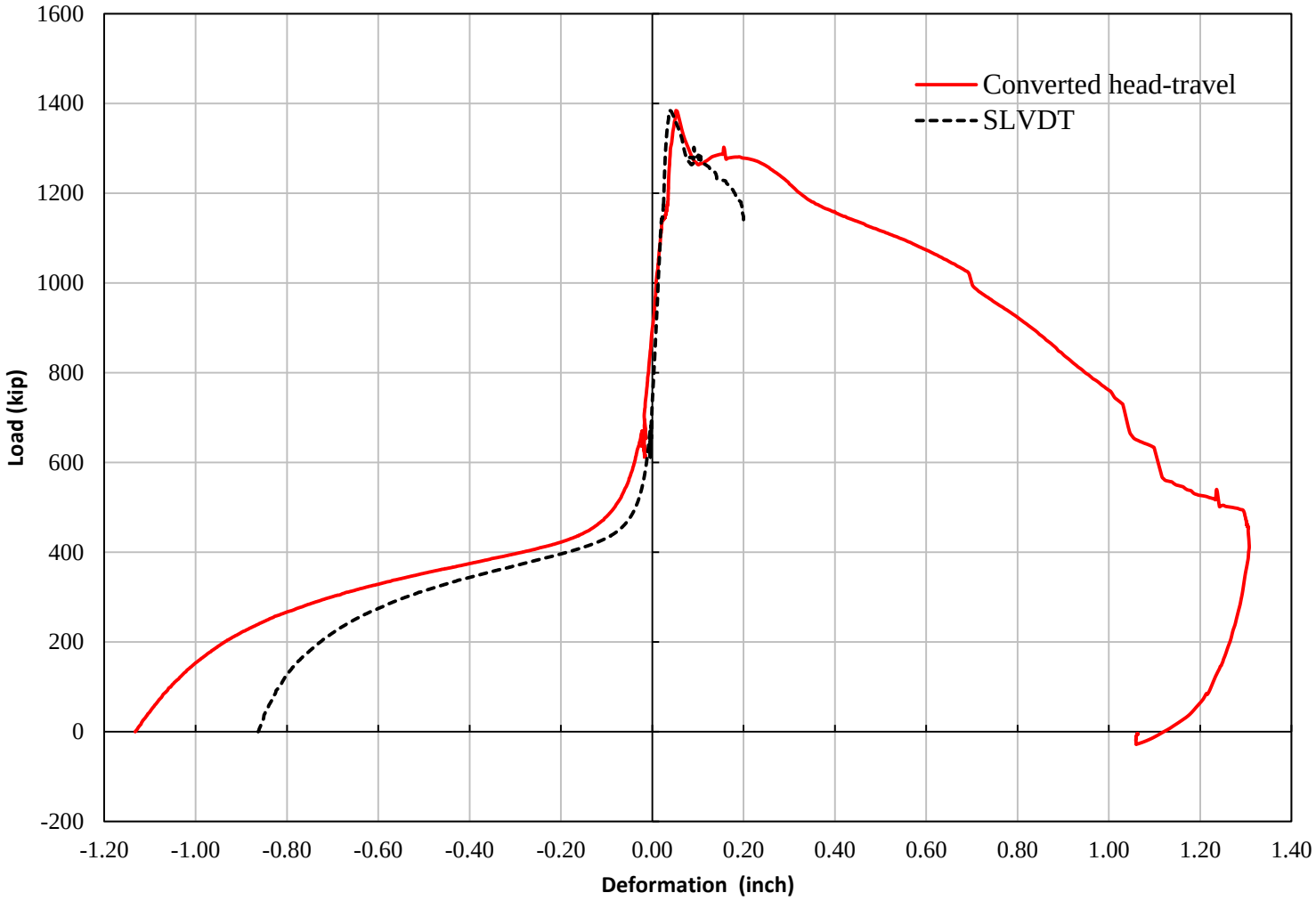

Figure 5-15: SLVDT and converted head-travel for TS02 (Load Step 29)

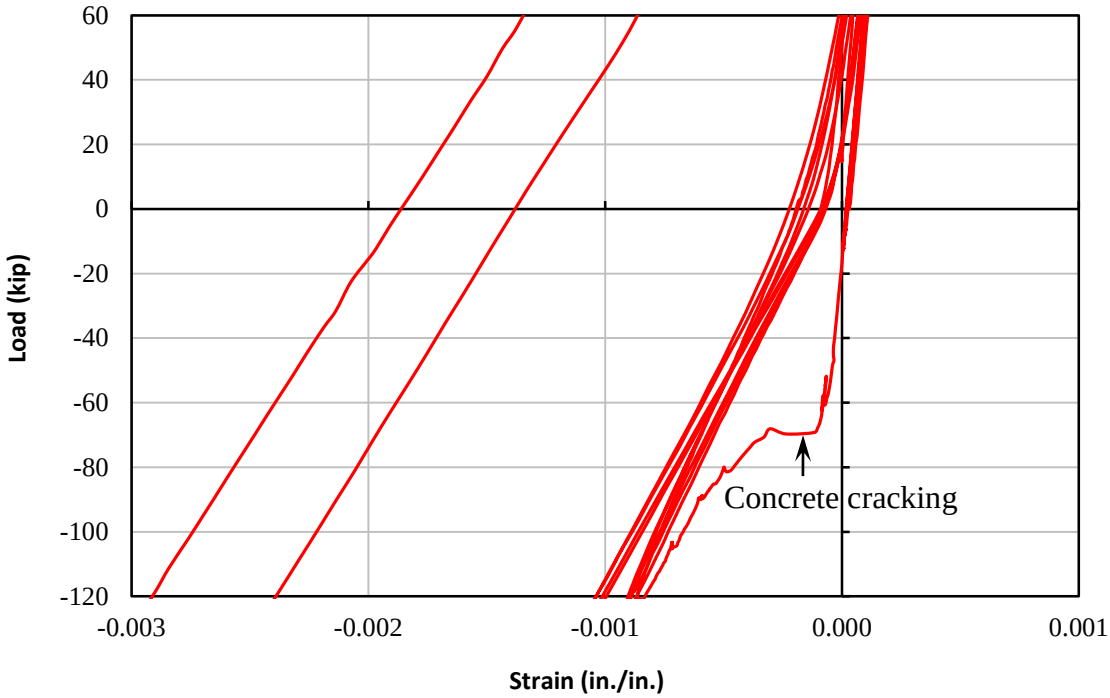

Figure 5-16: Testing region concrete cracking limit (Strain gage L1-R7-1, TS01)

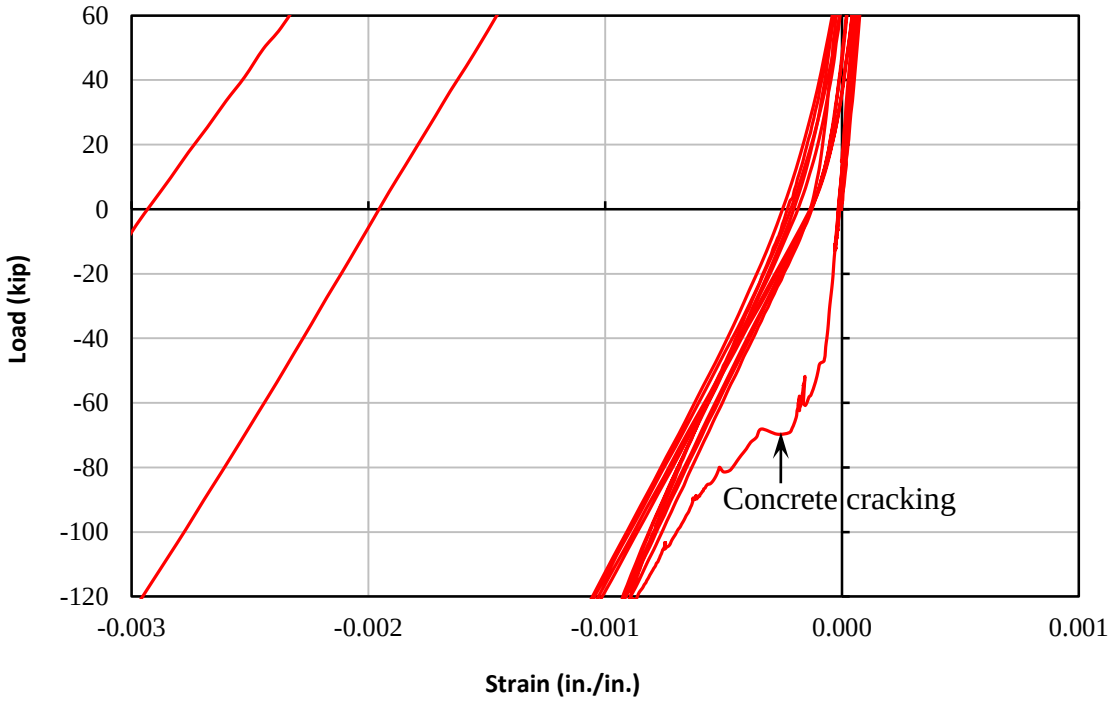

Figure 5-17: Testing region concrete cracking limit (Strain gage L1-R7-2, TS01)

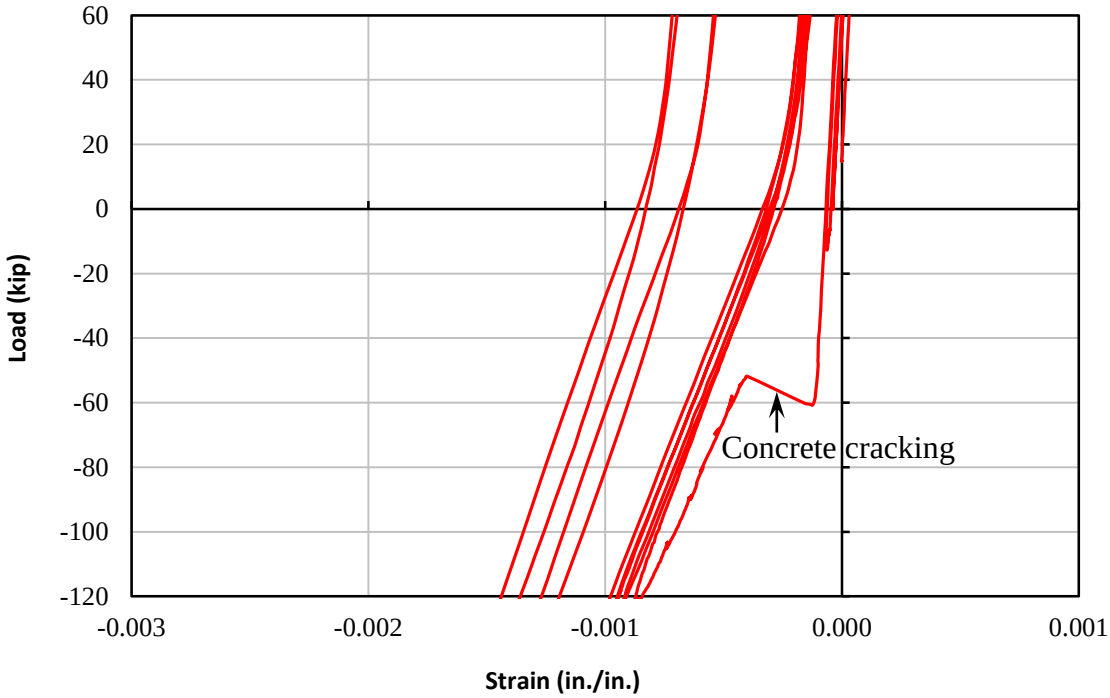

Figure 5-18: Testing region concrete cracking limit (Strain gage L2-R7-3, TS01)

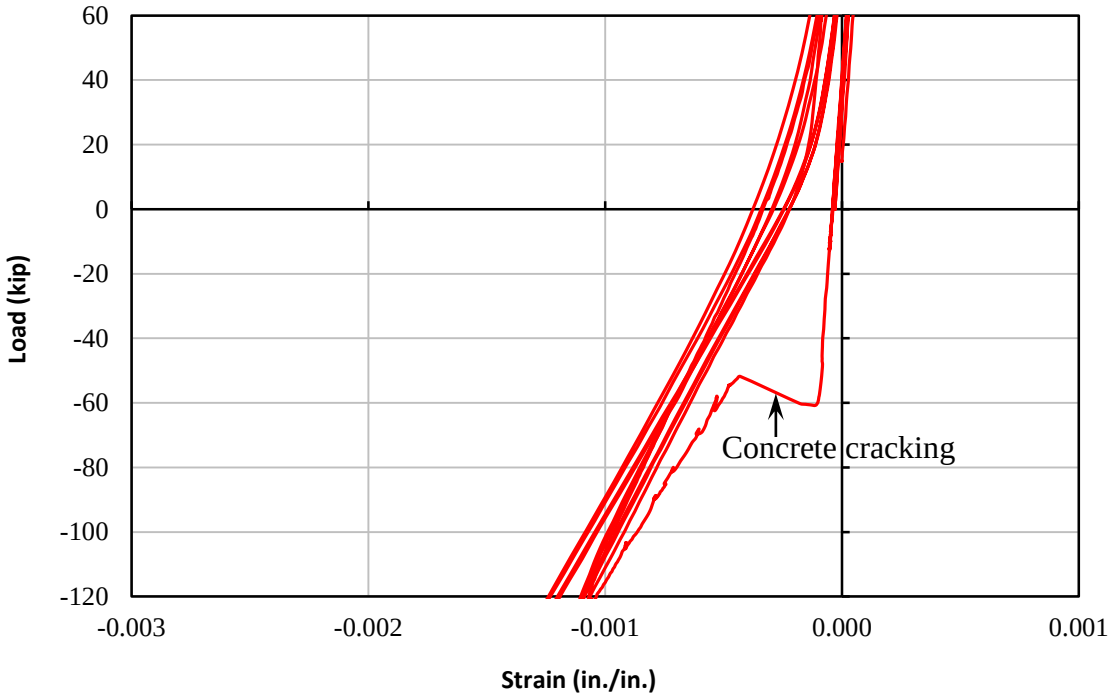

Figure 5-19: Testing region concrete cracking limit (Strain gage L2-R7-4, TS01)

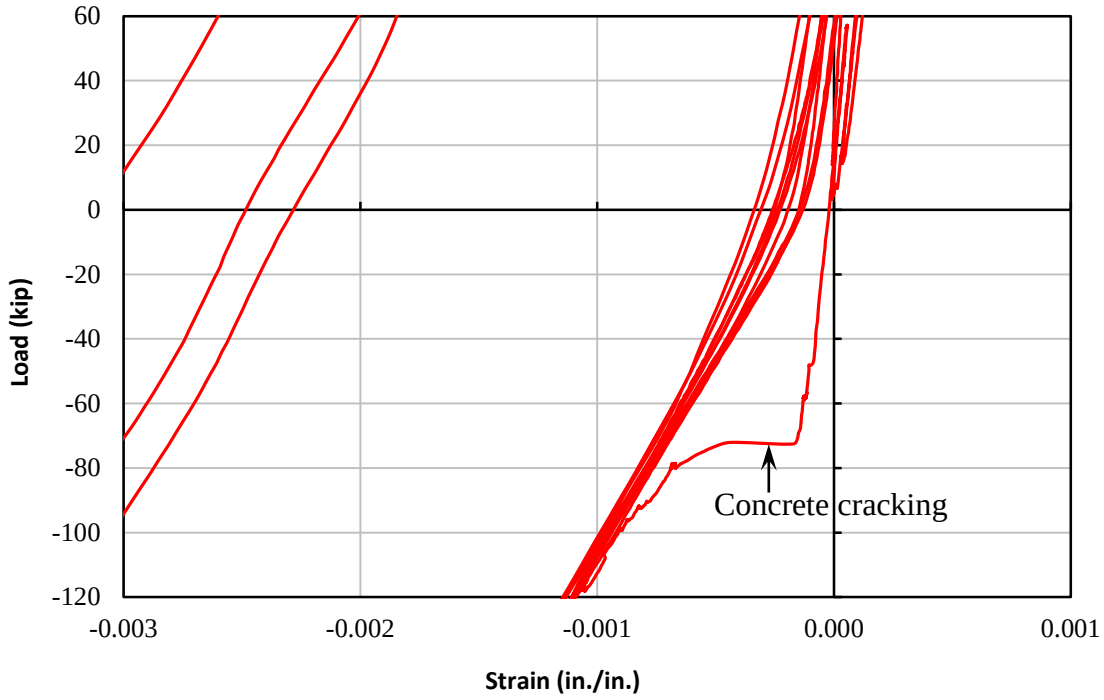

Figure 5-20: Testing region concrete cracking limit (Strain gage L2-R7-1, TS02)

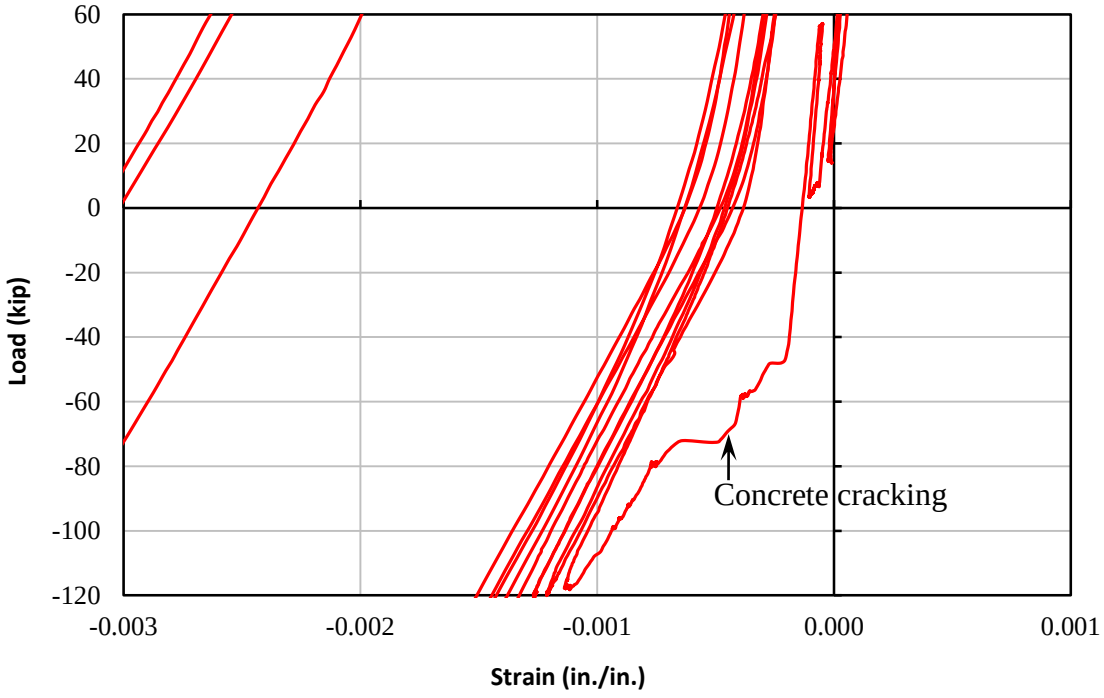

Figure 5-21: Testing region concrete cracking limit (Strain gage L2-R7-2, TS02)

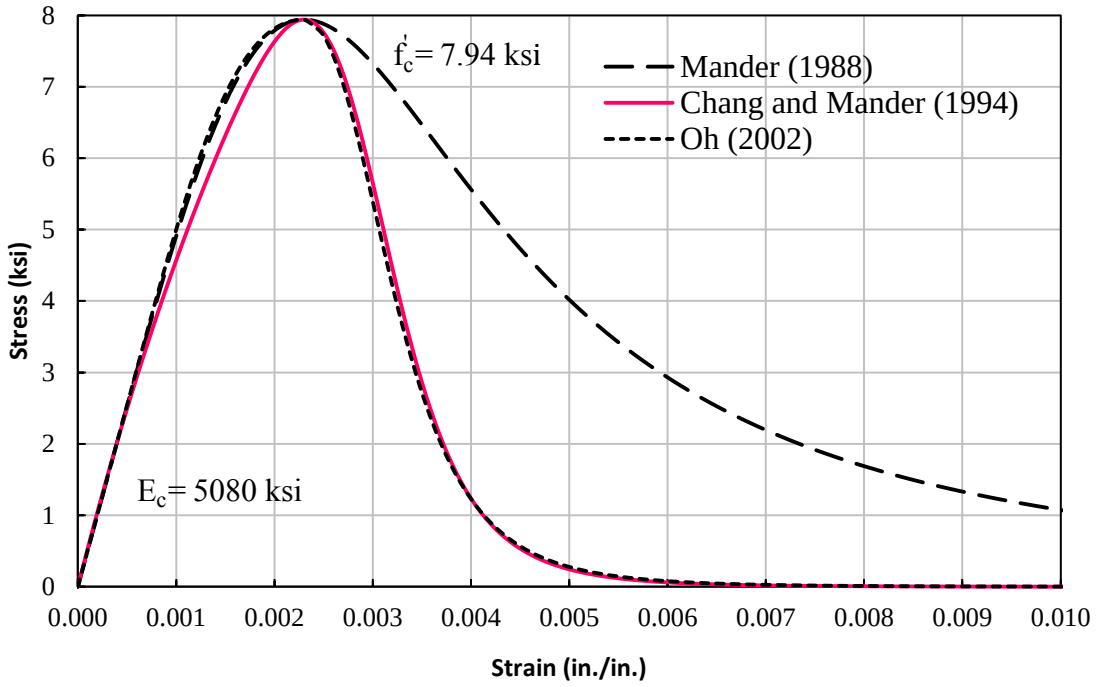

Figure 5-22: Compression stress-strain models for cover concrete

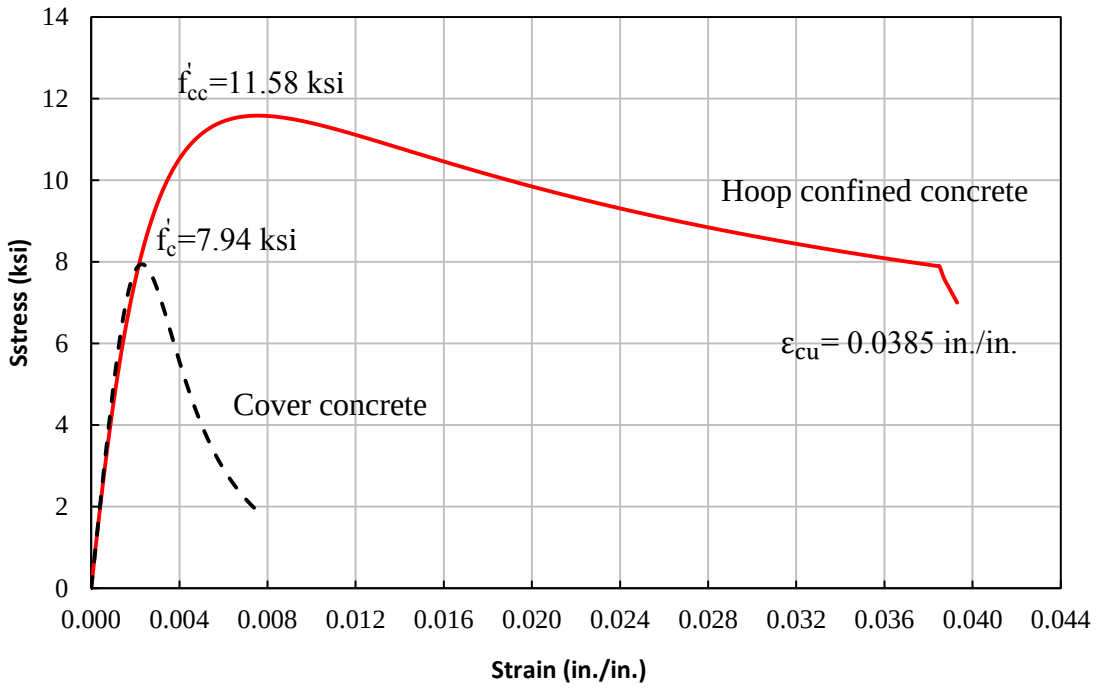

Figure 5-23: Mander (1988) stress-strain model

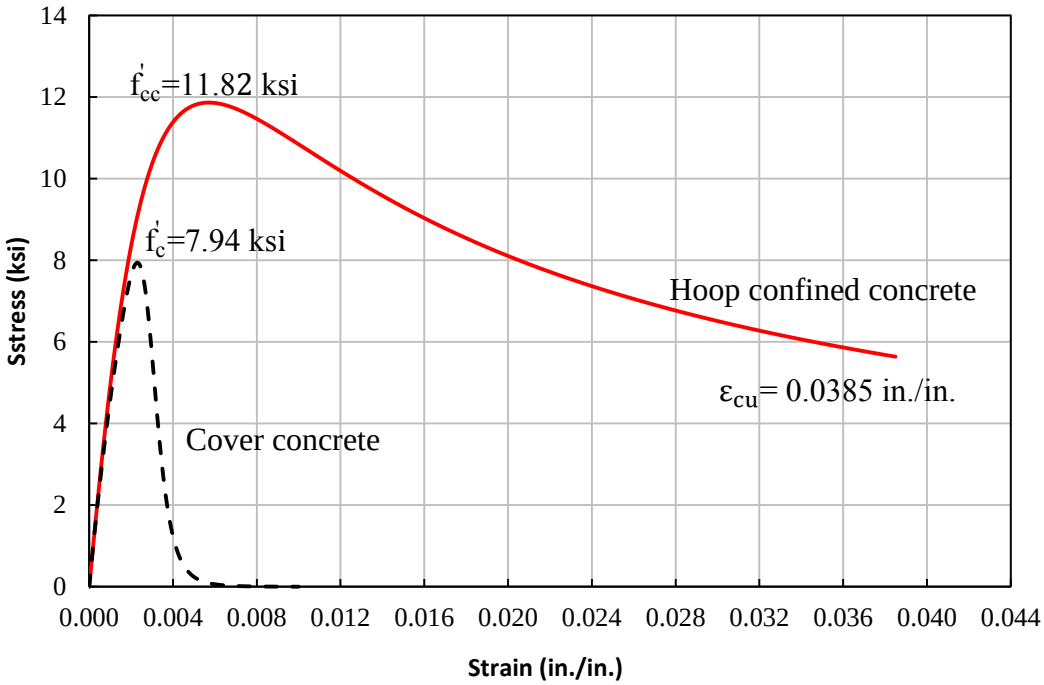

Figure 5-24: Chang and Mander (1994) stress-strain model

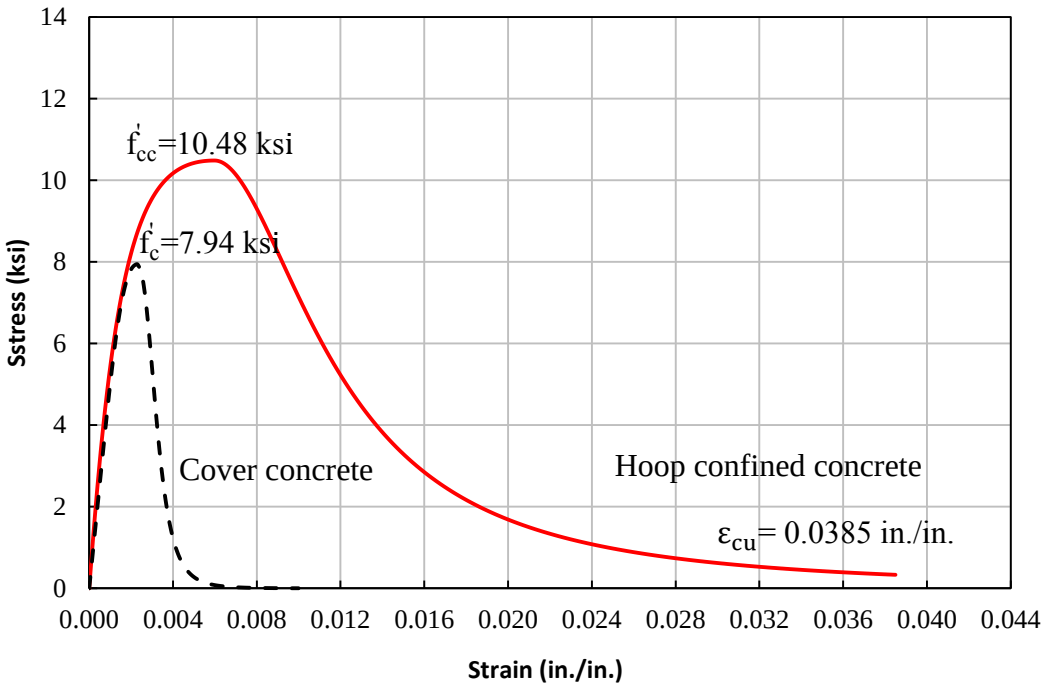

Figure 5-25: Oh (2002) stress-strain model

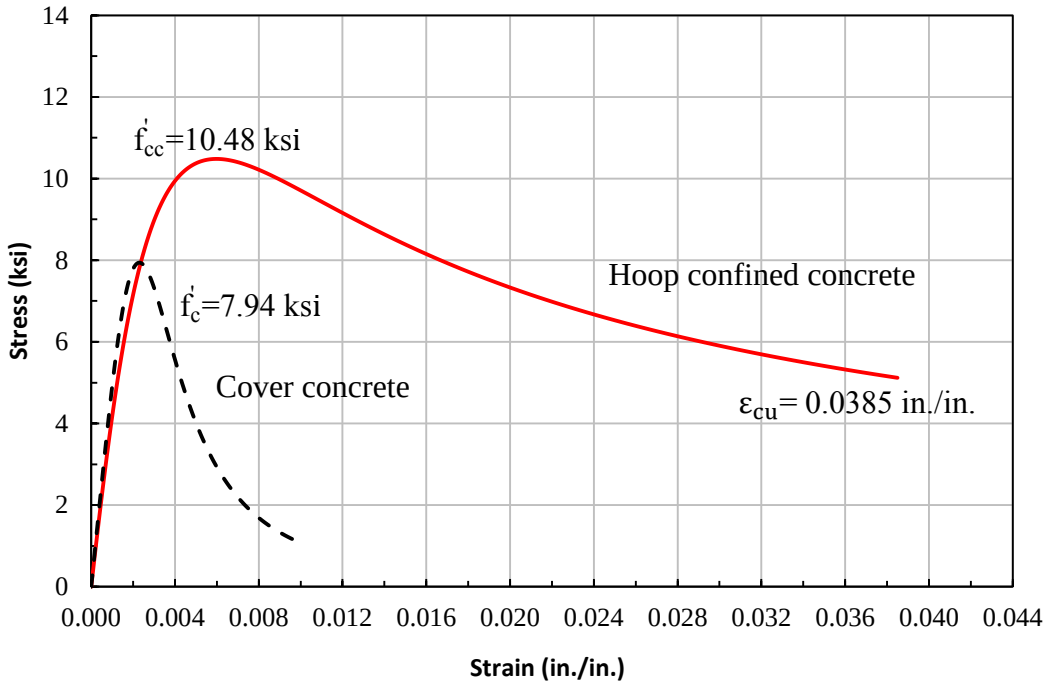

Figure 5-26: Mander (1988) stress-strain model with peak stress and the corresponding strain values from Oh (2002)

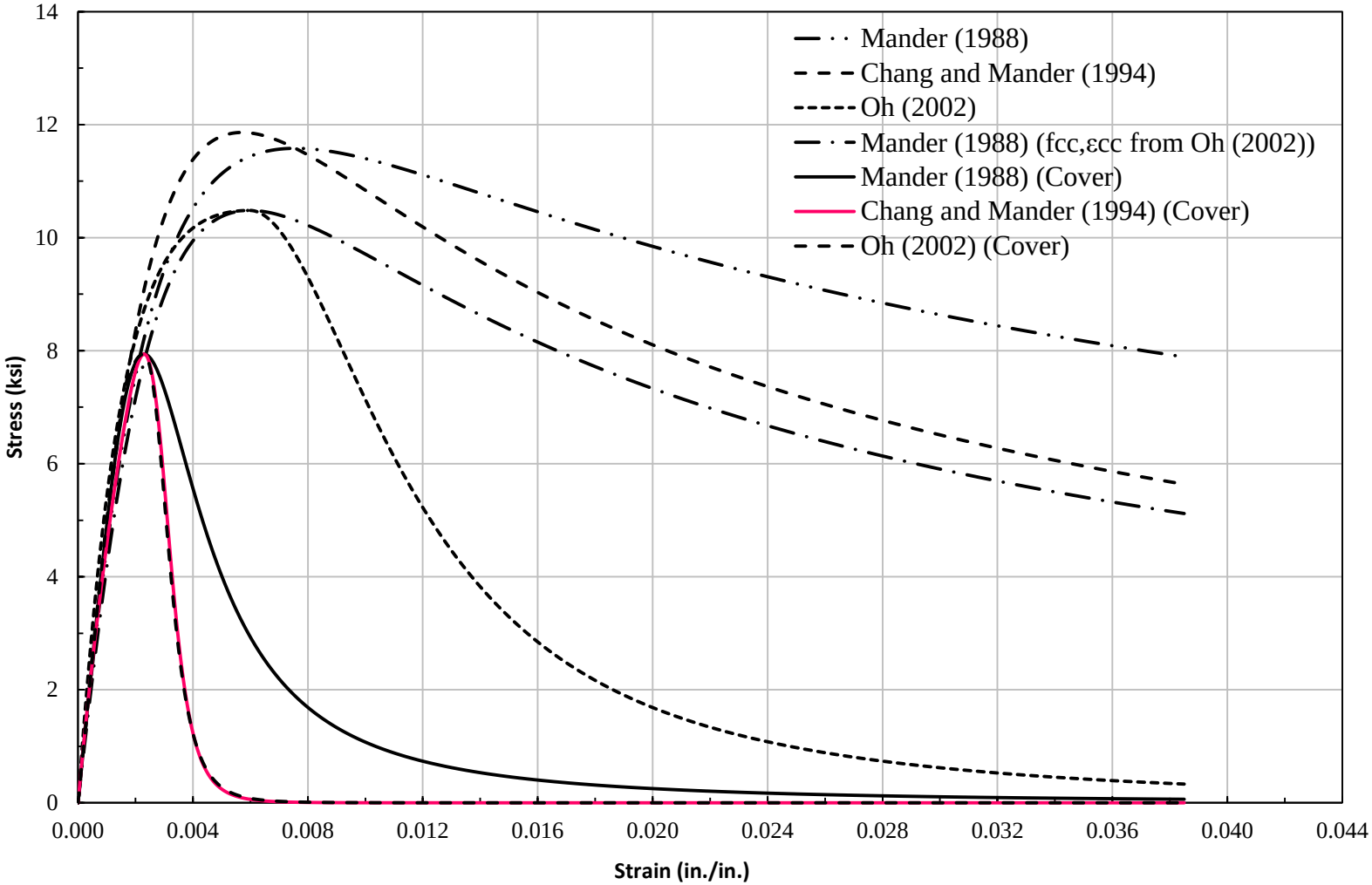

Figure 5-27: Confined and unconfined concrete stress-strain models for testing region

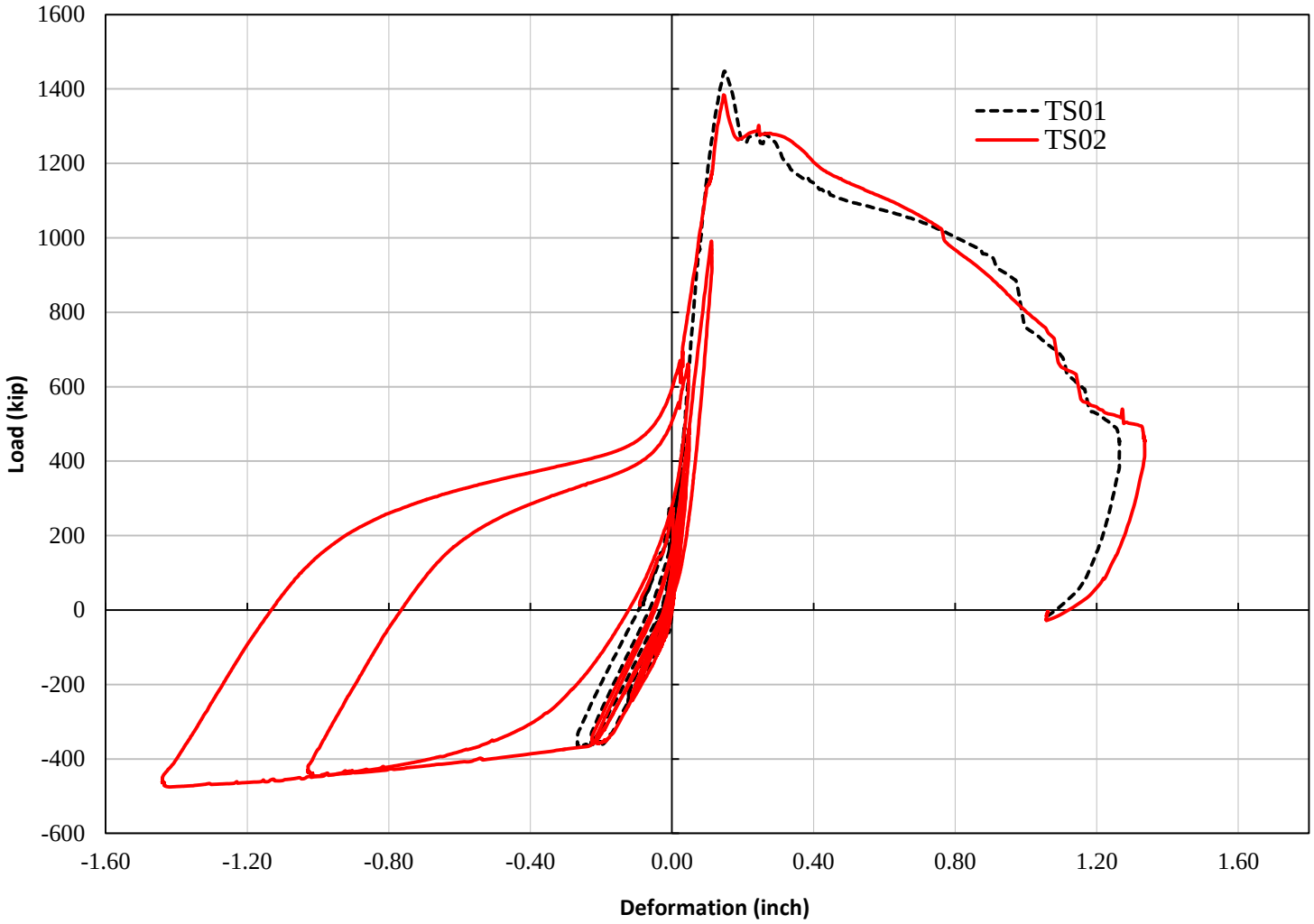

Figure 5-28: Load versus specimen deformation using head-travel data

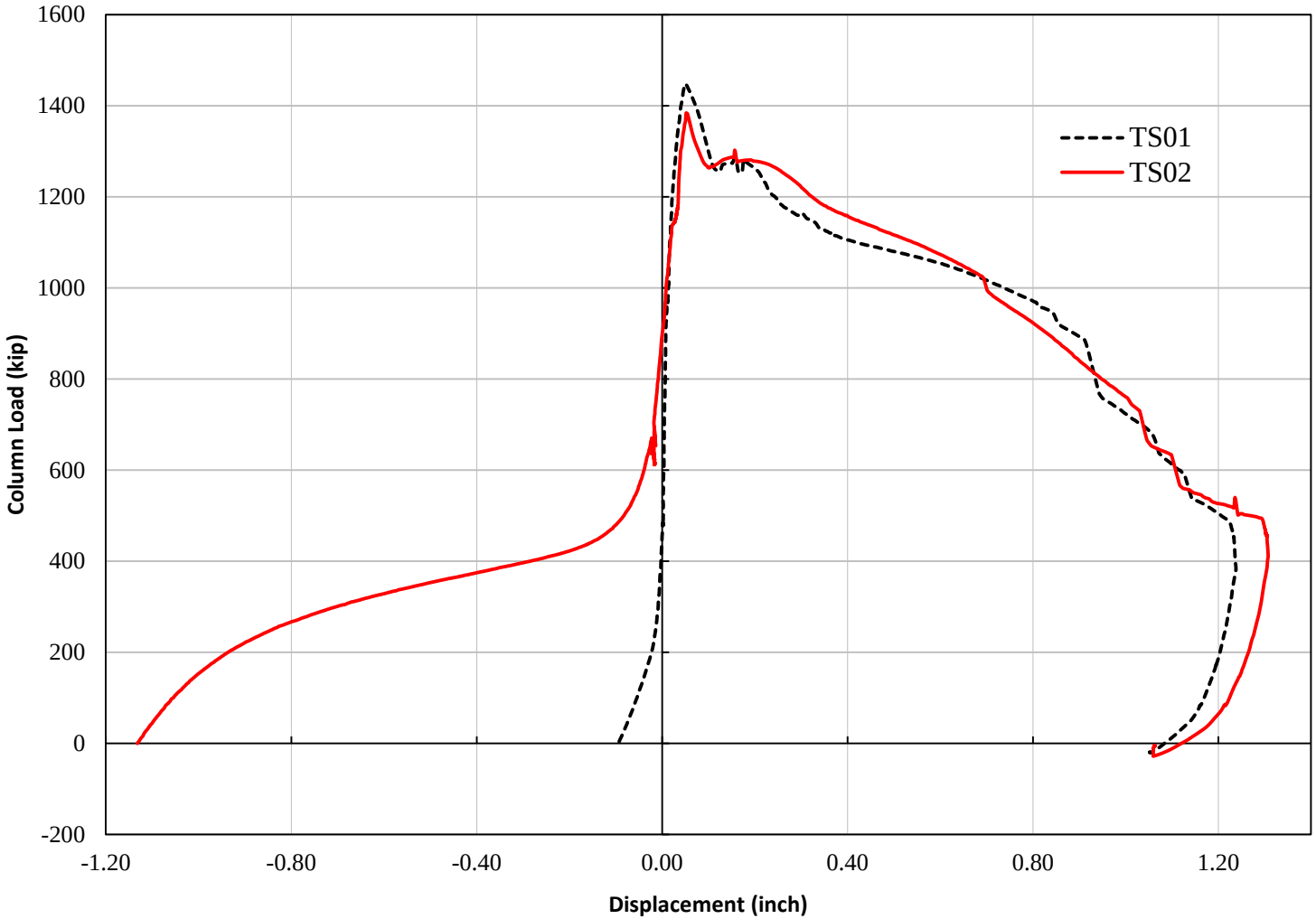

Figure 5-29: Load versus testing region deformation using head-travel data

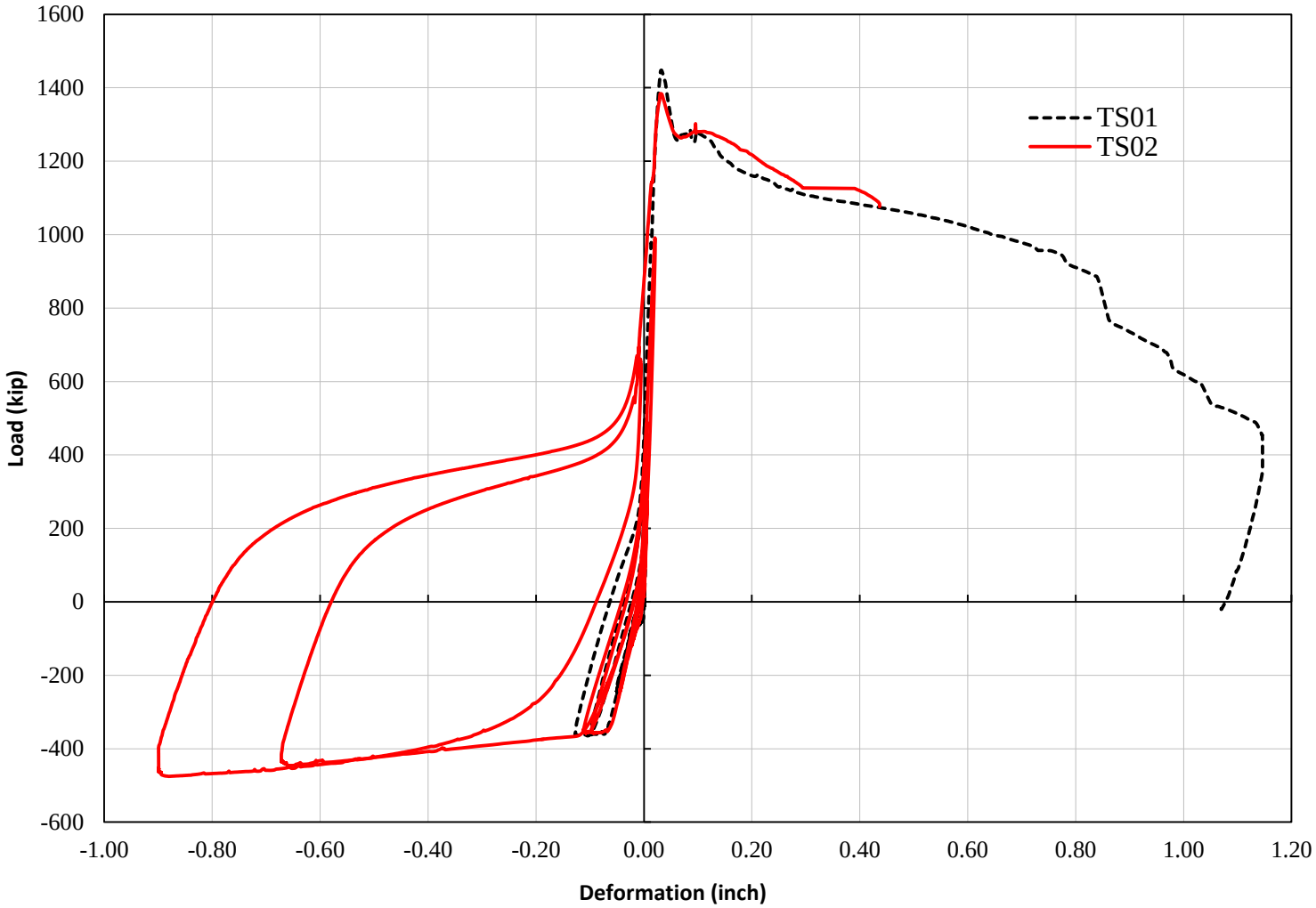

Figure 5-30: Load versus testing region deformation using the average of LVDT

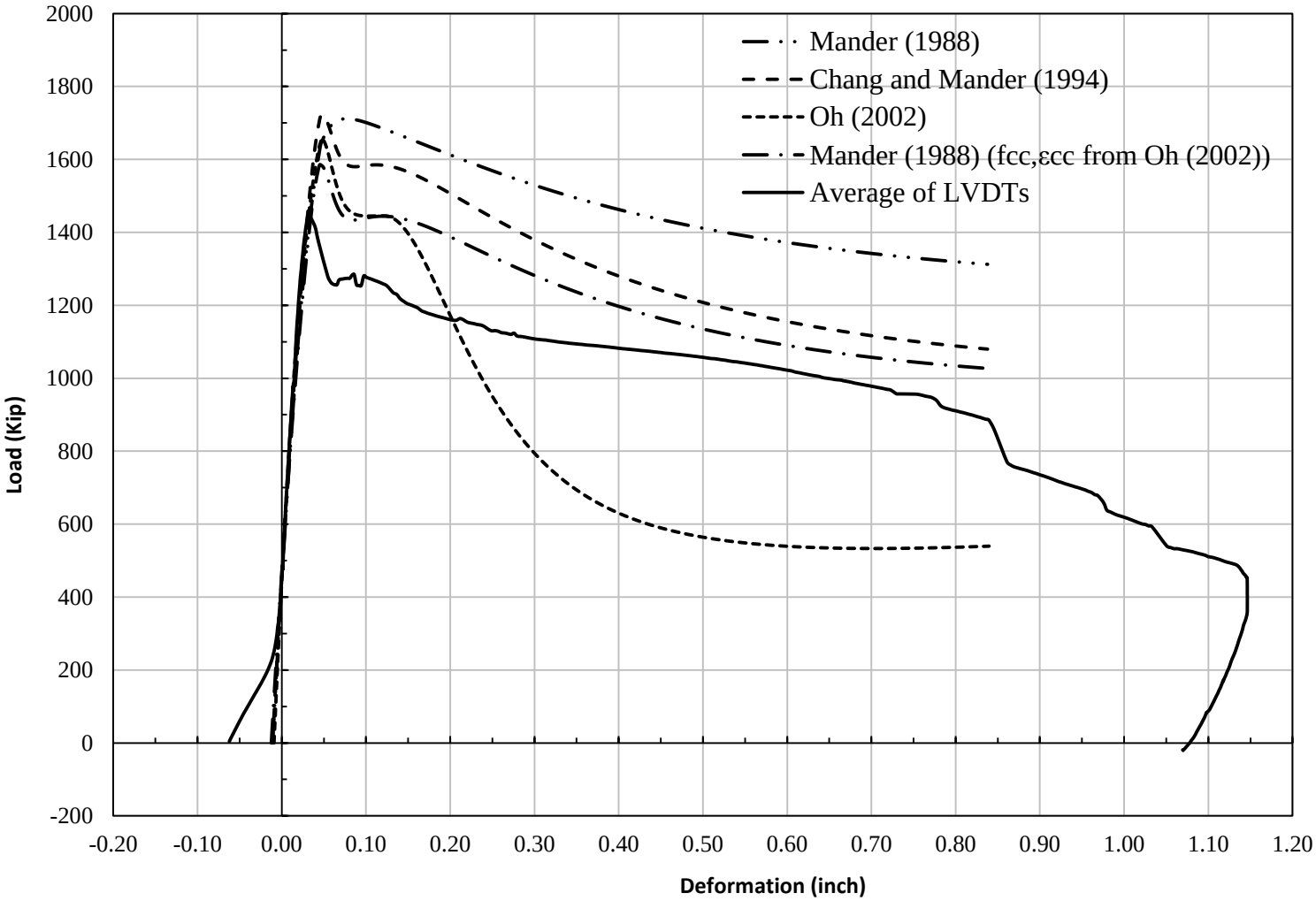

Figure 5-31: Theoretical deformation models and LVDT data for TS01

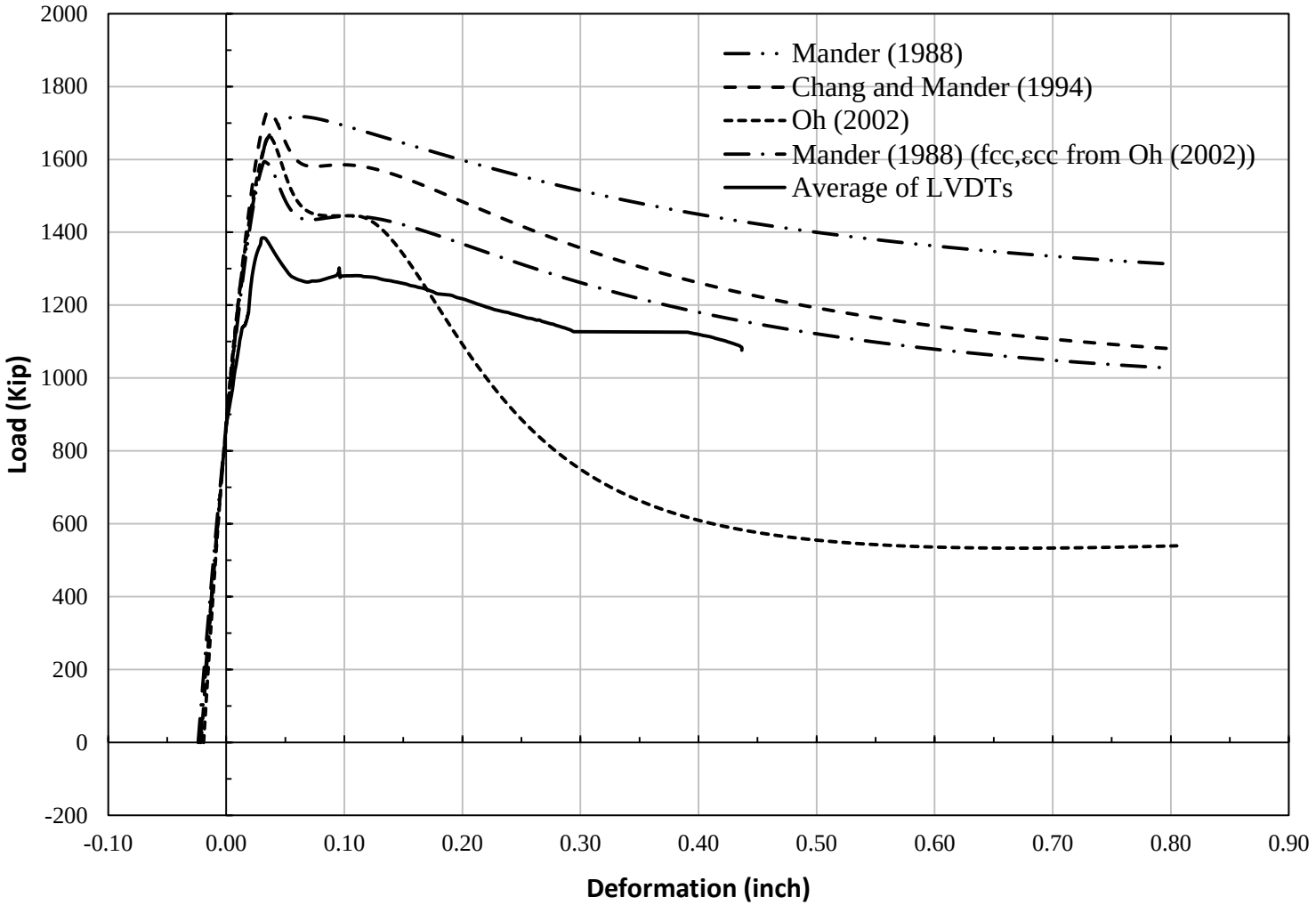

Figure 5-32: Theoretical deformation models and LVDT data for TS02

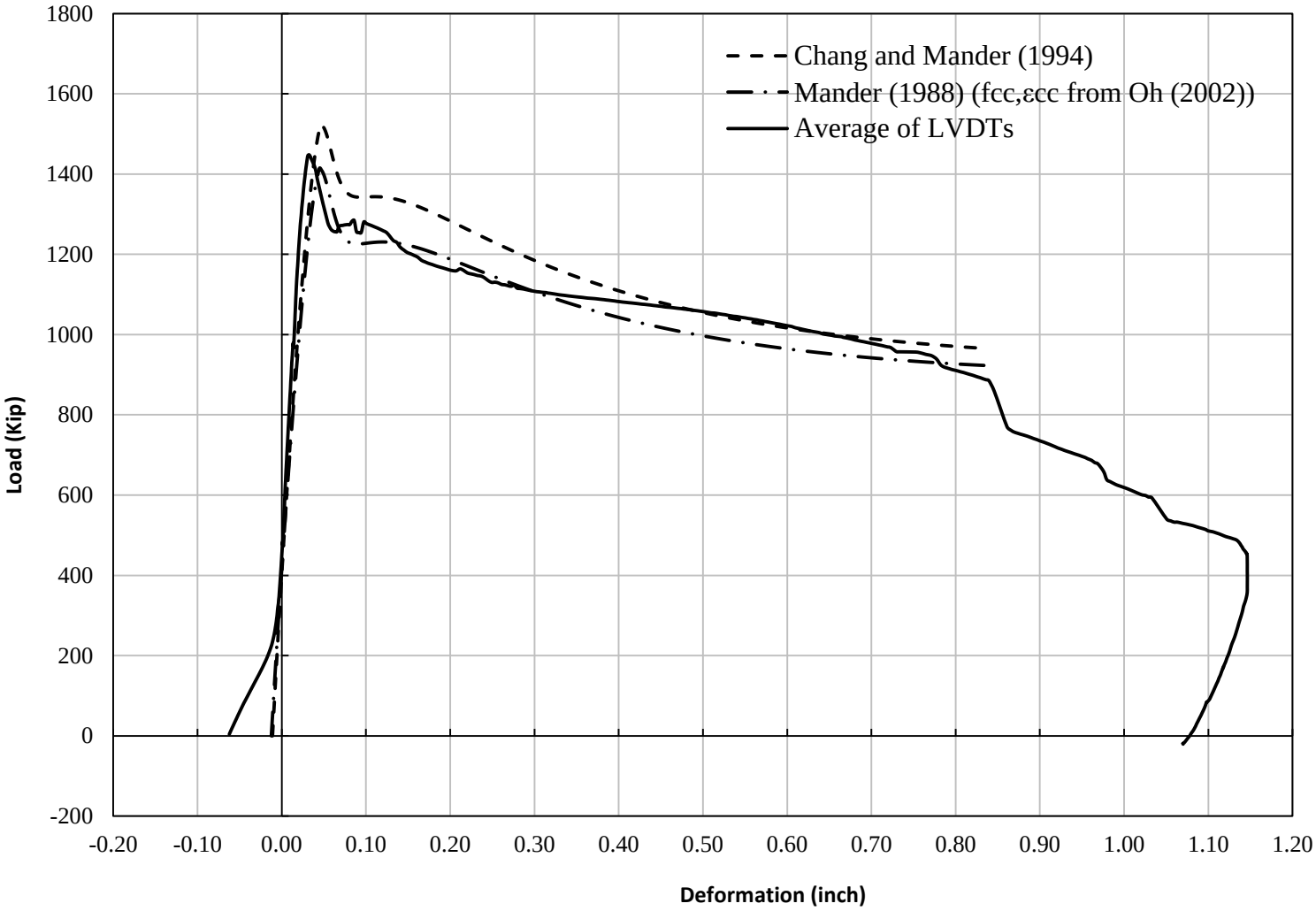

Figure 5-33: Reduced strength theoretical deformation models and LVDT data for TS01

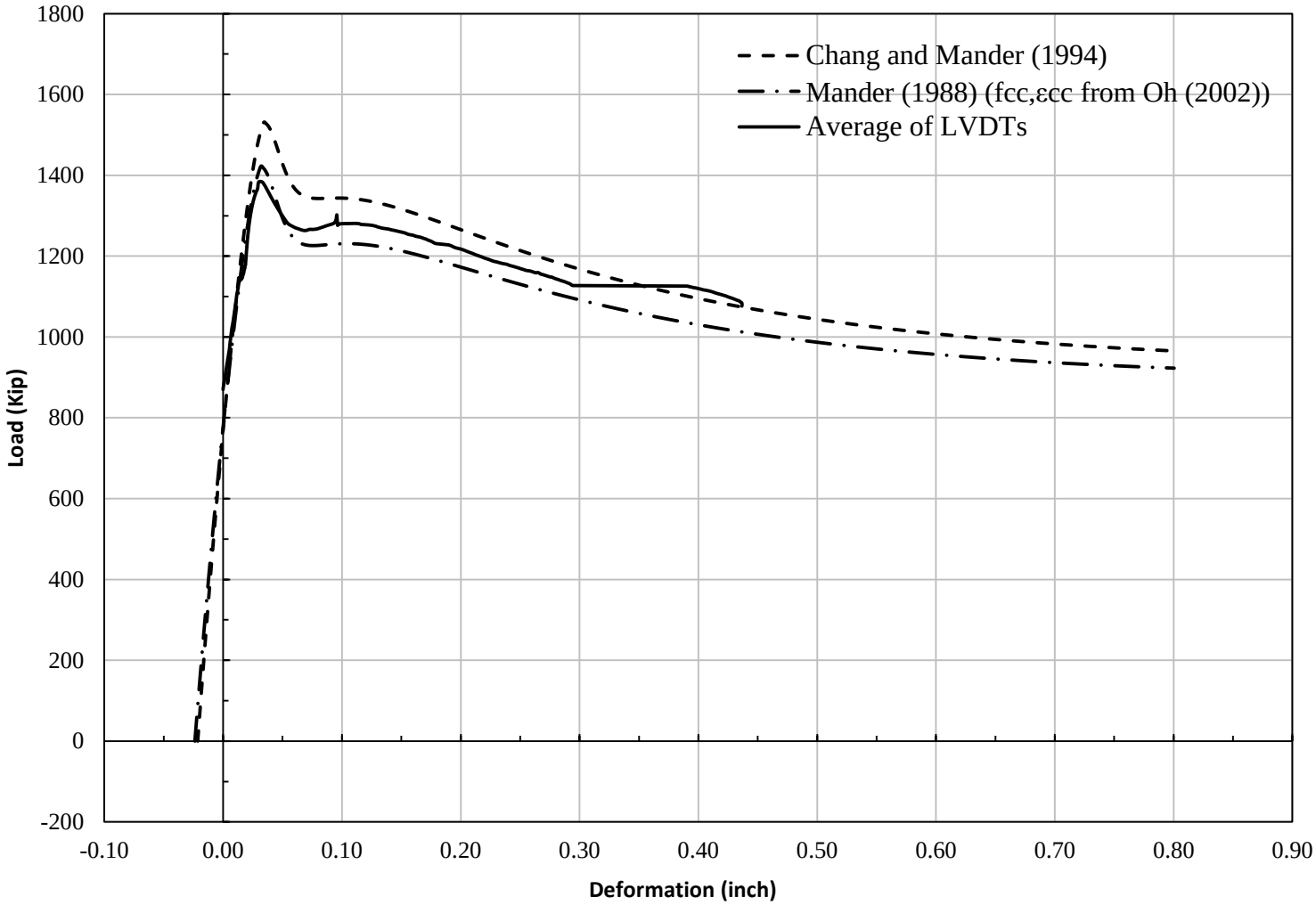

Figure 5-34: Reduced strength theoretical deformation models and LVDT data for TS02

CHAPTER 6

SUMMARY, CONCLUSIONS, AND FUTURE WORK

This chapter summarizes important finding and conclusions of the research. Section 6.1 briefly restates the objectives of the research, Section 6.2 presents conclusions of the research, and Section 6.3 outlines recommendations for future work.

6.1 SUMMARY

This research investigates the effects of inelastic tensile cyclic loading of the longitudinal mild steel reinforcement embedded in a confined concrete core on the behavior, strength, and ductility of the confined concrete. Repeated inelastic tensile deformations of the longitudinal mild steel reinforcement bars inside the confined concrete core cause large cracks in the confined concrete. Whether these inelastic steel deformations and cracks in the concrete affect the compression behavior, strength, and ductility of the confined concrete is studied.

The research is a study of the critical confined concrete crushing height of the boundary zone confined concrete in a well-detailed reinforced concrete lateral-load-resisting wall where the longitudinal mild steel reinforcement inside the confined core yields and develops a plastic hinge at the base of the wall. The material properties, concrete confinement geometry, and loading procedure for the test specimens are representative of the boundary zone confined concrete of an unbonded post-tensioned cast-in-place concrete special structural wall. The experimental program included two identical 10 in. x 15 in. cross-section confined concrete specimens. The specimens were loaded to two different ranges of quasi-static inelastic tensile cyclic loading of the longitudinal mild steel reinforcement bars. Test specimen 1 and Test specimen 2 were subjected to a peak tensile strain of 4 times and 16 times the yielding strain of the longitudinal mild steel reinforcement bars, respectively.

The test results for the two test specimens were compared to observe the effects of different levels of inelastic tensile cyclic loading of the longitudinal mild steel reinforcement bars inside the confined concrete. The test results were also compared with the theoretical results from previously developed confined concrete models under monotonic compression loading. These comparisons focused on the effects of tensile cyclic loading on the compression behavior, strength, and ductility of confined concrete.

6.2 CONCLUSIONS

Based on the research, the following conclusions are drawn:

1. The confined concrete compression behavior, strength, and ductility were similar for the two test specimens with two different inelastic tensile cyclic loading ranges. The difference in peak compression strength was 4.5%, and the compression stiffness and ductility were the same.

2. Based on comparison of the tests results with the theoretical models for monotonic compression loading, the compression stiffness and ductility of the confined concrete were not affected by inelastic tensile cyclic loading of the longitudinal mild steel reinforcement inside the confined concrete core.

3. It was noted that after inelastic tensile deformation of the longitudinal mild steel reinforcement inside the confined concrete core, the compression load required to close the cracks was greater than the prior tensile load. In the inelastic tensile deformation load steps, the reversing confined concrete compression strain was small compared to the tensile strain, and the reversing compression strain in longitudinal reinforcement bars was small compared to tensile strain.

4. In this research, it was assumed that the field-cured concrete cylinders correctly represented the in situ compression strength of the concrete in the test specimens. Based on this assumption and a comparison of experimental results with the theoretical models, there was a considerable reduction in the compression strength of confined concrete. On average for the two test specimens, the strength reduction was 18% compared to the Mander (1988) model, 18% compared to the Chang and Mander (1994) model, and 14% compared to the Oh (2002) model for confined concrete.

6.3 FUTURE WORK

1. From comparison of the test results with the theoretical models, it was noted that there was a reduction in the confined concrete strength in the test specimens relative to the models. To understand whether the inelastic tensile cyclic loading of the longitudinal mild steel reinforcement inside the confined concrete reduced the strength of the confined concrete, a specimen of the same design needs to be tested for monotonic compression loading. The results of the current test results can be compared with test results of the monotonic compression loading test specimen to figure out if the strength reduction was caused by the inelastic tensile cyclic loading.

2. As noticed from the test results, the confined concrete compression behavior, strength, and ductility were similar for the two test specimens with the two different inelastic tensile cyclic loading ranges. To understand whether greater inelastic tensile cyclic loading of the longitudinal mild steel reinforcement inside the confined concrete affects the compression behavior, strength, and ductility of confined concrete, a specimen of the same design needs to be tested with a higher inelastic tensile cyclic loading of the longitudinal mild steel reinforcement inside the confined concrete. The maximum limit of the tensile loading can be determined by the test results of unbonded post-tensioned cast-in-place concrete special structural wall specimen tested in ATLSS Center at Lehigh University.

REFERENCES

ACI Committee 318, "Building Code Requirements for Structural Concrete," American Concrete Institute, Farmington Hills, MI, August 2011.

ACI Subcommittee 445-1, "Examples for the Design of Structural Concrete with Strut-and-Tie Models," *Structural Journal*, American Concrete Institute, Farmington Hills, MI, September 2002.

Ahmad, S.H. and Shah, S.P., "Stress-Strain Curves of Concrete Confined by Spiral Reinforcement," *Structural Journal*, American Concrete Institute, Vol. 79, No. 6, December 1982, pp. 484-490.

Blume, J. A., Newmark, N. M., and Corning, L. H., "Design of Multi-Story Reinforced Concrete Buildings for Earthquake Motions," Portland Cement Association, Chicago, Chapter 5, January 1961.

Chang, G. A., and Mander, J. B., "Seismic Energy Based Fatigue Damage Analysis of Bridge Columns: Part I – Evaluation of Seismic Capacity," Technical Report NCEER-94-0006, State University of New York at Buffalo, Buffalo, NY, May 1994, pp. 210.

Dodd, L. L., and Restrepo-Posada, J. I., "Model for Predicting Cyclic Behavior of Reinforcing Steel," *Journal of Structural Engineering*, American Society of Civil Engineers, Vol. 121, No. 3, March 1995, pp. 433-445.

El-Sheikh, M., "Seismic Analysis, Behavior, and Design of Unbonded Post-Tensioned Precaste Concrete Frames," Ph.D. Dissertation, Department of Civil and Environmental Engineering, Lehigh University, Bethlehem, PA, 1997, pp. 456.

El-Sheikh, M., Sause, R., Pessiki, S., and L.-W., "Seismic Behavior and Design of Unbonded Post-Tensioned Precast Concrete Frames," *PCI Journal*, Precast/Prestressed Concrete Institute, Vol. 44, No. 3, May-June 1999, pp. 54-71.

Fafitis, A., and Shah, S. P., "Prediction of Ultimate Behavior of Confined Columns Subjected to Large Deformations," *Journal Proceedings*, American Concrete Institute, Vol. 82, No. 4, August 1985, pp. 423-442.

Joint ACI-ASCE Committee 445, "SP-273 Further Examples for the Design of Structural Concrete with Strut-and-Tie Models," American Concrete Institute, Chicago, IL, 2010.

Kent, D. C., and R. Park., "Cyclic Load Behavior of Reinforcing Steel," Strain, Vol. 9, No. 3, July 1973, pp. 98-103.

Kent, D. C., and Park, R., "Flexural Members with Confined Concrete," *Journal of Structural Engineering*, American Society of Civil Engineers, Vol. 97, No. ST7, July 1971, pp. 1969-1990.

KotsovosI, M. D., "Consideration of Triaxial Stress Conditions in Design: A Necessity," *Structural Journal*, American Concrete Institute, Vol. 84, No. 3, May 1987, pp. 266-273.

Kurama, Y. C., "Seismic Analysis, Behavior, and Design of Unbonded Post-Tensioned Precaste Concrete Walls," Ph.D. Dissertation, Department of Civil and Environmental Engineering, Lehigh University, Bethlehem, PA, 1997, pp. 491.

Kurama, Y. C., Sause, R., Pessiki, S., and Lu, L.-W., "Lateral Load Behavior and Seismic Design of Unbonded Post-Tensioned Precast Concrete Walls," *Structural Journal*, American Concrete Institute, Vol. 96, No. 4, July-August 1999b, pp. 622-632.

Mander, J., Priestley, M., and Park, R., "Observed Stress-strain Model for Confined Concrete," *Journal of Structural Engineering*, American Society of Civil Engineers, Vol. 114, No. 8, August 1988b, pp. 1827-1849.

Mander, J., Priestley, M., and Park, R., "Theoretical Stress-strain Model for Confined Concrete", *Journal of Structural Engineering*, American Society of Civil Engineers, Vol. 114, No. 8, August 1988a, pp. 1804-1826.

Montoya E., Vecchio, F. J., and Sheikh, S. A., "Compression Field Modeling of Confined Concrete," *Journal of Structural Engineering and Mechanics*, Vol. 12, No. 3, 2001, pp. 231-248.

Nilson, A. H., Darwin, D., and Dolan, C. W., *Design of Concrete Structures*, 14th Edition, McGraw-Hill, Inc., New York, NY, 2010, pp. 795.

Oh, B., "A Plasticity Model for Confined Concrete under Uniaxial Loading," Ph.D. Dissertation, Department of Civil and Environmental Engineering, Lehigh University, Bethlehem, PA, 2002, pp. 398.

Pakiding, Leary, "Analytical and Experimental Studies of Seismic Resistant Unbonded Post Tensioned (UPT) Special Reinforced Concrete (RC) Wall," Ph.D. Dissertation, Department of Civil and Environmental Engineering, Lehigh University, Bethlehem, PA, December 2014 (Expected).

Park, R., Priestley, M. J. N., and Gill, W. D., "Ductility of Square Confined Concrete Columns," *Journal of Structural Engineering*, American Society of Civil Engineers, Vol. 108, ST4, 1982, pp. 929-950.

Paulay, T., and Priestley, M. J. N., *Seismic Design of Reinforced Concrete and Masonry Buildings*, John Wiley and Sons, Inc., 1992, pp. 733.

Paultre, P., and Légeron, F., "Confinement Reinforcement Design for Reinforced Concrete Columns," *Journal of Structural Engineering*, American Society of Civil Engineers, Vol. 134, No. 5, May 2008, pp. 738-749.

Pauw, A., "Static Modulus of Elasticity of Concrete as Affected by Density," *Journal Proceedings*, American Concrete Institute, Vol. 32, No. 6, December 1960, pp. 679-687.

Perez, F. J., "Experimental and Analytical Lateral Load Response of Unbonded Post-tensioned Precast Concrete Walls," Ph.D. Dissertation, Department of Civil and Environmental Engineering, Lehigh University, Bethlehem, PA, 2004, pp. 353.

Perez, F. J., Pessiki, S., and Sause, R., "Experimental and Analytical Lateral Load Response of Unbonded Post-tensioned Precast Concrete Walls," Center for Advanced Technology for Large Structural Systems (ATLSS) Report No. 04-11, Lehigh University, Bethlehem, PA, May 2004, pp. 350.

Popovics, S., "A Numerical Approach to the Complete Stress-Strain Curve of Concrete," Cement and Concrete Research, Vol. 3, No. 4, September 1973, pp. 583-599.

Rahman, A. M. and Restrepo, J. I., "Earthquake Resistant Precast Concrete Buildings: Seismic Performance of Cantilever Walls Prestressed Using Unbonded Tendons," Civil Engineering Research Report No. 2000-5, University of Canterbury, Christchurch, New Zealand, August 2000, pp. 110.

Richart, F. E., Brandtzaeg, A., and Brown, R. L., "A Study of the Failure of Concrete Under Combined Compressive Stresses," University of Illinois Engineering Experimental Station, Bulletin No. 185, January 1928, pp. 104.

Rivera, M., "Experimental Laboratory Procedure for the Construction and Testing of Seismic Resistant Unbonded Post-Tensioned Special Reinforced Concrete Walls," M.Sc. Report, Department of Civil and Environmental Engineering, Lehigh University, Bethlehem, PA, October 2013 (Expected).

Scott, B. D., Park, R., and Priestley, M. J. N., "Stress-Strain Behavior of Concrete Confined by Overlapping Hoops at Low and High Strain Rates," American Concrete Institute, Vol. 79, No. 1, February 1982, pp. 13-27.

Sheikh, S. A., and Uzumeri, S. M., "Analytical Model for Concrete Confinement in Tied Columns," *Journal of Structural Engineering*, American Society of Civil Engineers, Vol. 108, ST12, December 1982, pp. 2703-2722.

Sheikh, S. A., and Uzumeri, S. M., "Strength and Ductility of Confined Concrete Columns," *Journal Proceedings*, American Society of Civil Engineers, Vol. 106, No. ST5, May 1980, pp. 1079-1102.

Sheikh, S. A., and Yeh, C. C., "Flexural Behavior of Confined Concrete Columns," *Journal Proceedings*, American Concrete Institute, Vol. 83, No. 3, June 1986, pp. 389-404.

Srivastava, S., “Analytical Lateral Load Response of Unbonded Post-Tensioned Cast-in-place Concrete Special Structural Walls with Bonded or Debonded Longitudinal Mild Steel Reinforcement,” M.Sc. Report, Department of Civil and Environmental Engineering, Lehigh University, Bethlehem, PA, January 2013, pp. 233.

Sulayfani, A. and Lamirault, J., “Contribution à l'analyse expérimentale du comportement mécanique cyclique du béton (in French),” Materials and Structures/ Matériaux et Constructions, Vol. 20, No. 118, July 1987, pp. 283-292.

Tsai, W. T., “Uniaxial Compressional Stress-Strain Relation of Concrete,” *Journal of Structural Engineering*, American Society of Civil Engineers, Vol. 114, No. 9, September 1988, pp. 2133-2136.